



Universiteit
Antwerpen

Faculteit Wetenschappen
Departement Fysica

*Advanced Algorithms for Quantitative Electron
Tomography*

*Geavanceerde Algoritmes voor Kwantitatieve
Elektronentomografie*

Proefschrift voorgelegd tot het behalen van de graad van Doctor in de
Wetenschappen aan de Universiteit Antwerpen, te verdedigen door

Daniele Zanaga

Promotor
Prof. Dr. Sara Bals

Antwerpen
November, 2017

Doctoral Committee

Chairman

Prof. Dr. Jan Sijbers, University of Antwerp - Belgium

Promoter

Prof. Dr. Sara Bals, University of Antwerp - Belgium

Members

Prof. Dr. Wim Wenseleers, University of Antwerp - Belgium

Prof. Dr. Werner Grogger, Graz University of Technology - Austria

Prof. Dr. Alfons van Blaaderen, University of Utrecht - The Netherlands

Prof. Dr. Francois Peeters, University of Antwerp - Belgium

Prof. Dr. Tom Breugelmans, University of Antwerp - Belgium

Contact information

Daniele Zanaga

University of Antwerp - Department of Physics

EMAT - Electron Microscopy for Materials Science

Groenenborgerlaan 171

B-2020 Antwerp

Belgium

daniele.zanaga@uantwerpen.be

Contents

Summary	1
Samenvatting	4
List of Abbreviations	7
1 Historical Perspective	11
1.1 Nanotechnology, Nanoscience & Nanomaterials	11
1.2 Transmission Electron Microscopy	13
1.3 Energy Dispersive X-ray Spectroscopy	15
1.4 Electron tomography	15
2 Electron Tomography Principles	19
2.1 Projections acquisition	19
2.1.1 Missing wedge artifacts	20
2.2 The reconstruction problem	21
2.3 Fourier slice theorem	24
2.4 Reconstruction methods	26
2.4.1 Fourier space methods	26
2.4.2 Direct methods: backprojection & weighted backprojection	26
2.4.3 Iterative techniques	27
2.5 Prior knowledge in the reconstruction	31
2.5.1 Discrete Algebraic Reconstruction Technique	31
2.5.2 Total variation minimization	32
2.5.3 Limitations and further developments	34
3 Electron Tomography in Practice	35
3.1 The transmission electron microscope	35
3.1.1 Imaging modes	36
3.1.2 Spectroscopic imaging modes	37
3.1.3 The ChemiSTEM system	39
3.1.4 Tomography holders	40

3.2	Experiment workflow	41
3.2.1	Sample preparation	41
3.2.2	Tilt series acquisition	42
3.2.3	Tilt series alignment	43
3.2.4	Tilt axis alignment	44
3.2.5	Offset correction	46
3.2.6	Non-linear thickness effects	47
3.2.7	Reconstruction and visualization	48
3.2.8	Tomography database	48
4	Quantitative Tomography of Nanoparticle Assemblies	53
4.1	Introduction	53
4.1.1	Self-assembly	53
4.1.2	Electron tomography of nanoparticles assemblies	53
4.2	Nanoparticles assemblies quantification	56
4.3	Prior-knowledge implementation	57
4.3.1	Mathematical formulation	57
4.3.2	Implementation	59
4.4	Phantom studies	60
4.4.1	Three-dimensional phantom study	62
4.5	Iron cobalt oxide assemblies obtained by spherical confinement	64
4.5.1	Synthesis and TEM preparation of the Fe–Co–O assemblies	64
4.5.2	Acquisition and alignment of the tilt series	65
4.5.3	SIRT and SSR comparison	65
4.5.4	Structural analysis	71
4.6	Beam sensitive assemblies and high throughput tomography	74
4.7	Accuracy and limitations of SSR	75
4.7.1	Spherical basis shape	76
4.7.2	Undetected particles	76

5	Sparse Sphere Reconstruction in Materials Science Studies	79
5.1	Supracrystalline Colloidal Eggs	79
5.2	Binary Assemblies.....	81
5.2.1	Binary SSR reconstruction	83
5.2.2	Structural characterization.....	85
6	Conclusions and Outlook on Part II.....	89
6.1	Conclusions	89
6.2	Outlook.....	89
6.2.1	Assemblies of atoms.....	89
6.2.2	Platelets, cubes and rods assemblies.....	91
6.3	Detailed list of contributions to part II	91
7	Quantitative EDXS in 2D	95
7.1	Introduction to quantitative EDXS.....	95
7.2	The Cliff-Lorimer Method	96
7.3	The ζ -factor Method	97
7.3.1	Equivalence of thin-film and nanoparticles formula	98
7.4	Determination of ζ -factors.....	99
7.4.1	Volume calculation.....	100
7.4.2	EDXS acquisition and beam current calibration	102
7.4.3	ζ -factor calculation and error estimation	104
7.5	Quantification and analysis of 2D EDXS data	108
7.5.1	Quantification of elemental maps in hetero nanoparticles	109
7.5.2	Application to Au-Pt hetero-nanostructures	110
7.6	Volume measurement of nanoparticles by means of EDXS	111
7.7	Thickness measurement by means of EDXS.....	114
7.7.1	Method.....	114
7.7.2	Experimental validation.....	116
8	Quantitative EDXS in 3D	125

8.1	Introduction	125
8.2	Detector shadowing	125
8.2.1	Strategies to overcome the shadowing problem	126
8.3	Quantitative 3D EDXS reconstruction method	127
8.4	Quantitative characterization of octahedral Au/Ag nanorattle with complex chemical structure	130
8.5	Error estimation	136
9	Quantitative 3D EDXS Tomography, Materials Science Studies	139
9.1	Au@Ag nanorattles obtained by galvanic replacement	139
9.1.1	HAADF-STEM and 2D EDXS analysis	139
9.1.2	3D quantitative EDXS tomography analysis	142
9.1.3	Galvanic replacement reaction mechanism in the presence of ascorbic acid.	147
9.2	Quantitative EDXS tomography of a AuAgPt nanorattle	147
9.3	Quantitative determination of the residual silver in nanoporous gold catalyst	151
9.3.1	2D STEM and EDXS analysis	152
9.3.2	3D quantitative EDXS tomography	153
10	Conclusions and Outlook on Part III	157
10.1	Conclusions	157
10.2	Outlook	157
10.3	Detailed list of contributions on part III	158
11	Appendix A – Bond Order Parameters	161
12	References	163
	List of scientific contributions	179
	Acknowledgements	182

Summary

In the last decades researchers started developing the ability to manipulate matter at the nano and atomic scales. The characterization of these materials revealed the influence of size, structure and composition on the peculiar properties exhibited. A fundamental instrument aiding the development of new nanomaterials by enabling their observation is the Transmission Electron Microscope (TEM). However, conventional TEM only allows for two-dimensional imaging of specimens, often hindering a complete characterization. Combination of TEM and tomography overcomes this limitation, allowing to retrieve a three-dimensional reconstruction of the analyzed sample.

The increasing complexity of synthesized systems though, built in the attempt of achieving particular properties for applications in several fields such as catalysis, signal enhancement or drug delivery, poses new challenges to researchers involved in their characterization. The development of new methods, techniques and instruments is therefore necessary in such occasions in order to obtain a complete description of these samples.

An example of complex systems requiring a challenging characterization is given by nanoparticle assemblies. These structures, created by promoting the self-assembly of hundreds or thousands of nanoparticles, can extend for hundreds of nanometers or even microns, with either an ordered or disordered configuration. Their properties can be tuned by changing the positions of the building blocks, the type of packing and the inter-particles distances. A thorough quantitative characterization is therefore needed to study the relationship between structure and properties, and how changing the former can influence the latter.

Another fundamental problem that has been tackled extensively by several research groups in the recent years, is the determination of the three-dimensional elemental distribution in nanostructures, which can be achieved by combining Energy Dispersive X-ray Spectroscopy (EDXS) and tomography. The recent introduction of multiple detectors systems such as FEI Super-X detector, finally enabled this combination, but earlier attempts, although producing promising results, were still hampered by instrument limitations and lack of proper EDXS quantification methods.

My work as a PhD student at EMAT has been focused on the development of techniques for electron tomography, and specifically oriented at the quantitative analysis of nanoparticles assemblies as well as quantitative EDXS analysis of metal nanoparticles in 2D and 3D. For this reason, the thesis is divided into three main parts, an introduction on the techniques used, a part on the quantitative analysis of nanoparticle assemblies and finally a part on quantitative EDXS tomography.

In more detail the layout is as follows:

Part 1: Introduction

Chapter 1: Historical perspective, presents the main historical events that brought to the development of the electron microscope.

Chapter 2: Electron tomography principles, summarizes the main concepts and state-of-the-art of electron tomography, introducing the foundations, applications and limitations of the technique on which this thesis work is based on.

Chapter 3: Electron tomography in practice, presents the experimental equipment used, and the steps involved in a typical electron tomography experiment, from a practical point of view.

Part 2: Quantitative tomography of nanoassemblies

Chapter 4: Quantitative tomography of nanoparticle assemblies covers the development of the so called Sparse Sphere Reconstruction technique, aimed at the characterization of complex nanoparticles assemblies.

Chapter 5: Sparse sphere reconstruction in materials science studies further introduces experimental studies where SSR was applied to perform a quantitative characterization of different systems, with a focus on the technique extension to the case of binary assemblies.

Chapter 6: Conclusions and outlook on part II summarizes the results presented in this second part of the thesis, including a discussion on the novelty introduced by the technique and the outlook for future applications. A detailed list of own contributions to the work is provided at the end of this chapter.

Part 3: Quantitative EDXS tomography

Chapter 7: Quantitative EDXS in 2D covers EDXS characterization and quantification of nanomaterials. In more detail, the ζ -factor method is introduced and a technique is developed for the measurement of ζ -factors from pure elemental nanoparticles. Experimental cases are shown as a validation of the method and as an example of quantitative EDXS studies.

Chapter 8: Quantitative EDXS in 3D further extends the domain of quantitative EDXS to 3D. Here, a new method developed to obtain quantitative EDXS tomographic reconstructions is presented, showing in detail how limitations such as *shadowing effects* and low morphological resolution of EDXS are overcome by combining EDXS and STEM tomography in a synergistic approach.

Chapter 9: Quantitative 3D EDXS tomography, materials science studies. The technique presented in the previous chapter is applied here to several materials science studies. Insights concerning the synthesis of these materials and their properties are obtained thanks to this characterization.

Chapter 10: Conclusions and outlook on part III summarizes the results presented in this third part of the thesis, and discusses the novelties introduced by the techniques presented and the outlook for future applications. A detailed list of own contributions to the work is provided at the end of this chapter.

Samenvatting

In de laatste decennia begonnen onderzoekers het vermogen te ontwikkelen om materie te manipuleren op zowel nano- als atomaire schaal. De karakterisering van deze materialen onthulde de invloed van grootte, structuur en samenstelling op de bijzondere eigenschappen van deze materialen. Een fundamenteel instrument, die meewerkte aan de ontwikkeling van deze nieuwe nanomaterialen door hun observatie mogelijk te maken, is de transmissie-elektronenmicroscop (TEM). Conventionele TEM maakt echter enkel tweedimensionale beeldvorming van objecten mogelijk, hetgeen vaak een volledige karakterisering bemoeilijkt. Een combinatie van TEM en tomografie overwint deze beperking, wat een driedimensionale reconstructie van het geanalyseerde object mogelijk maakt.

De toenemende complexiteit van gesynthetiseerde systemen, trachtend specifieke eigenschappen te bekomen voor welbepaalde toepassingen in verschillende gebieden, zoals katalyse, signaalversterking of medicijnafgifte, levert nieuwe uitdagingen voor onderzoekers, die betrokken zijn bij hun karakterisering, op. De ontwikkeling van nieuwe methodes, technieken en instrumenten is daarom noodzakelijk om een volledige beschrijving van deze objecten te verkrijgen.

Een voorbeeld van complexe systemen die een uitdagende karakterisering vereisen, zijn assemblages van nanodeeltjes. Deze structuren, gemaakt door het bevorderen van de zelfassemblage van honderden tot duizenden nanodeeltjes, kunnen dimensies hebben van honderden nanometers tot zelfs micrometers, met een geordende of ongeordende configuratie. Hun eigenschappen kunnen afgestemd worden door de posities van de bouwstenen, de soort symmetrie en de afstanden tussen de deeltjes aan te passen. Een grondige kwantitatieve karakterisering is daarom noodzakelijk om de relatie tussen de structuur en de eigenschappen te bestuderen, en hoe een verandering van de eerstgenoemde de laatstgenoemde kan beïnvloeden.

Een ander fundamenteel probleem dat uitgebreid werd bestudeerd door verschillende onderzoeksgroepen in de afgelopen jaren, is de bepaling van de driedimensionale chemische samenstelling van nanostructuren. Dit kan onderzocht worden door het combineren van energie dispersieve X-stralen spectroscopie (EDXS) en tomografie. De recente introductie van meerdere detectorsystemen zoals de FEI Super-X detector, maakte deze combinatie uiteindelijk mogelijk, maar eerder pogingen werden nog steeds gehinderd door instrument beperkingen en een gebrek aan goede EDXS kwantificatiemethoden, hoewel de resultaten er veelbelovend uitzagen.

Mijn werk als doctoraatsstudent aan EMAT is gericht op de ontwikkeling van technieken voor elektronentomografie, en specifiek op de kwantitatieve analyse van assemblages van nanodeeltjes evenals de kwantitatieve EDXS analyse van metallische nanodeeltjes in twee en drie dimensies. Het proefschrift is daarom verdeeld in drie hoofdonderdelen: een inleiding tot de gebruikte technieken, een

deel over de kwantitatieve analyse van assemblages van nanodeeltjes en ten slotte een deel over kwantitatieve EDXS tomografie.

In meer detail is de inhoud als volgt:

Deel 1: Introductie

Hoofdstuk 1: Historische achtergrond, introduceert de belangrijkste historische gebeurtenissen die de ontwikkeling van elektronenmicroscopie teweegbrachten.

Hoofdstuk 2: Elektronentomografie principes, vat de belangrijkste concepten en state-of-the-art elektronentomografie samen, waarbij de fundamentele, toepassingen en beperkingen van de techniek besproken worden.

Hoofdstuk 3: Elektronentomografie in de praktijk, bespreekt de gebruikte experimentele apparatuur en de verschillende stappen van een typisch elektronentomografie experiment, vanuit een praktisch oogpunt.

Deel 2: Kwantitatieve tomografie van assemblages van nanodeeltjes

Hoofdstuk 4: Kwantitatieve tomografie van assemblages van nanodeeltjes behandelt de ontwikkeling van de zogenaamde *Sparse Sphere Reconstruction (SSR)* techniek, gericht op de karakterisering van complexe assemblages van nanodeeltjes.

Hoofdstuk 5: Sparse sphere reconstruction in materiaalkundige studies introduceert verder de experimentele studies waarbij SSR werd toegepast om een kwantitatieve karakterisering van verschillende systemen uit te voeren, met de focus op de uitbreiding van de techniek om binaire assemblages te onderzoeken.

Hoofdstuk 6: Conclusies en outlook op Deel 2 vat de resultaten van het tweede deel van dit proefschrift samen, inclusief een discussie over de nieuwheid van de techniek en de vooruitzichten op toekomstige toepassingen. Een gedetailleerde lijst met eigen bijdragen aan het werk wordt aan het einde van dit hoofdstuk gegeven.

Deel 3: Kwantitatieve EDXS tomografie

Hoofdstuk 7: Kwantitatieve EDXS in 2D beschrijft de EDXS karakterisering en kwantificatie van nanomaterialen. Specifieker, de ζ -factor methode wordt geïntroduceerd en een techniek is ontwikkeld om de ζ -factoren te bepalen uit mono-metallische nanodeeltjes. Experimentele studies worden uitgevoerd om de methode te valideren en als voorbeeld van kwantitatieve EDXS onderzoeken te dienen.

Hoofdstuk 8: Kwantitatieve EDXS in 3D breidt het domein van kwantitatieve EDXS verder uit naar 3D. Hier, wordt een nieuwe methode ontwikkeld om kwantitatieve 3D EDXS reconstructies te verkrijgen gepresenteerd. Er wordt in detail uitgelegd hoe beperkingen zoals *schaduw effecten* en lage morfologische resolutie van EDXS worden overwonnen door het combineren van EDXS en STEM tomografie in een synergetische aanpak.

Hoofdstuk 9: Kwantitatieve 3D EDXS tomografie, materiaalkundige studies. De techniek die in het vorige hoofdstuk werd geïntroduceerd, wordt hier toegepast op verschillende materiaalkundige studies. Inzichten met betrekking tot de synthese van deze materialen en hun eigenschappen worden verkregen dankzij deze karakterisering.

Hoofdstuk 10: Conclusies en outlook op Deel 3 geeft een samenvatting van de resultaten uit dit derde deel van het proefschrift, en bespreekt de nieuwigheden van deze ontwikkelde technieken en de vooruitzichten op toekomstige toepassingen. Een gedetailleerde lijst met eigen bijdragen aan het werk wordt aan het einde van dit hoofdstuk gegeven.

List of Abbreviations

2D	Two dimensional
3D	Three dimensional
ADF	Annular dark field
ASTRA	All Scale Tomographic Reconstruction Antwerp
ART	Algebraic reconstruction technique
BF	Bright field
BP	Backprojection
DART	Discrete algebraic reconstruction technique
EDXS	Energy dispersive X-ray spectroscopy
EDS	Energy dispersive spectrometer
EELS	Electron energy loss spectroscopy
EFTEM	Energy filtered transmission electron microscopy
ESEM	Environmental Scanning Electron Microscope
ESF	Edge spread function
fcc	Face centered cubic
bcc	Body centered cubic
FEG	Field emission gun
FFT	Fast Fourier transform
FIB	Focused ion beam
GPGPU	General-purpose computing on graphics processing units
GPU	Graphics processing unit
HAADF	High angle annular dark field
hcp	Hexagonal close packed
NP	Nanoparticle
NC	Nanocrystal
IBF	Incoherent bright-field
SAED	Selected area electron diffraction
sc	Simple cubic
SIRT	Simultaneous iterative reconstruction technique
SERS	Surface Enhanced Raman Scattering
SSR	Sparse sphere reconstruction technique
STEM	Scanning transmission electron microscope
TEM	Transmission electron microscope
TVM	Total variation minimization
WBP	Weighted backprojection

Part I

Introduction

This first part of the thesis introduces the concepts underlying my research studies as a PhD student at EMAT. Starting with a brief historical overview in chapter one, it goes on drawing a temporal framework around the discovery of nanomaterials and how their investigation has been enabled by the invention of the Transmission Electron Microscope. Chapter two moves further to the principles of electron tomography and the theory behind the most common reconstruction algorithms. The last chapter of this first part, chapter three, covers the technical aspects regarding the acquisition methods and typical processing required to perform an electron tomography experiment.

1 Historical Perspective

1.1 Nanotechnology, Nanoscience & Nanomaterials

The term *Nanotechnology* was first used in the '80s and refers to that domain of science dedicated to the study and exploitations of the peculiar properties of nanomaterials, which can be described as objects showing one or more dimensions in the range 1-100 nm. Although the word *nano* recalls futuristic feelings, nanomaterials existed long before man could observe, describe and name them.

Even life forms exhibit and create nanostructures,^[1] for example, the super hydrophobic lotus leaf,^[2] the iridescent shells of certain beetles,^[3] the feathers of peacocks and the wings of *Morpho* butterflies (Figure 1.1).^[1, 4] These are all spectacular examples of natural nanostructures with peculiar properties. Figure 1.1a shows the beautiful metallic blue color of a *Morpho* male butterfly wings. The strong reflection of blue light and the *metallic* effect originates from the interaction of light with the periodic structures forming the wings (shown in the electron micrographs of Figure 1.1b,c). The development of electron microscopes enabled the observation of these bio-materials at the nanoscale opening the way to the investigation of the physical phenomena behind,^[5] and further design of artificial bio-inspired materials for advanced applications.^[6, 7]

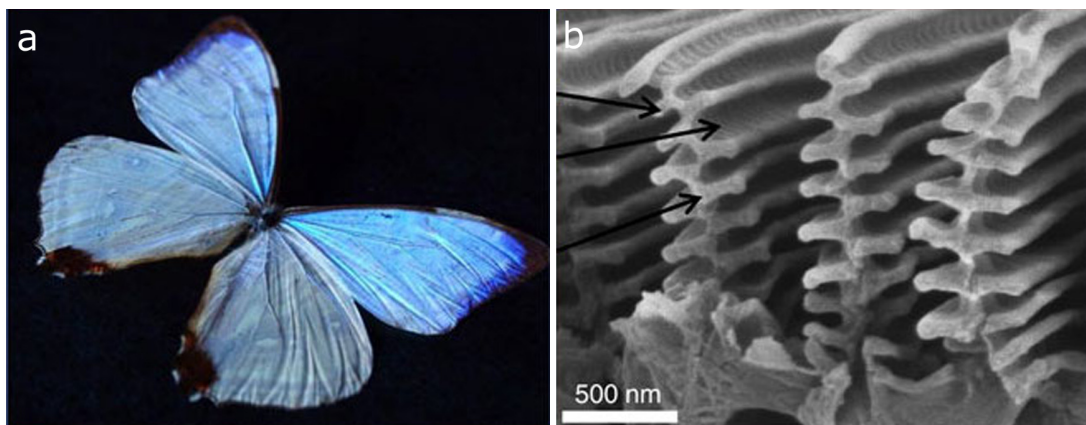


Figure 1.1 : (a) *Morpho sulkowskyi* butterfly, showing the beautiful *metallic* color of the male wings. (b) Scanning electron microscope images of a cross section of a scale of the male butterfly *Morpho sulkowskyi* wing. Images adapted from ref.^[7], Creative Commons Attribution 4.0 International license.

Proven historical uses of nanomaterials date back to the 4th century. It is well known the use of metal nanoparticles to produce colors in pottery and glass manufacturing from the Bronze age to the modern era,^[8]

a famous example of which is the Lycurgus cup (400 AD) (Figure 1.2),^[9] where golden nanoparticles are embedded in glass giving rise to dichroic light effects. Another known example concerns Indian blacksmiths that lived between the 10th and 17th centuries and who were forging steel blades containing carbon nanotubes, conferring particular mechanical properties to the metal.^[10]



Figure 1.2 : The Lycurgus Cup from 4th century AD appears green when lit from the front (left), and red when lit from the back (right). (Image from the free image service of the British Museum)

Nowadays, nanotechnology is very different from these empirical techniques developed in the ancient times by random trials and errors. Thanks to the revolutionary scientific discoveries of the last three-hundred years, humanity slowly came to understand what matter and light are, how atoms behave and how they can be observed and manipulated. The possibility of observing these materials down to the atomic scale is one of the factors that highly contributes to the progress of nanotechnologies.

One of the most important instruments developed in the last century, enabling humans to characterize nanomaterials down to the atomic scale is the Transmission Electron Microscope (TEM). There are plenty of applications and techniques for this incredible instrument, in this thesis I will present only few of them, along with my contributions to their progress in the characterization of complex nanomaterials.

1.2 Transmission Electron Microscopy

It was in 1928 when Louis de Broglie demonstrated the wave-particle duality,^[11] laying the foundations of quantum mechanics. Thanks to this property of matter, electrons can be used as probing waves. Their wavelength can be tuned by the acceleration voltage and their behavior can be manipulated by electromagnetic lenses, reaching resolutions far beyond those that can be obtained through an optical microscope, which are limited by size of the photons wavelength.

There exist different kinds of electron microscopes, the Scanning Electron Microscope (SEM), the Transmission Electron Microscope (TEM) and the Scanning Transmission Electron Microscope (STEM). In 1932, the first TEM was built at the Technological University of Berlin by Max Knoll and Ernst Ruska,^[12] opening the way to the direct observations of nanomaterials. In those years, nanomaterials became visible to the human eye and the field of nanotechnology was born. In the following years, microscopes started being manufactured by commercial companies around the world, which pushed the development forward. In 1938, Manfred von Ardenne, working for Siemens in Berlin, built the first STEM,^[13] realizing the first implementation of point-by-point scanning acquisition. However, the obtained results were not satisfying and the project was discontinued. It was thanks to the technological advancements made in the field of electronics and vacuum technologies that in 1970, Crewe was able to observe, for the first time, single heavy atoms on thin carbon layers (Figure 1.3),^[14] using a STEM. Crewe also created the first Annular Dark Field (ADF) detector, which collected the electrons scattered to high angles by the atoms nuclei, giving rise to contrast proportional to the atomic number Z , therefore known as *Z-contrast*.

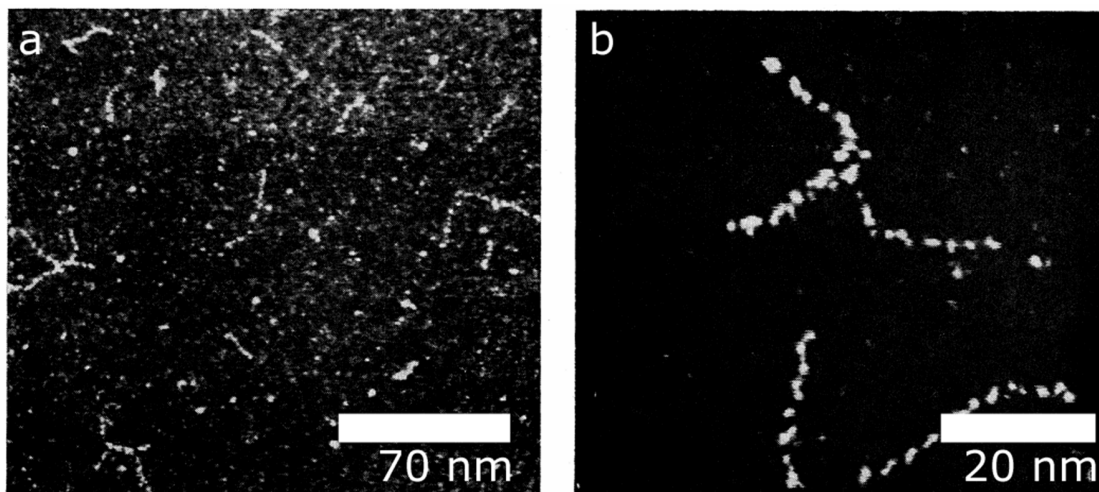


Figure 1.3 : Examples of micrographs from the work of Crewe on the imaging of heavy atoms on a thin carbon film, by Z-contrast in a STEM. (a,b) Samples obtained by depositing a dilute solution of thorium nitrate reacted with benzene tetracarboxylic acid. Chains of thorium atoms are expected to form due to the polymerization of carboxylic acid between thorium atoms. The strings of white spots are identified to be thorium atoms. Images adapted from ref.^[14], with permission of The American Association for the Advancement of Science.

The ADF detector was able to image single heavy atoms, but when used to image crystalline samples, the detector also collected Bragg diffracted electrons, with the relative contrast becoming difficult to interpret. For this reason, Howie introduced the High Angle Annular Dark Field (HAADF) detector in 1980,^[15] which almost completely eliminated diffraction contrast for crystalline materials.

With the advent of STEM and annular detectors, a new technique was also developed to retrieve information about the elements in the sample. The transmitted beam, along with electrons scattered at smaller angles was able to travel through a hole at the center of the detector and could be separated through a magnetic prism as a function of the electron's energy, forming a characteristic spectrum, related to the atomic species present in the sample. It was known that electrons would have interacted with atoms in several different ways and in some of these interactions they were expected to exchange energy with the sample. The analysis of these energy losses gives the composition of the sample for light elements. This technique is therefore known as Electron Energy Loss Spectroscopy (EELS) and was first demonstrated in the 1975 by members of Crewe's group.^[16]

1.3 Energy Dispersive X-ray Spectroscopy

As the electron beam passes through the sample, the high energetic electrons behave as ionizing radiation, and with a certain probability they can remove inner-shell electrons from their nuclei.^[17] Upon transferring energy to an atom, one of the inner-shell electrons acquires enough energy to abandon its orbital, leaving behind an electron-hole. This hole is immediately filled by a decaying electron coming from a higher energy external shell. This transition frees an amount of energy, equal to the energy difference of the two orbitals involved, usually in the form of an X-ray photon or an Auger electron. The emitted X-ray photon therefore possess only discrete quantities of energy which are related to the possible transitions in the given atom. Different atoms show different characteristic transitions and respective X-ray radiations, making their analysis a powerful way of determining the species present. The technique is known as Energy Dispersive X-ray Spectroscopy (EDXS) and together with EELS expands the capabilities of a conventional TEM/STEM instrument in what is also referred to as Analytical Electron Microscopy (AEM).

EDXS was developed starting from the 1940s. The basic principle involves the analysis of X-rays generated from a material under the exposure of a source. The first instrument embodying this principle was the Electron Probe Micro-Analyzer (EPMA), born as a technique to obtain localized compositional information from a material. Its development occurred simultaneously to the development of the SEM. The instrument consisted of an electron gun followed by electromagnetic lenses focusing the probe to a spot with a diameter of approximately 0.1-1 μm . The emitted X-ray radiation was analyzed with one or more wavelength dispersive spectrometers (WDS).^[18] Until 1968, SEM and EMPA were considered two different instruments, but with the introduction of the Energy Dispersive Spectrometer (EDS),^[19] the technique was eventually incorporated in the majority of commercial SEMs, conferring the ability of directly characterize chemical elements in the specimen. Following its diffusion in SEMs, the EDS detector was adopted in TEMs as well, expanding analytical analysis to the nanometer scale (if operated in STEM mode), starting from mid-1970s.^[17]

1.4 Electron tomography

The development of TEM enabled the characterization of nanomaterials, from imaging them down to the atomic scale to obtaining structural and chemical information. However, these techniques only provide a two-dimensional projection of a three-dimensional object. Interpretations based on 2D projections may often lead to wrong conclusions about the nature of the sample. A beautiful LEGO sculpture, *Dragon Butterfly Jet*, by artist John V. Muntean, shown in Figure 1.4, illustrates this concept. Here the three shadows projected by the object from different angles, cause the illusion of an object that is simultaneously

a dragon, a butterfly and a plane, while in reality it is none of them. The artwork represents an example of the difficulty of interpreting a 3D object from its 2D projections. For nanomaterials in a TEM, a similar problem arises, and the combination with tomography is a powerful way of extending TEM capabilities to the third dimension.

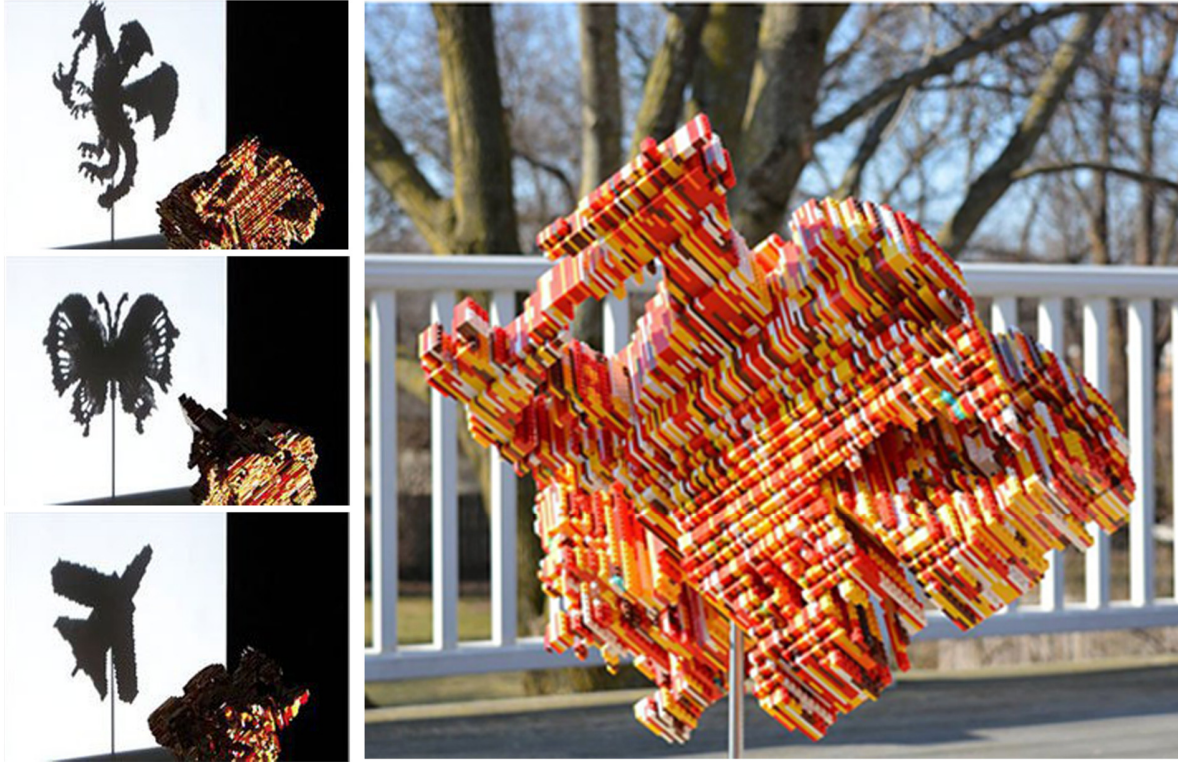


Figure 1.4: Magic angle LEGO sculpture, *Dragon Butterfly Jet*, by artist John V. Muntean, casting three different shadows. The sculpture represents the limitations in understanding a 3D object from its 2D projections.

The word *tomography* is derived from the Greek words τόμος (tomos), and γράφειν (gráphein), meaning “slice” and “to write” respectively. It refers to the technique used to reconstruct an object or an internal property of it, by acquiring projections from different directions and combining them through an algorithm. The mathematical foundations of the technique were first given by Radon in the 1917.^[20] Further development in the field came in the 1960s when a first application of X-ray tomography was proposed for medical purposes.^[21] Since then, the use and development of tomography scanners for medical imaging proliferated.

In the 1970s, the first attempts to obtain 3D reconstructions from TEM micrographs were carried out.^[22-24] These attempts are considered as the starting points for the development of electron tomography,^[25, 26] and in the following decades efforts were spent by several groups towards the development of the technique as

we know it today. A thorough review of these efforts is given by Frank, in his textbook on electron tomography for biological sciences.^[27]

The adoption of electron tomography in materials science started towards the end of 1980s, but only later saw general diffusion, upon the introduction of novel (tomographic) imaging modes, automation of microscope control and new reconstruction algorithms powered by an increased computation speed.^[26] The birth of modern electron tomography for materials science was finally marked in 2000 by the study of Koster and co-workers, who used bright field tomography for the reconstruction of porous zeolites,^[28] and later in 2003 by the paper from Weyland and Midgley,^[29] which presents the development of Z-contrast and EFTEM tomography.

2 Electron Tomography Principles

In chapter one, a general framework from an historical perspective was given for the topics covered by this thesis. In this second chapter, the details of electron tomography will be discussed, starting from the mathematical principles.

2.1 Projections acquisition

An electron tomography experiment starts with the acquisition of projections. Routinely, for materials science samples, the microscope is operated in STEM mode and the signal is collected with a HAADF detector, in order to avoid diffraction contrast which would violate the projection principle. The sample is tilted using a dedicated tomography holder (presented in section 3.1.4) over a tilt range limited between -80° and $+80^\circ$. Tilting to higher angles is usually not possible, since the holder tip touches the pole pieces of the objective lens (except in the case of an on-axis tomography experiment). Usually starting from an angle the closest possible to -80° , HAADF-STEM projections of the sample are acquired with a tilt increment of a few degrees (between 1° and 5°) as schematized in Figure 2.1a. After the series is acquired and aligned, it is used as an input for a mathematical algorithm, yielding the 3D reconstruction of the object investigated (Figure 2.1b).

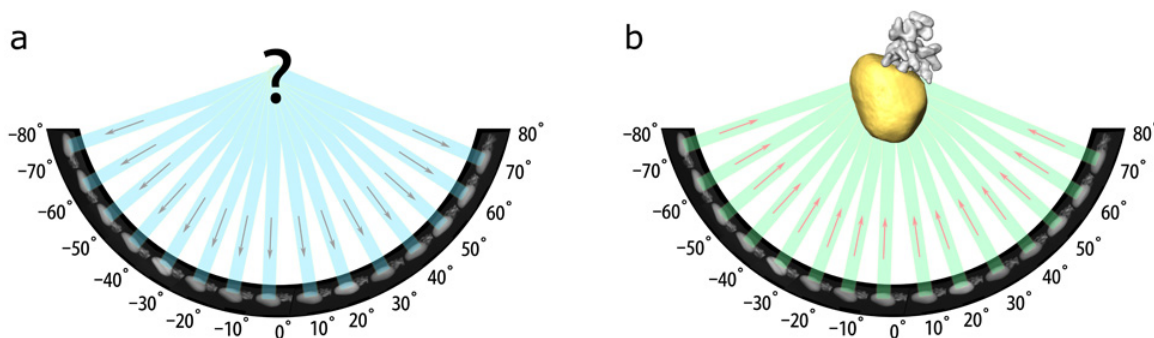


Figure 2.1: Schematization of a HAADF-STEM tomography tilt series experiment. (a) The tilt series is acquired by tilting the specimen and acquiring projections between -80° and 80° . (b) The projections are used to calculate the sample 3D reconstruction.

As opposed to X-ray tomography, where the scanner is free to rotate around the sample, in a TEM the source is fixed, therefore the sample is tilted instead, from which derives the limitation on the tilt range.

Considering the Fourier space representation, the impossibility of acquiring projections covering the full tilt range of 180° causes part of the frequency domain to be unsampled.

2.1.1 Missing wedge artifacts

In Fourier space, sampling with a limited tilt range, leaves out two wedges of frequencies. To minimize the volume of missing frequencies it is possible to perform a second acquisition after rotating the sample of 90° or by rotating gradually the sample at every tilt angle, forming respectively a missing pyramid or a missing cone of frequencies, as shown in Figure 2.2.

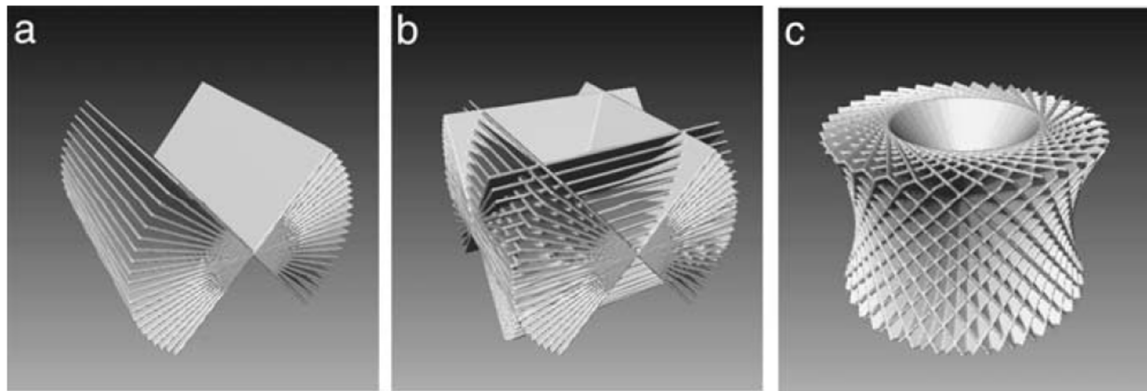


Figure 2.2: Representation of sampled frequencies in Fourier space for (a) linear tilt scheme, (b) dual-tilt scheme, (c) tilt-rotation scheme of acquisition, giving rise to a missing wedge, missing pyramid or missing cone of frequencies, respectively. Adapted from ref.^[27] with permission of Springer.

Lack of sampling of these frequencies leads to a blurring of object features defined by those frequencies and an elongation of the reconstructed object. An illustrative example of the type of artifacts is given in Figure 2.3 (the original phantom is shown in Figure 2.5a).

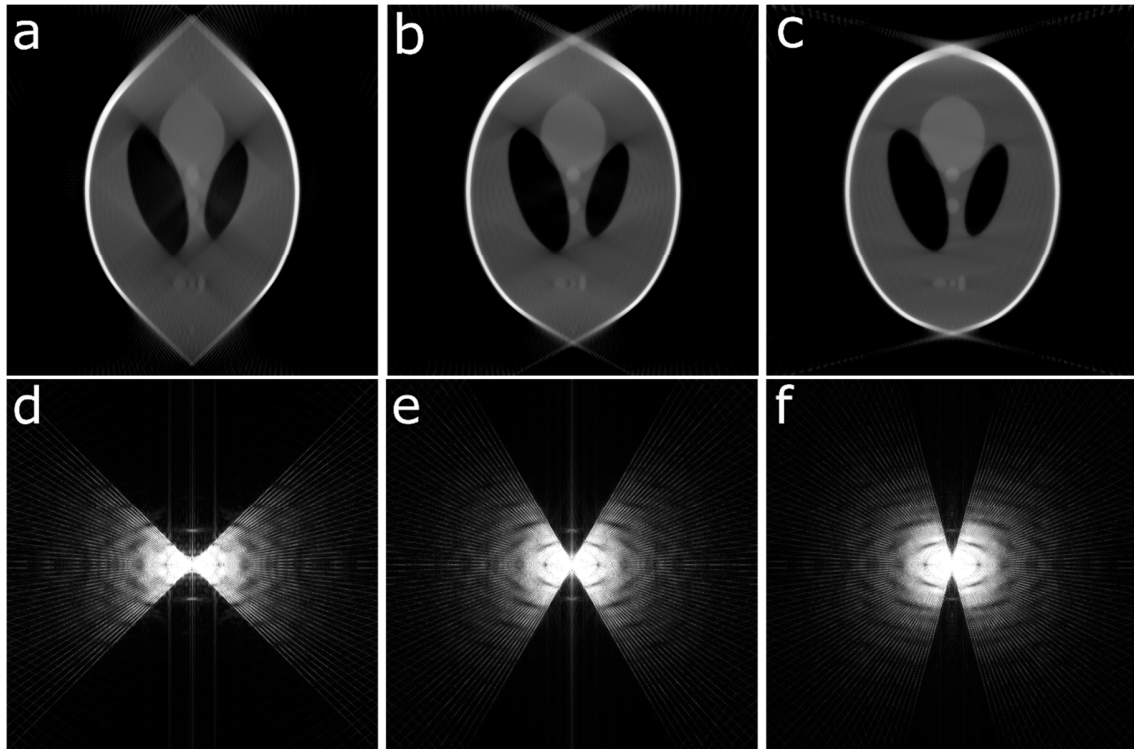


Figure 2.3: Phantom reconstruction of projections simulated with different tilt ranges: (a) -45° to 45° , (b) -60° to 60° , (c) -75° to 75° , all every 2° . (d,e,f) Discrete Fourier transforms of (a,b,c) respectively, showing the extent of the missing wedge, which explains the elongations artifacts observed in the reconstructions. These artifacts are known as *missing wedge artifacts*.

Missing wedge artifacts form a tedious problem in electron tomography, especially when reconstructing objects closely packed in the direction of the artifacts, since the elongation distortion leads to an overlapping of the boundaries, hampering the distinction of the single objects. There are different strategies to overcome missing wedge artifacts or minimize their effect, by either using a different acquisition scheme, an on-axis holder or advanced reconstruction algorithms, or possibly a combination of these approaches.

2.2 The reconstruction problem

The *reconstruction problem* arises in science whenever the non-destructive characterization of an internal property of an object is desired. Computerized X-ray tomography of living beings is a macroscopic example of such a case. For nanomaterials as well, due to other limitations, it is not possible in most cases to physically cut a nanoparticle and therefore a similar approach is adopted. In order to access internal structural information, a variety of probes, such as, electrons, X-rays, sound waves, to name a few, can be

used to extract information. Usually a source emits the signal, which travels through the object and is then collected by a detector. The process generates a so-called *projection* since the probe projects an internal property of the 3D object onto a 2D detector plane.

The mathematical framework of this process is described by the Radon transform.^[20] The Radon transform Rf of an object represented by the function f in an n -dimensional space, is given by integrating f over all the hyperplanes of dimension $n-1$. In the simple case of a 2D object Rf is defined by integrating $f(x,y)$ over its projections (line integrals) along all possible lines L of unit length ds :

$$Rf = \int_L f(x,y) ds \quad (2.1)$$

The figure represents a projection of three disks in a given direction.

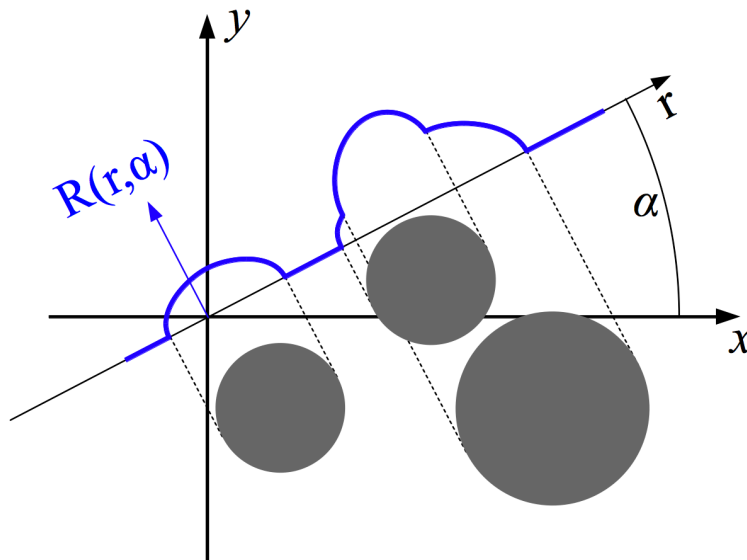


Figure 2.4: Schematic illustration of the projection $R(r,\alpha)$ of three disks (Illustration by Michael Schmid, Creative Commons license).

Given a two-dimensional object, the Radon transform can be visualized by displaying the one-dimensional projections obtained along the different angles as rows of pixels concatenated along the direction perpendicular to their dimension. The obtained figure is also known as sinogram, an example is given in Figure 2.5.

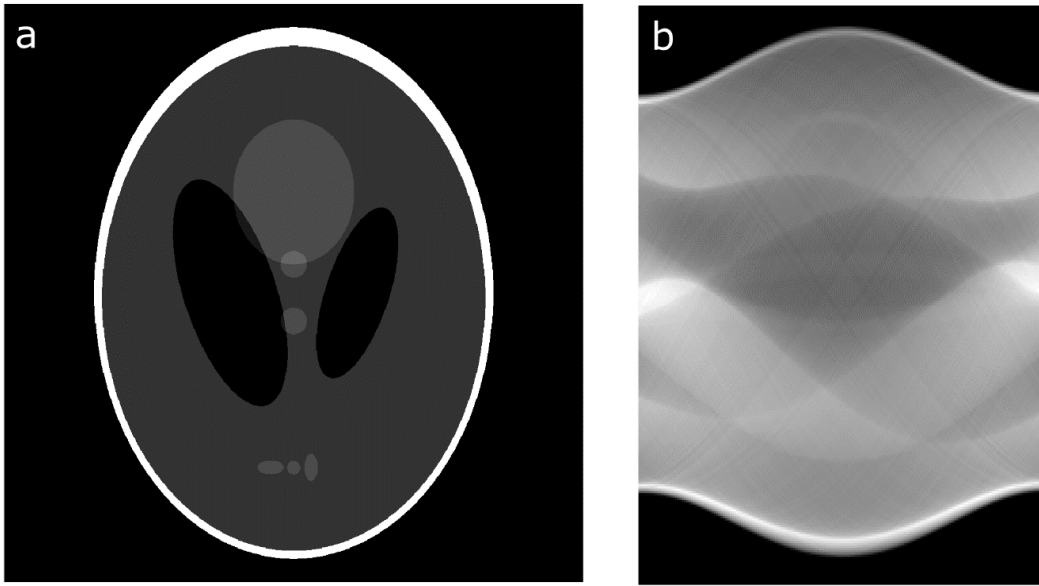


Figure 2.5: (a) Shepp-Logan phantom (standard test image). (b) Sinogram of the Shepp-Logan phantom projected every 1° from 0° to 180° .

Radon also described the inverse Radon transform, through which is possible to obtain a reconstruction of the object. In a real experiment though, we are limited to the acquisition of a discrete and finite number of projections, and as a consequence the reconstruction is usually an approximation of the object (Figure 2.6).

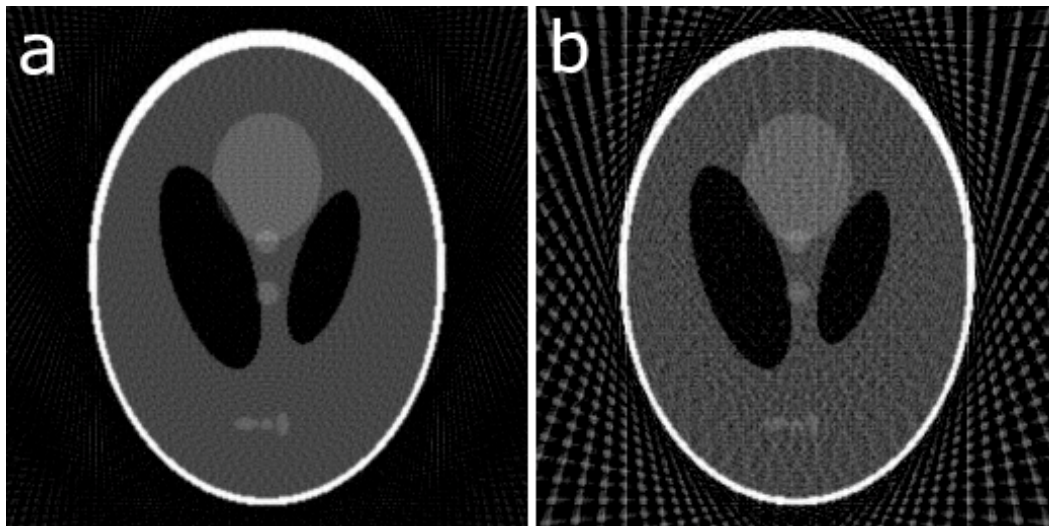
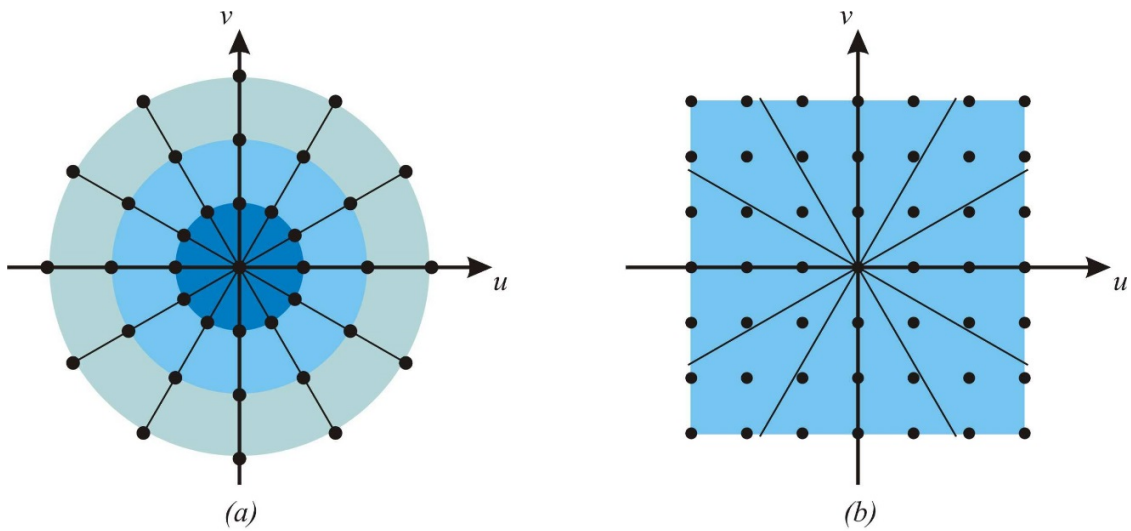


Figure 2.6: (a,b) Inverse radon transforms of the Shepp-Logan phantom projected from 0° to 179° every 2° and 5° respectively.

2.3 Fourier slice theorem

To understand why it is not possible to perfectly retrieve the original object by reconstructing a finite number of projections, it might be useful to consider an alternative representation of the problem in Fourier space. If an object is described by a function of space $f(x,y)$, then it is possible to perform a Fourier transform of this function, decomposing the object in a series of trigonometric functions. The coefficients and frequencies of the trigonometric basis represent the object in Fourier space.

According to the Fourier slice theorem, the Fourier transform of a 2D projection, is equivalent to a section of the 3D Fourier transform of the object (parallel to the projection plane and passing through the origin). Acquiring several projections along different angles it is therefore equivalent to sample different planes in Fourier space. This explains why, the most common artifact observable in reconstructions is the blurring of sharper features. These features are described by higher frequencies in Fourier space, and as a consequence of discrete number of acquired projections there is a lower density of sampled points in the regions far from the origin, e.g. there is always an undersampling of higher frequencies, as schematized in Figure 2.7. An example of the effect of this undersampling on a phantom image is given in Figure 2.8.



Frequency Domain

Figure 2.7: (a) Schematic illustration of the frequency space in a limited data tomography acquisition (2D object and 1D projections), the lines represent the 1D Fourier transform of the 1D projections, the density of points decreases as the distance from the center increases, showing the undersampling of higher frequencies. (b) As a comparison to (a), here a homogeneous sampling of the Fourier frequencies is shown for an ideal case.

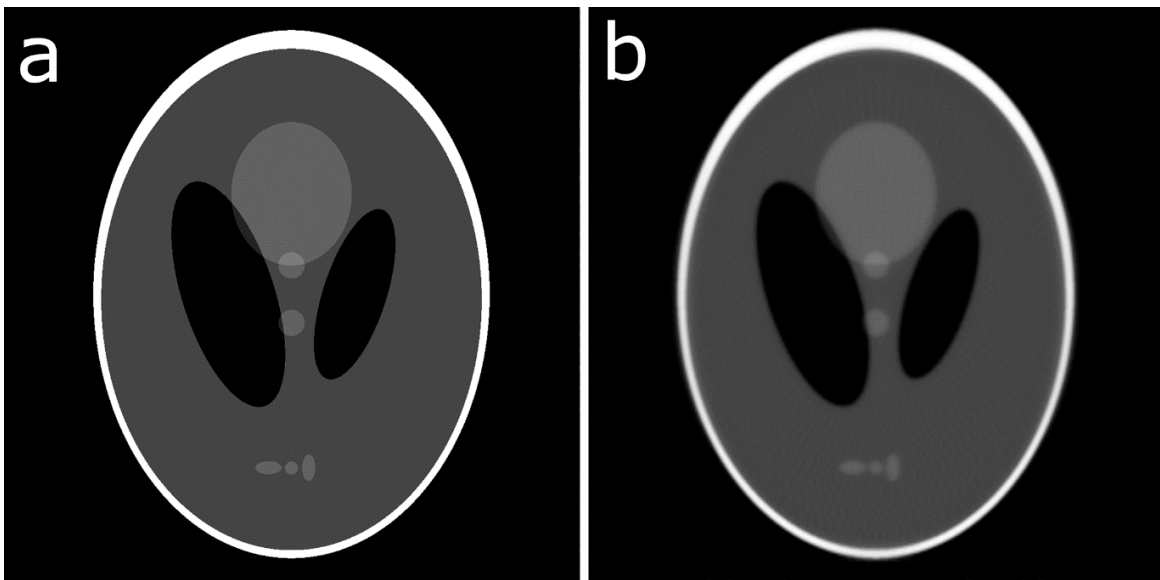


Figure 2.8: (a) Shepp-Logan phantom. (b) Reconstruction of (a) from simulated projections between 0° and 179° every 2° . Undersampling of higher frequencies and therefore blurring in the reconstruction can be observed.

2.4 Reconstruction methods

2.4.1 Fourier space methods

As a consequence of the Fourier slice theorem it is possible to obtain a reconstruction of an object by calculating an inverse Fourier transform from a set of Fourier transformed projections, as first proposed by Bracewell.^[30] Since projections are acquired in a discrete manner, in order to obtain a reconstruction, it is necessary to radially interpolate over the missing data in Fourier space. This approach is very sensitive of the interpolation method chosen,^[31] and due to its complexity and elevated computational costs, it has been superseded by real-space techniques, which arose as faster and computationally less demanding techniques. In the remainder of this thesis, we will consider real-space techniques, but it is worth mentioning that very recently, also thanks to the ever increasing computational power of modern computers and the advent of General-purpose computing on graphics processing units (GPGPU), a new and promising iterative Fourier space technique has been demonstrated.^[32]

2.4.2 Direct methods: backprojection & weighted backprojection

Backprojection is the simplest reconstruction technique possible, it consists in the act of smearing projections back along the directions of acquisition. This process is computationally fast, but the result lacks accuracy especially in the case of undersampling of the angular range. An example of how back projection works is given in Figure 2.9.

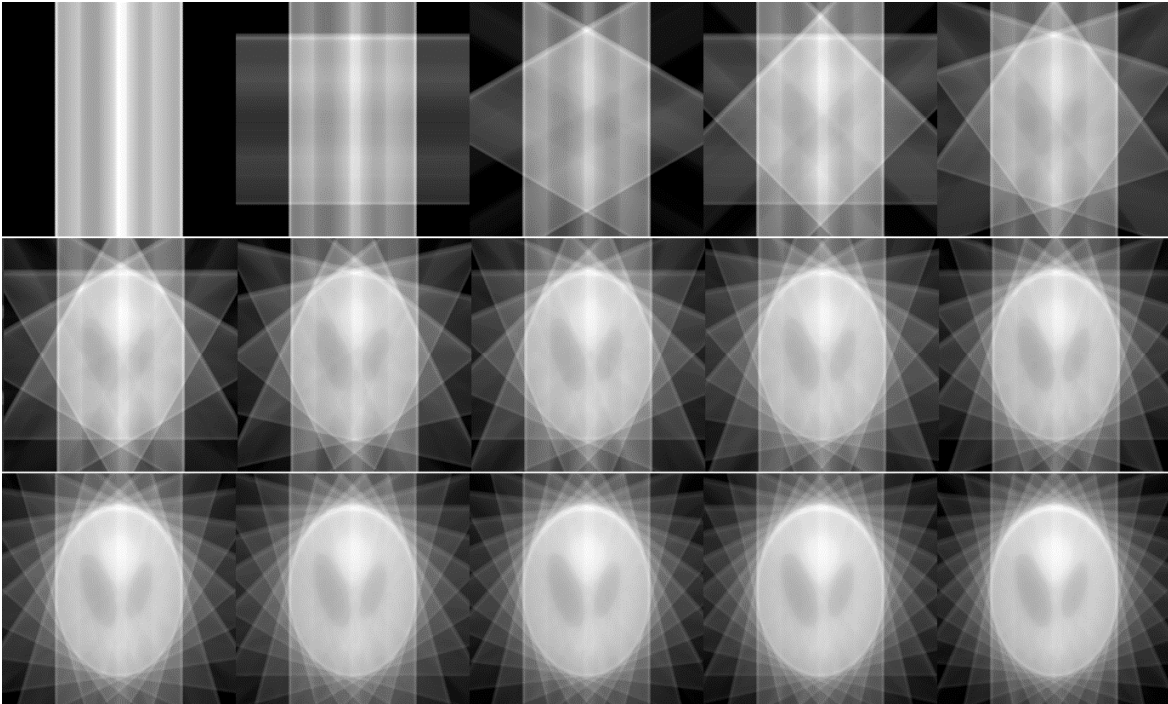


Figure 2.9: Backprojections montage for a phantom, with projections simulated between 0° and 180° for an increasing number of equally spaced angles. Starting with 1 projection angle in the upper left corner, up to 15 projections angles in the bottom right corner.

Backprojection was first introduced for X-ray tomography^[33] and later for electron tomography.^[34] Reconstructions obtained through this approach show extreme blurring, due to the undersampling of higher frequencies. An improvement is therefore achieved by applying a weighting filter to the reconstruction Fourier space, e.g. by convolving the reconstruction with a filter that has zero weight at the center and linearly increases towards the edge, therefore balancing the density of sampled information for the different frequencies. This approach is called *weighted backprojection* (WBP) and was first proposed by Vainshtein,^[34] Gilbert later showed that the results obtained were equivalent to Fourier space methods, with the advantage of a much simpler and faster calculation.^[35]

2.4.3 Iterative techniques

Advancements in the field of computer science prompted the development of iterative methods. In these methods, the solution to the reconstruction problem is iteratively refined. The idea behind can be simplified by considering that the acquired projections can always be used as a reference and therefore once an initial reconstruction is obtained, for example by backprojection, it is possible to forward project it along the acquisition directions. The forward projections should in principle correspond to the acquired projections. But since using the backprojection method results in reconstructions affected by blurring, as a consequence,

the forward projections will show differences with the original projections. By using this difference, also known as the *projection distance*, it is possible to refine the reconstruction in such a manner that the forward projections will better match the original projections. This process is iteratively repeated until a convergence criteria is met, e.g. the minimization of the projection distance is not improving anymore significantly.^[36]

This approach can be applied in several manners by using different ways of minimizing the projection distance. These methods can be described mathematically by assuming that the investigated object can be represented by a grid of unknowns. The unknowns are equivalent to the pixel values. In Figure 2.10 such a grid of length u and height h , is shown as an example. The object can be described by $N = u * h$ unknowns x_i , and any of its projections b_j , is given by the sum of the values traversed by the j -th ray. Every pixel will also have a weight $w_{i,j}$, associated with the ray j , given by the area of the ray passing through the pixel, over the area of the pixel itself.

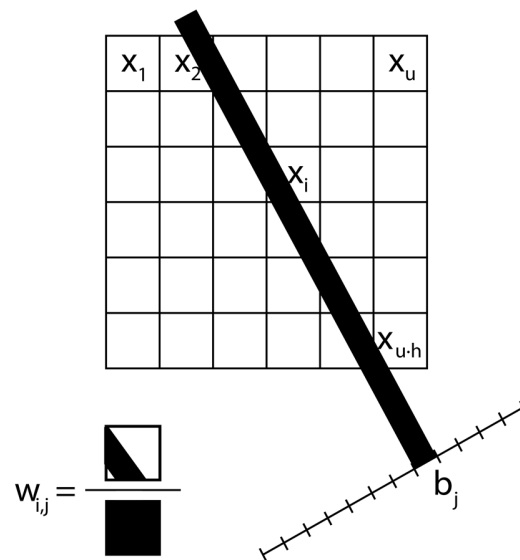


Figure 2.10: Scheme representing the discretization of an object in a grid of unknowns and their relation with a projection b along a certain direction.

The projection b_j is given by the sum of all the pixels, multiplied by the relative weight (pixels not traversed by the j -th ray will have zero weight).

$$\sum_{i=1}^N w_{j,i}x_i = b_j \quad j = 1, 2, \dots, M \quad (2.2)$$

Where M is the total number of rays. Every projection pixel can be therefore represented by a linear equation, and the full set of projections as a vector with elements b_j .

$$\begin{aligned} w_{1,1}x_1 + w_{1,2}x_2 + w_{1,3}x_3 + \dots + w_{1,N}x_N &= b_1 \\ w_{2,1}x_1 + w_{2,2}x_2 + w_{2,3}x_3 + \dots + w_{2,N}x_N &= b_2 \\ \vdots & \\ w_{M,1}x_1 + w_{M,2}x_2 + \dots + w_{M,N}x_N &= b_M \end{aligned} \quad (2.3)$$

In matrix notation this system can be written as:

$$Wx = b \quad (2.4)$$

In case N and M are small, the matrix W can be inverted by using conventional matrix theory methods. However, usually this is not the case when dealing with real data and inverting W to retrieve an exact solution is not possible. A typical electron tomography experiment can consist in the acquisition of approximately 70 projections from -70° to $+70^\circ$ every 2° . Each projection is 1024 by 1024 pixels, and therefore we would have approximately 70 million equations. Since the projections are 1024 by 1024, we assume that the object is contained in a cube of 1024^3 pixels, which makes approximately 1 billion unknowns. The size of our matrix W , also known as the *weighting matrix* is therefore, 70 million by 1 billion. This also shows that the problem is underdetermined, since the number of unknowns far exceeds the number of equations. The presence of experimental noise further makes the system inconsistent.

The system of equations in (2.3) is usually solved by minimizing some norm $\|Wx - b\|$. Several methods have been developed for this purpose, the first of which was proposed by Gordon,^[37] and is known as Algebraic Reconstruction Technique (ART). One year later, in 1971, Gilbert published a new study,^[35] in revision of the work of Gordon, highlighting limitations of ART and the fact that the technique was not yielding better results than the Fourier methods, as claimed, but was instead producing artifacts. Gilbert also proposed a modified approach able to produce an accurate reconstruction without artifacts as in the case of ART. The method takes the name of Simultaneous Iterative Reconstruction Technique (SIRT) and arose to be one of the most commonly used reconstruction techniques, in the field of electron tomography in the last decade.

Using this formalism, W represents the act of forward-projecting the object and forming the projections, while the transpose W^T is the act of back-projecting the projections b , forming a backprojection reconstruction. The update equation of SIRT is:^[38]

$$x^{(t+1)} = x^{(t)} + CW^TR(b - Wx^{(t)}) \quad (2.5)$$

In which C and R are diagonal matrices denoting the inverse of the sum of the columns, $c_{jj} = 1/\sum_i w_{ij}$, and rows, $r_{ii} = 1/\sum_j w_{ij}$, of W . These matrices are needed to compensate for the number of pixels hit by each ray, so that the update term $CW^TR(b - Wx^{(t)})$ is properly scaled. An example of a SIRT reconstruction in comparison to BP and WBP is given in Figure 2.11. Whereas WBP shows a great improvement in the reconstruction of sharper features, thanks to the filtering in Fourier space, it does not offer a reliable reconstruction of the gray levels, which is obtained by SIRT.

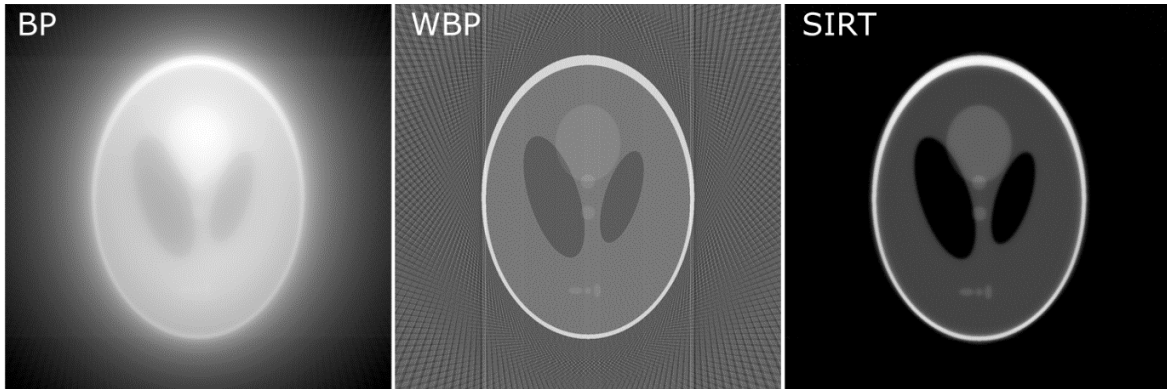


Figure 2.11: Comparison of three phantom reconstructions from projections simulated from -90° to 90° every 2° obtained by backprojection (BP), weighted back projection (WBP) and SIRT.

It is proven that in the absence of noise, SIRT converges to a weighted least square solution x^* :^[39]

$$x^* = \operatorname{argmin} \|Wx - b\|_R^2 \quad (2.6)$$

In comparison to analytical techniques, SIRT offers more flexibility, for example it is possible to include a positivity constraint to exclude negative intensities which would not have physical meaning, easing the convergence to the solution. The main disadvantage is the computational load of such a method, but fortunately the rise of GPUs and parallel computing prompted the development of open source libraries, such as the ASTRA toolbox,^[38, 40-43] enabling SIRT reconstructions to be computed in the order of minutes.

2.5 Prior knowledge in the reconstruction

Because of physical limitations in the acquisition process, such as, tilt range and electron dose tolerance, the amount of data that can be acquired can also be limited. For example, often one wants to analyze TEM samples that are unstable under long irradiation, and therefore this requires lower beam currents and shorter exposure times. As a result, noise increases and the number of acquired projections decreases. Artifacts originating from these two factors, and the missing wedge, hamper the characterization of such materials by means of conventional reconstruction techniques. In the last decade, a series of new approaches has been presented in order to overcome these limitations by incorporating *prior knowledge* information in the reconstruction process, in order to obtain a better reconstruction. An overview is presented below.

2.5.1 Discrete Algebraic Reconstruction Technique

The Discrete Algebraic Reconstruction Technique (DART), uses prior knowledge on the density of the object, e.g. its gray levels. If the investigated object can be described by gray levels that change only discretely, e.g. the material has regions of constant density with sharp interfaces, then the technique is able to produce an accurate reconstruction even from a limited number of projections.^[44, 45] DART is an iterative algorithm that combines SIRT with discretization steps. The values of the discrete gray levels are the prior-knowledge required, and can be estimated from an initial SIRT reconstruction. The algorithm determines boundary pixels through a segmentation step. The values of interior pixels are then fixed and SIRT iterations are only performed for boundary pixels, updating them. The procedure is repeated until a stop criterion is met. An example of a DART reconstruction, from the work of Batenburg et al.^[44] is shown in Figure 2.12, for a carbon nanotube containing a Cu catalyst (Figure 2.12a). SIRT reconstruction slices (Figure 2.12b-d) are compared to DART reconstruction slices (Figure 2.12e-g). Minimization of missing wedge artifacts can be observed by comparing Figure 2.12b and Figure 2.12e.

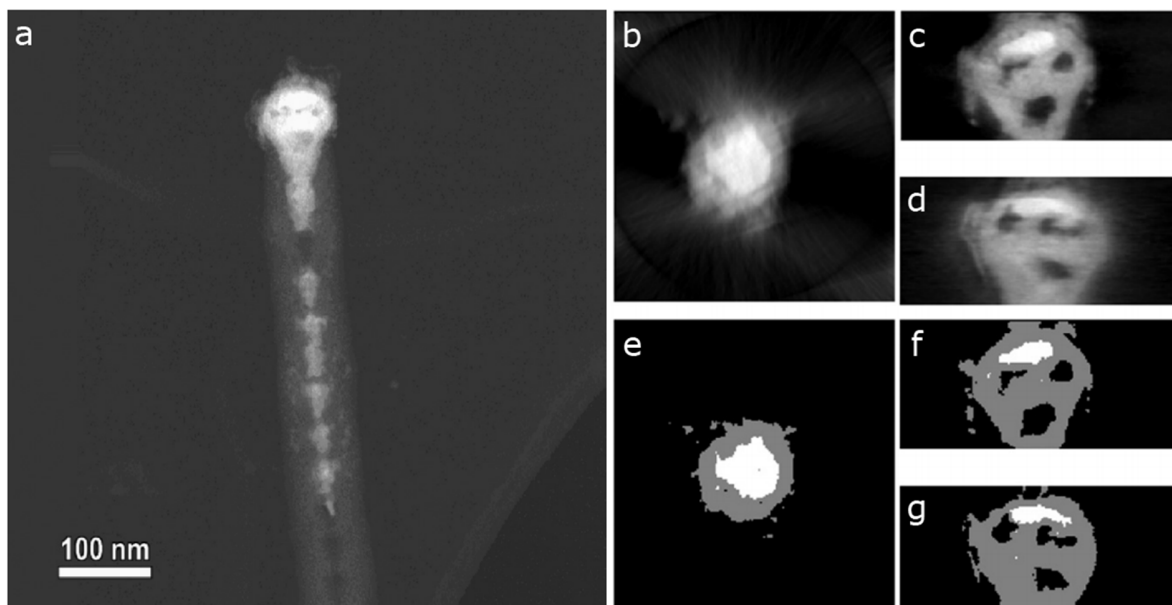


Figure 2.12: (a) HAADF-STEM image of the catalyst particles, a carbon nanotube containing Cu/CuO₂ catalyst nanoparticles in a *bamboo-like* structure. (b,c,d) Slices from the SIRT reconstruction of the structure. (e,f,g) Slices from the DART reconstruction, highlighting the improvement over SIRT in the minimization of blurring and missing wedge artifacts. Images adapted from ref.^[44] with permission of Elsevier.

It has been demonstrated how DART can yield an improvement on the SIRT reconstruction (Figure 2.12) of certain materials, especially in minimizing missing wedge artifacts.^[44] Nevertheless, its application is suitable to only a certain kind of samples for which a discrete number of gray levels can be expected. This and the additional computational cost, which causes it to be slower than SIRT, have limited its adoption to only specific cases.

2.5.2 Total variation minimization

Another technique, nowadays often used in electron tomography, is the Total Variation Minimization (TVM) reconstruction method. The technique belongs to the field of compressive sensing,^[46] and was first introduced as a de-noising technique.^[47] TVM use has been recently extended to tomography reconstruction techniques,^[48] demonstrating significant improvements in the reduction of missing wedge artifacts. The prior knowledge involved here, is the assumption that the object has finite interfaces, as its surface. As a consequence, the gradient image, representing its boundaries, is sparse. This sparsity assumption can be included in the algebraic technique by simultaneously minimizing the projection distance and the total variation (norm of the gradient) of the reconstructed object.^[48, 49]

$$x^* = \operatorname{argmin} (TV(x) + \frac{\mu}{2} \|Wx - b\|_R^2) \quad (2.7)$$

An example of TVM reconstruction, from the work of Goris et al.^[48], of Pb nanoparticles embedded in a Si needle, is shown in Figure 2.13. Comparison of a SIRT and TVM reconstruction slices, Figure 2.13c and Figure 2.13d respectively, reveals the significant improvement in the minimization of noise and missing wedge artifacts.

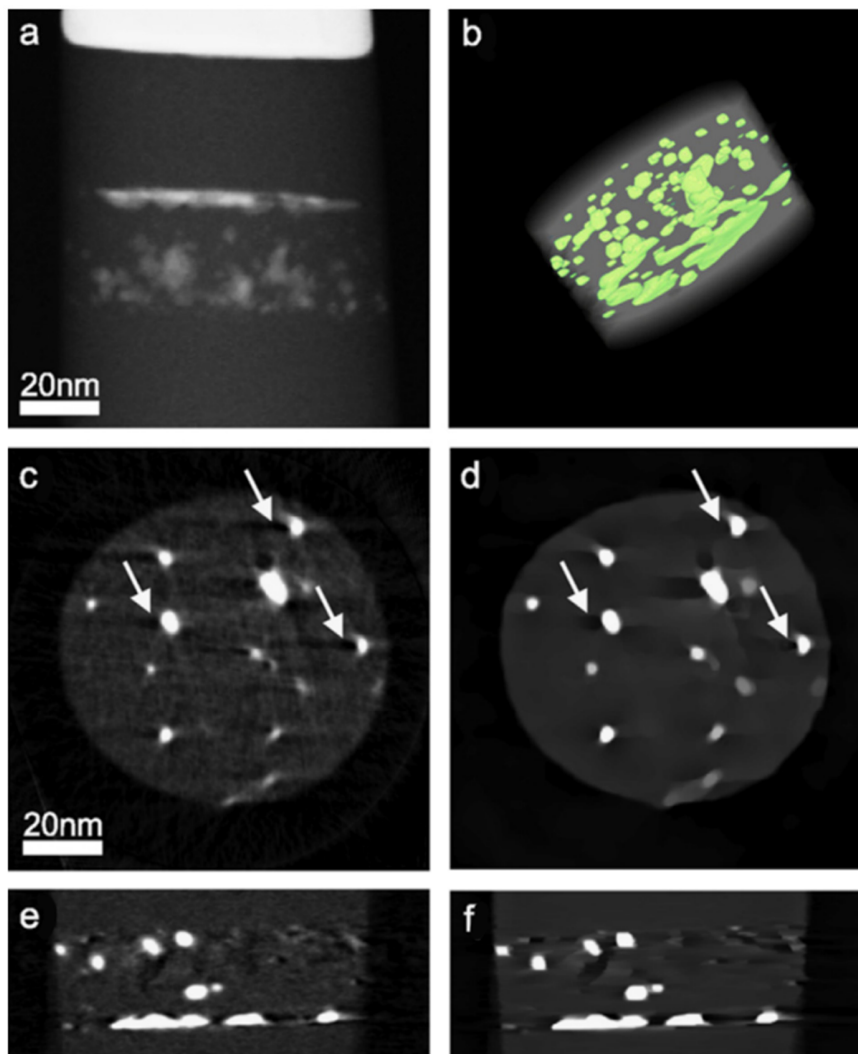


Figure 2.13: (a) HAADF-STEM projection of a Si needle containing Pb particles. (b) Reconstruction rendering, highlighting the 3D distribution of Pb particles in the needle. (c,e) SIRT reconstruction slices. (d,f) TVM reconstruction slices. Images adapted from ref.^[48] with permission of Elsevier.

2.5.3 Limitations and further developments

The presented approaches, although performing better than SIRT in certain situations, are still limited to general priors, which in complex cases do not enable the desired characterization. For example, in systems of closely packed nanoparticles, even though DART and TVM can be applied, the improvement over SIRT is not sufficient to enable the distinction of particles in contact, since overlapping of boundaries occurs anyway. Given the increasing complexity of nanomaterials systems that are being developed, it is often necessary to go one step forward in trying to include any possible prior knowledge available for the investigated sample, in order to obtain a relevant reconstruction.

In chapter 4 a new approach is presented, dedicated to the reconstruction of nanoparticle assemblies and their quantification. The technique is based on the possibility of using a new basis for the tomography problem, in the case of assemblies of spheres, exploiting the knowledge that these particles assemblies are made of a repetitive building block. The approach will enable a full quantification and characterization of assemblies of closely packed nanoparticles, which could not be obtained by using the techniques presented above.^[50]

3 Electron Tomography in Practice

3.1 The transmission electron microscope

The instrument is composed by a steel column, usually kept in high vacuum conditions (10^{-7} mbar) through a complex pumping system. These conditions are essential to enable free travelling of the electron beam and therefore good resolution. The column can be divided in three main parts, as shown in Figure 3.1: the illumination system, the objective stage and the imaging system.

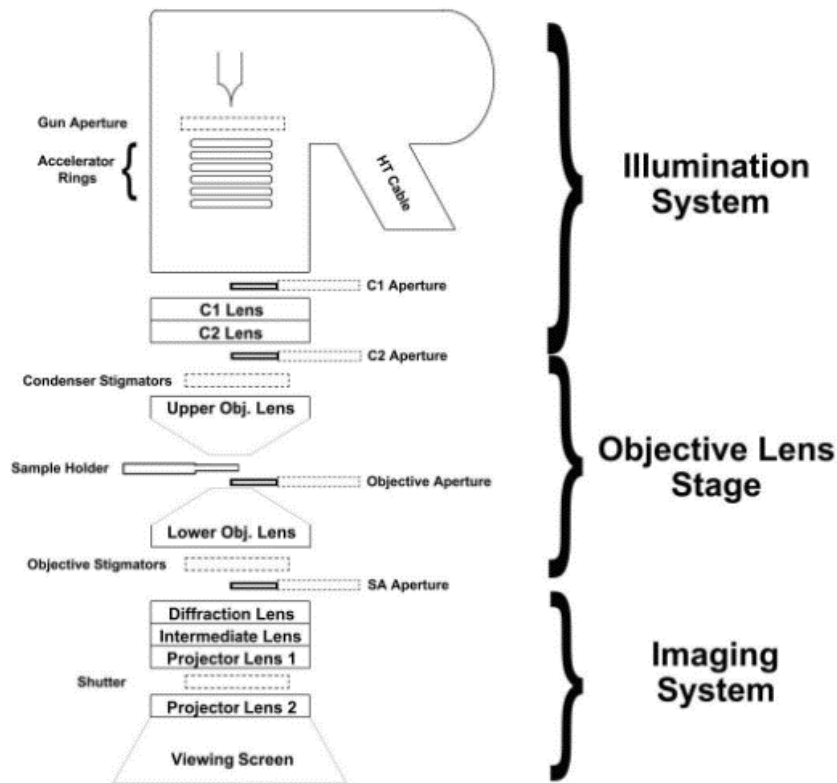


Figure 3.1: Schematic representation of the main components of a TEM column.

The illumination system consists of an electron gun, acceleration coils and the condenser system (C apertures and lenses) which are positioned at the top of the column in the most common designs, but can also be found at the bottom, as it is the case for Nion microscopes. Due to its significant weight, having the illumination system at the bottom, reduces the instability of the column. Nevertheless, besides the inverted

order, the same principles hold for both designs and in the remainder of this thesis we will only consider *traditional* TEMs, with the source at the top, as the instruments used during my PhD were designed according to this principle.

Going down the column, we find the objective lens stage, the heart of the instrument. Situated at the center of the column, this is where the interaction between sample and electrons occurs. The sample is inserted in the narrow space between the objective lens pole pieces. Images formed from the objective lens system are then magnified and displayed/recorded by the imaging system.

3.1.1 Imaging modes

When the electrons traverse a material, there is a certain probability that they will interact with the Coulomb potentials of the atoms, and that they will be scattered as a result of this interaction. Electron scattering is the fundamental mechanism that enables contrast formation in TEM by changing the amplitude and phase of the electron wave. Contrast mechanisms are therefore divided in *amplitude contrast* and *phase contrast*. Phase contrast is generated by the interference of at least two electron waves, and is usually exploited to obtain high-resolution TEM images (HRTEM). Amplitude contrast is divided in *mass-thickness contrast* and *diffraction contrast*, and is used to form both TEM and STEM images. Mass-thickness contrast depends on Z and it is given by incoherently scattered electrons, its dependency on Z is given by the Rutherford scattering cross-section and it is approximately proportional to Z^n , with $1.5 < n < 2$. Diffraction contrast, on the other hand, is given by coherently and collectively scattered electrons from parallel atomic planes, according to Bragg's law. For amorphous samples, there is no diffraction contrast, so the image is formed due to mass-thickness contrast only, while for crystalline samples, both mechanisms contribute to the image formation.

It is possible, through the use of the objective aperture or by tilting the beam in TEM mode, or using a proper detector in STEM mode, to select the contrast formation mechanism. In TEM, it is possible to include the direct beam (central spot in the diffraction pattern) forming a bright-field image (BF-TEM) or exclude it by selecting another region of the diffraction pattern with the objective aperture and therefore obtaining a so called dark-field image (DF-TEM) with reversed contrast. In STEM, the concept is similar, but since there is no longer a parallel beam, here the direct beam is included in the image by using a detector collecting electrons scattered at low angles, (BF-STEM), or excluded by collecting electrons scattered at larger angles, giving dark-field images (DF-STEM). Nowadays instruments can be equipped with a series of detectors for STEM mode, schematized in Figure 3.2.

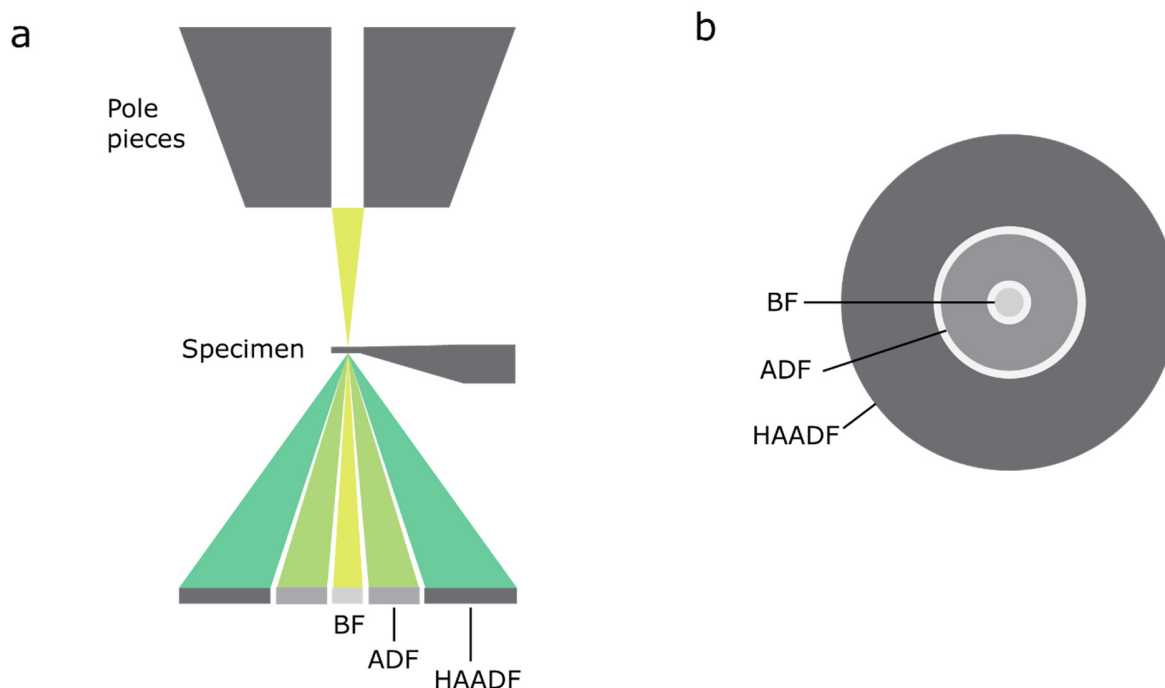


Figure 3.2: Schematic representation of the typical STEM detectors. (a) Side view, (b) top view.

In general, when operating in STEM mode and analyzing crystalline samples, it is preferable to use a HAADF detector in order to exclude contrast contributions from diffracted beams. This is particularly important when acquiring data for an electron tomography experiment. Diffraction contrast causes a violation of the *projection principle*, according to which, projection intensities should be a monotonic function of a given property of the material.^[29, 51]

3.1.2 Spectroscopic imaging modes

In the case of inelastic scattering, electrons will transfer energy to the sample. This energy transfer is at the origin of a whole series of signals that are subsequently emitted by the sample: characteristic X-ray photons, secondary electrons, Auger electrons and visible light. As we have already introduced in the previous chapter, electrons that lost energy and X-ray photons can be acquired to characterize chemical properties of the material through STEM-EELS and STEM-EDXS. We should also mention Energy Filtered TEM (EFTEM), which allows to obtain TEM images from electrons that have lost a certain amount of energy, therefore describing a chemical component of the sample. These three techniques can all be used in combination with electron tomography.^[29, 52-60]

The STEM mode enables the collection of a spectroscopic signal for each point, generating a data cube where every pixel of a micrograph is associated to a spectrum carrying chemical information of the structure in that point. An analysis of the spectra yields intensities for a selected property, and this information can

be used for a tomographic reconstruction of that property. An example of EDXS map and respective spectra are given in Figure 3.3.

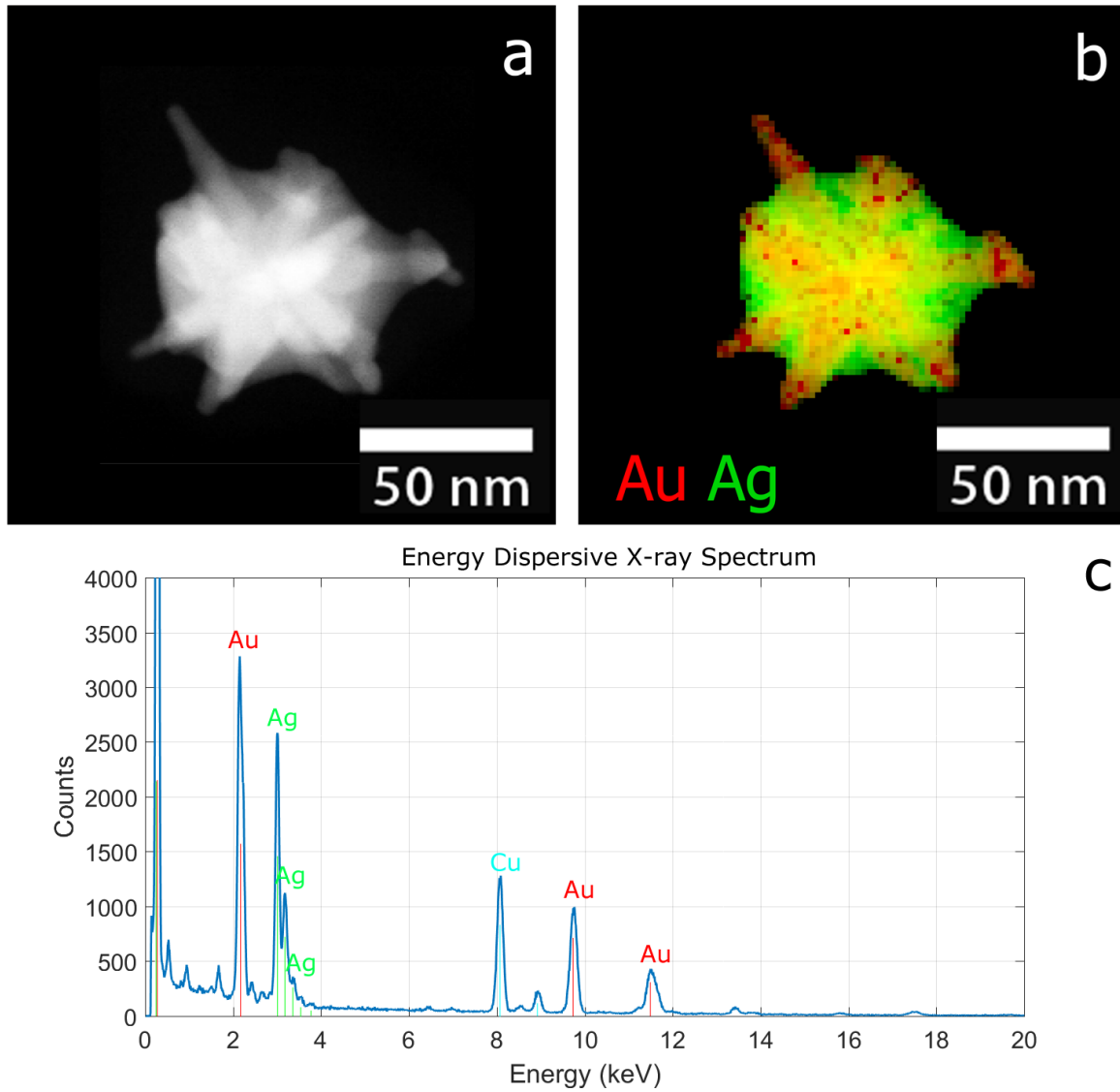


Figure 3.3: (a) HAADF-STEM image of a nanoparticle with complex structure. (b) EDXS mapping of the particle reveals the morphology as a Au star surrounded by Ag. (c) Spectra of the integrated signal from the whole nanoparticle showing the composition. The copper peak at 8 keV is as spurious peak generated by the Cu TEM grid.

3.1.3 The ChemiSTEM system

An important advancement in the field of EDXS has been the recent advent of multiple^[61, 62] X-ray detectors systems for TEM. Previous generation detectors consists of only one X-ray detector positioned on the side of the sample in the objective lens system. This has two main disadvantages, first the collection solid angle $\Omega \sim 0.25$ sr allowed for a limited amount of counts to be collected, which in a TEM, given the usually small size of the sample, implied very long acquisition times in order to collect enough counts to properly quantify compositions. This factor hampered the development of quantitative EDXS in TEMs, usually limiting the technique to qualitative analysis, for the determination of the chemical species present in the sample, rather than determining their concentrations. The second problem of these mono-detector designs is the complete shadowing of the detector at certain tilt angles. When the sample is tilted towards the detector, this does not occur, but when it is tilted in the opposite direction, the holder structure blocks all the X-ray photons emitted from the sample, completely shadowing the detector. This drawback impedes the application of electron tomography, since signal from every direction is required to perform a three-dimensional reconstruction. The introduction of multiple detectors, and specifically of the Super-X detector in FEI microscopes, depicted in Figure 3.4, enabled the collection of signal at any tilt angle, opening the way to the combination of EDXS with electron tomography.

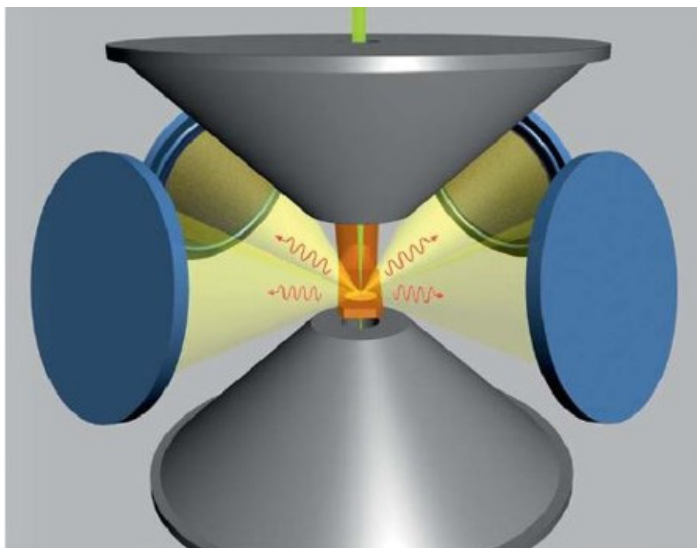


Figure 3.4: Super-X detector schematization. The 4 detectors are symmetrically arranged around the specimen, positioned between the objective lens pole pieces.^[61] Image adapted with permission from ref.^[63], copyright 2017 John Wiley & Sons Ltd.

Furthermore, the collection angle $\Omega \sim 0.9$ sr is also increased significantly relatively to previous generation detectors. This increased efficiency allows for shorter acquisition times and greater counts rate, which are paramount for quantitative studies. The third part of this thesis will be specifically dedicated to my work on quantitative EDXS studies of nanoparticles in 2D and 3D.

3.1.4 Tomography holders

Another fundamental apparatus of the electron microscope is the sample holder. Every microscope manufacturer has its own sample stage mechanism and consequently requires a specific holder design. For FEI microscopes, the standard FEI *CompuStage double tilt* specimen holder (Figure 3.5a), has a tip of 6 mm width, and can be tilted on the holder axis (α tilt) or perpendicularly (β tilt) to approximately $\alpha = \pm 30^\circ$ and $\beta = \pm 30^\circ$. This is typically enough for TEM/STEM analysis of samples, but it is not sufficiently large to obtain a tomography tilt series. The narrow gap between the SuperTWIN objective lens pole pieces (5.2 mm),^[29] needed in order to reach the highest resolution possible, does not allow for greater α tilt. For this reason, dedicated holders with a narrower tip have been developed, an example, extensively used for the experiments presented in this thesis, is the Fischione 2020 tomography holder (Figure 3.5b). Other tomography holders available at EMAT and used for experiments presented in this thesis, are the Fischione 2030 Ultra-Narrow Gap Tomography Holder (Figure 3.5c), Fischione 2040 Dual-Axis Tomography Holder (Figure 3.5d), Fischione 2050 On-Axis Rotation Tomography Holder (Figure 3.5e).

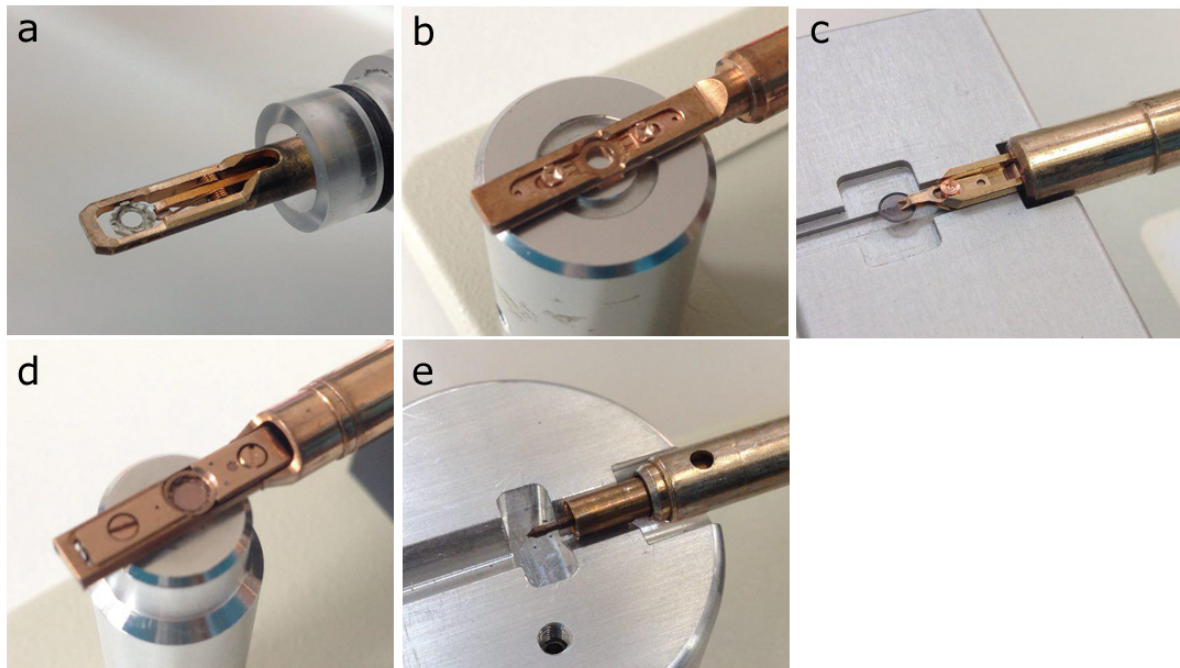


Figure 3.5: (a) FEI double tilt holder. (b) Fischione 2020 tomography holder. (c) Fischione 2030 Ultra-Narrow Gap Tomography Holder. (d) Fischione 2040 Dual-Axis Tomography Holder. (e) Fischione 2050 On-Axis Rotation Tomography Holder.

3.2 Experiment workflow

This section covers the main steps involved in the experimental acquisition of an electron tomography series along together the methods we developed to optimize the various steps, minimizing experimental errors which compromise the quality of the final reconstruction. The successful outcome of a tomography experiment is in fact subject, not only to the choice of a proper reconstruction algorithm, but also to the quality of the experimental data, for which optimization of the acquisition is essential.

3.2.1 Sample preparation

Nanoparticles and nanoassemblies are usually prepared using different methods. Based on the synthesis method, they may be dispersed in liquid, as a powder or embedded in a matrix. Routinely, if not already in a liquid, the powder is dispersed in water or ethanol and a drop is casted on a holey carbon coated TEM copper grid. The grid is loaded onto the TEM holder, and inserted in the microscope. For tomography experiments, it is preferable to orient the grids meshes at 45° relative to the holder axis, so that by selecting a particle approximately in the center of the mesh, it is possible to achieve the highest tilt before the beam

is blocked by the mesh borders. It is also important to obtain the right degree of dilution for the sample; a sample not diluted enough would lead to crowded grids with particles overlapping each other during the tilting, causing artifacts in the reconstruction, while sample diluted too much will decrease the probability of finding a particle close to the center of the mesh.

3.2.2 Tilt series acquisition

Prior to the actual acquisition, several parameters should be correctly chosen. For crystalline materials, a low camera length is usually needed (75 mm), ensuring the collection of electrons scattered at relatively higher angles, avoiding strong diffraction contrast. The *beam current*, which can be controlled using a monochromator (if available), or by changing the beam spot size or C2 aperture, is set to a screen value between 50 pA and 250 pA. Higher currents, provide a better signal-to-noise ratio, which yields higher quality reconstructions. Lower currents on the other hand, are often unavoidable due to sample stability. Since a typical tomography series consists in the acquisition of approximately 70 projections, limiting the total dose before deforming the sample is paramount in most cases. Routinely a frame size of 1024 squared pixels is chosen, with an exposure time of 10 s for a frame and a beam current of 50 pA.

In cases where a higher signal-to-noise is desired, it is possible to acquire multiple fast scans and then average them later. In this manner, image distortions due to sample drifting during the acquisition of a frame are minimized. This strategy has been extensively used for the studies of assemblies of closely packed particles presented in this thesis, where acquisition optimization is essential to minimize artifacts that would hamper the quantification. The approach developed to average the images after the multiple scans acquisition consisted in aligning first all the images to the first scan (by cross-correlation), averaging them and then align again all the images to the averaged image. This second step is then iterated until convergence is reached and no more shifts are detected. This is needed since the images are highly noisy, and the iterative process exclude alignment errors that can occur due to noise. In Figure 3.6 a comparison of high-resolution HAADF-STEM images of a gold nanorod is shown, where Figure 3.6a is a single frame, acquired with an exposure time of 2 s, and Figure 3.6b is the averaged image obtained by iteratively aligning 10 frames acquired in sequence for a total exposure time of 20 s. Figure 3.6c and Figure 3.6d are the magnified regions in the red squares of Figure 3.6a and Figure 3.6b respectively. In this manner, it is possible to acquire images with relatively higher signal-to-noise ratio, while minimizing images deformations that occur when the samples drifts in one direction during a single long acquisition.

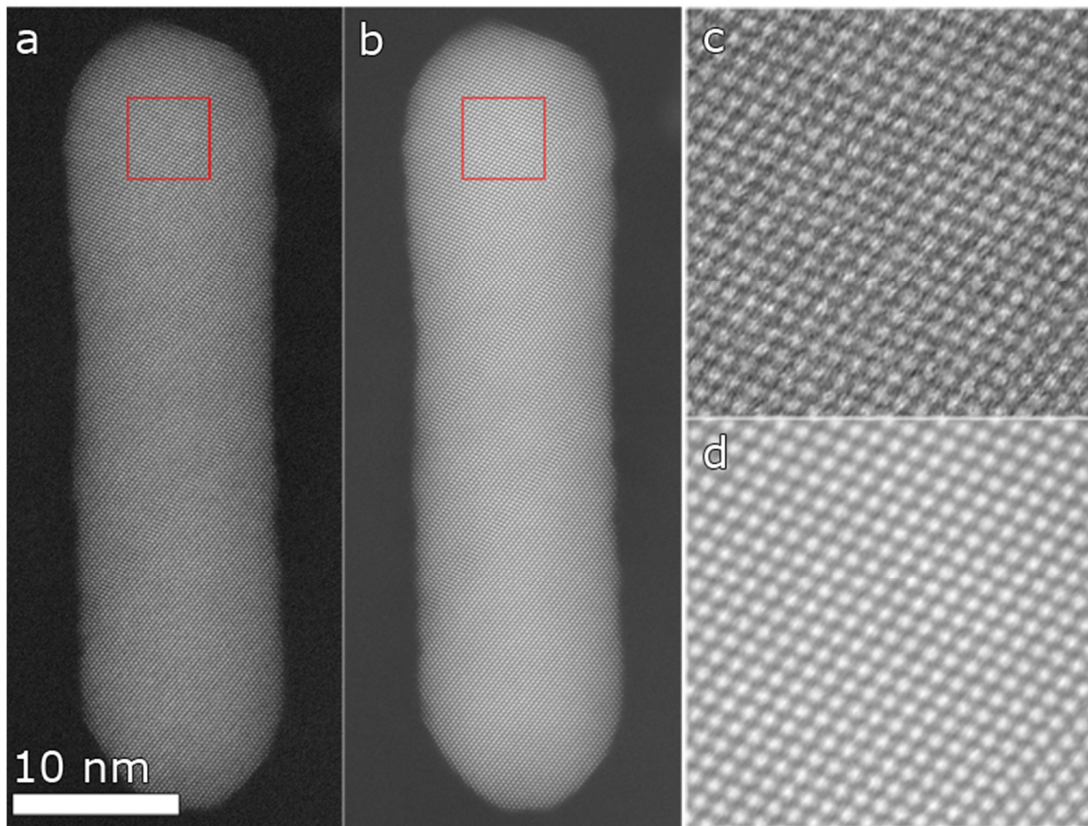


Figure 3.6: (a) HAADF-STEM image of a gold nanorod, single frame, exposure time of 2 s. (b) Averaged image from 10 consecutive scans, for a total exposure time of 20 s. (c,d) Magnified areas from the highlighted regions of (a,b) for a better comparison of the improvement in terms of signal over noise.

3.2.3 Tilt series alignment

After recording the projections, the tilt series needs to be registered. In biological sciences, it is common to use fiducial markers and usually a high-contrast colloidal dispersion (gold) which is deposited on the sample, allows a straightforward alignment of images in BF-TEM tomography of amorphous tissues.^[27] The nanoparticles act as reference markers, enabling the tracking of the sample. In materials science, fiducial markers are avoided, since they can overlap with the structure of interest and in general the imaged area is much smaller, making it difficult to use fiducial markers effectively. *Markerless alignment* of projections is therefore a necessary and can be usually achieved with different methods: maximizing the cross-correlation,^[64] minimizing the projection distance^[65, 66] or manually or by a combination of these approaches.

During my research I developed Matlab routines for all the three approaches. The most commonly used being based on sub-pixel cross-correlation.^[67] Cross-correlation is fast and works well for a rough alignment, but there are some drawbacks. The assumption that subsequent images in the tilt series do not vary dramatically, such to enable an accurate cross-correlation, is not always valid, and some errors can occur. Since images are aligned sequentially, only two at a time, it is also frequent that even though, images close in the tilt series are well aligned among each other, if an error occurs at some point, images at end of the series will not be aligned well with images at the beginning of the series.

Where cross-correlation fails, an alignment by projection distance minimization can be performed. In this case, instead of operating an alignment using only the images in the tilt series, the alignment is iteratively refined by comparing the projections to the forward projections simulated from an intermediate reconstruction. Initially the projections are aligned through cross-correlation or manually, a first reconstruction is calculated and then forward projections are simulated. The experimental projections are then aligned by cross-correlation to the simulated projections and the process is repeated until convergence. This technique is particularly useful when an high degree of accuracy is needed to achieve the desired resolution, as in the case of atomic resolution tomography.^[66]

3.2.4 Tilt axis alignment

Tilt axis alignment is another fundamental alignment to perform on the tilt series. In this case, by convention, the tilt axis of the series should pass by the center of the projections, vertically (parallel to the y-axis). In order to perform this alignment I developed a Matlab interface (Figure 3.7) that facilitates the evaluation of slices from the reconstruction. This interface operates similarly to FEI Inspect3D software. The advantage of using it was merely practical, since it eliminated the need of any external software, allowing all the workflow from alignment to reconstruction to be performed in Matlab. Typical artifacts in the reconstruction, known as *banana shapes* (red circles in the top row of Figure 3.8) indicates misalignment of the tilt axis. When the banana shapes of a top and bottom slice point in opposing directions, the tilt axis needs to be rotated, while when they point in the same direction the tilt axis needs to be translated without rotation. When the tilt axis is aligned, no artifacts should be visible anymore in slices from the top and bottom parts of the structure. In the example of Figure 3.8, the axis needed to be rotated of 21° clockwise and translated of 9 pixels in order to align the tilt axis. Applying the correction removes the artifacts in the reconstruction (bottom row of slices in Figure 3.8).

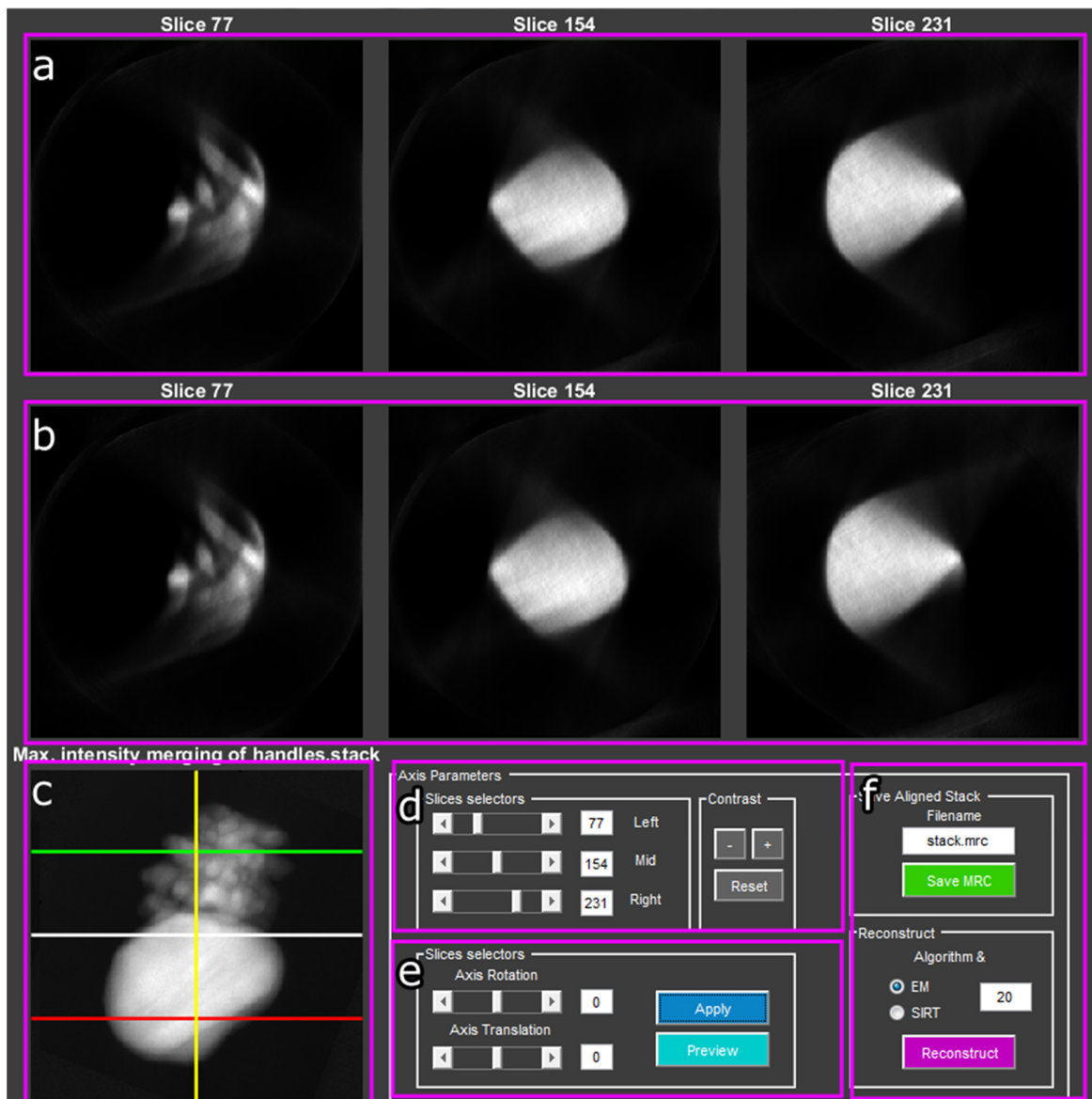


Figure 3.7: Matlab interface for tilt axis alignment. (a) The top rows of slices, shows the slices before any modification. (b) The second row shows the slices after application of any modification of the tilt axis. (c) Displays the maximum intensity merging of the projections of the tilt series, e.g. an image showing the maximum value of the tilt series for each pixel. (d) Sliders that control the selected slices and allow a change in contrast to enhance visualization of *banana shapes*. (e) Sliders to apply modification to the axis rotation and translation. (f) Saving the aligned stack to an MRC Extended^[68] type file or reconstruct it.

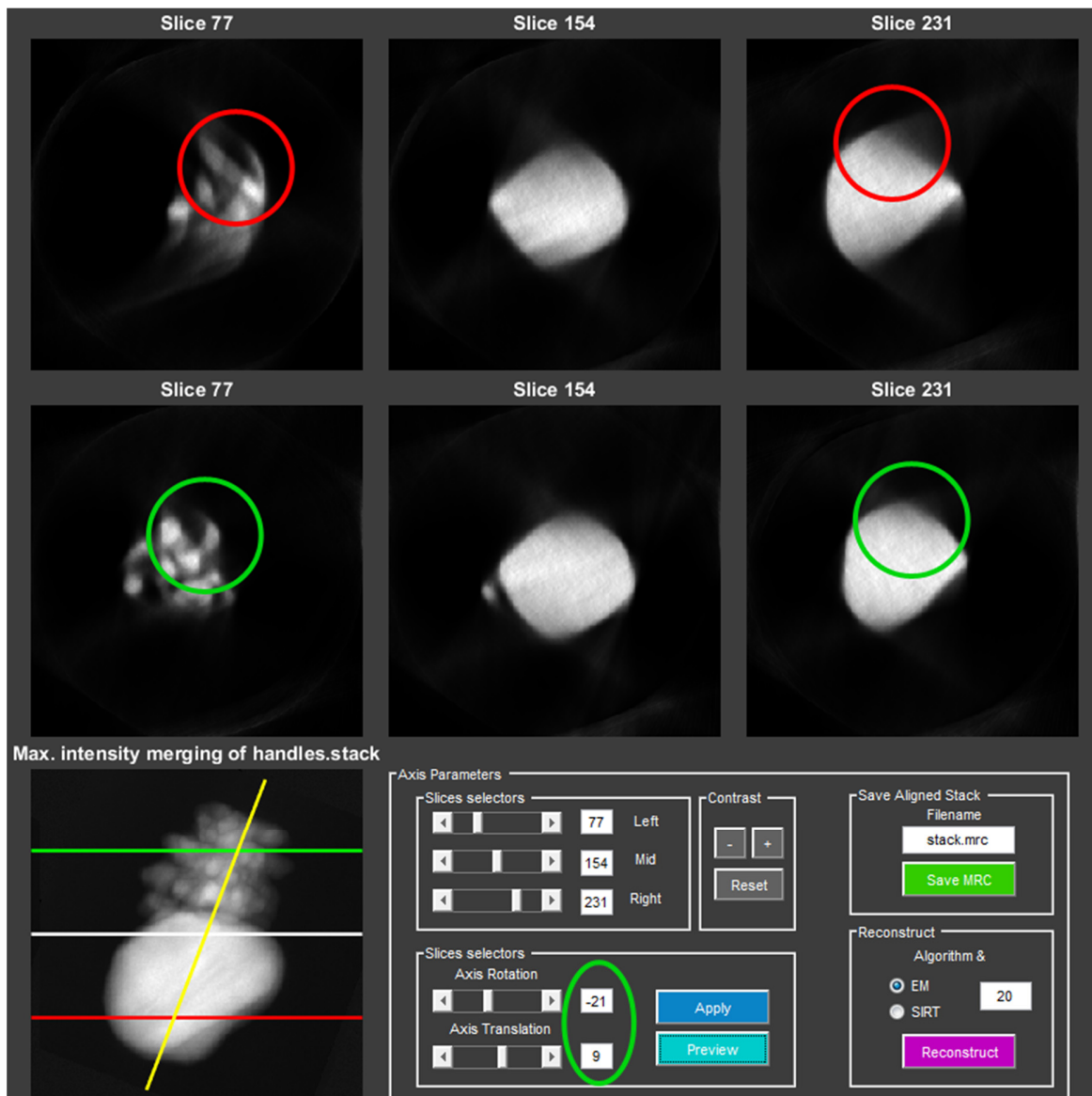


Figure 3.8: After applying an axis translation of 9 pixels and a rotation of -21° , the tilt axis is properly aligned, correcting the *banana shapes* artifacts (green circles).

3.2.5 Offset correction

Finally, after the series and tilt axis have been aligned, it is worth to mention the background correction. The carbon support is generally ignored, but its thickness varies as a function of the tilt angle, and can cause contrast variations that can generate artifacts. It is possible to correct for this effect by calculating the average value of the carbon support, by selecting a small background region, in each projection, and subtracting that value from the same projection. This correction is simple and often improves the quality of the final reconstruction.

3.2.6 Non-linear thickness effects

Another important artifact, especially for big assemblies or *heavy* particles is caused by nonlinear thickness effects,^[69] resulting from the exponential damping of the incoming beam traversing the sample. As a consequence, the linear model used in the reconstruction will produce artificial contrast, increased on the border of the structure, causing the intensity profile to look similar to a *cup*, from which this artifact takes the name of *cupping artifact*. An example is shown in Figure 3.9, for an assembly of Au nanoparticles. More details about this sample can be found in ref.^[70]. Figure 3.9a shows an HAADF-STEM projection extracted from the tilt series of the assembly. The large size (approximately 650 nm) and Z number of Au cause nonlinear effects in the formation of projections which affect the reconstruction. Figure 3.9b shows a slice from the SIRT reconstruction, where it can be observed a lower contrast for the particles in the center relatively to the particles towards the sides.

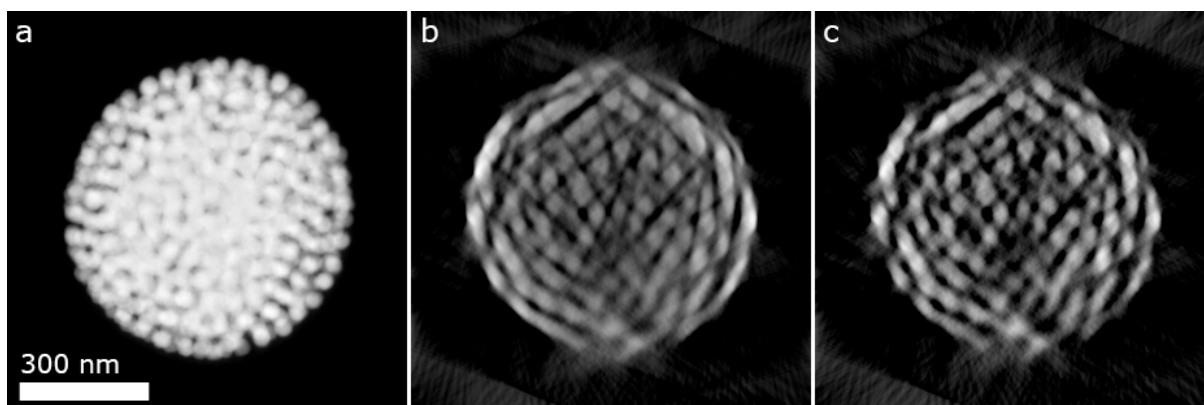


Figure 3.9: (a) HAADF-STEM image from the tilt series of an assembly of Au nanoparticles. (b) SIRT reconstruction slice obtained from the tilt series. Higher contrast for the particles at the left and right border of the assembly can be observed. (c) SIRT reconstruction slice obtained after correcting the projections intensities. Cupping artifacts are reduced and homogeneous intensity for the Au particles all over the structure is observed.

In order to correct for this artifact, it is possible to combine different acquisition strategies, as for example using a BF detector in STEM,^[70, 71] the technique is known as Incoherent Bright Field STEM (IBF-STEM), and/or directly apply a numerical correction to the intensities, as described in ref.^[69] Figure 3.9c shows a slice from the SIRT reconstruction, after the intensities correction is applied to the HAADF-STEM projections. As a result, the reconstruction intensities become homogeneous for the all Au particles, independently of their position.

3.2.7 Reconstruction and visualization

Once the tilt series are properly aligned, they can be used as input for a reconstruction algorithm. Several research groups developed software tools for the reconstruction of tomograms, for example IMOD^[72] and TomoJ.^[73] Commercial options as FEI Inspect3D are also available. A recent alternative, has been developed in collaboration between CWI in Amsterdam and VisionLab in Antwerp: the ASTRA toolbox.^[38, 40-43] ASTRA offers the possibility of exploiting Nvidia GPUs computation power, through the CUDA libraries, significantly cutting down on the time required to compute tomographic reconstructions (from hours to minutes). Furthermore, ASTRA is open source, freely available and comes with a Matlab and Python interfaces, which enable fast prototyping and development of custom algorithms. For these reasons, the ASTRA toolbox became the standard tool for the computation of reconstructions presented in this thesis, as well as the platform used for the new methods developed. Once the reconstruction volume is obtained, further analysis, as segmentation and visualizations through volume renderings are performed in FEI Amira software.

3.2.8 Tomography database

The final outputs of tomography experiments are three-dimensional reconstructions. Sharing these results in a static figure inside a text is therefore limiting. Usually, when a tomography study is published in scientific journals, it is made available with movies of the reconstructions, which can be found in the supplementary material on the publisher website. In an effort to further extend the experience of the interested researchers, our lab compiled a tomography database available online, where movies of tomography results from our group are presented, along with a gallery of interactive models. At the time of writing the COLOURATOM website project is available at: <http://ematweb.uantwerpen.be/colouratoms/>. QR codes providing linking to the database are also available in Figure 3.10 and Figure 3.11 for the models and movies galleries respectively.



Figure 3.10: QR code linking to the EMAT tomography database *Models* gallery (<http://ematweb.uantwerpen.be/colouratoms/pages/tomography.html>).



Figure 3.11: QR code linking to the EMAT tomography database *Movies* gallery (<http://ematweb.uantwerpen.be/colouratoms/pages/movies.html>).

Part II

Quantitative tomography of nanoassemblies

This second part presents the development of a new electron tomography methodology, aimed at the quantitative analysis of nanoparticles assemblies. In chapter four, the theoretical principles of the technique are shown along with phantom studies and in-depth analysis of experimental applications. The limitations of current electron tomography methods in retrieving quantitative information about nanoparticle assemblies are discussed, highlighting the advantages introduced by the new method. Application to other materials science cases are then shown in chapter five, where two different systems are studied. Chapter six presents the conclusions to this second part and an outlook to future developments in the field of shape models tomography.

4 Quantitative Tomography of Nanoparticle Assemblies

This chapter is based on the work published in the journal article of ref.^[50]: “Quantitative 3D analysis of huge nanoparticle assemblies”, D. Zanaga, F. Bleichrodt, T. Altantzis, N. Winckelmans, W. J. Palenstijn, J. Sijbers, B. de Nijs, M. A. van Huis, A. Sánchez-Iglesias, L. M. Liz-Marzán, A. van Blaaderen, J. K. Batenburg, S. Bals, G. Van Tendeloo, *Nanoscale* 2016, 8, 292.

4.1 Introduction

4.1.1 Self-assembly

The term self-assembly is defined as the autonomous organization of components into patterns or structures, without human intervention,^[74] or more precisely, as the spontaneous organization in structures of many discrete components that interact with one another directly and or indirectly through the environment.^[75] Self-assembly processes occur naturally in the formation of complex and large structures, with biological functions, at the basis of life.^[76] Besides its role in living systems, interest in self-assembly also derives from its potential as a manufacturing technique for nanotechnology devices. Using self-assembly to build nanomaterials through a *bottom up* approach is in fact cheaper and more accessible than current *top down* approaches, such as lithographic techniques^[77] or other methods that can be used to directly manipulate nanomaterials and atoms.^[78] One of the main applications of self-assembly is crystallization of components at all scales,^[74] such as colloids with diameters in the hundreds of nanometers,^[79, 80] nanoparticles with size in the tens of nanometers,^[81] and molecules.^[82] Systems of crystallized components show peculiar properties relatively to those of their building blocks or bulk counterparts.^[83] These properties can be tuned by adjusting the stacking of the individual nanoparticles, the distances between them and the overall size and shape of the assembly.^[84, 85] Nanoassemblies are suitable for applications in different fields,^[86-88] such as plasmonics,^[89] signal enhancement,^[90, 91] sensoric,^[92] catalysis^[93, 94] and data storage.^[95] In order to understand the properties of both nanocrystals and their assemblies, rigorous structural characterization of the obtained systems is critical.^[81] However, as the synthesized systems become more complex, an accurate characterization of the structure becomes more demanding.

4.1.2 Electron tomography of nanoparticles assemblies

Electron tomography is nowadays a standard for the qualitative structural and morphological characterization of nano-assemblies,^[70, 96, 97] yielding a three-dimensional description of the morphology and inner structure of the assembly, which is required to optimize the synthesis and to understand the

connection between the structure and properties. Furthermore, a quantitative description of the stacking of the individual nanoparticles forming these complex structures enables a comparison with simulations from theoretical models.^[98-101] In this manner, a better understanding of the mechanisms which rule the self-assembling process can be obtained. Determination of particles positions and inter-particles distances from a tomography reconstruction, is usually straightforward in the case of assemblies with few or well separated nanoparticles, as those shown in Figure 4.1. For such samples, formed by polystyrene stabilized Au nanoparticles^[102] can be easily quantified by applying a threshold segmentation of the reconstruction, which enables the separation of all the particles from the background.

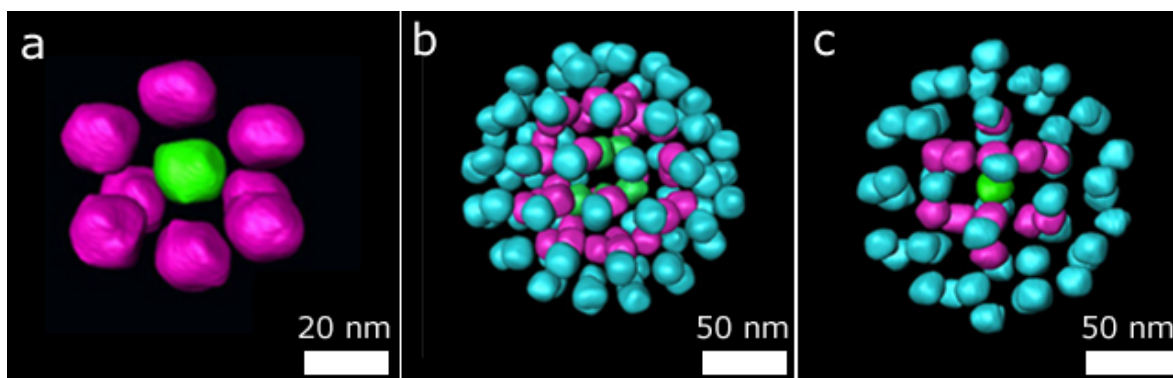


Figure 4.1: Manually segmented reconstruction renderings of Au nanoparticles assemblies. Different colors indicate a different shell, highlighting the structure. Images adapted with permission from ref.^[100] Copyright 2017 American Chemical Society.

Despite the clear advantages and the valuable information that can be obtained by electron tomography, the technique suffers from a number of restrictions, which limit the accuracy because of artifacts in the final reconstruction. Classical reconstruction algorithms, such as WBP,^[33] SIRT,^[35] ART,^[37] all yield 3D images that suffer from such artefacts.

As seen in sections 2.4 and 2.5, advanced algorithms have been proposed recently to improve the reconstruction process and to compensate for missing wedge artifacts through the implementation of prior knowledge concerning the nature of the sample. For example, compressive sensing techniques can be applied if the reconstructed image has a sparse representation with respect to a certain set of basis functions (e.g. Fourier components or wavelets^[103]). A variant of this concept is used in the case of TVM^[48, 104, 105] to recover an accurate reconstruction if it can be assumed that the object has a sparse gradient. Another successful example of prior knowledge exploitation is represented by the DART,^[45] where it is assumed that the object possesses a set of constant densities and the expected gray values related to these densities are known.

Here, we consider samples consisting of iron cobalt oxide spherical nanoparticles, in a closed packed arrangement, as those shown in Figure 4.2. For these kind of structures, the inter-particles distances can be considered to be negligible. Furthermore, in the reconstruction of tomographic series from such assemblies, blurring occurs due to under-sampling of the higher frequencies in Fourier space and the elongation introduced by the missing wedge leads to a superposition of the particles boundaries, hampering to distinguish them. An example of a SIRT reconstruction is given in Figure 4.3b, to illustrate this. Although, DART and TVM are known to reduce missing wedge artifacts, they do not provide improvement due to the overlapping of particles, and therefore the identification of their positions cannot be carried out even using these advanced approaches.

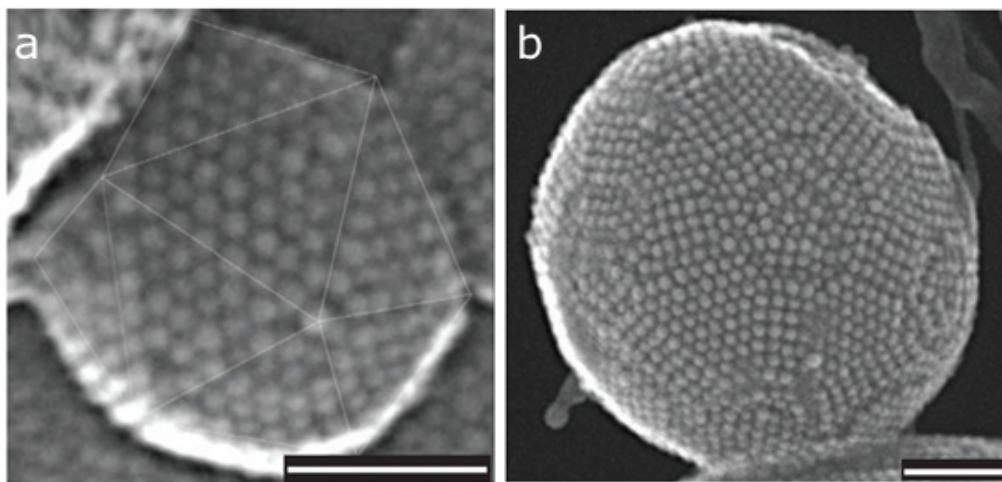


Figure 4.2: Secondary electron scanning transmission electron microscopy (SE-STEM) images of nanoparticle assemblies containing closely packed cobalt iron oxide nanoparticles. All scale bars are 50 nm. Images adapted from ref.^[100] with permission of the Nature Publishing Group.

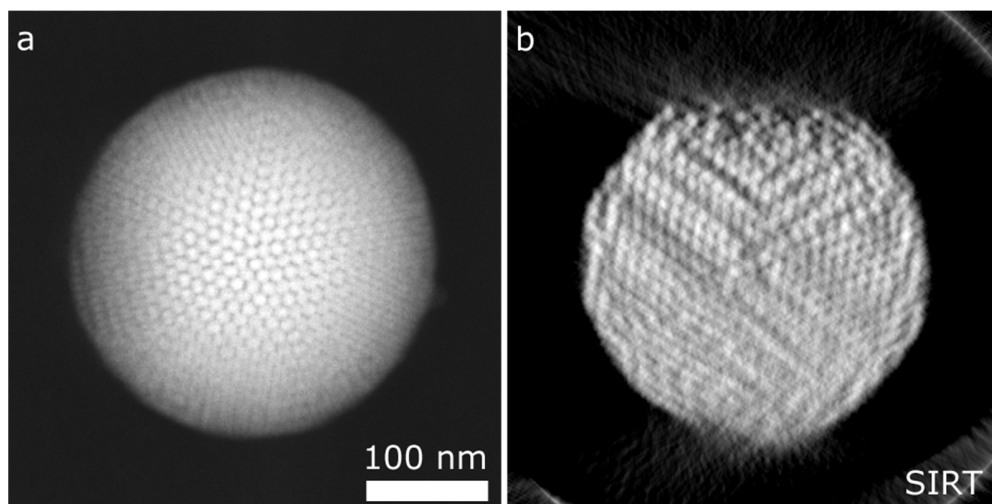


Figure 4.3: (a) STEM-HAADF projection of an iron cobalt oxide nanoparticles assemblies, extracted from a tomography tilt series. (b) SIRT reconstruction of the tilt series from (a). Single particles are hardly or not at all distinguishable due to a series of artifacts caused by a non-optimized acquisition and reconstruction.

4.2 Nanoparticles assemblies quantification

The information required to fully quantify an assembly of particles essentially consists of the number of particles and their positions. Usually, with assemblies of closely packed particles, if a small number of them is present, it is possible to manually segment the reconstruction to separate the volumes. In this manner, the number of particles can be determined and their coordinates can be estimated. However, if the number of particles increases, manual segmentation becomes more difficult, time consuming and most importantly subjective. The complexity of the structure and reconstruction artifacts prevents a reliable manual segmentation of the assembly and therefore a quantitative interpretation concerning the number of particles, the symmetry of the stacking and the positions of the building blocks becomes impossible.

The underlying reasons for performing electron tomography experiments for such samples are related to the 3D stacking of the individual particles. The outcome of these experiments can be used as an input for modeling studies enabling one to predict the final 3D structure as a function of the parameters used during the synthesis.^[98] As an input for modeling, it is important to determine the coordinates of each particle in order to obtain inter-particle distances and investigate the 3D symmetry of the stacking. During such studies, the exact shape of the individual particles is not of crucial interest and it is acceptable to assume that they correspond to perfect spheres.

Exactly this property, that the full object is an assembly of spheres, implies that these monodispersed nanoparticle assemblies exhibit a particular form of sparsity: *they have a sparse representation on a set of basis functions that consists of spheres*. In the following paragraphs we will see that by using sparse reconstruction techniques for this particular basis we are able to obtain a quantitative tomographic reconstruction of complex assemblies that previously failed to be reconstructed with the available techniques described in sections 2.4 and 2.5.

4.3 Prior-knowledge implementation

4.3.1 Mathematical formulation

As seen in paragraph 2.4.3, the system of linear equations representing the tomography problem can be written in matrix notation as $Wx = b$ (eq. (2.4)). This system of equations is usually underdetermined due to the limited number of projections and therefore has infinitely many solutions, leading to an ill-posed inverse problem. Moreover, the presence of noise causes the equation system to be inconsistent. For these reasons, the system is solved in a least squares sense, minimizing $\|Wx - b\|_2$ and regularization techniques are used to find a unique solution. One possibility for regularization is to use the fact that many structures exhibit sparse boundaries, in which case TVM can be used.

Nanoassemblies of spherical particles do not have a sparse representation on a voxel grid, which is used in the linear model in eq. (2.4). However, we can still employ sparsity promoting linear solvers by using a sparse image representation. If we assume that all particles are perfect spheres and if the size of the particles can be estimated, we can use discretized spheres as basis elements and encode an image of spheres by the center coordinates of these spheres. This concept is explained in the following example. For simplicity we start from the 2D case where we use disks of radius r , instead of spheres, but the extension to 3D is straightforward.

Let's consider the following image transformation:

$$x = Cy \tag{4.1}$$

where $y_i = 1$ if a sphere center is located at pixel x_i . Each column \vec{c}_j is a vectorized $u \times h$ image containing one discrete disk with its center at pixel x_j . This matrix C is too large, especially in the 3D case to form it explicitly. However, we can also see it as a convolution operator, where we convolve the disk centers y by the discrete $2r \times 2r$ image of a single disk. This operation can be done efficiently by using Matlab's built-in image convolution method.

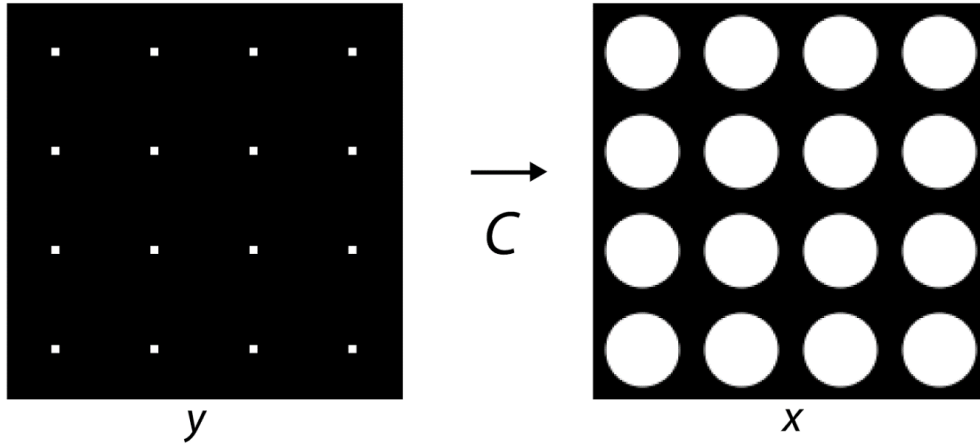


Figure 4.4: Representation of equation (4.1), where x is obtained by convolving the particles centers by the basis shape (in this 2D example, a disk).

We can now substitute this image representation in our tomography problem such that:

$$WCy = b \quad (4.2)$$

Since the number of particles in the sample is small compared to the number of voxels, the coefficient vector y will be very sparse. To incorporate this sparsity assumption in the reconstruction, we solve the following problem:

$$\min_y \|y\|_1 \text{ subject to } \|WCy - b\|_2 \leq \sigma \quad (4.3)$$

where σ is the noise level. This approach is known as Basis Pursuit Denoising (BPDN) and an algorithm for solving it has been implemented in the Matlab package SPGL1.^[106] In the remainder of this thesis, we will refer to this approach as *Sparse Sphere Reconstruction* (SSR).

As further demonstrated for experimental data, this approach is particularly useful when investigating compact assemblies. For these studies, other algorithms do not yield sufficient resolution to allow the user to separate the single particles by application of a threshold. Since the spheres are close together, both the gradient of the image (TVM) and the knowledge of the gray level (DART) will not be sufficient to resolve the very small distances. Furthermore, even in the case of a phantom, where the lack of experimental errors in the acquisition should in principle result in a null projection distance, it is not straightforward to measure the number of spheres when they are in contact with each other. A manual segmentation step would be

required, and in the case of hundreds or even thousands of particles the process would be extremely time consuming. Moreover, and maybe even more importantly, manual segmentation is a subjective process which can therefore not result in quantitative results.

4.3.2 Implementation

The use of GPUs has become a widespread approach to tackle heavy computational problems.^[73] The recent release of the ASTRA toolbox (All Scale Tomographic Reconstruction Antwerp),^[40, 107] an open source, GPU-accelerated library for 3D image reconstruction in tomography, enables the development of custom algorithms and methods in Matlab and Python. We developed the new approach described here, following the method proposed in ref.^[42] by combining the ASTRA and the SPOT^[108] toolboxes to generate the problem in matrix notation (in Matlab) and then use a general sparse solver SPGL1^[106] for the SSR problem.

Note that the matrix C could be seen as a convolution operator, but forming the matrix explicitly is not practical due to its size (the same goes for the weighting matrix W). We can use image convolution of the sphere centers y with a discretized sphere of size $2r \times 2r \times 2r$ by using one of Matlab's convolution routines such as `imfilter` (or implementing a convolution in the Fourier domain with `fft`). The SPOT operator is an object that can be used with Matlab's matrix syntax (e.g. to compute $x = C*y$), but internally it calls the `imfilter` routine to actually perform this matrix operation. This allows easy implementation of eq. (4.3) which is simply reduced to:

$$y = \text{spgl1}(W*C, b);$$

In practice, the weighting matrix W and the convolution matrix C are generated in Matlab through the SPOT toolbox. The SPOT operators/objects, are handled by Matlab as if they are explicit matrixes, while actually it is the SPOT toolbox that generates the matrix values needed for the calculation *on the spot* as they are requested. This enables the use of matrix solvers such as `spgl1` or `lsqr`, without actually defining W and C explicitly. Instead, W will make use of ASTRA projectors that operate over the GPU, to compute the forward and back-projections and C will use Matlab's `imfilter` routine. The prior knowledge about the sample is introduced here in the reconstruction algorithm by defining the operator C , since that represents the convolution operator by a sphere of radius r . The radius of the basis shape, composing the assembly of particles that is going to be investigated is usually estimated from a preliminary SIRT reconstruction or directly from the HAADF-STEM projections.

Once the SPOT operators have been declared, it is possible to use `spgl1` to solve eq. (4.3), which represents the first step in obtaining the final reconstruction. This solution should be the sparse representation y but as can be observed from column 2 of Figure 4.6, it is still not a perfect grid of ones and zeroes representing the centers of the disks. Blurring and striking artifacts due to under-sampling of higher

frequencies and missing wedge also occur. Nevertheless the sparse representation can be easily recovered and the artifacts eliminated by applying a local maximum extraction routine. To do that, each pixel is compared with its neighbors and selected as a local maximum if the neighbors are smaller than the current pixel value. The neighbors are defined by a *neighborhood*, which is a small mask of zeros and ones, indicating whether a pixel is in the neighborhood or not. The mask will be a spherical mask with radius of $1.8r$. The second step of the reconstruction will be then carried out through the application of the local maximum extraction in order to remove the artifacts and recover the expected sparse representation y and the application of the operator C (eq. (4.1)) to this in order to obtain the final reconstruction of the object.

4.4 Phantom studies

The most intuitive case to demonstrate the operating principle is a two-dimensional phantom composed of discs of known radius (Figure 4.5c).

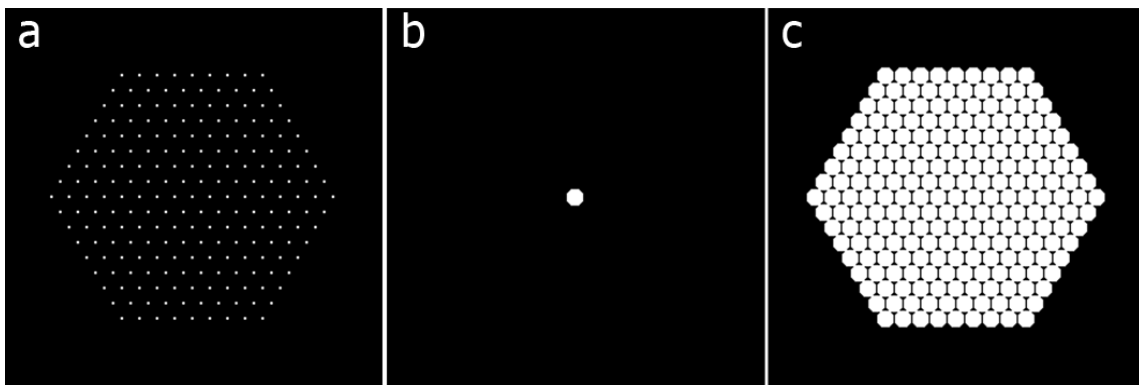


Figure 4.5: A hexagonal lattice of pixels (a) is convolved with (b) to generate the phantom (c). In the sparse formulation of eq. (4.1), (c) represents x , (b) represents the prior knowledge implemented through the matrix C and (a) is the exact solution y .

In Figure 4.6, SIRT and SSR reconstructions for different missing wedges and different angular sampling frequencies are compared to show how the SSR approach, in contrary to a SIRT algorithm, enables to recover the missing information yielding a perfect reconstruction. As explained in section 4.3.2 two consequent steps are implemented after the minimization leading to the sparse solution (Figure 4.6b): a local maxima extraction and a convolution of the local maxima with the prior knowledge disc (Figure 4.5b), leading to the final reconstruction (Figure 4.6c).

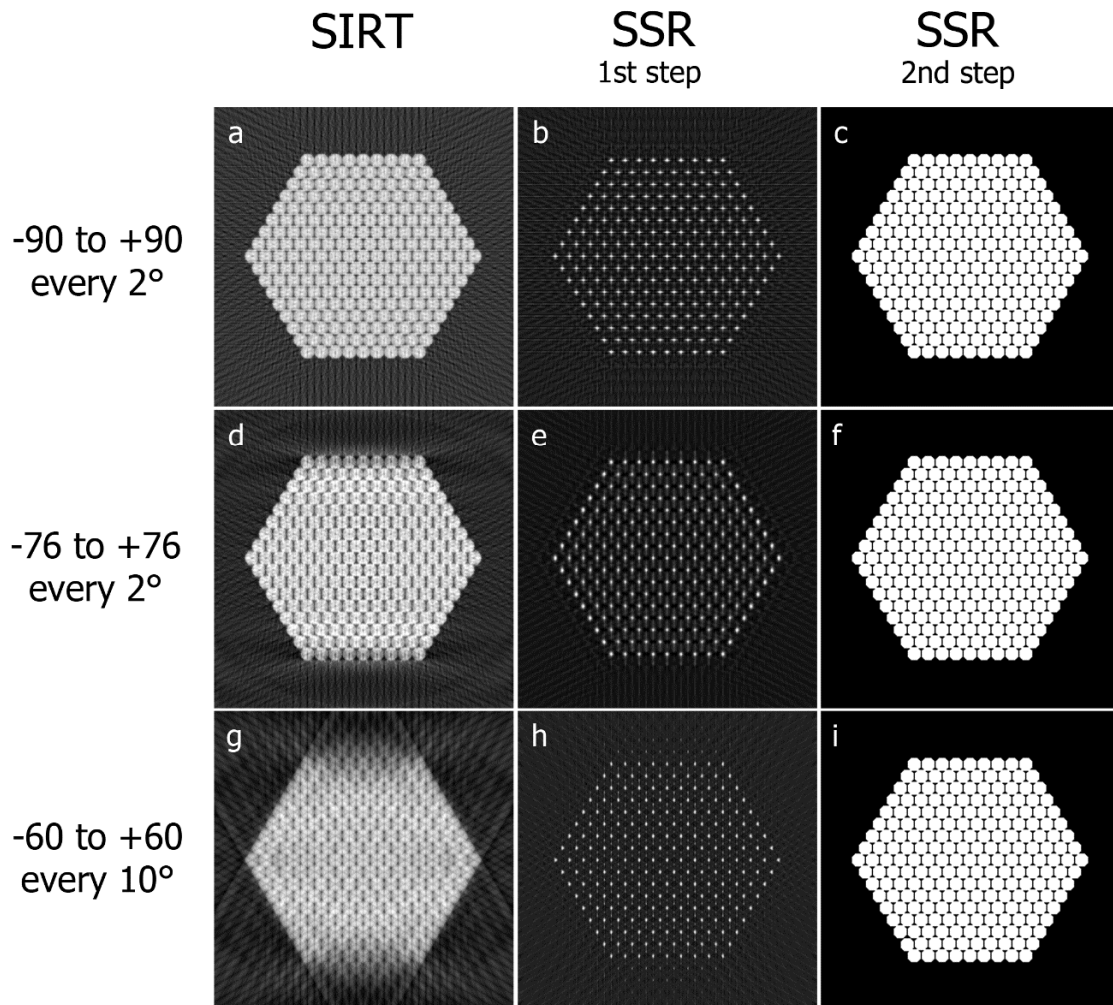


Figure 4.6: SIRT reconstructions (a, d, g) of the phantom in Figure 4.5c for different angular intervals and sampling frequencies. Solution retrieved minimizing $\|W Cy - b\|_2$ (b, e, h). And finally in (c, f, i) are shown the reconstructions obtained extracting the local maxima from (b, e, h) and convolving them for the prior knowledge shape (Figure 4.5b).

Figure 4.6 also shows that the method differs in principle and results from a deconvolution of the SIRT reconstruction with the prior knowledge kernel. The SSR reconstruction clearly recovers the lost information due to the missing wedge and limited projection angles. In these cases SSR results in a perfect reconstruction of the phantom (Figure 4.6c, f, i). Further evidence is presented in Figure 4.7, where a line profile of the reconstructions is acquired along the direction hampered by the missing wedge and along a

diagonal of the hexagon. In Figure 4.6g and Figure 4.6h it is shown how the SSR algorithm enables to detect and automatically quantify all the particles. These results are in contrast to the SIRT reconstruction, where the discs are almost unrecognizable.

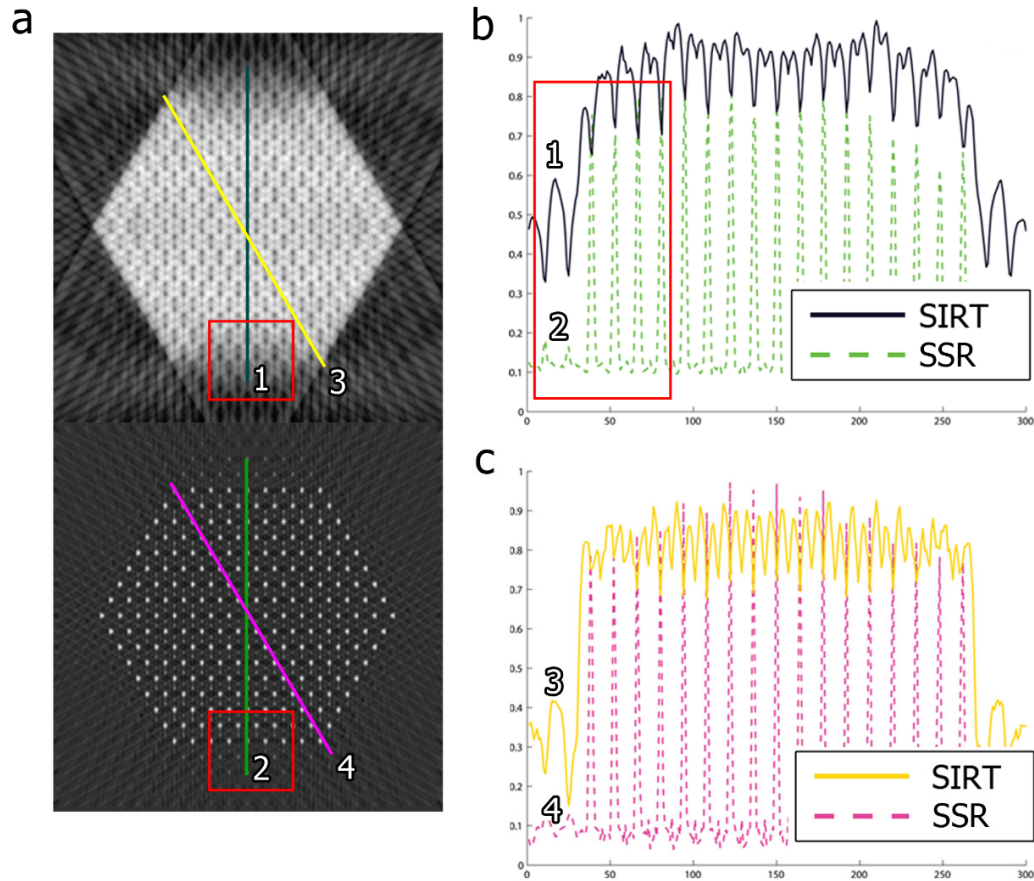


Figure 4.7: (a) SIRT and SSR reconstructions with lines indicating the direction of the profiles shown in (b) and (c). The rectangle highlights the recovered information in the zone that is most affected by the missing wedge artifact. A continuous noisy gradient is observed in the SIRT with a pronounced anisotropy of the reconstruction, which is not present in the SSR one.

4.4.1 Three-dimensional phantom study

The extension of the approach explained above to the three dimensional case is straightforward from a theoretical point of view and the main difference is the computational load. Figure 4.8 shows a three-dimensional phantom along with its SIRT and SSR reconstructions from a simulated acquisition with an angular interval from -60° to $+60^\circ$ every 10° .

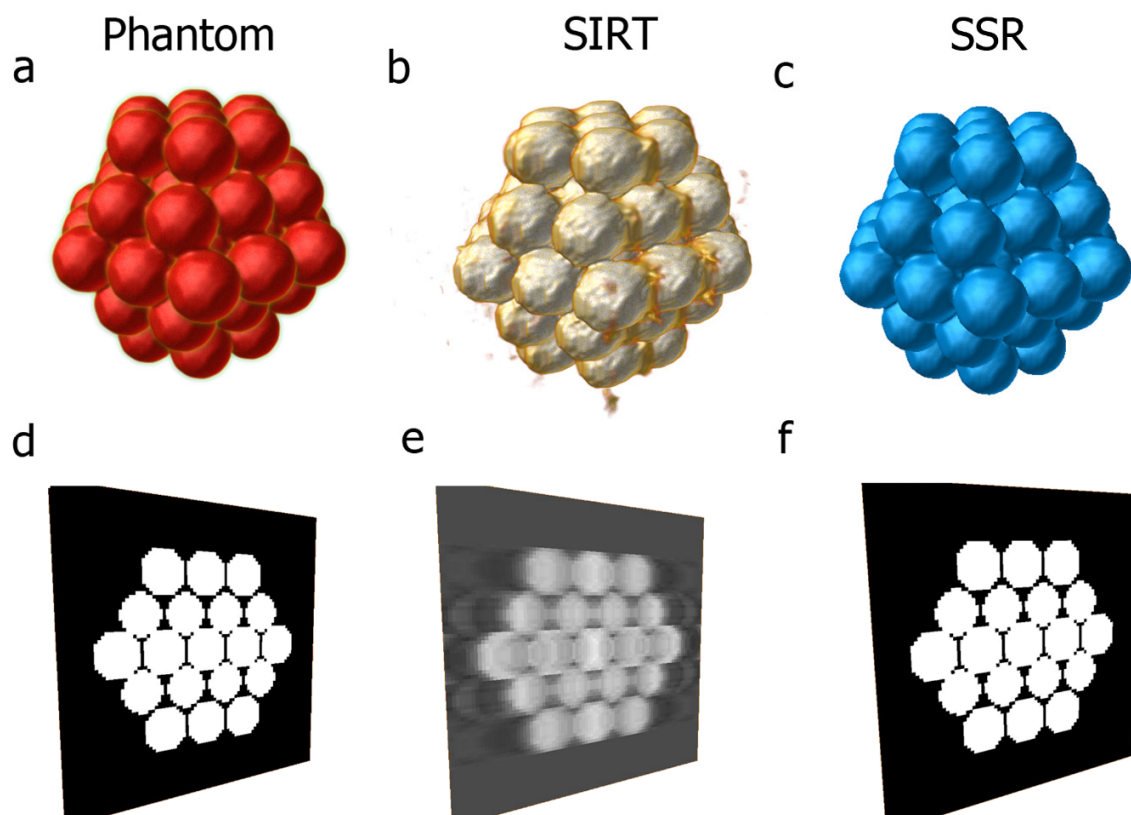


Figure 4.8: (a) Phantom of a hexagonal closed-packed cluster and a slice through it (d). (b, e) 3D visualization of a SIRT reconstruction with a slice through the reconstruction. (c, f) 3D visualization of a SSR reconstruction with a slice through the reconstruction.

From Figure 4.8e it is possible to understand how in a SIRT reconstruction, particles close cannot be automatically segmented by selecting a threshold, since they overlap on the borders due to missing wedge elongation (horizontal direction here) and features blurring. The SSR reconstruction (Figure 4.8f) on the other hand, intrinsically yields the coordinates of all the particles, therefore overcoming this limitation. In the following sections, we will see how the technique is applied to real cases, enabling quantitative characterization of complex structures.

4.5 Iron cobalt oxide assemblies obtained by spherical confinement

In the work of de Nijs et al.^[100], an investigation on the origin of the icosahedral symmetry, commonly found in systems such as liquids, glasses, atomic clusters, quasicrystals and virus-capsids, is presented. The investigation revealed that, contrary to what was previously believed, inter-particle attractive interactions are not essential to obtain a high degree of icosahedral order from tens of particles or more. Our collaborators from the Soft Condensed Matter, Debye Institute for Nanomaterials Science of Utrecht University demonstrated with simulations and experimental cases, how icosahedral symmetry also occurs in the absence of attractive interactions, due to entropy and spherical confinement, providing insights into the interplay between confinement and crystallization.

To experimentally study the behavior of colloidal spheres in spherical confinement, cobalt iron oxide nanoparticles were synthesized,^[109] with a core diameter of 6 ± 0.29 nm (9 nm effective due to interdigitating oleic acid ligands). The nanoparticles were dispersed in an apolar solvent, the dispersion was emulsified into an oil-in-water emulsion and then the solvent in the suspended emulsion droplets was evaporated slowly, causing the packing fraction of nanoparticles in the droplets to increase, which eventually caused crystallization of the nanoparticles in assemblies such as those shown in Figure 4.2. In order to characterize the inner structure and confirm the icosahedral symmetry highlighted in Figure 4.2a, coordinates of the particles need to be retrieved to perform quantitative analysis.

4.5.1 Synthesis and TEM preparation of the Fe–Co–O assemblies

The assemblies were synthesized using the emulsion based bottom-up self-organization method.^[110] First, the core-shell FeO/CoFe₂O₄ nanocrystals were synthesized according to the procedure of Kovalenko et al.^[111]. These pre-synthesized nanocrystals are redispersed in cyclohexane. This oil phase containing the nanocrystals is mixed with an aqueous solution containing multiple surfactants (sodium dodecylsulfate, dextrane (mol wt 1 500 000–2 800 000) and distilled water) through vigorous stirring. To make sure that the clusters are monodispersed, the pre-mixed emulsion is pumped into a couette shear mixer.^[112] Next, cyclohexane is evaporated from the sheared emulsion by heating it to 68 °C. Evaporation of cyclohexane from the oil micro-emulsion droplets cause them to shrink, and the rising of nanocrystals concentration promotes their self-assembly into 3D colloidal spheres. In order to study the assemblies in the electron microscope, TEM grids need to be prepared. However, depositing a solution drop onto the grid and letting it dry at room temperature would cause the assemblies to deform because of the capillary forces between the assemblies and the carbon coated grid. Therefore, the solution is deposited on the TEM grid, immediately vitrified at liquid nitrogen temperature and then sublimated in an Environmental Scanning Electron Microscope (ESEM) at a controlled temperature and pressure. This avoids contact between the

colloidal particles composed of the nanocrystals and a drying liquid that is on the outside of the supraparticles, preventing the deformation of the assemblies.

4.5.2 Acquisition and alignment of the tilt series

All series were acquired in STEM mode with the use of a HAADF detector. The tilt series were acquired using an aberration corrected cubed FEI Titan 60–300 electron microscope, operated at 300 keV. A Fischione 2020 single tilt tomo-holder was used for all the experiments, with the following tilt ranges: -48° to $+62^\circ$ with an increment of 2° for the 50 nm Co–Fe–O assembly (Figure 4.9a), -58° to $+76^\circ$ with an increment of 2° for the 100 nm Co–Fe–O assembly (Figure 4.9b), -32° to $+76^\circ$ with an increment of 2° for the 150 nm Co–Fe–O assembly (Figure 4.9c), -71° to $+76^\circ$ with an increment of 1° for the 300 nm Co–Fe–O assembly (Figure 4.9d) and -70° to $+78^\circ$ with an increment of 2° for the Au sample shown in section 4.6. Alignment of the tilt series was performed through Matlab routines based on cross-correlation and manually with IMOD.^[72] The series were corrected for cupping artifact as described by Van den Broek et al.^[69] and denoising of the series was performed through the application of a Gaussian filter. We observed that noise reduction at the expense of a loss of resolution in the starting series resulted in a better quality of the final reconstruction.

It is also important to mention that we observed a slight shrinkage of assembly upon initial illumination under the electron beam, probably due to general shrinkage of the nanoparticles ligands. For this reason, we usually illuminated the assembly for approximately half hour before starting the tomography tilt series, in order to let it stabilize.

4.5.3 SIRT and SSR comparison

Assemblies of different size were analyzed. STEM tomography tilt series were acquired for the particles shown in Figure 4.9.

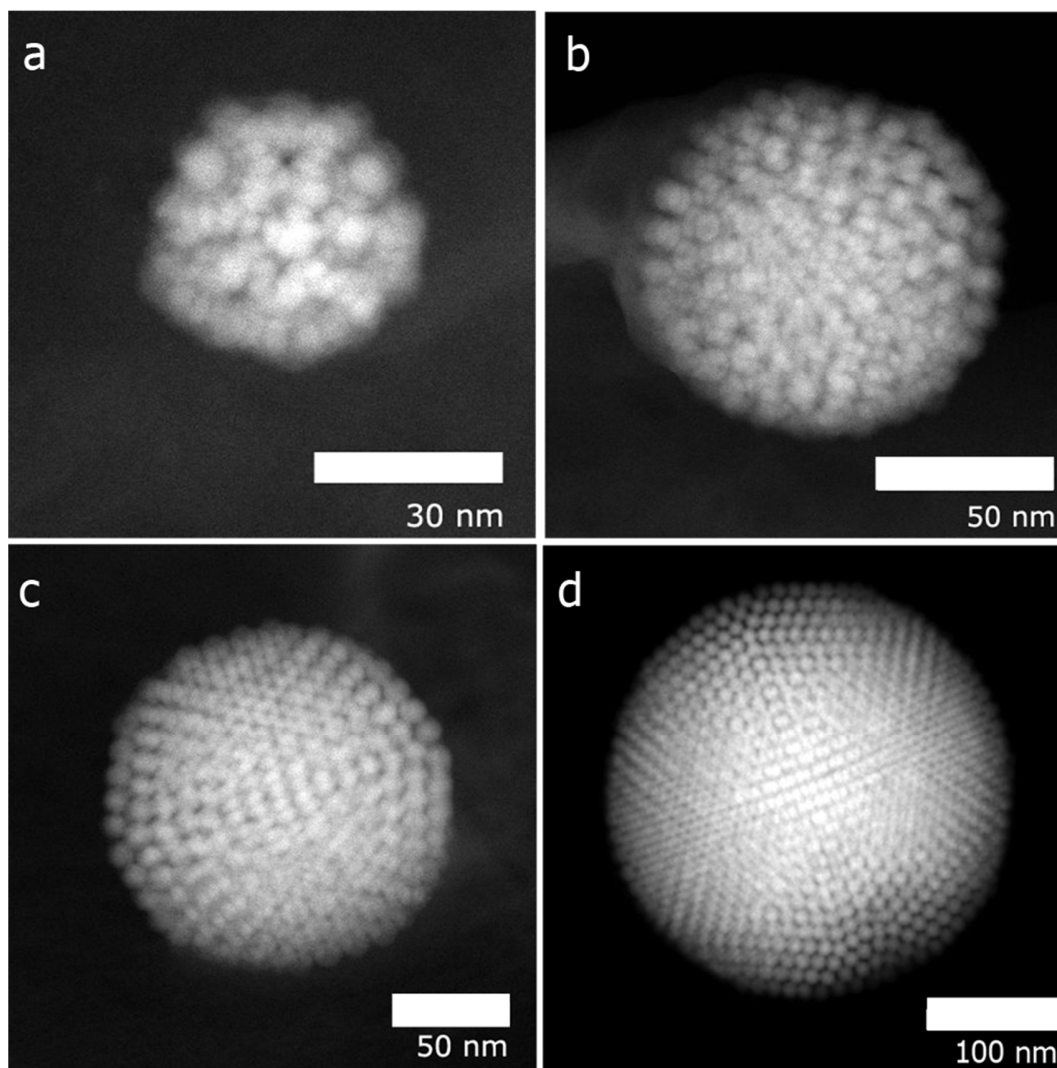


Figure 4.9: Assemblies of iron cobalt oxide nanoparticles with a diameter of approximately (a) 50 nm, (b) 100 nm, (c) 150 nm, (d) 300 nm.

Figure 4.10 shows the SIRT reconstructions for the assemblies of Figure 4.9. Due to the poor positioning on the grid, very limited tilt ranges were possible for the assemblies of 50 nm, 100 nm and 150 nm (Figure 4.10a,b,c) and as a consequence, strong missing wedge artifacts with elongation of features can be observed in the volume renderings of the SIRT reconstructions.

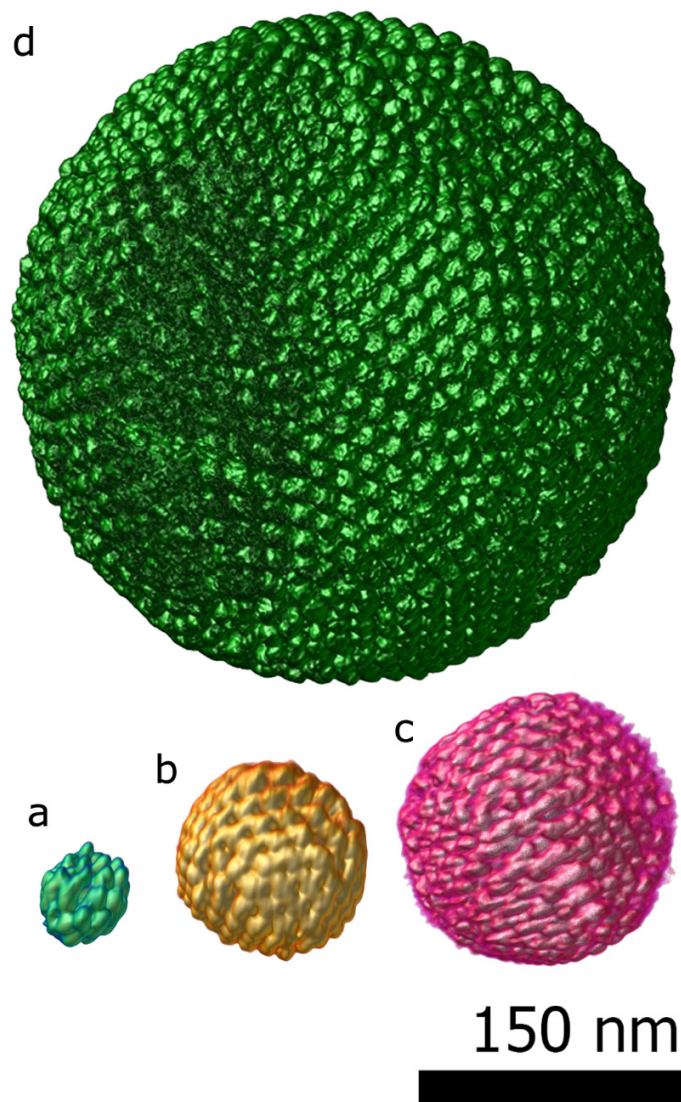


Figure 4.10: SIRT reconstructions of Fe-Co-O nanoparticles assemblies with different diameter of approximately: (a) 50 nm, (b) 100 nm, (c) 150 nm (the icosahedral symmetry of the particle is observed this view) and (d) 300 nm.

From the SIRT reconstructions it is not possible to manually segment the particles, since the missing wedge artifacts and number make the process too subjective and time consuming. Applying the SSR reconstruction algorithm on the other hand, successfully yields the structure of the assemblies enabling their analysis. A comparison of slices from the SIRT and SSR reconstructions of the assemblies is shown in Figure 4.12 and Figure 4.13.

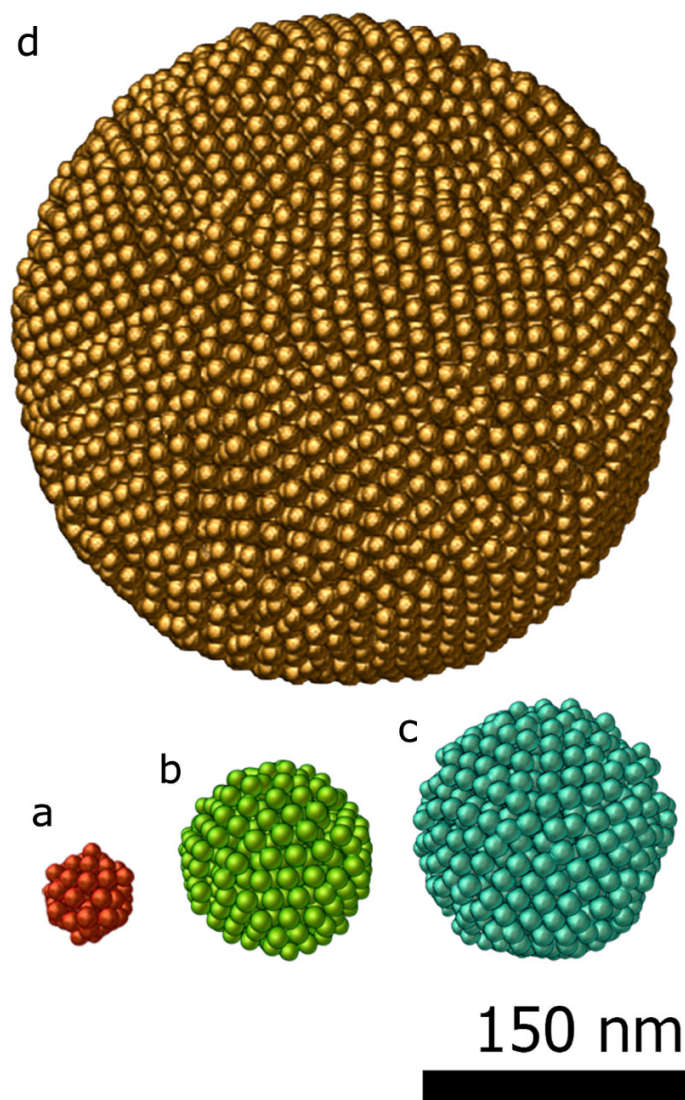


Figure 4.11: SSR reconstructions of Fe–Co–O nanoparticles assemblies with different size: (a) 50 nm diameter containing 70 particles. (b) 100 nm diameter containing 574 particles. (c) 150 nm diameter containing 1305 particles. The icosahedral symmetry of the particle is clear from this view. (d) 300 nm diameter containing 9301 particles.

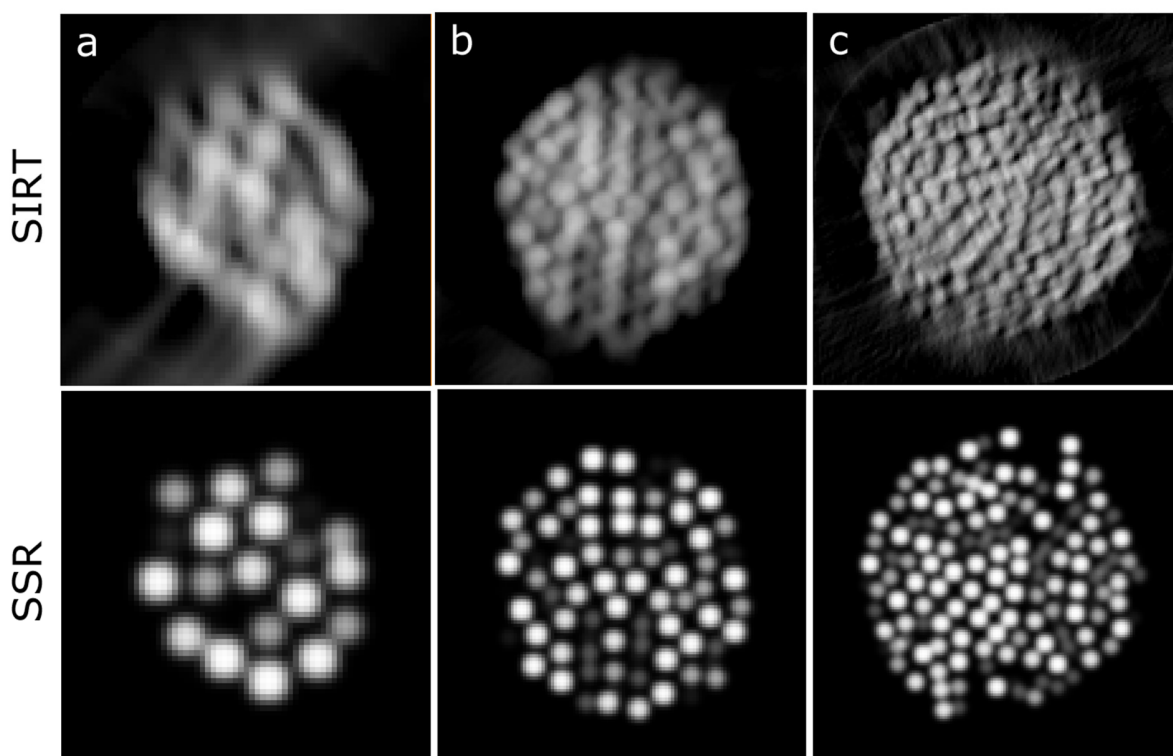


Figure 4.12: Comparison of slices from the SIRT and SSR reconstructions of Fe–Co–O nanoparticles assemblies with different size: (a) 50 nm diameter. (b) 100 nm. (c) 150 nm diameter.

Taking a closer look at the 300 nm assembly in Figure 4.13, which due to its size represents the most challenging case in terms of acquisition optimization and reconstruction, we can see how the missing wedge artifacts, noise and blurring hinder any quantitative analysis based on the SIRT reconstruction (Figure 4.13a, c). In comparison, the SSR reconstruction shows a perfect surface reconstruction (Figure 4.13b), as well as complete recovery of the information lost due to missing wedge artifacts, highlighted by the red box in Figure 4.13d.

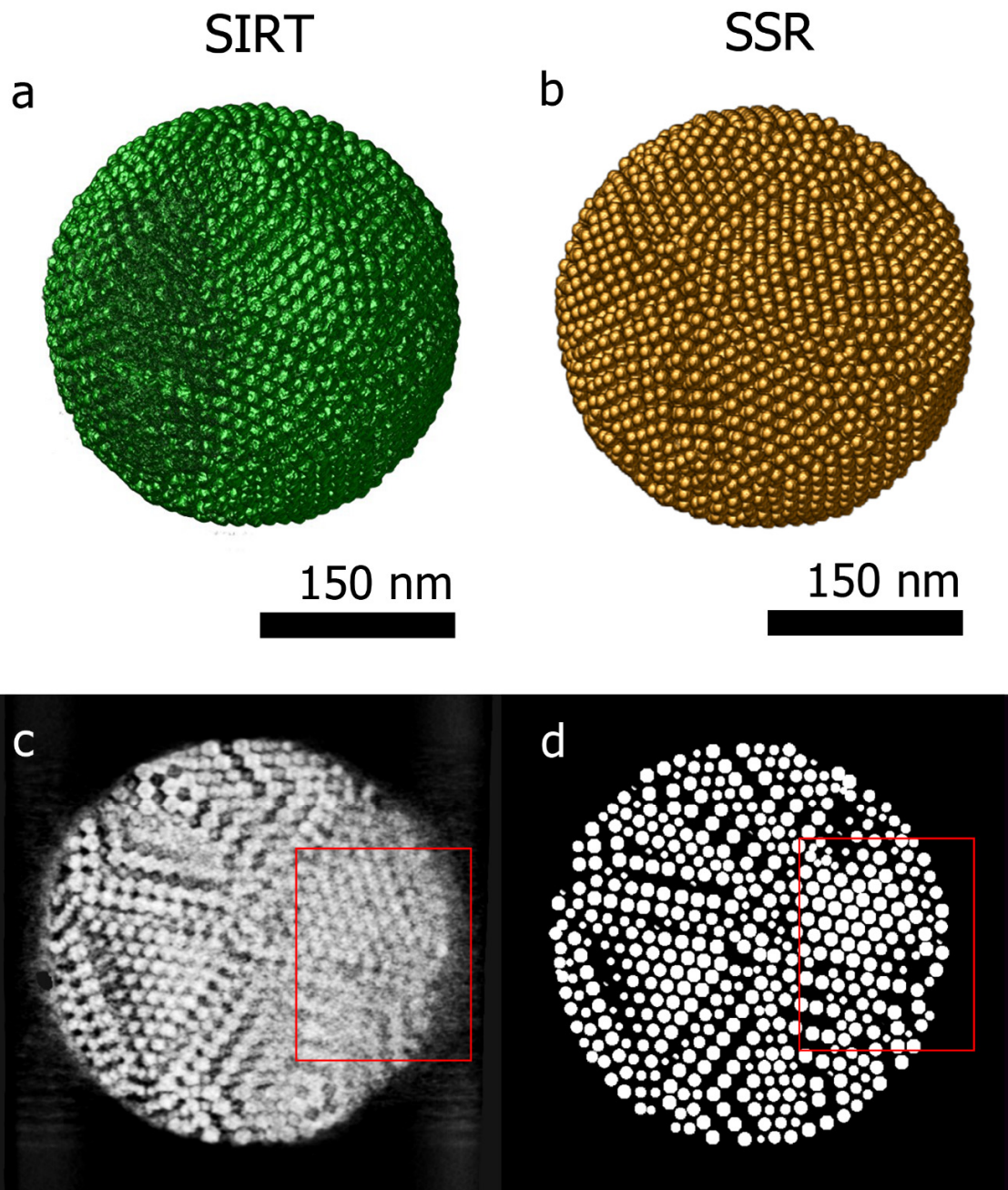


Figure 4.13: (a) 3D visualization of the SIRT reconstruction of an assembly of about 9000 Fe–Co–O particles. (c) Slice acquired through the SIRT reconstruction, missing wedge artifacts are highlighted by the red rectangle. (b, d) 3D visualization and slice of the corresponding SSR reconstruction.

Once the coordinates are obtained, further analysis can be performed to investigate which type of stacking is observed inside the assembly. According to simulations a *face centered cubic* (fcc) type of stacking was

expected for this kind of assemblies obtained by spherical confinement.^[100] Further investigation of this hypothesis is now possible thanks to the determination of the particles positions by means of electron tomography and SSR reconstruction.

4.5.4 Structural analysis

In order to determine the type of packing and confirm the structure, the coordinates obtained through SSR are used to calculate the bond order parameters of every particle.^[113, 114] Bond order parameters analysis is a standard method used in the determination of crystal structures. These parameters are rotationally invariant scalars which depend exclusively on the relative position of neighboring atoms/points and are used as a fingerprint of a given type of packing. By comparing bond order parameters obtained from the system under investigation, with those obtained from ideal structures it is possible to identify which type of crystalline arrangement is present. More details on the technique can be found in Appendix A and in ref.^[113, 114]. To extract them, a radial distribution function of the particle coordinates is first calculated in order to estimate the cutoff length determining the first neighbors. The cutoff is taken as the position of the first well after the first peak of the radial distribution function. Once the cutoff length is obtained, the algorithm provided by Wang et al.^[114] is used to calculate the scalar values of the bond order parameters for each particle.

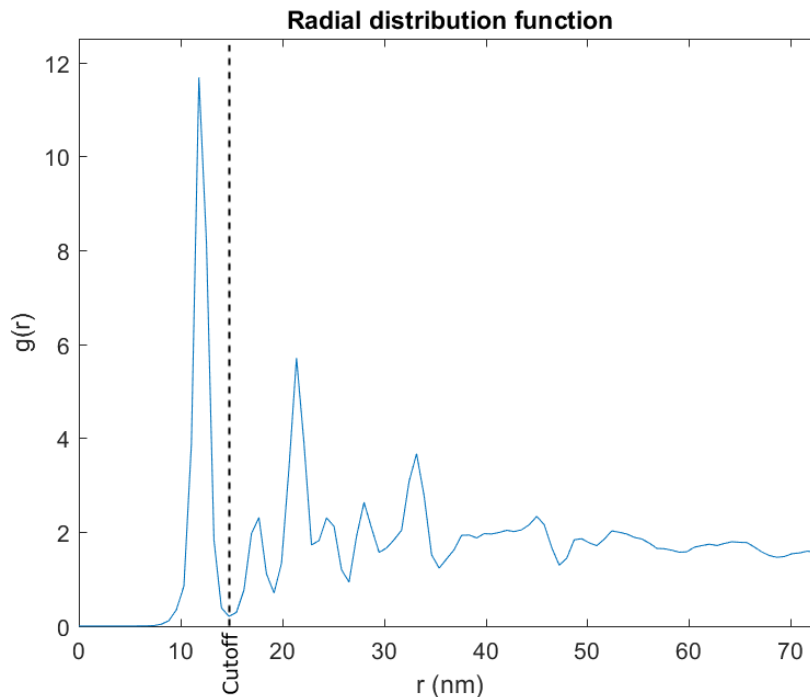


Figure 4.14: Radial distribution function for the Fe-Co-O assembly shown in Figure 4.13.

The obtained parameters are then clustered through a k-means algorithm,^[115] and the clusters center values are compared to literature values for the types of packings expected. The algorithm enables the partition of a group of vectors (in this case the bond-order parameters of the particles in the assembly) in k sub-groups, where k is the groups number provided as an input. The algorithm iteratively identifies the clusters centroids and clusters populations until it converges to a minimization of the intra-cluster variances.

The comparison of the bond order parameters obtained from the coordinates of the particles yielded by the SSR algorithm enables a detailed characterization of the structure, shown in Figure 4.15. Starting from the coordinates, we produced a model of the reconstruction with smaller particles (Figure 4.15a) such that the particles would not overlap, making an easy manual segmentation possible to highlight the rhombicosidodecahedral surface termination. Clustering of the bond order parameters revealed three groups of particles in different stackings: fcc (Figure 4.15b,c,e), hexagonal close packed (hcp) (Figure 4.15f) and decahedral (Figure 4.15d). The fcc particles represent the majority of the structure, forming an inner core corresponding to a Mackay icosahedron^[116] consisting of 20 tetrahedra (Figure 4.15b). The tetrahedra are separated from each other and are arranged with five-fold symmetry (Figure 4.15b,d). Twinning planes are also found between the tetrahedra and the outer shell of the assembly which yields an hcp stacking. Figure 4.15f presents a slice through the reconstruction showing areas with hcp stacking, whereas Figure 4.15c shows a slice through areas with fcc stacked particles. The outer shell is mostly composed by particles in an fcc arrangement (Figure 4.15e) forming a surface with anti-Mackay icosahedral termination. Interestingly, Figure 4.15d shows all the particles arranged in a decahedral packing, with five particles above and five below forming a pentagonal prism. It can be seen that they extend along the tetrahedral edges highlighting the icosahedral core structure. The five-fold icosahedral symmetry has been shown to be the most favorable geometry in short-range ordered clusters composed of particles with attractive interactions and is found in many systems.^[117, 118] It is a relatively new finding that the icosahedral ordering is the equilibrium structure also for hard particles, for which entropy is the only deciding contribution to the free energy, that are made to self-assemble in a spherical confinement.^[100] Assemblies up to 700 particles are expected to carry an icosahedral structure, which changes to a rhombicosidodecahedral symmetry between 700 and 70 000 particles and finally pure bulk fcc for more than 70 000 particles.^[100] Here, with 9 300 particles, the structure observed is a rhombicosidodecahedron presenting an inner distorted Mackay icosahedron, in perfect agreement with the theoretical models of de Nijs et al.^[100] The distortion of the icosahedron is caused by defects in some of the tetrahedra. This can be observed in Figure 4.15c where, a slice through the structure shows two of the tetrahedra (red triangle) affected by defects that alter the perfect tetrahedral shape, causing general inhomogeneity in the size of all the other tetrahedra.

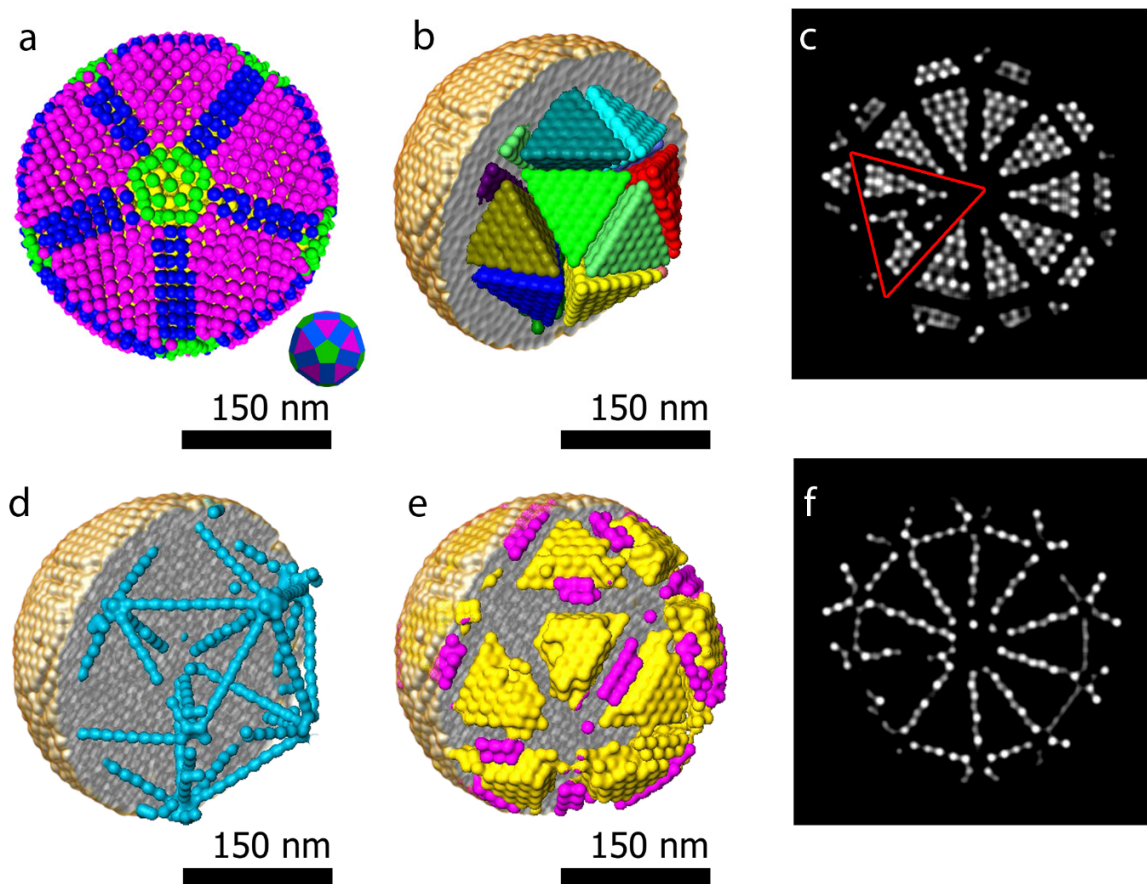


Figure 4.15: (a) 3D visualization of the rhombicosidodecahedral outer structure. (b) icosahedral core consisting of 20 tetrahedra with particles in an fcc stacking (different colors are used to highlight separated tetrahedra and improve the visualization of the 3D structure). (c) Slice through the reconstruction showing only the particles in an fcc stacking. The red triangle highlights a defect in two tetrahedra, which causes a deformation of the Mackay icosahedral core. (d) Particles with decahedral packing, the tetrahedra visualized by the blue particles are also arranged in five-fold symmetry. (e) fcc stacked particles composing part of the outer shell (different colors are used to highlight separated fcc clusters on the surface and improve the visualization of the 3D structure). (f) Slice through a 3D visualization of the particles forming the twin planes (hcp stacking). An interactive model and a movie of this reconstruction are available online in the tomography database (links in section 3.2.8).

4.6 Beam sensitive assemblies and high throughput tomography

In this case study we aim to demonstrate the possibility of using SSR for the reconstruction of beam sensitive assemblies or high throughput tomography studies. The need for long acquisition times is indeed one of the main drawbacks of tomography, limiting the technique to beam resistant samples and/or low throughput results. Reducing the angular sampling frequency would enable one to reduce the electron dose and increase the efficiency of the technique. However, a limited number of projections typically results in a poor quality of the final reconstruction. In Figure 4.16a a 3D visualization of a SIRT reconstruction of an assembly of gold quasi-spherical particles embedded in a polystyrene matrix is shown (more details on the synthesis and properties of these assemblies are available in ref.^[102]). The reconstruction is based on a series of 75 projections, from -70° to $+78^\circ$ with a tilt increment of 2° . Segmentation and labeling with different colors is performed to enable a better visualization of the three-dimensional structure. From the same series, 8 projections were extracted, from -70° to $+70^\circ$ every 20° and the corresponding SIRT and SSR reconstructions are visualized in Figure 4.16b and Figure 4.16c respectively. Even though the details about the shape of every individual particle are lost, valuable information concerning the structure (such as inter-particle distances and local symmetries or 3D stacking) is completely retrieved (Figure 4.16c). Obviously, the fact that we are able to reduce the number of projection images by a factor of ten opens up the route to retrieving detailed 3D quantitative information on beam sensitive systems as well. In addition, information with statistical relevance can be obtained since more 3D reconstructions can be obtained within the same measurement time.

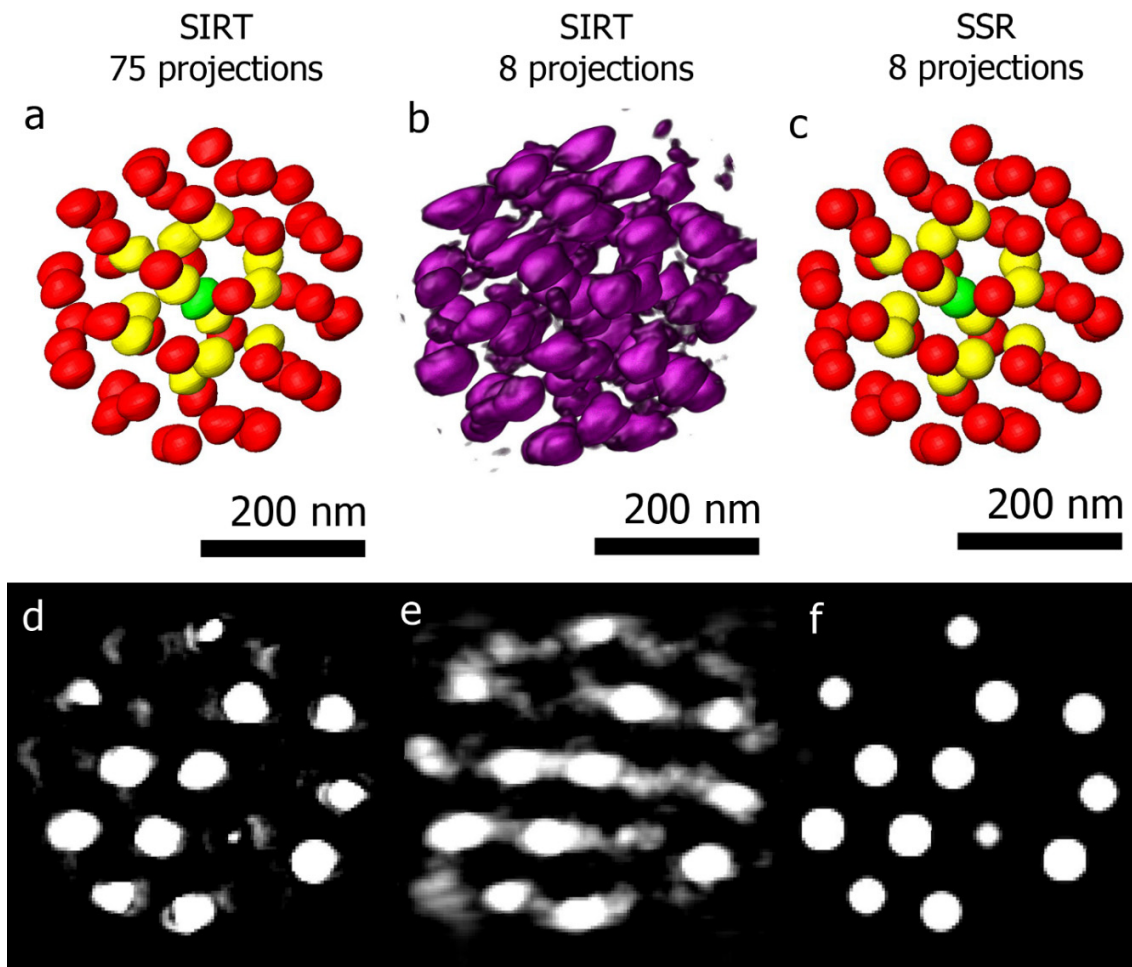


Figure 4.16: (a) 3D visualization of a SIRT reconstruction of an assembly of Au spheres (75 projections). (d) Slice acquired through the SIRT reconstruction. (b, e) 3D visualization and slice of the corresponding to the SIRT reconstruction from only 8 projections of the same assembly. (c, f) SSR reconstruction and slice from the same 8 projections.

4.7 Accuracy and limitations of SSR

In the previous sections it was shown how the SSR technique was developed and how it can be used to retrieve a quantitative 3D reconstruction of assemblies of spherical particles. Here, limitations of the technique will be presented along with an estimation of the accuracy and a method to identify undetected particles.

4.7.1 Spherical basis shape

The fundamental concept behind the technique is the assumption that the investigated assembly is made of spheres. This assumption is not always fulfilled, often nanoparticles show deviations from a perfect spherical shape, as expected for real case studies. Based on our experience, we have observed in several cases that the outcome of an SSR reconstruction is robust against this problem, meaning that a non-perfectly spherical shape does not alter the characterization, and the position of each particle can still be determined accurately. An example is given for the assembly in Figure 4.16a, for which pseudo-spherical nanoparticles were used.

In this case, since the particles can be segmented from a SIRT reconstruction (Figure 4.16a), their centroid can be calculated from the segmented regions, and compared with the SSR coordinates. For this comparison we used all the 75 projections, which were binned to a size of 141 x 141 pixels. The pixel size is 1.5 nm, which means that the expected precision for the SSR centroids determination is ± 1.5 nm (1 pixel). The accuracy can be determined in this case by comparing the distance between the centroids measured from the segmented SIRT reconstruction and the SSR centroids. The average absolute difference in pixel units, for all the 59 particles is 0.50 pixels with a standard deviation of 0.14. From which we can conclude that SSR accurately determines the positions of these nanoparticles even if they do not have a perfect spherical shape. An overlap of the SIRT and SSR reconstruction renderings is shown in Figure 4.17a.

It is important to consider that the shape of the nanoparticles is only a minor factor among those that have an influence on the accuracy of SSR. In general, we observed that the main limitations to the accuracy and positive outcome of an SSR reconstruction are posed by the goodness of the tilt series alignment, the quality of the projections, for which it is paramount to have the best signal-to-noise ratio possible and also a structure that does not deform during the acquisition.

4.7.2 Undetected particles

In more challenging cases, such conditions (good tilt series alignment, signal-to-noise ratio and stable structure) are not always achievable. As a result, the SSR reconstruction might be affected by artifacts which can hamper the detection of all the particles. An estimation of the number of undetected particles in such cases can be obtained by computing an *error reconstruction*. The error reconstruction is obtained by reconstructing the projection distance between the forward projections of the SSR reconstruction and the acquired projections. An overlap of the SIRT and SSR reconstructions for the assembly of Figure 4.16a, is presented in Figure 4.17a. A rendering of the reconstruction error is presented in Figure 4.17b (transparent rendering of the SSR reconstruction is present as reference for the structure), confirming that no particles are missing. To simulate the effect of a missing particle, two particles were randomly deleted and a defective SSR reconstruction was computed (red arrows in Figure 4.17c indicate the locations of the removed

particles). Calculating the error reconstruction for this defective SSR reconstruction finally yields the missing particles (Figure 4.17d).

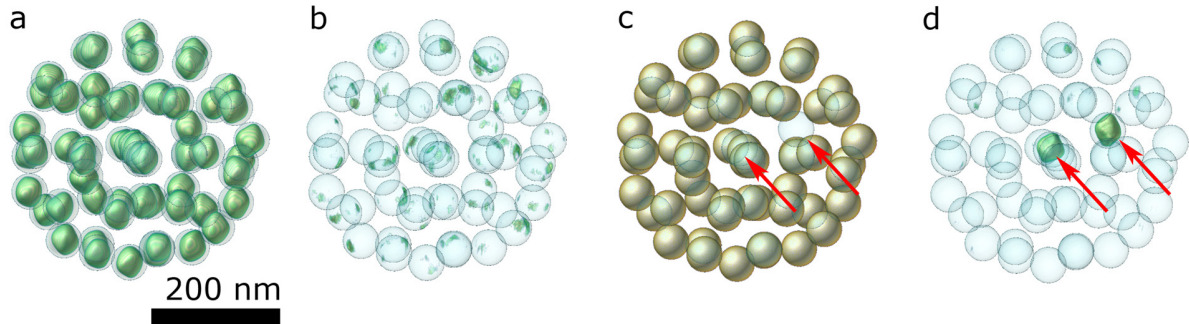


Figure 4.17: (a) SIRT (green) and SSR (transparent blue) reconstructions renderings of the assembly described in section 4.6. (b) SIRT error reconstruction (green) for the SSR reconstruction (transparent blue – included as reference). (c) Simulated SSR reconstruction with two missing particles. (d) SIRT error reconstruction for the simulated defective SSR reconstruction shown in (c).

As an example, the method is applied to the Fe-Co-O nanoparticle assembly of Figure 4.13. Results are shown in Figure 4.18. In this case, the complexity of the structure hampers the direct evaluation of the error reconstruction, as in the previous case. Missing wedge artifacts and close packing of the particles cause the error reconstruction to be of difficult interpretation. To identify the undetected particles it is needed to apply further constraints. First, the error reconstruction is segmented using a threshold value of $0.9i$ where i is the intensity value of the gray level expected for a nanoparticle as determined from the SIRT reconstruction. Afterwards, a second threshold is imposed on the volume of the segmented blocks, which should be at least comparable to the volume of a spherical nanoparticle of radius $0.8r$, where r is the radius used as prior-knowledge in the SSR reconstruction. This allows to exclude small patches of noise and contrast caused by artifacts and blurring of the SIRT error reconstruction. Finally, the detected nanoparticles are shown in Figure 4.18. It can be observed that even after applying the two constraints described above, few blocks of pixels (indicated by the black arrows in Figure 4.18) should not be considered spherical nanoparticles missing from SSR, but rather artifacts of the SIRT error reconstruction, since they do not display a spherical shape. Nevertheless, even considering these elements as possible particles, the number of identified missing particles is 19, which accounts approximately for the 0.2% of the total number of particles.

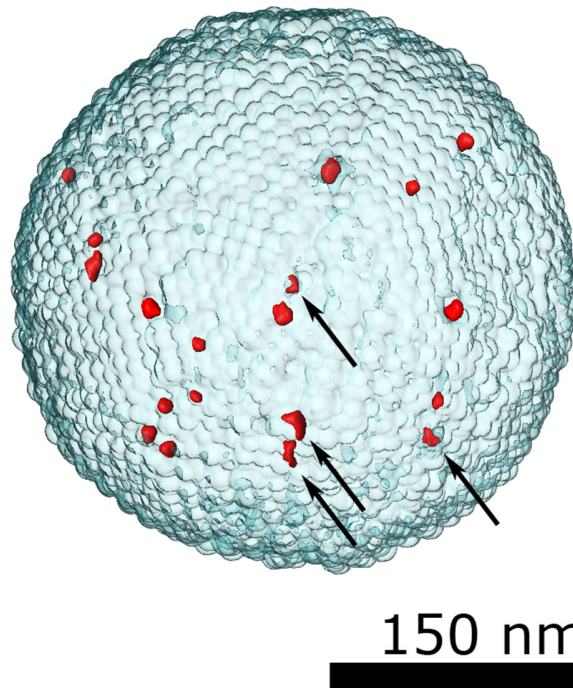


Figure 4.18: SSR reconstruction (transparent blue) and SIRT error reconstruction (red) of the missing particles identified for the Fe-Co-O nanoparticles assemblies presented in section 4.5.

5 Sparse Sphere Reconstruction in Materials Science Studies

5.1 Supracrystalline Colloidal Eggs

This section is based on the work published in the journal article of ref. ^[119]: “Supracrystalline colloidal eggs: epitaxial growth and freestanding three-dimensional supracrystals in nanoscaled colloidosomes”, Z. Yang, T. Altantzis, D. Zanaga, S. Bals, G. Van Tendeloo, M.-P. Pileni, J. Am. Chem. Soc 2016, 138, 3493.

In this study, it is demonstrated the design of a new system, called *supracrystalline colloidal eggs*, obtained by controlled assembly of nanocrystals into complex colloidal supracrystals, through superlattice-matched epitaxial overgrowth along the existing colloidosomes. Fe₃O₄ nanoparticles are made to self-assemble in a spherical assembly, where only half of the assembly is filled by close packed particles. More details on the complex synthesis procedure is given in ref.^[119]

Also in this case, questions regarding the internal structure of the building blocks can only be answered by performing a quantitative three-dimensional characterization. From the SSR reconstruction of the Fe₃O₄ nanoparticles assembly (slice is shown in Figure 5.1d), surrounded by a stabilizing silica shell (visible in the projection of Figure 5.1b and rendering of Figure 5.1c), it is possible to observe several twinning planes and antiphase boundaries. Bond order parameters analysis of the coordinates revealed an fcc type of packing.

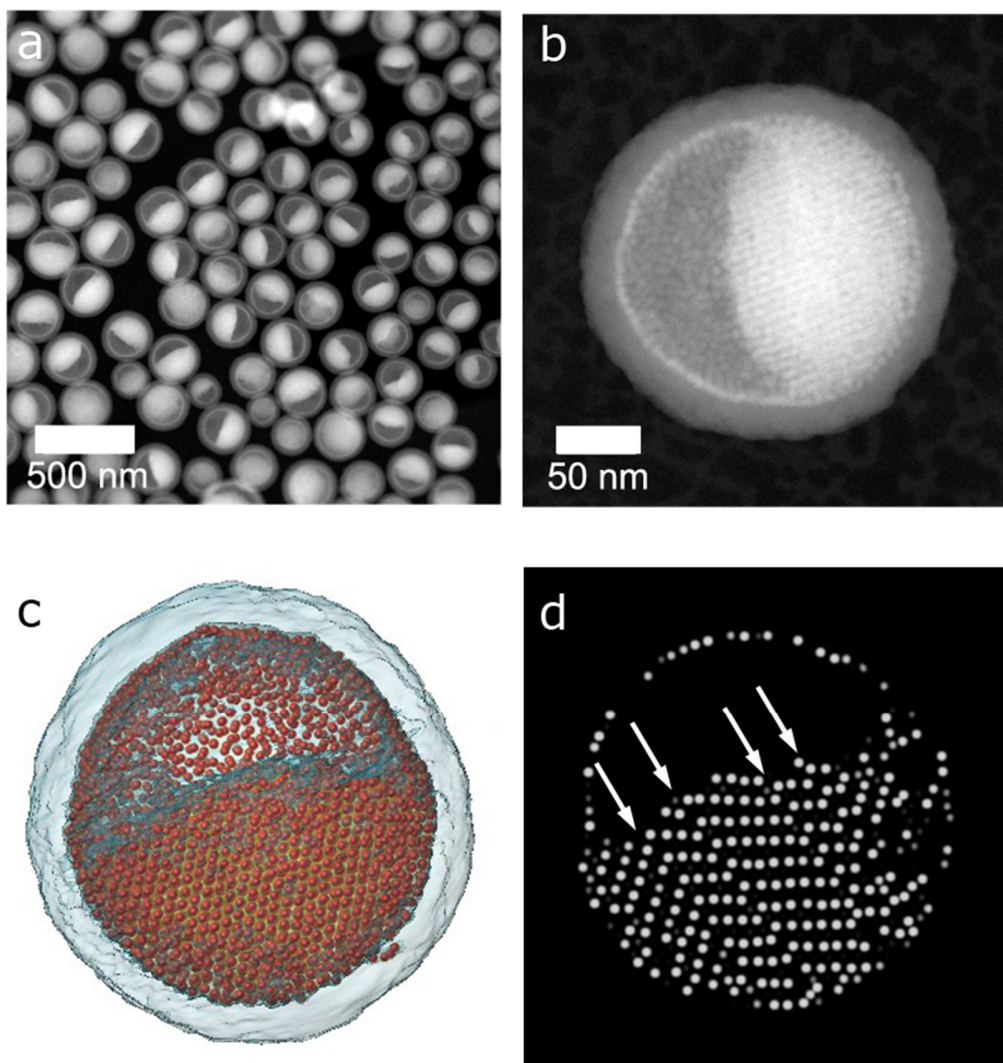


Figure 5.1: (a) HAADF-STEM overview image of the half-filled colloidosomes. (b) 2D HAADF-STEM projection image from the tilt series. (c) 3D representation of the SSR reconstruction. (d) Slice from the SSR reconstruction, highlighting different defects in the nanocrystals stacking (white arrows). An interactive model and a movie of this reconstruction are available online in the tomography database (links in section 3.2.8).

It is important to note that determining the structure, crystalline packing and presence of defects is of great value for the synthesis groups, and this information would not be accessible otherwise through conventional characterization techniques, or tomography SIRT reconstructions. SSR enabled a deeper understanding of the products of the synthesis process developed.

5.2 Binary Assemblies

Assemblies of binary crystals represent the next step in creating complexity and functionality through self-assembly. In an analogous way to what happens when packing atoms of different species, here packing nanoparticles of different materials conveys new properties to the assemblies. By using different kind of building blocks it is possible to create a large variety of metamaterials with broad structural diversity.^[120] Packing of anisotropic structures offers a further degree of freedom giving access to even more structures.^[121] The majority of these structures have been realized in planar assemblies and their applications are therefore limited. It is still unreported the formation of binary assemblies by spherical confinement. Spherical assemblies offer different advantages from an application point of view. They can be freely dispersed in solution and used as mesoporous carriers. Tuning the porosity is linked with the ability of obtaining different structures. These assemblies can also be made to crystallize together creating multi-scale porosity materials. Moreover, spherical confinement can generate additional geometries and symmetries, as in the case of the icosahedral Fe-Co-O assembly shown in the previous chapter.

Here we present the structural characterization of binary assemblies, where CdSe and PbSe nanocrystals are made to self-assemble by spherical confinement. The two types of particles, used for the assembly, have an average size of 5 nm and 6 nm respectively, and due to the different Z number, show a different contrast in HAADF-STEM. Overview images are presented in Figure 5.2, together with a projection from a single assembly acquired along one of the main *zone-axis* orientations.

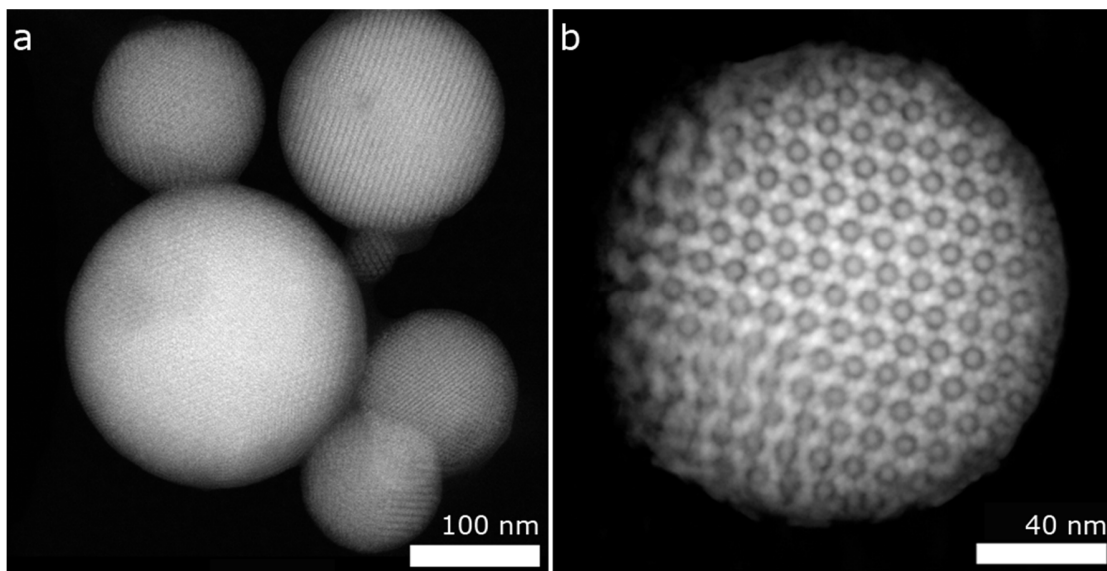


Figure 5.2: Binary assemblies, (a) overview and (b) projection from tilt series

HAADF-STEM imaging of the assemblies reveals the presence of an ordered structure in the assemblies (Figure 5.2a,b). Further investigation of the type of packing is therefore performed by means of electron tomography. A HAADF-STEM tilt series of an assembly with a diameter of approximately 120 nm is acquired every 2°, from -72° to 66°, using a Fischione 2020 tomography holder and a cubed FEI Titan, operated at 300 keV. Multiple projections are acquired with a low exposure time and merged to obtain a single image for each angle, with an improved signal to noise ratio, while minimizing deformations caused by sample drift (as described in section 3.2.2). Two projections extracted from the tilt series are shown in Figure 5.3a,b. A SIRT reconstruction of the tilt series is calculated and a rendering is shown in Figure 5.3c along with two slices through the reconstruction. The SIRT reconstruction is difficult to interpret, but allows the evaluation of the nanoparticles sizes and gray level which can be used as prior knowledge for the binary SSR reconstruction.

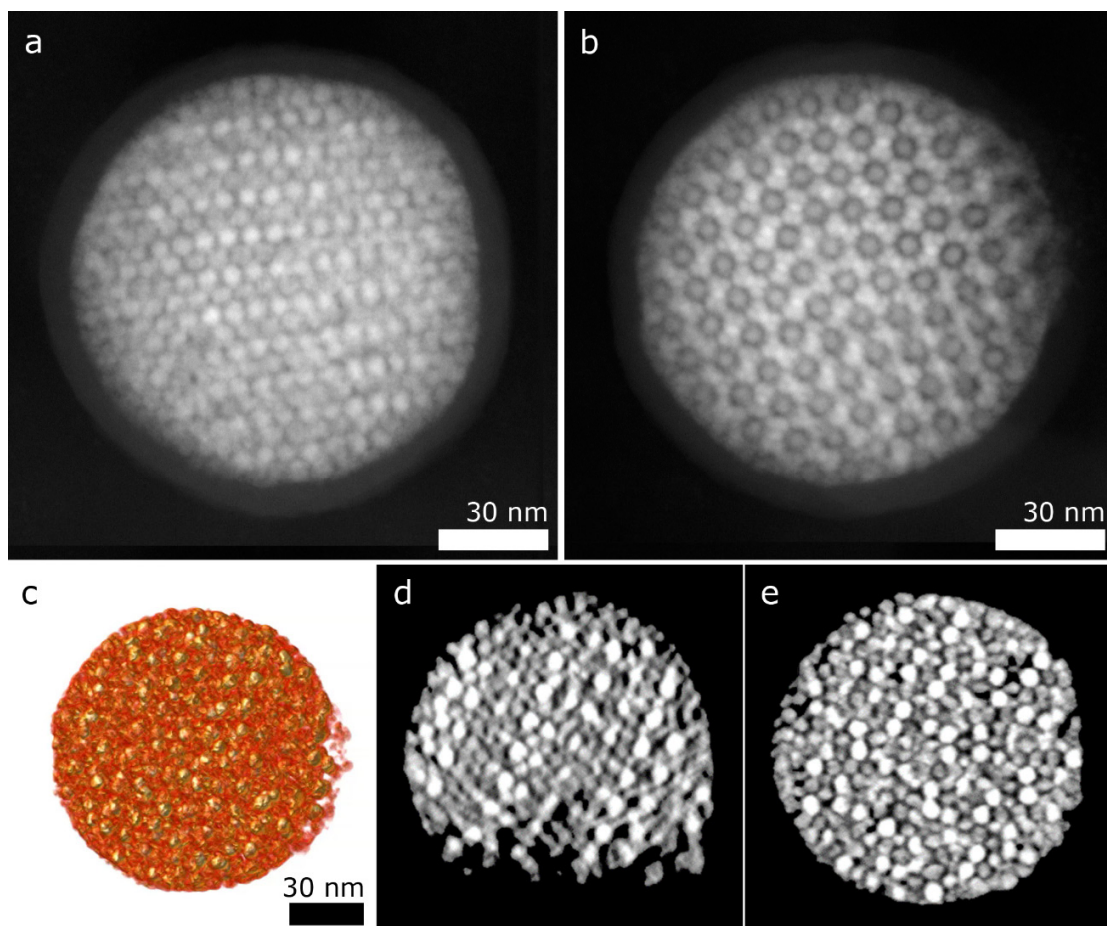


Figure 5.3: (a) and (b) show two HAADF-STEM projections of a binary assembly acquired along different directions. (c) SIRT reconstruction rendering of the tilt series acquired from the same assembly. (d) and (e) are slices through the SIRT reconstruction. Overlapping of boundaries and blurring hamper distinguishing the particles.

5.2.1 Binary SSR reconstruction

The SSR technique is applied to the tilt series by setting the basis shape radius to a single size, the radius in pixels of the smaller nanoparticles species. In this case the tilt series was binned to a size of 228x228 pixels, and the two particles radii were estimated to be 9 and 7 pixels, for the PbSe (brighter due to the higher Z number of Pb) and CdSe particles respectively. Since the two types of particles only differ for few pixels, in practice for the reconstruction algorithm they are equivalent. As explained in section 4.3.2, the first step of the method, e.g. solving eq. (4.3), yields a sparse solution, where the centers of the particles are blurred due to the experimental limitations and undersampling. In the case of particles of different size and different contrast, the result is analogous, with slightly more diffused intensity for bigger particles.

Extracting the local maxima positions therefore produces a list of coordinates for both particles indistinctively.

In order to discern the two families of particles, the average gray value of a spherical neighborhood (7 pixels radius) of each coordinate, is extracted from the SIRT reconstruction and the two populations are then clustered through a k-means algorithm.^[115] Once the two populations of particles coordinates are identified, the second step of the SSR reconstruction is applied by convolving each population by a sphere of the appropriate size. A rendering from the obtained reconstruction is shown in Figure 5.4a. Increasing the transparency of the rendered particles of Figure 5.4a produces a projection of the assembly, enabling the observation of the periodic structure composed by the two different particles (Figure 5.4b). Slices from the reconstruction are shown in Figure 5.4c and Figure 5.4d.

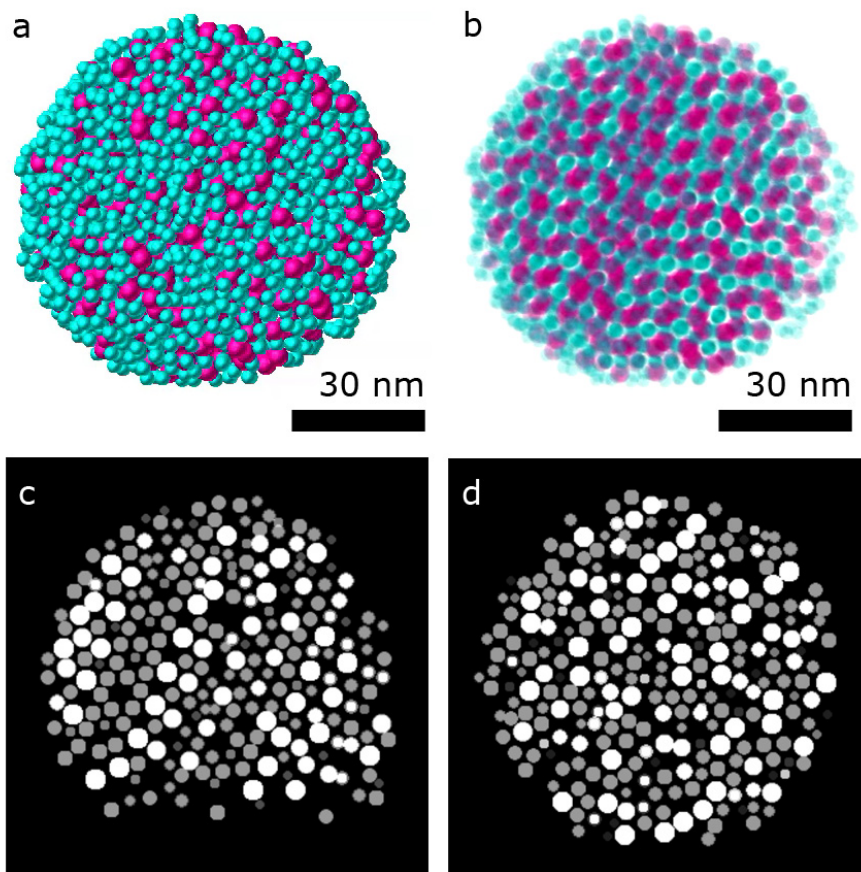


Figure 5.4: (a) SSR reconstruction rendering of the assembly shown in Figure 5.3. (b) Same rendering shown in (a) but with increased transparency, highlighting the ordered structure. (c) and (d) are slices through the SSR reconstruction.

5.2.2 Structural characterization

Due to the binary nature and complexity of the structure, the bond order parameters analysis did not allow to determine the type of packing in this case. We therefore produced a reconstruction with a reduced size of the particles (Figure 5.5a), such that they would not overlap, allowing an easier visualization and manual isolation of a smaller region (Figure 5.5b), in order to further study the structure. Figure 5.5c shows a model built on the coordinates extracted from the isolated cell of the reconstruction. The particles were found to occupy the vertices and center of two icosahedra, sharing one face.

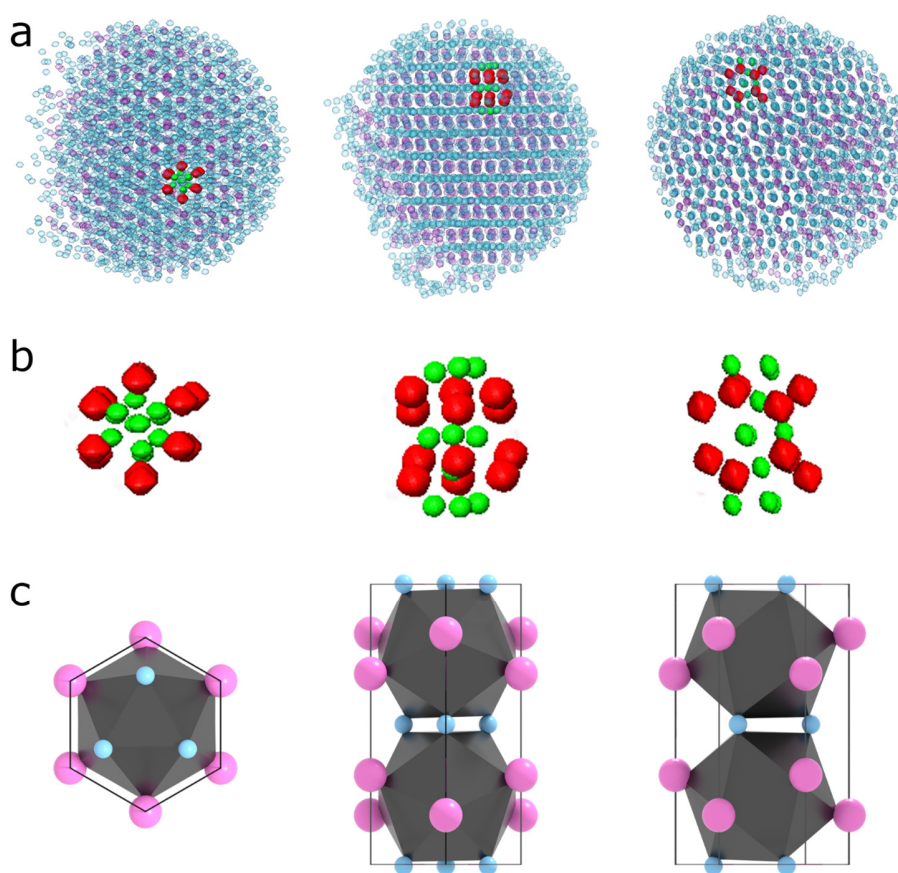


Figure 5.5: (a) SSR reconstruction of the binary assembly, simulated with a reduced particles size enabling an easier manual segmentation. (b) Isolated region of the assembly is segmented from the reconstruction to allow further study of the structure. (c) Model built from the coordinates of the manually segmented region.

From the isolated particles we built a model that further enabled the determination of the unit cell of the crystal, which was found to be the structure of the hexagonal MgZn_2 Laves phase.^[122, 123]

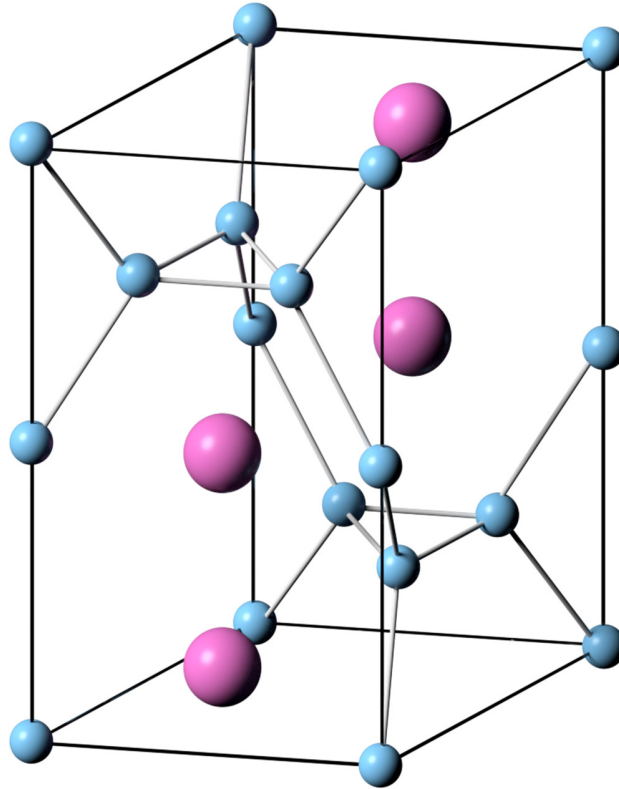


Figure 5.6: Unit cell confirming the MgZn_2 structure for the binary assembly.

Once the structure was obtained, further confirmation was given by producing a spherical model of the crystal by replicating the unit cell. Figure 5.7 shows a visualization of such model assembly, casting three orthogonal shadows, corresponding to the main directions and highlighting the structure with relative orientations. The model is shown along the same directions in Figure 5.8.

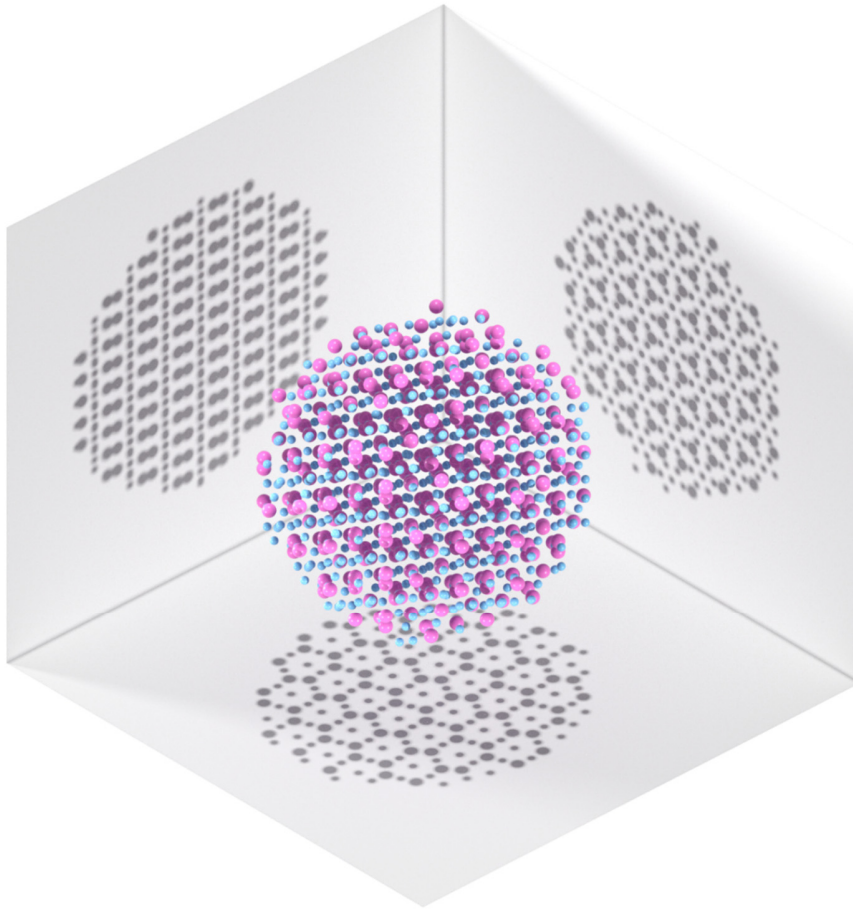


Figure 5.7: Model of the structure casting three orthogonal shadows, showing the main *zone-axis*.

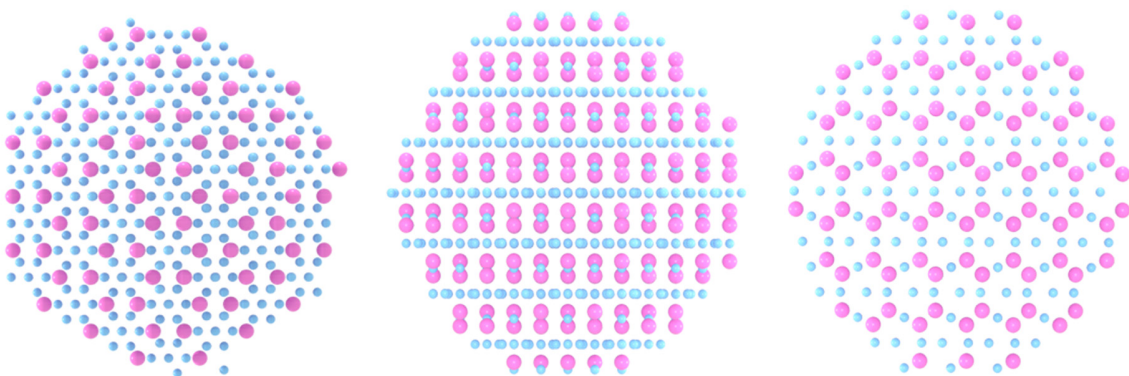


Figure 5.8: Structure model observed along the main directions.

The same analysis was performed on a second assembly, shown in Figure 5.9, confirming the observations made. The tilt series was acquired on a FEI cubed Titan, operated at 300 keV, with a tilt range of 2° from -76° to 62°, using a Fischione 2020 tomography holder. In this case the assembly had a slightly larger diameter of approximately 150 nm.

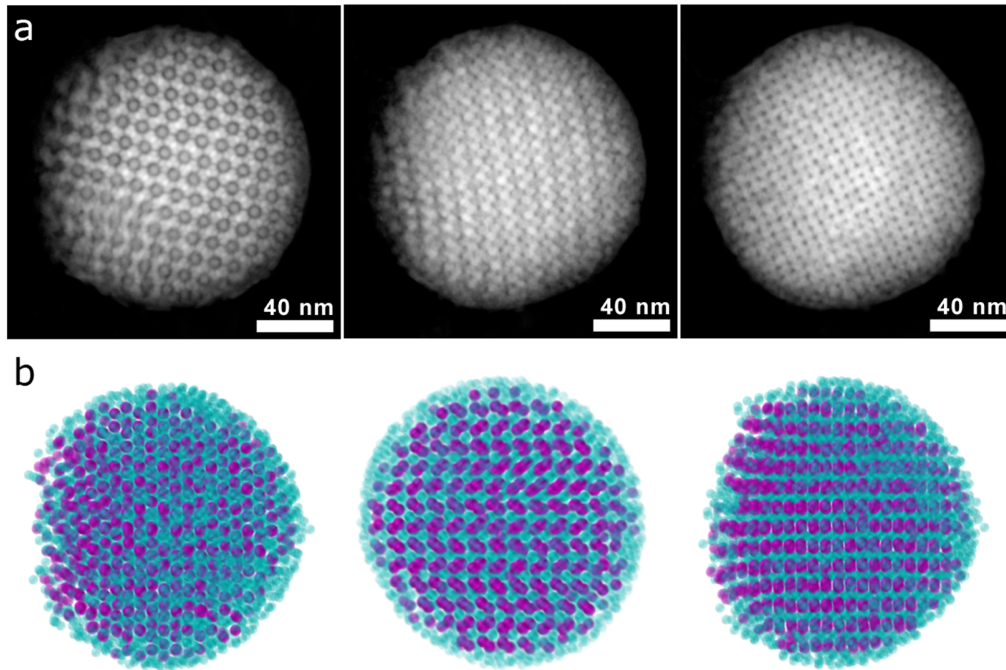


Figure 5.9: a) HAADF-STEM projection images extracted from the acquired tilt series. b) SSR reconstruction renderings of the structure along the main orientations.

For the first assembly (diameter of 115 nm), 3432 particles were detected, with 1009 particles of the larger (PbSe) species, and 2423 of the smaller (CdSe). For the second assembly (diameter of 150 nm), 5762 particles were detected, 1837 of the larger species and 3925 of the smaller. The different ratio, from the expected 2-to-1 stoichiometry, is explained by the presence an outer layer of CdSe particles, usually found at the external boundary of the assemblies. Careful observation of Figure 5.9b shows a ring of CdSe particles (light blue) surrounding the assembly.

6 Conclusions and Outlook on Part II

6.1 Conclusions

So far 3D reconstructions of nanoparticles assemblies were performed using conventional reconstruction techniques. A further segmentation step was then needed to retrieve quantitative information about the position and number of particles in the assembly. However, this segmentation step is only possible when the inter-particle distances are greater than the resolution limit obtainable with standard reconstruction techniques such as SIRT or TVM. The resolution obtainable with these techniques is approximately of the order of 1 nm in the best cases. Therefore for assemblies of closed packed particles, the resolution of conventional techniques did not allow a quantitative characterization and structural information could not be obtained. As demonstrated in these chapters, the development of SSR opened the way to this possibility for assemblies of spheres, enabling a quantitative characterization of nanoparticles assemblies of thousands of particles in a closed packed arrangement. SSR yields information that can be used to perform structural analysis that would not be possible otherwise for these complex structures.

In more details, in this second part of the thesis it has been shown how introducing prior-knowledge in the reconstruction algorithm can push farther the intrinsic limitations of electron tomography. In the case of SSR, prior knowledge was implemented through the introduction of a new basis for the tomography problem. Exploiting sparsity in the new basis, enabled the recovery of information lost in the acquisition which allowed a quantitative reconstruction of the assemblies investigated. Furthermore, it has been shown how the technique can be extended to more complex cases, such as the case of binary assemblies and how quantitative information about particles positions can be used to perform in-depth structural analysis of these systems.

6.2 Outlook

6.2.1 Assemblies of atoms

As an outlook for potential future applications we considered the possibility of investigating nanoparticles at an atomic resolution. At this scale, the atomic potentials can be represented by Gaussian distributions. Given the spherical symmetry of such distribution, the basis change operated at the core of the SSR technique can be in principle extended to the case of nanoparticles, as assemblies of atoms, instead of spherical nanoparticles.

Even though this adaptation would be straightforward from the method point of view, there are still technical limitations arising due to the typical size of nanoparticles that can be investigated at an atomic level, through electron tomography. Typically, small nanoparticles (less than 50 000 atoms, equivalent to particles with a diameter in the order of 10 nm or less) show stability issues towards the acquisition of a full tilt series at the required magnification, while larger particles can be imagined, but require a bigger frame. In our experience, the technical limitations of SSR have been shown to require at least a kernel of 10 pixels in diameter, for the sphere basis, and a maximum frame size of approximately 700 squared pixels for the projections. Larger frames, involve larger reconstruction volumes and bigger number of unknowns, which cause the solving algorithm to fail in converging, producing artifacts in the solution. To give an idea of typical execution times, for a frame of approximately 600 squared pixels, with a basis kernel of 12 pixels in diameter, the algorithm takes between 5 to 10 hours to complete, according to the complexity/quality of the data and the processing power available. Due to these limitations, at the time of writing, we were not able, in practice, to extend the use of SSR to nanoparticles.

It is worth mentioning though, an alternative technique that has been recently proposed for the reconstruction of nanoparticles at the atomic scale by exploiting prior knowledge of the atomistic nature of the particle and assuming a Gaussian distribution as prior knowledge for the shape of atoms. In this case, the method explained in Goris et al.^[66] is not based on a basis change and a sparse reformulation of the tomography problem as it is the case of SSR, but rather on an iterative approach. Here, an initial SIRT reconstruction is computed, the reconstruction is then filtered in Fourier space, to eliminate noise, and a segmentation is applied. From the segmentation, a fitting procedure identifies atoms that have been correctly segmented. The positions of these atoms are used as a prior information and further SIRT iterations are performed, now including the already segmented particles in the reconstruction. This improves the result obtained from the supplementary SIRT iterations, enabling the identification of more atoms. The procedure is repeated until convergence. A detailed explanation of the method is given in ref.^[66]. An example of such a reconstruction is given in Figure 5.10.

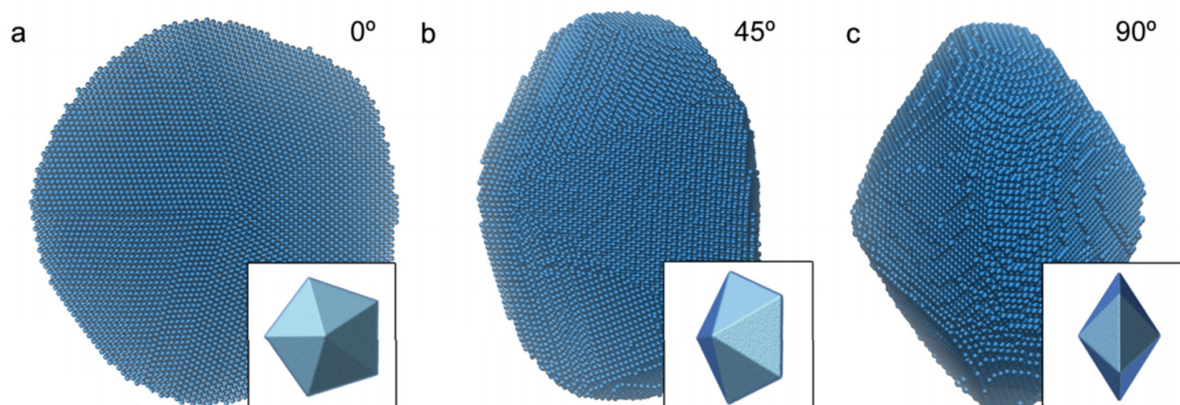


Figure 5.10: Atomic reconstruction rendering obtained from a gold nanoparticle using the technique described above. The reconstructed Au decahedral particle contains more than 90'000 atoms.

Even though the technique developed by Goris et al.^[66] is based on a very different approach from that of SSR, we mentioned it here because the two approaches share the same basic concept of improving the reconstruction resolution and quantifying the structure components by using prior-knowledge on the shape of these components. For this reason both techniques belong to a broader ensemble of techniques to which we refer to as *shape models reconstruction techniques*. SSR was the first of such techniques that was developed in our lab and demonstrated the potentiality of this approach for the first time.

6.2.2 Platelets, cubes and rods assemblies

Spherical particles are the most common type of building blocks used for nanoparticles assemblies. However, different morphologies are also used, such as platelets, cubes,^[124] rods,^[125] nanodumbbells^[126] or nanostars^[127] for example. Application of the SSR method in these cases is not directly possible, since the convolution operator requires spherical symmetry, but alternative shape models reconstruction techniques are being investigated to obtain the quantitative reconstruction of these kind of assemblies. Other researchers in our group are currently exploring the possibility of extending the method by Goris et al.^[66] to these different shapes. In general we believe that in the future, more and more custom algorithms in the frame of shape models tomography will be developed for the quantitative investigation of assemblies or nanoparticles (intended as assemblies of atoms).

6.3 Detailed list of contributions to part II

Sections 4.1-4.4

The basis shape approach for a 2D case was proposed by F. Bleichrodt and J. K. Batenburg. Own contributions: extension and implementations of the method for the three-dimensional case. Phantom studies, implementation and optimization of the technique. Application to real case studies, development and implementation of the methodology presented.

Sections 4.5-4.7

Acquisition of the experimental data for the assemblies of Figure 4.9a,b,c, acquisition of the series of the assembly of Figure 4.9d together with T. Altantzis. Computation of the SSR reconstructions and structural analysis of these assemblies as presented in section 4.5.4. Acquisition of the tilt series for the assembly of Figure 4.16 together with T. Altantzis, computation of its SSR reconstruction. Development of the error reconstruction method to identify undetected particles presented in section 4.7.

Section 5.1

Computation of the SIRT and SSR reconstructions and structural analysis for the assembly presented in Figure 5.1.

Section 5.2

Computation of the SIRT and SSR reconstructions and structural analysis for the binary assemblies presented in this section.

Part III

Quantitative EDXS tomography

This final part is dedicated to the development of novel methods for the 2D and 3D quantitative analysis of chemical compositions in nanomaterials. Chapter six starts by presenting an alternative approach developed for the determination of ζ -factors from pure element nanoparticles, which in turn enables accurate quantitative EDXS studies in 2D. In chapter seven, a new technique about the synergistic combination of 2D quantitative EDXS and STEM tomography is demonstrated. This method allows to overcome instrument limitations that hampered earlier attempts to obtain quantitative three-dimensional chemical information by means of EDXS. The technique is applied to different materials science cases in chapter eight. Finally, in chapter ten, the conclusions to this third part are drawn, along with considerations and an outlook regarding future developments and applications of EDXS tomography.

7 Quantitative EDXS in 2D

This chapter is based on the work published in the journal article of ref.^[128]: “An alternative approach for ζ -factor measurement using pure element nanoparticles”, D. Zanaga, T. Altantzis, J. Sanctorem, B. Freitag, S. Bals, *Ultramicroscopy* 2016, 164, 11.

7.1 Introduction to quantitative EDXS

New developments in the field of nanotechnology drive the need for advanced quantitative characterization techniques that can be applied to complex nanostructures. Many of these nanostructures are composed of different compounds. For example, it is known that bimetallic nanostructures show enhanced stability and catalytic selectivity in comparison to their parent materials.^[129] Understanding the connection between physical properties and the local structure or composition of nanomaterials is therefore of crucial importance.

Although TEM is an ideal tool to investigate nanostructures,^[130] it is surprisingly difficult to obtain reliable quantitative chemical information at the nanometer level. In the past, investigations using EDXS in a TEM were especially hampered by the low efficiency of the EDXS detector systems. As a result of the development of novel detectors yielding improved performance in combination with brighter electron sources in state-of-the-art TEM instruments, a significant level of X-ray counts can nowadays be collected within realistic acquisition times, also when investigating relatively small nanostructures (>10nm).^[54, 131-133] A remaining problem however, is the lack of a reliable quantification method for EDXS spectroscopy in the TEM.^[61, 62]

Quantification of EDXS data acquired using TEM is mostly carried out using so-called “k-factors” that form the basis of the Cliff-Lorimer method.^[134] Over the past 40 years, this approach has been used extensively, especially during the characterization of thin films and even optimized in combination of tilt schemes.^[135] As explained in ref.^[136] the Cliff-Lorimer technique is an accurate method when using experimentally estimated k-factors from calibration samples where the composition is accurately known. Unfortunately, such estimation is not always possible due to the lack of suitable standards. Even when standards are available, the calibration is difficult and time consuming. Therefore, experimental EDXS results are typically quantified using k-factors that are calculated using a priori principles and implemented in commercial software. Although this approach is straightforward and user friendly, inaccuracies of 15%-20% might occur.^[137] In parallel, various alternatives have been proposed, including the so-called “ ζ -factor” method.^[136] This methodology has been shown to be a powerful approach that is able to overcome some of

the main limitations of the Cliff-Lorimer method. In contrast to k-factors, the experimental determination of ζ -factors is possible from a pure element standard and should only be determined once for each element. However, when determining ζ -factors from pure element standards, the thickness of the sample should be precisely measured. In the past, this requirement has limited the applicability of the ζ -factor method to thin films.

In our study,^[128] we used electron tomography to overcome this limitation. In this manner, the volume (and thickness) of nanoparticles can be determined. As a consequence, systematic errors resulting from wrong estimations of sample thickness can be overcome. Our methodology, coupled with state-of-the-art instrumentation, enabled us to expand the use of the ζ -factor method to the study of a variety of nanomaterials. In this manner, reliable and quantitative chemical information can be acquired at the nanometer level.

7.2 The Cliff-Lorimer Method

The Cliff-Lorimer method is a ratio technique that was developed to overcome problems related to an absolute quantification of EDXS data acquired by TEM. Thanks to the relative nature of the approach, variations in the signal detection due to instabilities of the instrument, such as beam current fluctuations, shadowing and contamination build-up, are canceled out when calculating the intensities ratios, yielding the concentrations through the k-factors (eq. (7.1)). For this reason the technique has become widely used during the last decades, and is still the most common approach to obtain the concentrations of elements in a TEM sample. Characteristic X-rays intensities I_A and I_B of elements A and B respectively are measured and the ratio of their concentrations C_A and C_B is determined using a predefined factor k_{AB} :

$$\frac{C_A}{C_B} = k_{AB} \frac{I_A}{I_B} \quad (7.1)$$

As mentioned in the previous section, the experimental determination of k-factors is tedious and unpractical, constituting a major limitation to an accurate quantification of EDXS measurements. Nowadays, concentrations are routinely determined using commercial software that calculates the k-factors from a priori principles. This is usually sufficient to estimate the elemental distribution in the sample to a low degree of uncertainty, nevertheless if one wants to obtain accurate results the only solution is to measure experimental sensitivity factors.

Furthermore, absorption of X-rays inside the sample can occur for thicker specimens, especially for lower energy X-rays (<3 keV), causing inaccuracies in the quantification. X-ray absorption can be corrected using an additional term in eq. (7.1), but requires the knowledge of the mass-thickness of the sample. Since a

measure of the thickness of a thin specimen is not straightforward and requires additional measurements and instruments, such as a profilometer, usually quantification of thicker samples or light elements (low energy X-ray lines) is avoided.

7.3 The ζ -factor Method

The ζ -factor method adds to the benefits of a ratio technique such as the Cliff-Lorimer technique, the possibility of determining the sensitivity factors from pure elements standards and a straightforward method for correcting absorption effects without the requirement of knowing the specimen thickness. The ζ -factor is defined by the following equation from ref.^[136]:

$$\rho t = \zeta_A \frac{I_A}{C_A D_e} \quad (7.2)$$

where ρ is the density, t the thickness, I_A the X-ray intensity (net counts), C_A the concentration and D_e the total electron dose, which is defined as:

$$D_e = N_e I_p \tau \quad (7.3)$$

with N_e the number of electrons per Coulomb, I_p the probe current and τ the total measure time. The beam current can be measured through the use of an in-situ faraday cup, EELS drift tube or a calibrated viewing screen.^[136] The ζ -factor method was originally developed for thin films, for which the thickness is expected to be uniform across the sample. However, it is not straightforward to accurately measure the thickness using conventional (2D) TEM. It can be done by using Electron Energy Loss Spectroscopy (EELS),^[138, 139] but this requires a calibration of the inelastic mean free path. This calibration is time demanding and requires a needle shaped sample with the same phase of the thin film for which the thickness has to be measured. This might result difficult for some samples, and furthermore, there is an increasing demand to obtain quantitative results for nanomaterials different from thin films as well.

In our study,^[128] we expanded the use of the ζ -factor method to the investigation of nanoparticles by using electron tomography. The use of nanoparticles hereby offers many advantages: they are usually cheaper than pure element thin film standards and they are often already available in most labs or can be relatively easily synthesized. In order to determine ζ -factors using nanoparticles instead of thin films we proposed an equivalent definition of the ζ -factor replacing the sample thickness by the probed sample volume, which can be measured by electron tomography. We assume that the probed volume is the scanned area multiplied

by the thickness t . That means that the total (live) time τ can be written as $\tau = \tau_d * A$, where A is the scanned area in m^2 , and τ_d is therefore the spectral acquisition time per pixel area. In this manner, we obtain the expression below, in which C is omitted since we assume a pure element standard during the determination of the ζ -factor:

$$\rho V = \zeta_A \frac{I_A}{N_e I_p \tau_d} \quad (7.4)$$

Once the ζ -factors are obtained, the concentration of the elements is given by the following expression:

$$C_j = \frac{\zeta_j I_j}{\sum_i \zeta_i I_i} \quad (7.5)$$

with:

$$\sum_i C_i = 1 \quad (7.6)$$

For a system of two elements we obtain:

$$\frac{C_A}{C_B} = \frac{\zeta_A I_A}{\zeta_B I_B} \quad (7.7)$$

This expression is equivalent to eq. (7.1), where $k_{AB} = \frac{\zeta_A}{\zeta_B}$. It should be mentioned that absorption is so far neglected in these expressions. As explained in the work by Watanabe et al.,^[136] this approximation is expected to be valid for the samples investigated in the remainder of this thesis, given their size and the X-ray lines used.

7.3.1 Equivalence of thin-film and nanoparticles formula

To demonstrate the equivalence of eq. (7.2) and eq. (7.4), we consider the case of a thin film: when analyzing a single pixel, the probed volume is given by the product of the thickness and the pixel area. For a pure element nanoparticle, the thickness will not be constant and will be a function of the position of the pixel:

$$\rho t_i A_i = \zeta \frac{I_i}{N_e I_p \tau_d} \quad (7.8)$$

where t_i represents the thickness of the particle at the i -th pixel, A_i the pixel area and I_i the X-ray intensity measured in that point. Summing over all the pixels will lead to eq. (7.4) since:

$$\sum_i t_i A_i = V \quad (7.9)$$

and

$$\sum_i I_i = I \quad (7.10)$$

7.4 Determination of ζ -factors

In order to determine the ζ -factors, the volumes of 8 particles consisting of Au, Ag and Pt respectively were determined by electron tomography. Synthesis details about the Au, Ag and Pt nanoparticles used can be found in ref.^[128]. Experiments were performed using an FEI Titan probe corrected TEM, operated at 120 kV in STEM mode and equipped with a Super-X detector. Tilt series for each particle were acquired from -75° to 75° with a tilt increment of 3° . A Fischione 2020 Single Tilt Tomography holder was used. Alignment of the tomographic series was performed with Matlab routines based on cross-correlation and manually with IMOD.^[72] The SIRT algorithm implemented in the ASTRA Toolbox^[38, 40, 107] was used for all the reconstructions. Figure 7.1 shows a rendering of the obtained reconstructions.

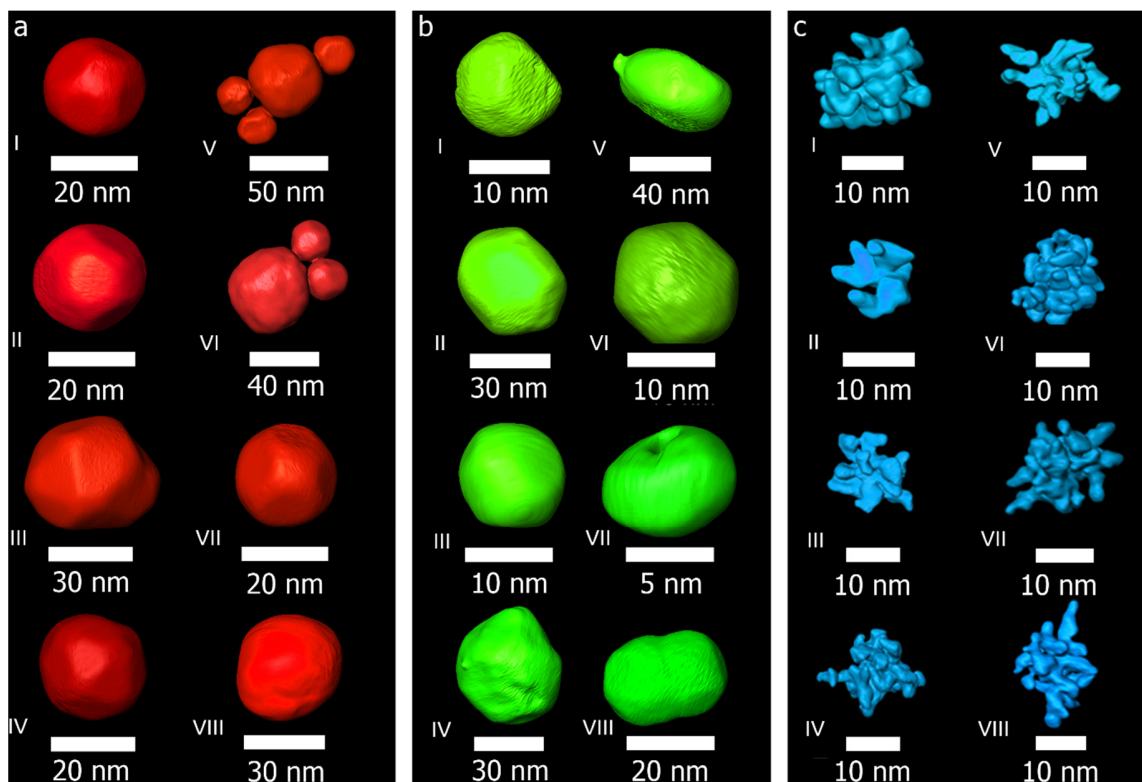


Figure 7.1: Renderings of the Au (a), Ag (b) and Pt (c) particles used for the determination of the ζ -factors.

7.4.1 Volume calculation

The volume is calculated from the obtained reconstructions. Unfortunately the reconstructed volume is distorted by noise and missing information,^[27, 140] resulting in a blurred reconstruction. Because of the blurring that occurs in the reconstructed object, it is usually unclear where the boundary of the reconstructed particle is located, introducing an uncertainty about the actual volume of the particle. The process of assigning voxels to the particle or the exterior is called segmentation.^[27] Segmentation may be a subjective factor and may therefore affect the reliability of the measurements. Here, we implemented an automatic routine in Matlab for the segmentation of a reconstructed volume. A line profile is extracted from the reconstruction (Figure 7.2a) and a so called edge spread function (ESF) is fitted to the intensity profile in the particle boundary region (Figure 7.2b).^[36, 141]

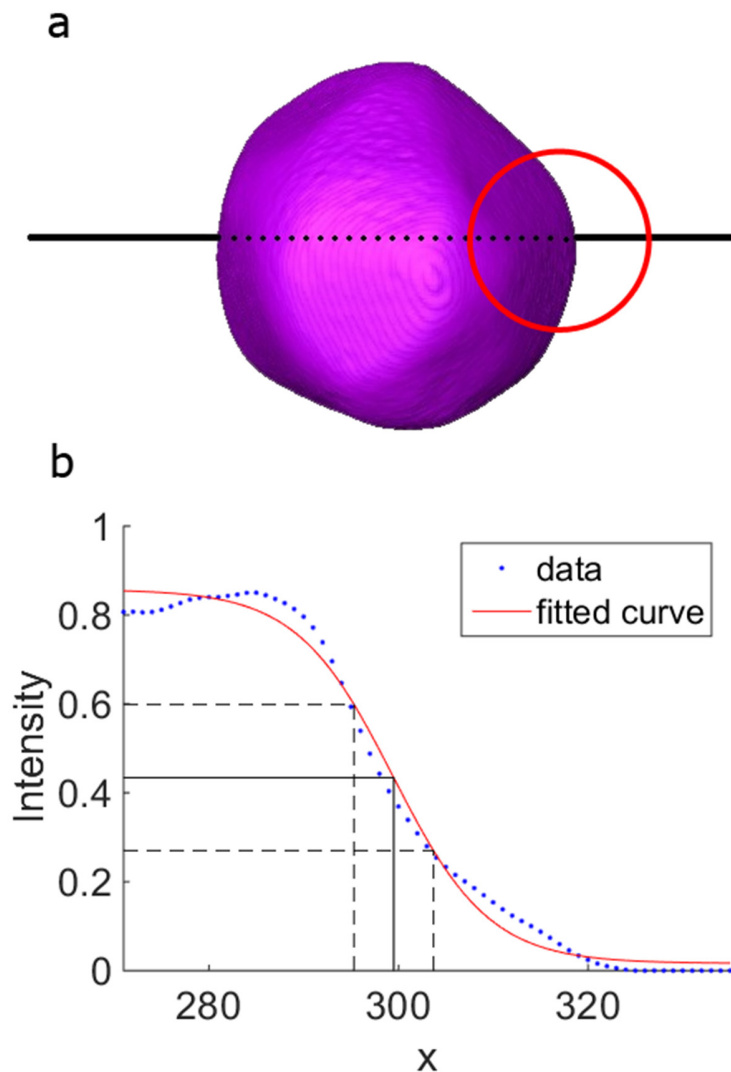


Figure 7.2: (a) Au particle rendering and schematization of a line profile going through it. (b) Part of the line profile shown in the red circle in figure (a), with its ESF fitted and the intervals determined for the error calculation.

We assume that the most probable position for the threshold will be in the middle of the fitted edge profile, with an estimated spatial error of $\pm 15\%$ of the edge width, from its maximum to its minimum. In practice, the threshold position can be found by calculating the first derivative of the ESF and its maximum. For statistical reasons, 12 edge profiles in different spatial directions are selected and fitted for every particle, resulting in 12 thresholds. The average of these thresholds is taken as the best estimate for the true threshold (denoted I_{thr}), and the maximum error found among all the estimated errors for the single thresholds is taken as a measure of uncertainty (ΔI_{thr}). Using this average as the final threshold, the particle volume can

be calculated directly from the segmented reconstruction. The error on the calculated volume is the following:

$$\Delta V = \frac{(V_0 - V_+) + (V_- - V_0)}{2} = \frac{V_- - V_+}{2} \quad (7.11)$$

where V_0 is the volume calculated with I_{thr} , V_+ the volume calculated with $I_{thr} + \Delta I_{thr}$ and V_- the volume calculated with $I_{thr} - \Delta I_{thr}$. Using this approach, it is possible to calculate the volume in a deterministic rather than an arbitrary manner, as is the case in manual threshold selection. As a consequence, this method enables the estimation of the error in the volume, and therefore the calculation of the final error in the ζ -factor. This procedure was fully automated in Matlab, including fitting, threshold selection and volume calculation. The resulting volume measurements are presented in Table 7.1, Table 7.2 and Table 7.3.

7.4.2 EDXS acquisition and beam current calibration

For each particle, an EDXS map was collected with an acquisition time of 3 minutes. A tilt angle of 17° was chosen to minimize shadowing effects and increase the collected signal. A beam current of approximately 250 pA was used. A reliable measurement of the beam current is of crucial importance in the ζ -factor method, therefore we used the pico-amperemeter connected to the phosphor screen present in FEI instruments. The screen current is typically calibrated by the manufacturer using a Faraday cup and a verification of the linearity of the current measuring device can be conducted by varying the beam current and acquiring an EDXS map of the same nanoparticle. Plotting the current against the total number of counts over background for the element composing the nanoparticle should result in a linear fit obeying eq. (7.4). The intercept on the y axis is considered as an estimate of the error on the measured current. Although such experiment cannot determine if the actual current is off by a constant factor, the proportionality factor will cancel out when determining concentrations using the same microscope and voltage.

Equation 7.4 can be written as follows:

$$I_p = \frac{\zeta_A}{N_e \tau_d \rho V} I_A + \Delta I_p \quad (7.12)$$

In this expression, ΔI_p corresponds to an error associated with the beam current calibration. By acquiring different EDXS maps of the same Au nanoparticle using different currents, the net counts can be plotted against the current. In this manner, the linearity of the pico-amperemeter can be verified. Figure 7.3 shows the results for two different particles. The intercepts are $\Delta I_{p,1} = -5$ pA and $\Delta I_{p,2} = -4$ pA. For a minimum value

of 50 pA, this corresponds to a 10% relative error, which is the error that we consider for our pico-amperemeter.

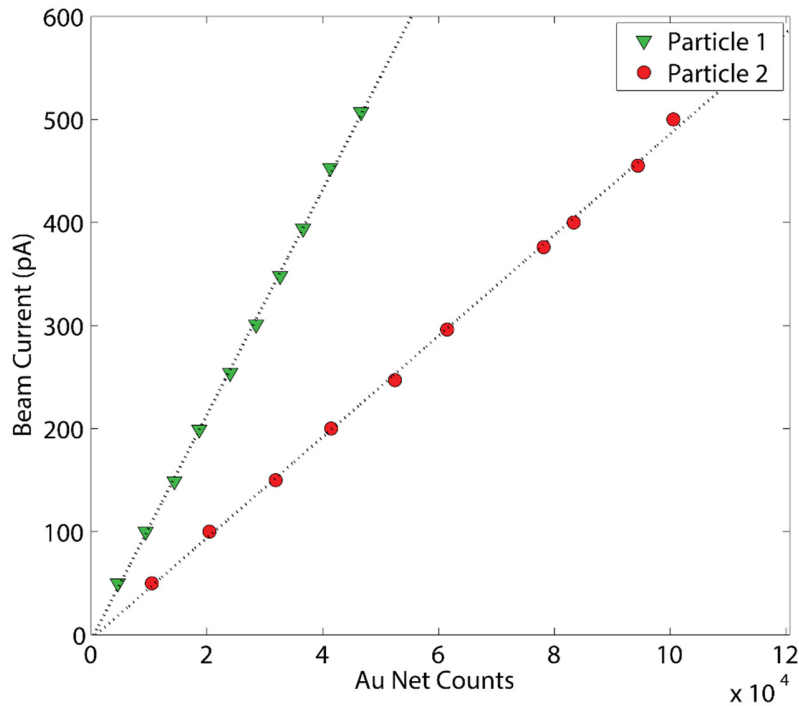


Figure 7.3: Beam current against net counts for two different Au particles. The excellent fit of the data points with a linear function confirms that the beam current measurement is linear.

For all particles, diffraction patterns and High-Resolution STEM images were acquired, confirming the crystallinity and fcc structure. We ensured that this tilt angle corresponded to an off-axis condition for the particles analyzed, in order to avoid unwanted channeling effects. Since the structures of the particles were confirmed to be the same of the relative bulk materials, bulk densities were used in the calculation of the ζ -factor: $\rho_{\text{Au}} = 19\,320 \text{ kg/m}^3$, $\rho_{\text{Ag}} = 9\,320 \text{ kg/m}^3$ and $\rho_{\text{Pt}} = 21\,450 \text{ kg/m}^3$.

It should be noted that during the measurement of the ζ -factors, all experiments (different particles and different elements) were performed using the same experimental conditions, such that the effects of shadowing remain the same. However, once the ζ -factors are determined, they can be used to quantify maps at any tilt angle, since shadowing will affect the signal from different elements in the same manner. Therefore, the ratio between the intensities will still be proportional to the ratios between the ζ -factors. An exception has to be made for soft X-rays with energy less than 3 keV. In this case, greater mass-absorption coefficients^[142] are linked to absorption effects that can lead to quantification errors. In general, it should be verified that the specimen thickness is less than a certain critical value for which absorption is below

5%, this is known as the *thin film approximation*. If not, absorption effects should be taken into account.^[133, 136]

Following the acquisition, the raw datacubes were treated in Matlab in which a two window method^[17] was used to fit the background radiation. The net counts for the L lines of Au, Ag and Pt were obtained by integrating over the signal characteristic peaks, after the background subtraction. The net counts measured for each particle are listed in Table 7.1, Table 7.2 and Table 7.3 along with the measured beam current.

7.4.3 ζ -factor calculation and error estimation

For each particle, the ζ -factor is determined from equation (7.4) using the volume V measured by electron tomography and the intensity I measured by EDXS for the same particle. As expected, a linear behavior is observed as demonstrated in Figure 7.4. The final values of the ζ -factors for Au, Ag and Pt for our experimental conditions are calculated through a weighted mean as described in ref.^[136] and found to be $\zeta_{\text{Au}} = 751 \pm 52 \text{ kg/m}^2$, $\zeta_{\text{Ag}} = 300 \pm 35 \text{ kg/m}^2$ and $\zeta_{\text{Pt}} = 724 \pm 50 \text{ kg/m}^2$. The values that we obtained for the ζ -factors cannot be compared directly with values reported in literature since the outcome of our approach depends on experimental parameters such as e.g. the holder, grid and tilt angle chosen. Nevertheless, ratios of the ζ -factors should be similar for different experimental settings.

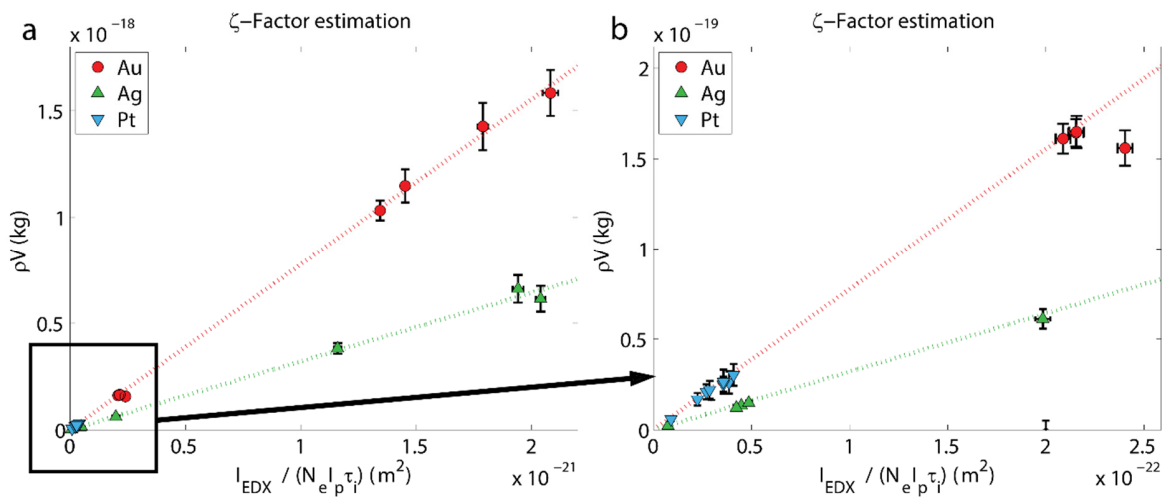


Figure 7.4: (a) The linear relation is clearly shown by the plots. (b) Magnification of the area close to the origin, where multiple data points are condensed due to the similar volumes of the particles. Error bars smaller than the markers are omitted.

To determine the error in a single ζ -factor measurement, we can use the principle of propagation of uncertainty,^[136, 143, 144] hereby assuming that the variables are uncorrelated. In the case of a Gaussian distribution and no correlation between the parameters, the formula to calculate the uncertainty on a function $f = f(p_1, p_2, \dots, p_n)$, depending on several variables p_j is given by:

$$\sigma_f^2 = \sum_{j=1}^n \left(\frac{\partial f}{\partial p_j} \right)^2 \sigma_{p_j}^2, \quad (7.13)$$

where σ_{p_j} denotes the error in the individual variable p_j . Applying this technique to the ζ -factor formula yields the following expression for the error in the ζ -factor from a single measurement:

$$\Delta\zeta = \zeta \sqrt{\left(\frac{\Delta I_p}{I_p} \right)^2 + \left(\frac{\Delta\tau_i}{\tau_i} \right)^2 + \left(\frac{\Delta I}{I} \right)^2 + \left(\frac{\Delta V}{V} \right)^2} \quad (7.14)$$

In this expression ΔI_p , $\Delta\tau_i$, ΔI and ΔV are the errors on I_p , τ_i , I and V , respectively. The uncertainty of the beam current and dwell time depends on the accuracy of the instrumental measurements, whereas the uncertainty in the X-ray intensity is determined by Poisson counting statistics, leading to $\Delta I = v\sqrt{I}$,^[145] where v is a factor that depends on the chosen confidence limit (e.g., $v = 1$ for a 68% confidence limit, $v = 2$ for 95% and $v = 3$ for 99%), in this work we used $v = 3$. In order to improve the statistical accuracy, the ζ -factor was measured for multiple nanoparticles consisting of the same element. Since the relative error on these individual measurements may vary significantly because of volume differences, the final estimate of the ζ -factor is calculated by means of a weighted arithmetic mean, given by Galassi et al.^[146]

$$\bar{\zeta} = \frac{\sum_{j=1}^n w_j \zeta_j}{\sum_{j=1}^n w_j}, \quad (7.15)$$

In which the weight corresponding to the individual measurements is given by their error

$$w_j = \frac{1}{\Delta\zeta_j} \quad (7.16)$$

The estimated variance of the weighted dataset is calculated as

$$\hat{\sigma}^2 = \frac{\sum_{j=1}^n w_j}{\left(\sum_{j=1}^n w_j \right)^2 - \sum_{j=1}^n (w_j)^2} \sum_{j=1}^n w_j (\zeta_j - \bar{\zeta})^2 \quad (7.17)$$

Since the true variance σ^2 is unknown and only the estimated variance $\hat{\sigma}^2$ is available, the total error in the ζ -factor is given by:^[147]

$$\Delta\bar{\zeta} = t_{\alpha}^{n-1} \frac{\hat{\sigma}}{\sqrt{n}} \quad (7.18)$$

where t_{α}^{n-1} is the Student's t-value for a given confidence limit α and n measurements, resulting in $n - 1$ degrees of freedom. In this way, the total error in the final ζ -factor resulting from multiple measurements can be calculated from the errors on the initial experimental variables.

Au particles	I	II	III	IV	V	VI	VII	VIII
Volume (nm ³)	8504	8335	59384	8529	81963	73810	8068	53428
Δ Volume (nm ³)	1040	1571	9144	1031	20090	12527	1119	11614
Net Counts	29418	28306	71905	29015	35344.00	60615.00	36871	63018
Δ Net Counts	514	504	804	511	564.00	738.60	576	753
Beam Current (pA)	264	262	261	260	260	260	261	262
Δ Beam Current (pA)	26	26	26	26	26	26	26	26
Measure Time per pixel area (s/nm ²)	0.083	0.083	0.030	0.083	0.010	0.021	0.094	0.029
Δ Measure Time per pixel area (s/nm ²)	0.0012	0.0012	0.0003	0.0012	0.0001	0.0002	0.0010	0.0002
Pixel size (nm)	0.135	0.135	0.190	0.135	0.380	0.269	0.190	0.269

Table 7.1: Measured data for the 8 Au particles used in the determination of the Au ζ -factor.

Ag particles	I	II	III	IV	V	VI	VII	VIII
Volume (nm ³)	1436	41981	1367	74993	70913	1595	239	6563
Δ Volume (nm ³)	278	6488	341	8352	15385	280	68	1776
Net Counts	17600	55878	15145	89708	65507	18694	11241	25265
Δ Net Counts	398	709	369	899	768	410	318	477
Beam Current (pA)	250	255	255	244	257	260	260	246
Δ Beam Current (pA)	25	26	26	25	26	26	26	25
Measure Time per pixel area (s/nm ²)	0.252	0.03	0.225	0.029	0.021	0.237	0.939	0.083
Δ Measure Time per pixel area (s/nm ²)	0.0074	0.0003	0.0047	0.0002	0.0002	0.0070	0.0400	0.0012
Pixel size (nm)	0.068	0.190	0.0.096	0.269	0.269	0.068	0.047	0.135

Table 7.2: Measured data for the 8 Ag particles used in the determination of the Ag ζ -factor.

Pt particles	I	II	III	IV	V	VI	VII	VIII
Volume (nm ³)	1218	272	787	1174	978	1412	1238	1174
Δ Volume (nm ³)	606	89	333	405	397	577	687	513
Net Counts	9788	6748	11126	12855	9677	14801	12808	8042
Δ Net Counts	297	246	316	340	295	365	340	269
Beam Current (pA)	248	247	243	244	244	244	243	242
Δ Beam Current (pA)	25	25	25	25	25	25	25	25
Measure Time per pixel area (s/nm ²)	0.164	0.490	0.327	0.237	0.237	0.238	0.237	0.186
Δ Measure Time per pixel area (s/nm ²)	0.0034	0.0208	0.0096	0.0070	0.0070	0.0070	0.0070	0.0055
Pixel size (nm)	0.096	0.047	0.068	0.068	0.068	0.068	0.068	0.068

Table 7.3: Measured data for the 8 Pt particles used in the determination of the Pt ζ -factor.

7.5 Quantification and analysis of 2D EDXS data

To test the validity of the proposed methodology, the composition of a Au@Ag core-shell nanoparticle was quantified (Figure 7.5a). In a previous study, these particles were found to yield sharp interfaces without any alloying.^[148] The outcome of the EDXS quantification based on our methodology will be compared to the volumes of the Au core and the Ag shell obtained from an independent 3D HAADF-STEM reconstruction (Figure 7.5b), which we here consider as the ground truth. Quantification of the 3D HAADF-STEM reconstruction is relatively straightforward, based on the different intensities observed for Au and Ag. In this manner, the volumes were measured to be $197\,980 \pm 37\,118 \text{ nm}^3$ and $49\,470 \pm 4\,452 \text{ nm}^3$ for Ag and Au respectively. This corresponds to approximately 1.86 fg (femtograms) of Ag and 0.95 fg of Au and the weight concentrations estimated in this manner are found to be $C_{\text{Au-STEM}} = 0.65 \pm 0.05$ and $C_{\text{Ag-STEM}} = 0.35 \pm 0.05$.

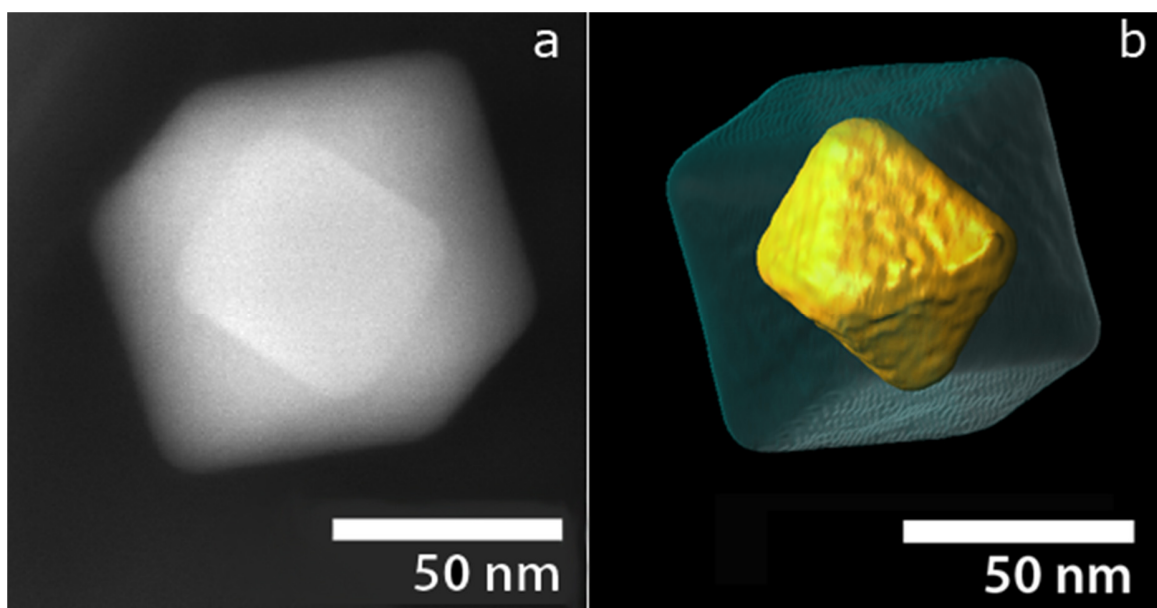


Figure 7.5: (a) HAADF STEM projection. (b) HAADF STEM tomography reconstruction rendering after segmentation of the core (Au) and shell (Ag).

In order to evaluate the reliability of the approach based on the ζ -factors, these values were compared to the quantified 2D EDXS data. An EDXS map (Figure 7.6) was collected from the same particle for 120 s with a current of 258 pA at 120 kV and a tilt angle of -60° . The concentrations were determined using the measured ζ -factors and were found to be: $C_{\text{Au}} = 0.64 \pm 0.04$ and $C_{\text{Ag}} = 0.36 \pm 0.04$. These values are clearly in good agreement with the quantification based on HAADF-STEM electron tomography. The same data

was also quantified using the Cliff-Lorimer method, implemented in the available software (Bruker Esprit). The values obtained were $C_{\text{Ag}} = 0.73 \pm 0.22$ and $C_{\text{Au}} = 0.27 \pm 0.08$. From this comparison, we conclude that quantification using the modified ζ -factor approach is reliable and that the method can be used to investigate nanostructures for which it is difficult or even impossible to use HAADF-STEM tomography to determine the chemical concentrations of the elements present. It should be mentioned, that the discrepancy with the quantification performed using Bruker Esprit is due to the calculated k-factors obtained by the software. Using a different theoretical model would lead to a different result.

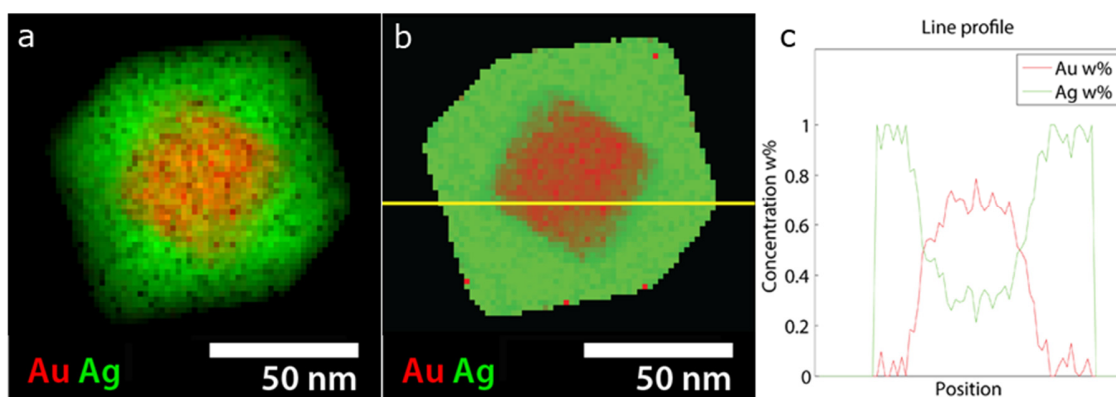


Figure 7.6: (a) EDXS map of the particle of Figure 7.5. (b) Quantified EDXS map. (c) Line profile through the quantified map (yellow line in (b)) showing the concentrations of Au and Ag in the projection direction.

7.5.1 Quantification of elemental maps in hetero nanoparticles

During the chemical analysis of nanoparticles by EDXS, the final goal is often to determine the distribution of the different elements over the particle. Such investigations are mostly based on EDXS maps. These so-called “elemental” maps are obtained by analyzing the collected datacube pixel-by-pixel, fitting the background with a two window method and measuring the net counts for each element in the specified energy interval.^[17] An example is provided in Figure 7.6a. After elemental maps are obtained, *quantified* maps can be calculated by applying eq. (7.5) in each pixel of the elemental map. The result, shown in Figure 7.6b, is a concentration map for each element with values ranging from 0 to 1. In this case, the HAADF-STEM image was used as a mask to define the boundaries of the particle and improve the visualization by suppressing any signal outside the particle. A line profile (indicated by the yellow line Figure 7.6b) is presented in Figure 7.6c to enable a more straightforward interpretation of the quantified data.

7.5.2 Application to Au-Pt hetero-nanostructures

Once the validity of our approach has been determined, we can apply the method to nanostructures for which HAADF-STEM fails to give any indication about the chemical composition. For example, since Au and Pt have an atomic number Z equal to 79 and 78 respectively, no contrast difference is expected when using HAADF-STEM to investigate Au-Pt hetero structures.^[149] However, these structures are of great interest due to their catalytic activity.^[149-152] We here investigated a Au-Pt hetero-nanostructure, shown in Figure 7.7a, that consists of spherical Au particles, grown on a platinum nanodendritic seed, yielding a core-satellite structure.^[149] In order to quantify the chemical composition and the distribution of the different elements, we applied the ζ -factor method using the values for Au and Pt. In this manner, the overall concentration was measured to be $C_{\text{Au}} = 0.77 \pm 0.02$ and $C_{\text{Pt}} = 0.23 \pm 0.02$. Background subtraction and a peak deconvolution, implemented in Matlab, were applied to the EDXS data to separate the Au and Pt contributions to the signal, since the L peaks for Au and Pt overlap partially. A map representing the resulting Au and Pt counts is shown in Figure 7.7b. Figure 7.7c, shows a quantified map from the same data, which confirms the core-satellite structure with the Pt seed located at the center and pure Au particles surrounding it. The line profile in Figure 7.7d, shows the actual values of the wt% concentration of Pt and Au along the yellow line, and we can conclude that the Au particles around are pure Au particles and no alloying with Pt is observed.

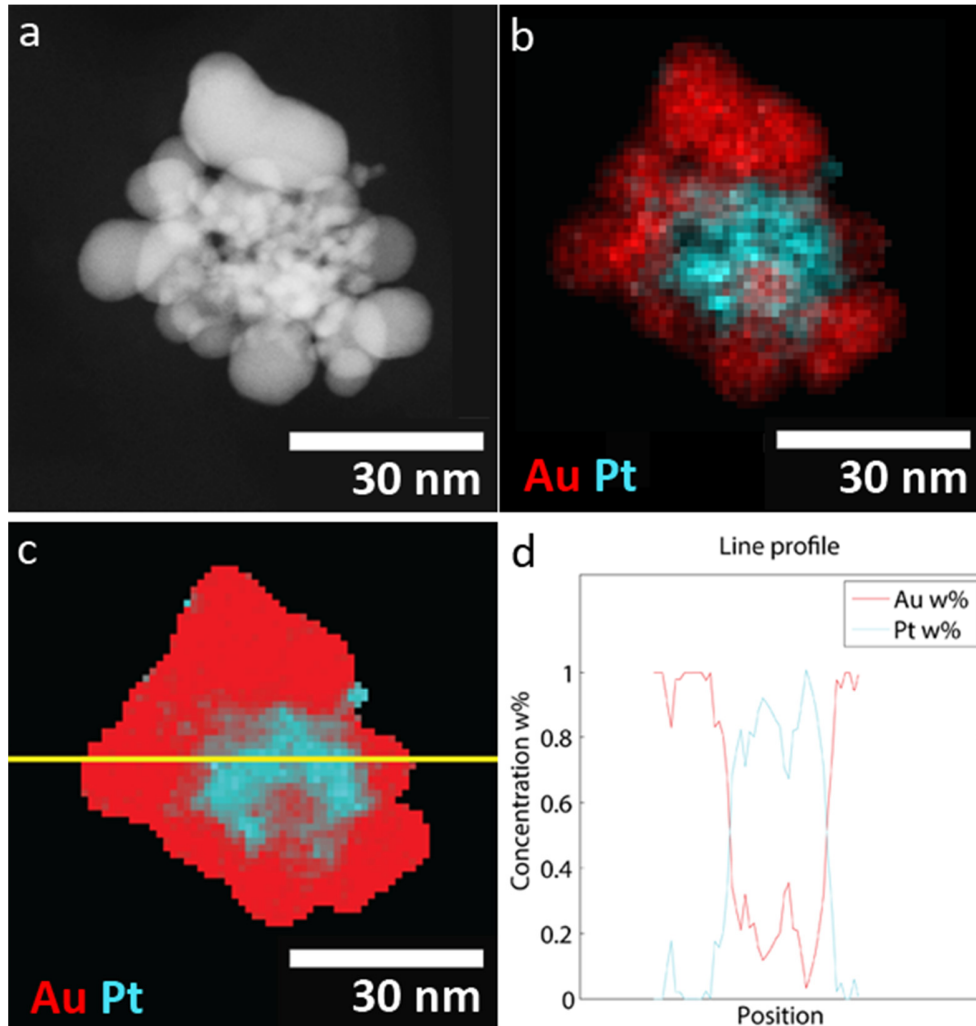


Figure 7.7: (a) HAADF STEM image. (b) EDXS elemental map. (c) Quantified EDXS map. (d) Line profile through the quantified map (yellow line in (c)) showing the concentrations of Au and Pt in the projection direction.

7.6 Volume measurement of nanoparticles by means of EDXS

Interestingly, once the ζ -factors for a given material are known, it is possible to measure the volume of a nanoparticle of the same material (in the absence of absorption) by acquiring a single EDXS map and using eq. (7.4). Since the ζ -factors were determined through EDXS maps acquired at 17° , eq. (7.4) only holds for that tilt angle. However, incorporating a shadowing term S_f , we obtain eq. (7.19), which enable us to calculate the volume of a nanoparticle from the net counts I_A , extracted from an EDXS map acquired at any tilt angle.

$$\rho V = \zeta_A \frac{S_f I_A}{N_e I_p \tau_d} \quad (7.19)$$

The shadowing scaling term $S_f = \frac{S_{17^\circ}}{S_\alpha}$ is calculated through a calibration curve (Figure 7.8). The curve is obtained by measuring the net counts of EDXS maps acquired from the particle shown in Figure 8.3, every 10° from -70° to 70° , and normalizing by the minimum value. S_{17° is therefore the shadowing factor interpolated from the data points, at 17° (tilt angle used for our ζ -factor) and S_α is the shadowing factor at the tilt angle used to acquire the map.

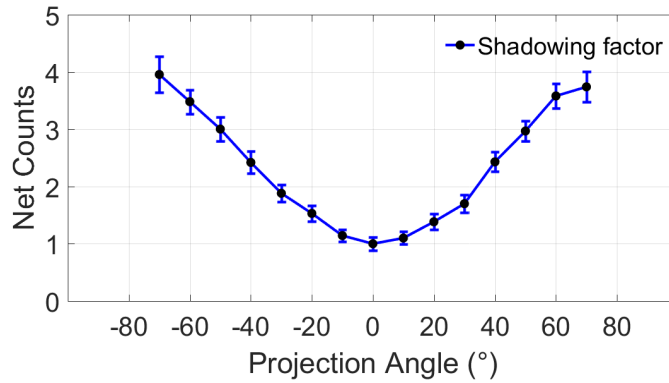


Figure 7.8: Normalized net counts (shadowing factor) for Au L lines of EDXS maps acquired from the particle shown in Figure 8.3, every 10° from -70° to 70° .

We tested this approach on the Ag@Au core-shell nanoparticle of Figure 7.5. Volume measurement was performed for three EDXS maps, collected at $+50^\circ$, $+20^\circ$ and -30° , and compared to the volume measurements performed by electron tomography. The data is given in Table 7.4. The volume estimation is consistent through the different maps, with the volumes measured for Au at $+50^\circ$, $+20^\circ$ and -30° being respectively $V_{50} = 47\,929 \pm 4\,830 \text{ nm}^3$, $V_{20} = 45\,859 \pm 4\,622 \text{ nm}^3$, $V_{-30} = 40\,872 \pm 4\,119 \text{ nm}^3$, and the volume measured by tomography $V_{\text{Tomog}} = 49\,470 \pm 4\,452 \text{ nm}^3$.

Angle	50	20	-30
Beam Current (pA)	258	258	258
ΔBeam Current (pA)	26	26	26
Au Net Counts	31837	14420	17430
ΔAu Net Counts (3σ confidence)	535	360	396
Ag Net Counts	144788	60731	76158
ΔAg Net Counts (3σ confidence)	1142	739	828
Shadowing Factor	0.44	0.94	0.69
ΔShadowing Factor	0.09	0.2	0.15
Acq. Time per pixel area (s/nm²) [τ_i]	0.006802093	0.006879	0.006848
ΔAcq. Time per pixel area (s/nm²) [τ_i]	7.69468E-06	7.69E-06	7.69E-06
Density Au (kg/m³) [ρ]	19320	19320	19320
ΔDensity Au (kg/m³) [ρ]	1	1	1
Density Ag (kg/m³) [ρ]	9320	9320	9320
ΔDensity Ag (kg/m³) [ρ]	1	1	1
Number Electrons in 1 Coulomb [N_e]	6.241E+18	6.24E+18	6.24E+18
ζ-factor Au	724	724	724
$\Delta\zeta$-factor Au	50	50	50
ζ-factor Ag	300	300	300
$\Delta\zeta$-factor Ag	35	35	35
Volume from EDXS			
Volume Au (nm ³)	47929	45859	40872
Δ Volume Au (nm ³)	4830	4622	4119
Volume Ag (nm ³)	187229	165898	153397
Δ Volume Ag (nm ³)	18868	16719	15459
Volume from Tomography			
Vol. Au (nm ³)	49470		
Δ Vol. Au (nm ³)	4452		
Vol. Ag (nm ³)	197980		
Δ Vol. Ag (nm ³)	37118		

Table 7.4: Data for the volume calculation of the Au@Ag nanoparticle of Figure 7.5, according to equation 7.19. The volume measured by tomography is also shown for comparison.

The possibility of determining the volume of a nanoparticle through a single EDXS maps could represent an interesting opportunity for including prior-knowledge in a tomographic reconstruction technique, especially in the case of limited tilt ranges, for example when using an FEI double tilt holder, which cannot

be tilted beyond $\pm 30^\circ$. As seen in the previous chapters, including prior-knowledge about the sample is a valuable approach in minimizing missing wedge artifacts.

7.7 Thickness measurement by means of EDXS

Another interesting application of EDXS, is the measurement of thin film thicknesses (or depth position of nanoparticle in a matrix) through the acquisition of a single EDXS map. This is possible by exploiting the different absorption of X-rays towards the different detectors of the Super-X system. These results should be considered a proof of concept and outlook to further applications.

7.7.1 Method

In order to estimate the thickness of a thin-film or the position of a particle inside a matrix, we can exploit the X-ray absorption effect, obeying the Lambert-Beer law. This is possible only for certain types of samples, where the absorbing layer is composed by a different material and is deposited above the emitting layer/particle. An example of such a specimen will be given in the next section. If we approximate the emitting source as a point source of X-rays, we obtain that that the measured intensity I will be:

$$I = I_0 e^{-\left[\frac{\mu}{\rho}\right]^A \rho_B l} \quad (7.20)$$

In the equation, $\left[\frac{\mu}{\rho}\right]^A$ is the mass absorption coefficient of element A , ρ_B is the density of the matrix B and l is the path length of the X-rays inside the matrix.

The path length l can also be written as a function of the thickness z and the take-off angle α_{TO} , as $l = z/\sin(\alpha_{TO})$. The take-off angle α_{TO} is defined as the angle between the surface of the specimen and the line between the X-ray origin and the detector center. For a system of detectors not parallel to the holder axis, as in the case of the Super-X system, the variables describing the system are the specimen tilt angles, α and β , the detector elevation angle θ_e and the azimuthal angle θ_A which is the angle between the holder axis and the line that connects the optical axis to the center of the detectors. The schemes in Figure 7.9 and Figure 7.10, show these variables in more detail.

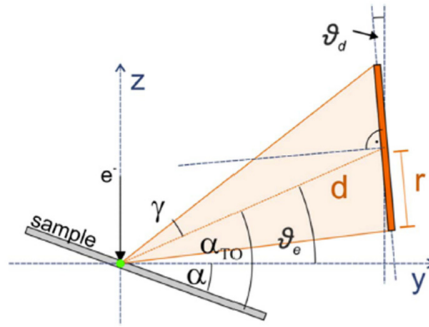


Figure 7.9: Side view scheme of holder and detector, depicting the take-off angle α_{TO} and elevation angle θ_e . Image adapted from ref.^[153] with permission of Elsevier.

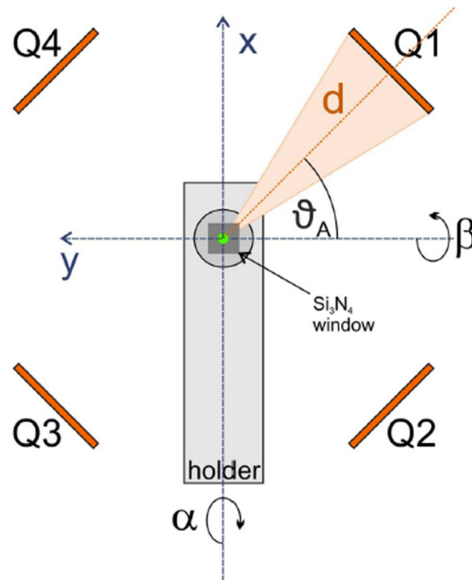


Figure 7.10: Top view scheme of holder and Super-X system, depicting the azimuthal angle θ_A . Image adapted from ref.^[153] with permission of Elsevier.

With these variables defined, the take-off angle α_{TO} can be written as:^[153]

$$\alpha_{TO} = \arcsin \left(\frac{\cos\theta_e (\sin\beta \cos\theta_A - \sin\alpha \cos\beta \sin\theta_A) + \cos\alpha \cos\beta \sin\theta_e}{\sqrt{(\sin\beta \cos\theta_A - \sin\alpha \cos\beta \sin\theta_A)^2 + (\cos\alpha \cos\beta)^2}} \right) \quad (7.21)$$

Substituting α_{TO} and l in equation (7.20) yields the model describing the intensity of X-rays measured from a detector with azimuthal angle θ_A , elevation angle θ_e , from a particle of element A, embedded in a matrix

with density ρ_B , as a function of the emitted intensity I_0 , the specimen tilt angles, α and β , and the depth of the particle in the matrix, z .

$$I = I_0 e^{-\left[\frac{\mu}{\rho}\right]^A} \rho_B \frac{z}{\sin(\alpha_{TO})} \quad (7.22)$$

Considering now the signal from two different detectors, I_1 and I_2 , we end up with two equations (7.22) which we can divide and rearrange to obtain an expression for z :

$$z = \frac{\sin(\alpha_{TO,1})\sin(\alpha_{TO,2})}{\left[\frac{\mu}{\rho}\right]^A \rho_B (\sin(\alpha_{TO,1}) - \sin(\alpha_{TO,2}))} \ln\left(\frac{I_1}{I_2}\right) \quad (7.23)$$

Where I_1 , I_2 , $\alpha_{TO,1}$ and $\alpha_{TO,2}$ are the intensities and take-off angles of detector 1 and detector 2 respectively.

In order to consider detector efficiency and shadowing, we also add another factor, such that the measured intensity for detector one I_1 should be scaled by the detector shadowing/efficiency factor at that given tilt angle, position and z-height such that $I_1 = (\sigma_{1,\alpha,\beta,x,y,z} I_0) e^{-\left[\frac{\mu}{\rho}\right]^A} \rho_B \frac{z}{\sin(\alpha_{TO})}$.

Therefore, substituting this to equation (7.22), yields the final equation:

$$z = \frac{\sin(\alpha_{TO,1})\sin(\alpha_{TO,2})}{\left[\frac{\mu}{\rho}\right]^A \rho_B (\sin(\alpha_{TO,1}) - \sin(\alpha_{TO,2}))} \ln\left(\sigma_{1,2} \frac{I_1}{I_2}\right) \quad (7.24)$$

where $\sigma_{1,2} = \frac{\sigma_{2,\alpha,\beta,x,y,z}}{\sigma_{1,\alpha,\beta,x,y,z}}$.

7.7.2 Experimental validation

We consider a Super-X detector of a FEI Osiris with the following configuration: $\theta_e = 22^\circ$, and $\theta_A = 315^\circ, 225^\circ, 135^\circ, 45^\circ$, for detectors Q₁, Q₂, Q₃, and Q₄ (Figure 7.10), respectively, according to manufacturer specifications. In order to test the approach, we performed an experiment on a two multilayer thin films samples prepared by sputtering different materials on carbon coated Cu Quantifoil grids. The sputter was set to deposit 10 nm of Ni and 100 nm of Ag for Sample $Ni_{10}Ag_{100}$, and 10 nm Ag and 100 nm

Au for Sample $Ag_{10}Au_{100}$. In this manner, X-rays emitted from the lower layer towards the detectors, would travel in the upper layer yielding information about its thickness.

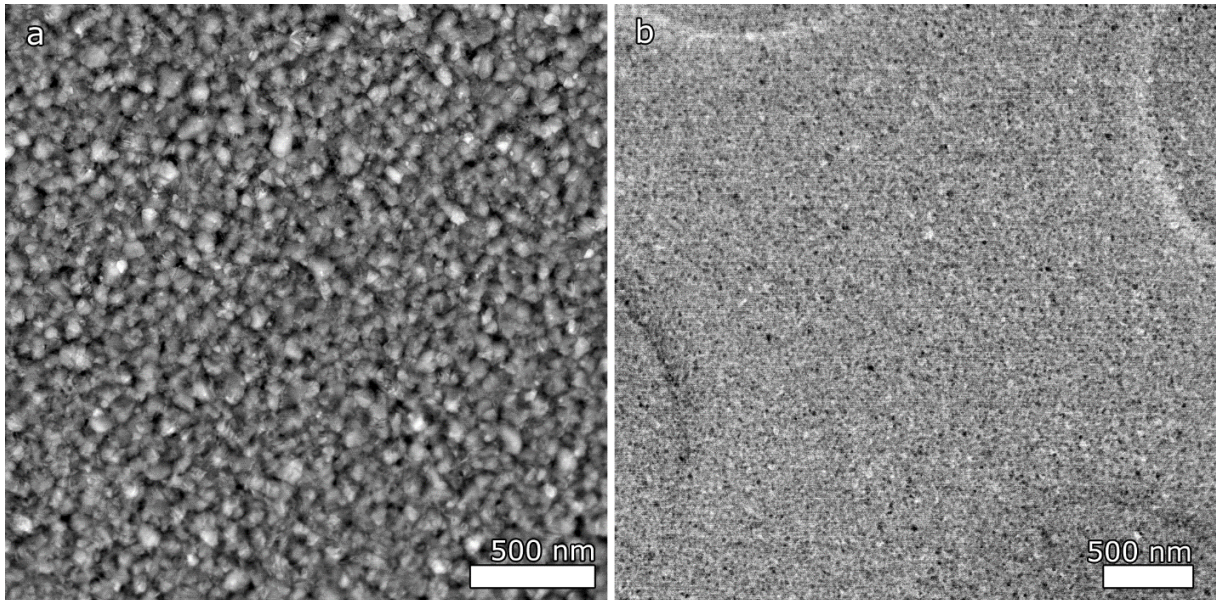


Figure 7.11: Overview HAADF-STEM images of samples (a) $Ni_{10}Ag_{100}$ and (b) $Ag_{10}Au_{100}$.

A series of EDXS maps was collected on a FEI Osiris operated at 200 kV, using an FEI double tilt holder and with the following parameters: $\alpha = 10^\circ, 12.5^\circ, 15^\circ, 17.5^\circ, 20^\circ$, $\beta = 5^\circ$ and a beam current of approximately 2.4 nA. The α and β values were chosen in order to give an inclination to the sample which would cause a different path length towards the different detectors, but still trying to minimize shadowing effects for at least detector 1 and detector 2. The net counts were extracted from the maps and reported in the following tables:

α	Detector 1	Detector 2	Detector 3	Detector 4
10°	33321	23728	12161	23905
12.5°	33928	26164	10272	22514
15°	34849	26574	8263	20923
17.5°	33786	27614	7144	20445
20°	34410	29408	5954	18819

Table 7.5: Net counts for sample $Ag_{10}Au_{100}$, Ag L lines at 2.9 keV.

α	Detector 1	Detector 2	Detector 3	Detector 4
10°	18253	10361	2952	6941
12.5°	20002	11539	1785	5969
15°	21964	14871	1270	5367
17.5°	23710	16473	1050	4494
20°	24624	18747	428	3257

Table 7.6: Net counts for sample Ni₁₀Ag₁₀₀, Ni L lines at 0.85 keV.

In order to estimate the shadowing/efficiency factors, we performed a calibration, by acquiring EDXS maps of three Au nanoparticles, for which we know that absorption effects can be ignored, using the same experimental conditions, except a different goniometer position $(x,y,z) = (111 \mu\text{m}, 71 \mu\text{m}, -53 \mu\text{m})$. Even though, the different goniometer position and different grid could possibly determine different shadowing conditions, this experiment enables an estimation of a starting point, for eventual optimizations of these parameters, and allows to verify that the four detectors of the Super-X systems behave all in the same way and have the same efficiency. Net counts for the Au M peaks (2.1 keV) are extracted.

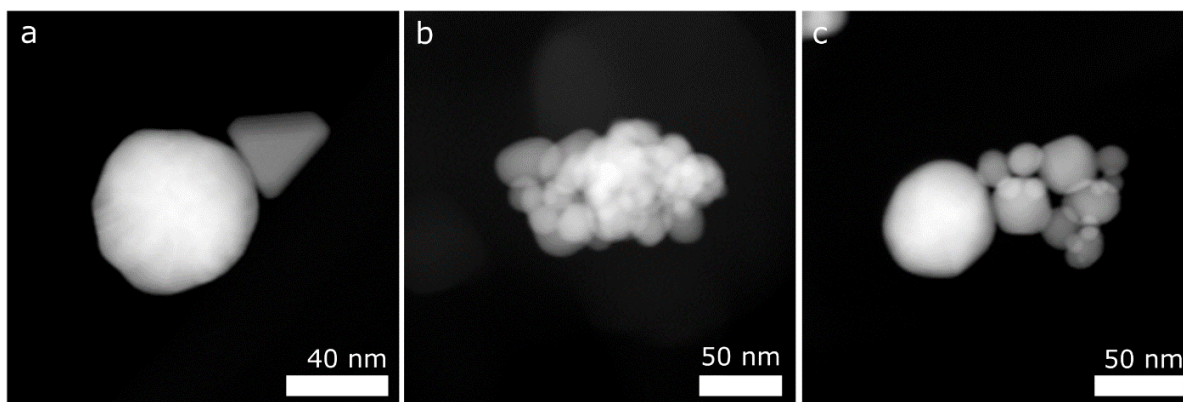


Figure 7.12: Au particles used for detectors shadowing/efficiency factors estimation.

α	Detector 1	Detector 2	Detector 3	Detector 4
10°	70066	69777	34279	55286
12.5°	68747	70049	28013	50154
15°	71332	73537	23430	44207
17.5°	69979	71390	17610	38553
20°	68776	71035	12405	32427

Table 7.7: Net counts for particle of Figure 7.12a.

α	Detector 1	Detector 2	Detector 3	Detector 4
10°	53083	52704	25692	41430
12.5°	53189	54213	21676	41430
15°	53526	54692	17152	34014
17.5°	52996	54606	13158	29439
20°	52951	54148	9476	25308

Table 7.8: Net counts for particle of Figure 7.12b.

α	Detector 1	Detector 2	Detector 3	Detector 4
10°	33922	34508	15698	26848
12.5°	35020	35218	13308	24026
15°	34488	35470	11089	21686
17.5°	34512	35773	8427	18334
20°	33774	34904	5886	15656

Table 7.9: Net counts for particle of Figure 7.12c.

By inspecting the above tables we see that basically, detector 1 and 2 show little to no shadowing, as expected, whereas we have more shadowing for the detectors 3 and 4. To estimate the shadowing factors, we divided every calibration set by the value at $\alpha = 10^\circ$ and $\beta = 5^\circ$, we then averaged the 3 sets and obtained an estimation of the shadowing/efficiency factors, for each detector and angle. The obtained values are the following:

α	Detector 1	Detector 2	Detector 3	Detector 4
10°	1	1	0.48	0.79
12.5°	1.01	1.02	0.4	0.73
15°	1.01	1.04	0.33	0.64
17.5°	1	1.03	0.25	0.55
20°	0.99	1.02	0.18	0.47

Table 7.10: Normalized and averaged shadowing/efficiency factors for the detectors.

Net counts values for the two thin-film samples analyzed are then scaled based on this estimation of the shadowing factors and on the life time of the detector for each map acquired. The scaled data is shown in the following tables:

α	Detector 1	Detector 2	Detector 3	Detector 4
10°	1178.67	791.46	622.19	994.72
12.5°	1235.46	876.66	591.43	959.29
15°	1299.58	897.82	550.8	948.42
17.5°	1307	979.89	585.45	1040.09
20°	1343.55	1052.62	653.45	1055.36

Table 7.11: Normalized and averaged shadowing/efficiency factors for the detectors.

α	Detector 1	Detector 2	Detector 3	Detector 4
10°	363.68	206.81	111.27	169.48
12.5°	403.18	229.14	77.22	154.92
15°	448.57	292.47	64.98	154.49
17.5°	486.56	327.13	69.17	147.41
20°	518.72	380.68	38.47	122.89

Table 7.12: Normalized and averaged shadowing/efficiency factors for the detectors.

We are finally able to evaluate equation (7.24) and determine the thickness of the deposited films. For this purpose we used the mass absorption coefficient for Ag in Au, obtained from ref.^[142] $\left[\frac{\mu}{\rho}\right]^{Ag} = 2.17 \cdot 10^3 \frac{cm^2}{g}$ and a density for Au of $\rho_{Mg} = 19.3 \frac{g}{cm^3}$, and the mass absorption coefficient for Ni in Ag, obtained from ref.^[142] $\left[\frac{\mu}{\rho}\right]^{Ag} = 1.02 \cdot 10^4 \frac{cm^2}{g}$ and a density for Au of $\rho_{Mg} = 10.49 \frac{g}{cm^3}$.

We applied equation (7.24) by using the scaled intensities from detector 1 as I_1 and the scaled intensities from detectors 2,3,4, as I_2 , obtaining the following thicknesses for the two samples in the different cases:

α	Detectors 1&2	Detectors 1&3	Detectors 1&4
10°	205	47	31
12.5°	201	42	35
15°	245	36	34
17.5°	215	24	19
20°	204	14	16

Table 7.13: Estimated thickness (nm) of the Au film for sample $Ag_{10}Au_{100}$.

α	Detectors 1&2	Detectors 1&3	Detectors 1&4
10°	114	34	55
12.5°	129	36	52
15°	111	32	45
17.5°	116	23	40
20°	101	20	37

Table 7.14: Estimated thickness (nm) of the Au film for sample $Ni_{10}Ag_{100}$.

The measurements are in the right order of magnitude when using scaled intensities for detector 1 and detector 2, therefore in a situation of negligible shadowing. For detectors 3 and 4, shadowing estimation seems to be too far from the actual value, requiring further calculations of actual shadowing factors for each measurement positions, according to the method proposed in ref.^[153]. The obtained values for detector 1 and 2 average to 214 ± 18 (std) nm and 114 ± 10 (std) nm for the thickness of the Au film on sample $Ag_{10}Au_{100}$ and the Ag film thickness on sample $Ni_{10}Ag_{100}$ respectively. Given an expected thickness of 100 nm, these preliminary results show the validity of the approach as a promising method to estimate thickness of films or depth position of particles in a matrix by means of a single EDXS map.

Sources of inaccuracies for these calculations can be identified in several factors. Variations on the expected thickness of the films deposited by the sputterer. Lower density of the sputtered film could also be hypostasized, while bulk values were used. Furthermore, the correct elevation angles for the detectors should also be measured. We performed an approximate measurement of the thin films in a FIB microscope. For sample $Ag_{10}Au_{100}$ we could not distinguish Ag from Au given the poor contrast difference, and we only observed a single layer of approximately 100 nm. For the $Ni_{10}Ag_{100}$ sample we could observe a very irregular Ag film with a thickness oscillating between 50 nm and 90 nm, and Ni film of approximately 20 nm. These

measurements have to be considered only rough estimations of the thicknesses, giving the resolution of the instrument.

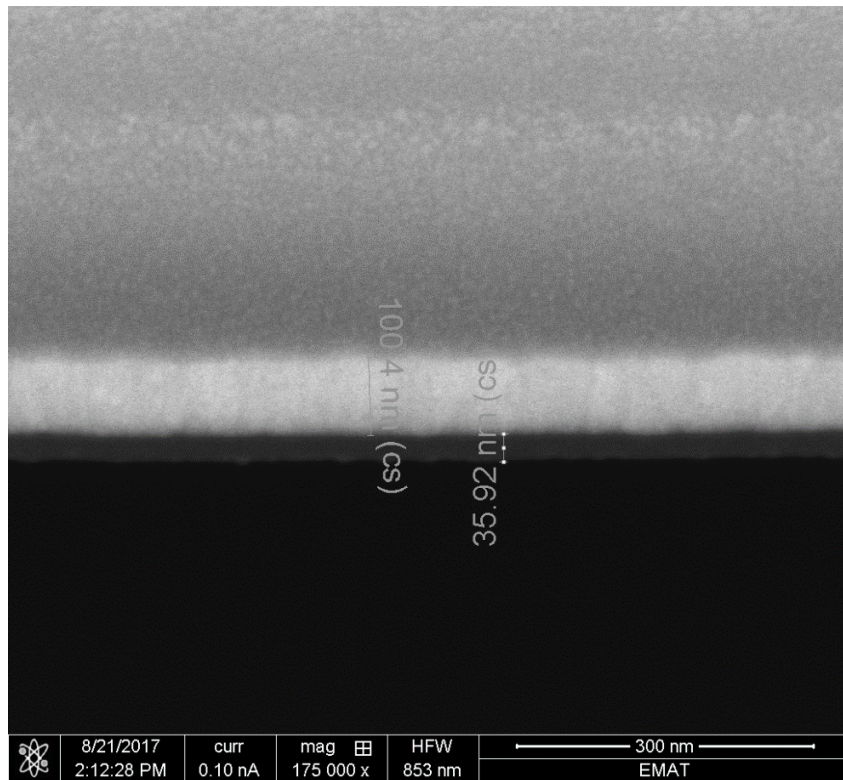


Figure 7.13: SEM image of sample $Ag_{10}Au_{100}$ cross section. Displayed lengths are corrected for the tilting angle of observation. The bright layer is the metal (Ag+Au) layer above the darker carbon layer.

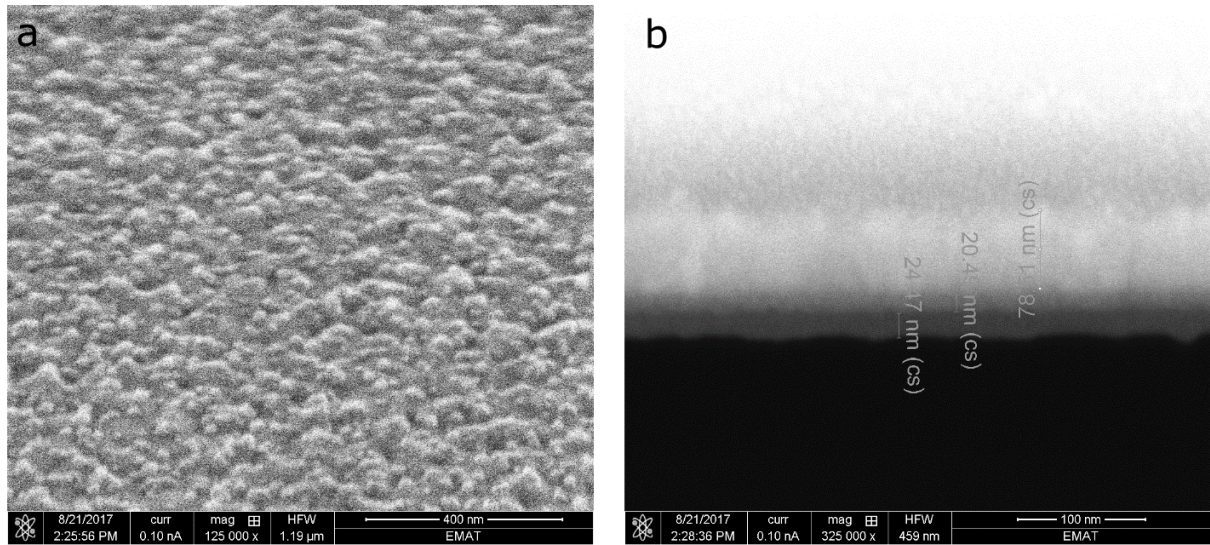


Figure 7.14: SEM images of sample $Ni_{10}Ag_{100}$, (a) top view, (b) cross section. Displayed lengths are corrected for the tilting angle of observation. The top view image in (a) shows the irregular surface of the layer. The cross section view in (b) shows an estimation of the thicknesses, with a darker carbon layer on the bottom followed by the Ni layer and the Ag layer on top.

The observed thicknesses show that in both cases the method overestimates the real thickness of the film, with slightly better agreement for sample $Ni_{10}Ag_{100}$. Further investigations will be needed to understand the reasons of this overestimations and to further optimize the measurement parameters.

8 Quantitative EDXS in 3D

This chapter is based on the work published in the journal article of ref.^[154]: “A new method for quantitative XEDS tomography of complex heteronanostructures”, D. Zanaga, T. Altantzis, L. Polavarapu, L. M. Liz-Marzán, B. Freitag, S. Bals, *Particle & Particle Systems Characterization* 2016, 33, 396.

8.1 Introduction

Over the last decades, electron tomography based on HAADF-STEM has evolved into a standard technique to investigate the morphology and inner structure of nanomaterials.^[29] The HAADF-STEM intensity depends on sample thickness but also scales with the atomic number Z and therefore, chemical compositions can be studied from these three-dimensional (3D) reconstructions.^[155, 156] Nevertheless, it is not straightforward to interpret the gray levels in a 3D HAADF-STEM reconstruction in an absolute manner. Therefore, it becomes very challenging to use HAADF-STEM tomography for samples in which mixing of elements is expected. Also for samples that contain unknown elements or elements with atomic number Z close to each other, HAADF-STEM tomography is no longer applicable.

However, it is well known that the properties and applications of nanostructures are strongly dependent on their morphology as well as their chemical composition.^[157] Traditional electron microscopy techniques do not provide quantitative information on the composition of single nanoparticles. Early attempts to investigate the composition of nanomaterials in 3D involved the use of EFTEM tomography^[29, 52] as well as EDXS mapping tomography.^[52] Due to instrument limitations the technique did not develop further. More recently, an increasing number of studies was published, where EDXS is combined with tomography to understand complex nanostructure morphology and composition in 3D. These studies rely on newly developed EDXS detectors^[61, 62] such as the Super-X detection system. Although qualitative results obtained by EDXS tomography have been reported,^[53, 54, 131, 132, 158] it remains challenging to obtain quantitative information by 3D EDXS and therefore further progress is required.

8.2 Detector shadowing

By using the Super-X detector, one is able to overcome problems that were previously related to extreme shadowing of the EDXS signal caused by the sample-detector configuration. Although this problem can be largely overcome, some shadowing effects remain,^[153, 159, 160] as illustrated in Figure 8.1.

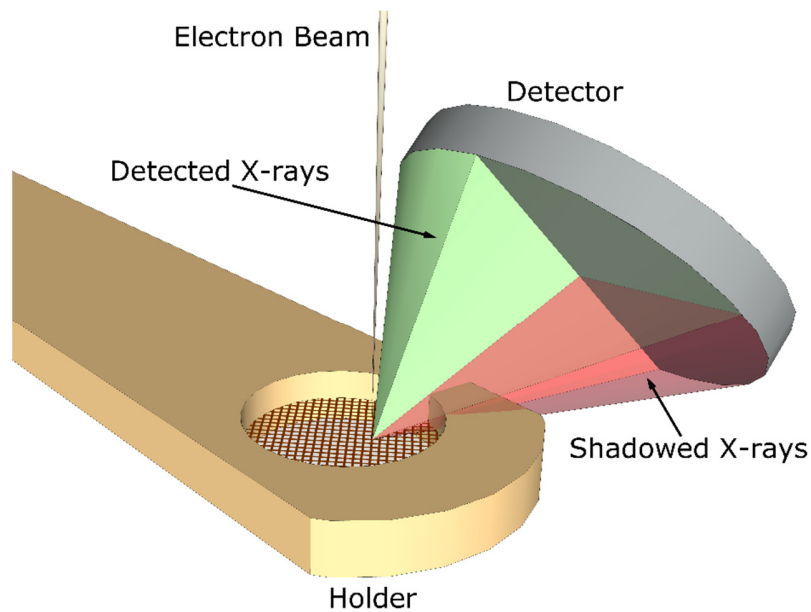


Figure 8.1: The figure schematically shows how detection of X-rays is hampered by the holder. The detectable X-rays emitted from the sample are indicated by the green cone, while those blocked by the holder are indicated by the red cone. Only one of the four Super-X detectors is depicted, but the scheme holds generally for all detectors. Upon tilting the sample, the effect of shadowing changes as a function of the tilt angle.

Since such shadowing effects vary for different tilt angles, the EDXS signal integrated over the four detectors will also depend on the tilt angle^[153, 159-161] and the projection principle for electron tomography is no longer fulfilled.^[160]

8.2.1 Strategies to overcome the shadowing problem

Different methodologies have been proposed to overcome the shadowing challenge. For example, signals from individual detectors can be combined,^[133, 159] the acquisition time can be adjusted as a function of the tilt angle^[160] or the total signal for every map can be normalized to the same value.^[161] However, in order to maximize the signal-to-noise ratio, it is of great importance to collect as many counts as possible. Selectively switching off detectors is therefore disadvantageous and normalizing the signal after acquisition cannot lead to accurate results because of the noise present. Changing the acquisition time improves the quality of the tilt series but a calibration of the holder is required and the final result is still hampered by inaccuracies.^[160]

In our work,^[154] we proposed a novel and straightforward approach to minimize the impact of shadowing effects during EDXS tomography. The method relies on a synergistic combination of quantified EDXS data and HAADF-STEM tomography. HAADF-STEM yields a relatively high signal-to-noise ratio, and does not suffer from shadowing effects other than those related to the “missing wedge”.^[29] EDXS, on the other hand, yields chemical information, even when no prior knowledge of the sample is available or for samples that contain elements with a small difference in atomic number Z .

As a proof of principle, we applied our methodology to a nanostructure containing a mix of Au and Ag atoms. However, it must be noted that the approach we propose here enables quantitative 3D chemical characterization of a broad variety of nanostructures. Examples of materials science studies will be shown in the next chapter.

8.3 Quantitative 3D EDXS reconstruction method

There are different possibilities to obtain a quantitative 3D EDXS reconstruction. The most straightforward approach is based on EDXS maps, from which the background is subtracted leading to net counts maps. These maps can be used directly as an input for a tomographic algorithm such that a different reconstruction for each element is obtained.^[54, 131] Next, these reconstructions can be quantified by analyzing the voxel intensities using the Cliff-Lorimer or ζ -factor method.^[133] The outcome of this approach is predominantly determined by the quality of the tomogram and therefore by the number of available projections. However, due to the relatively long acquisition times, EDXS tilt series are typically acquired with an increment that is larger in comparison to HAADF-STEM e.g. every 10° . Furthermore, noise and shadowing effects such as illustrated in Figure 8.1 will degrade the quality of the reconstruction. Shadowing effects affect the EDXS intensity and therefore, an EDXS map is not simply a function of sample thickness or chemical concentration. In this study, we overcome this problem by using maps based on the ratios between specific elements. Such maps are not affected by shadowing effects since the EDXS counts for both types of elements are acquired at the same tilt angle and are influenced by shadowing in the same manner. This assumption is valid for “hard” X-rays with energies > 3 keV, else an absorption correction method^[133, 136] should be applied.

A new approach to obtain ratio maps has been recently proposed, which is based on using the well-known ζ -factor method.^[136] In short, the method is similar to the conventional Cliff-Lorimer method,^[134] but presents major advantages regarding correction of absorption effects and experimental determination of the sensitivity factors, the so-called “ ζ -factors”. Here, ζ -factors were determined from particles comprising a single element, through the technique described in the previous chapter by combining EDXS analysis and electron tomography. Once the ζ -factors are known, quantification of EDXS data can be carried out.^[136]

By applying the ζ -factor method, reliable ratio maps are obtained, which are not affected by shadowing effects. However, it is important to note that these maps no longer contain any information on sample thickness and consequently do not fulfill the projection requirement. Our approach therefore relies on combining these ratio maps with thickness information extracted from a HAADF-STEM reconstruction of the same nanostructure.

To measure the particle thickness, a HAADF-STEM reconstruction is computed using the SIRT algorithm.^[35] The SIRT reconstruction is segmented to obtain a binary volume where voxel values are either equal to 1 if they belong to the particle or equal to 0 elsewhere. Next, the segmented STEM reconstruction is forward projected along the same directions as those that were used to acquire EDXS maps. The EDXS maps are then aligned to the forward projections using filtered normalized cross-correlation.^[67] It should be noted that this approach does not require the EDXS and HAADF-STEM series to be acquired simultaneously or using the same experimental parameters. By multiplying the ratio maps with the relative particle thickness, extracted from 3D HAADF-STEM reconstructions, chemically quantified projections are obtained. The projections fulfill the projection requirement and contain reliable quantitative chemical information. These elemental projections are used as an input for a tomography algorithm and a quantified 3D reconstruction of the nanostructure is obtained, from which both the structure and the composition can be investigated. A schematic workflow of our approach is presented in Figure 8.2.

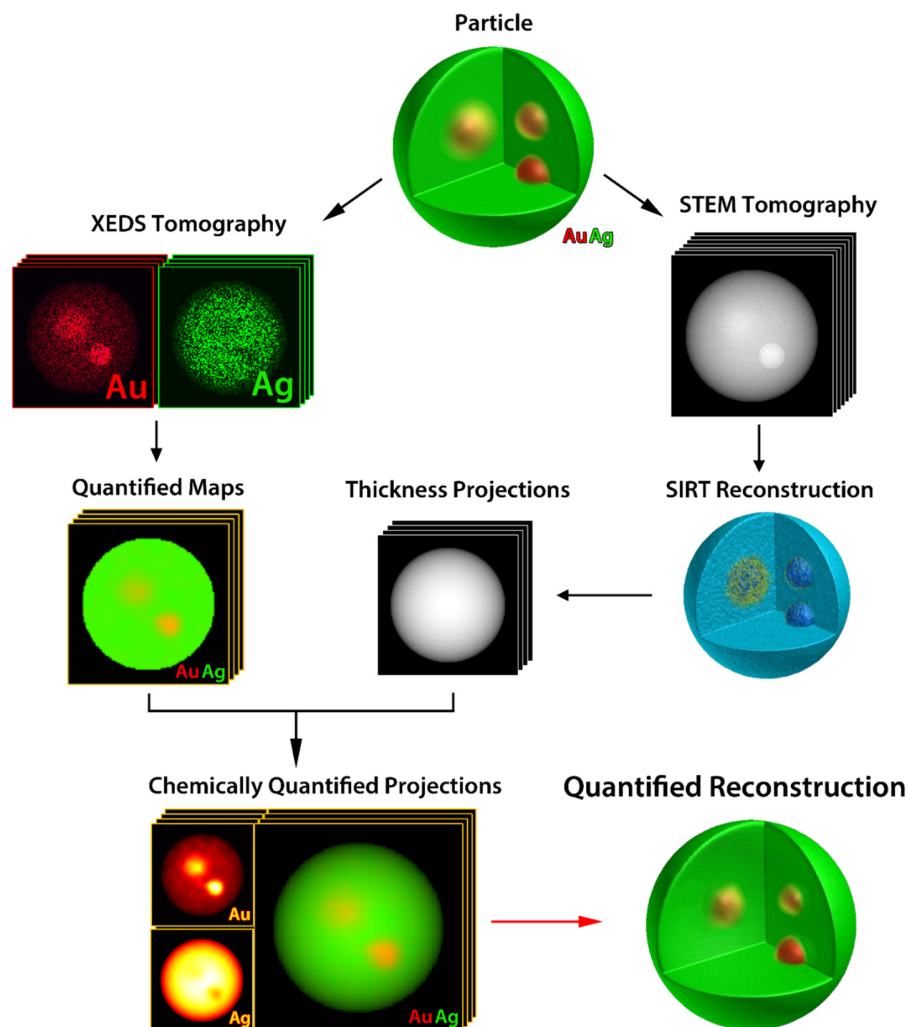


Figure 8.2: The figure schematically shows the principal steps of the technique proposed on a simulated particle of Au and Ag.

HAADF-STEM tomography yields a more accurate description of the particle shape and morphology, which can be used as prior knowledge in the reconstruction of the elemental projections by using the segmented HAADF-STEM reconstruction as a binary mask during the reconstruction. Since it is reasonable to assume that the total composition in each voxel of the reconstruction equals 1, this constraint is also implemented during the final reconstruction. Further details regarding the reconstruction algorithm are discussed in the next section.

8.4 Quantitative characterization of octahedral Au/Ag nanorattle with complex chemical structure

To demonstrate our approach, we performed the 3D characterization of an octahedral Au/Ag nanorattle with a complex chemical structure. The investigated sample was prepared via the well-known galvanic replacement reaction between Au octahedra@Ag core-shell nanocubes (same structure as the one shown in Figure 7.5) and gold (III) chloride, which is often used to obtain porous and hollow metal nanostructures.^[131, 162-165] The synthesis of the nanorattles has been performed by our collaborators, and the details are reported in ref.^[154, 166] Due to the presence of cavities and the possible formation of alloys, understanding the 3D structure of such complex particles is far from straightforward based on 2D TEM images. The chemical transformation during a galvanic replacement reaction was recently investigated by 3D EDXS elemental mapping, but only in a qualitative manner.^[131, 132] We demonstrate here that quantitative investigation of the Ag distribution is possible in these hollow Au/Ag nanostructures.

The tomographic series were acquired using an aberration corrected cubed FEI Titan 60-300 electron microscope operated at 200 kV, equipped with a Super-X detector. HAADF-STEM projections were acquired over a tilt range from -72° to $+75^\circ$ with an increment of 3° . In Figure 8.3a, the HAADF-STEM image acquired at 0° is presented.

EDXS maps were acquired over a tilt range from -70° to $+70^\circ$ with an increment of 10° . The acquisition time for each map equals 3 minutes and a screen current of approximately 250 pA, was applied. The data was binned to a canvas of 52×52 pixels to improve the number of counts per pixel and a two window method^[17] was used to fit the background radiation and extract the Au and Ag net counts from their relative L lines. Quantified ratio maps were obtained by using the ζ -factor method^[136] and ζ -factors obtained as described in previous chapter and ref.^[128]. The ζ -factors values for the L lines of Au and Ag, determined at 200 kV, were respectively: $\zeta_{\text{Au}} = 1177 \pm 93 \text{ kg/m}^2$ and $\zeta_{\text{Ag}} = 492 \pm 46 \text{ kg/m}^2$. In Figure 8.3b and Figure 8.3c, the net counts maps and the ratio maps at 0° are presented.

In order to combine the EDXS and STEM data while preserving details of the morphology and performing the reconstruction on a larger voxel grid, the ratio maps were scaled up to the size of the forward projections (268×268 pixels), using a nearest neighbor interpolation method, which avoids blurring and preserves the original distribution and *look* of the quantified pixels (see Figure 8.5d). The tomographic tilt series were registered through cross-correlation routines implemented in Matlab.^[67] Once aligned, the series were reconstructed using the ASTRA^[38, 107] and SPOT toolboxes.^[41, 108] The reconstruction algorithm was implemented by generating the projection matrix and using a Chambolle-Pock^[167, 168] solver to perform a TVM^[48] reconstruction.

The HAADF-STEM reconstruction was segmented according to its histogram, determining the shape of the particle, and forward projected (with the ASTRA toolbox) along the directions used to acquire the EDXS maps. In this manner the particle thickness relative to the ratio maps was measured. In the case of the EDXS reconstruction, the Chambolle-Pock solver was modified to include a constraining mask, implementing prior-knowledge on the shape of the particle (obtained from the HAADF-STEM reconstruction) and on the concentrations in the final reconstruction (e.g. $C_{Au} + C_{Ag} = 1$ in every voxel).

The total net count values for every angle are presented in Figure 8.4a,b. The total concentrations were calculated for every angle and are presented in Figure 8.4c,d. The net counts values were found to decrease as the tilt angle approached zero, reflecting the position of maximum shadowing from the holder used. At 0° the signal is almost a quarter of the signal that can be collected at $\pm 70^\circ$. As expected, in the absence of absorption effects, shadowing has no impact on the concentrations, which show a consistent value over the whole tilt range (Figure 8.4c,d). The error bars were determined through error propagation as described in the literature.^[17, 128, 136]

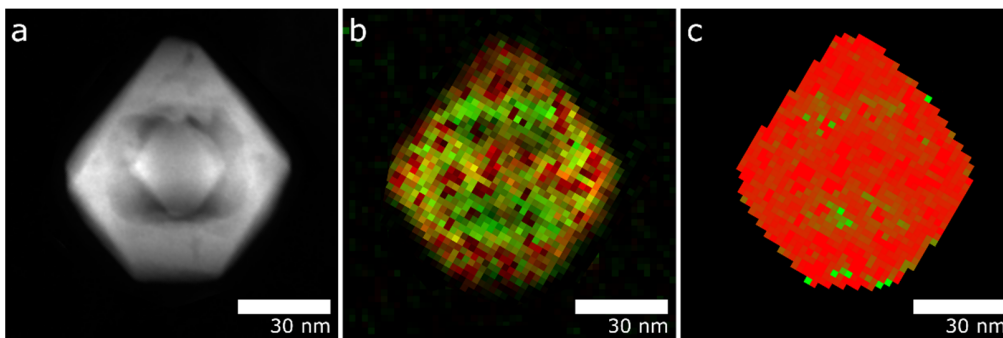


Figure 8.3: (a) HAADF-STEM projection at 0° . (b) EDXS net counts maps for Au (red) and Ag (green) after background subtraction. (c) Ratio map obtained with the ζ -factor method.

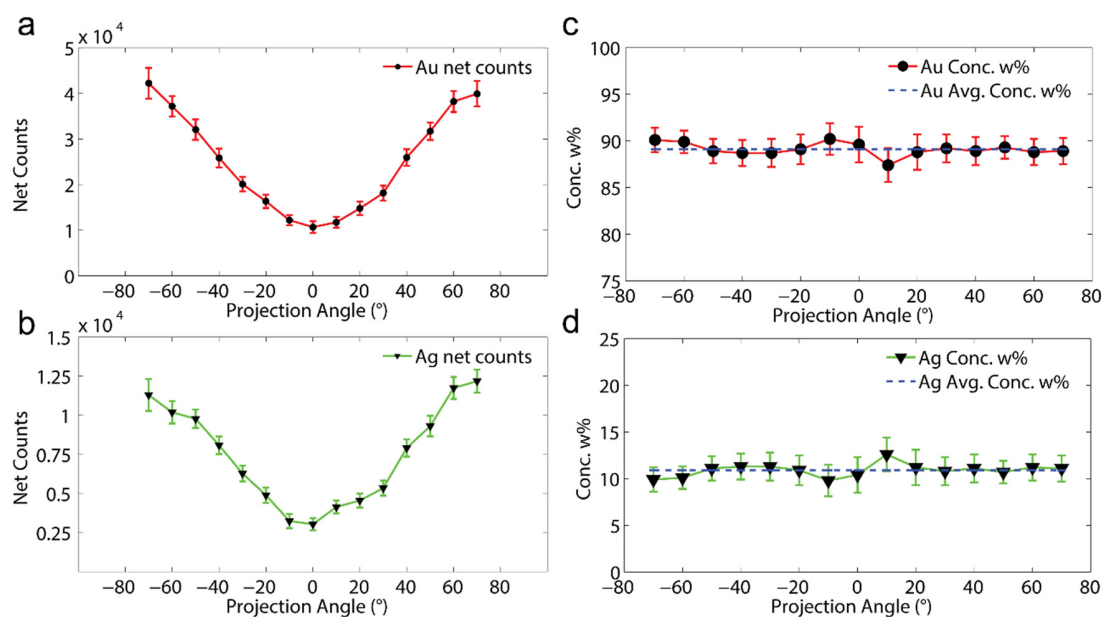


Figure 8.4: (a,b) Au and Ag total net counts for every dataset acquired from -70° to $+70^\circ$. (c,d) Au and Ag concentrations as a function of the acquisition angle, calculated with the ζ -factor method. Single values are consistent with the average value calculated (dashed blue line) as expected in the presence of negligible absorption effects.

A volume rendering of the HAADF-STEM reconstruction is presented in Figure 8.5a and its inner structure is illustrated in Figure 8.5b. Next, thickness maps (Figure 8.5c) were calculated according to the workflow presented above and were multiplied by the ratio maps to obtain elemental projections (Figure 8.5d). Figure 8.6 presents an overview of the original maps based on the net counts and the final projections to be used for 3D reconstruction. From Figure 8.6a,b the effect of shadowing is clear. In Figure 8.6c,d,e (last three rows) finally, the chemically quantified projections obtained with our method are presented, where shadowing effects have clearly been suppressed. These projections were used to calculate the quantified reconstruction using a TVM^[48] algorithm based on a Chambolle-Pock solver derived from the work of Sidkey et al.^[168]

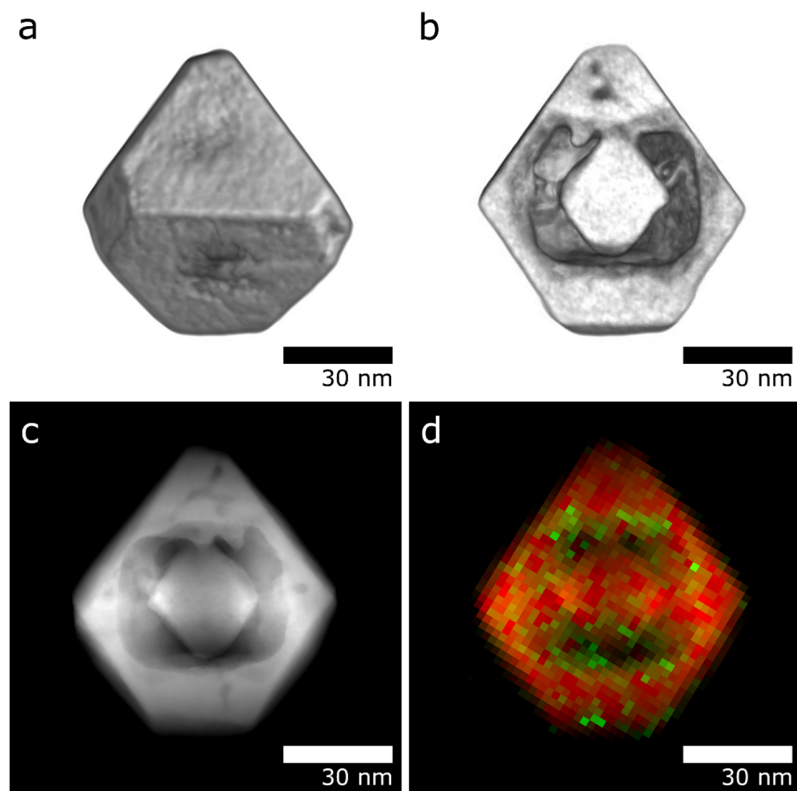


Figure 8.5: (a) Volume rendering of the HAADF-STEM reconstruction. (b) Inner structure of the same reconstruction. (c) Forward projections of the segmented SIRT reconstruction, corresponding to the thickness of the particle expressed in voxel units. (d) Chemically quantified elemental projection obtained by multiplying the EDXS quantified maps of Figure 8.3c and the forward projection of Figure 8.5c.

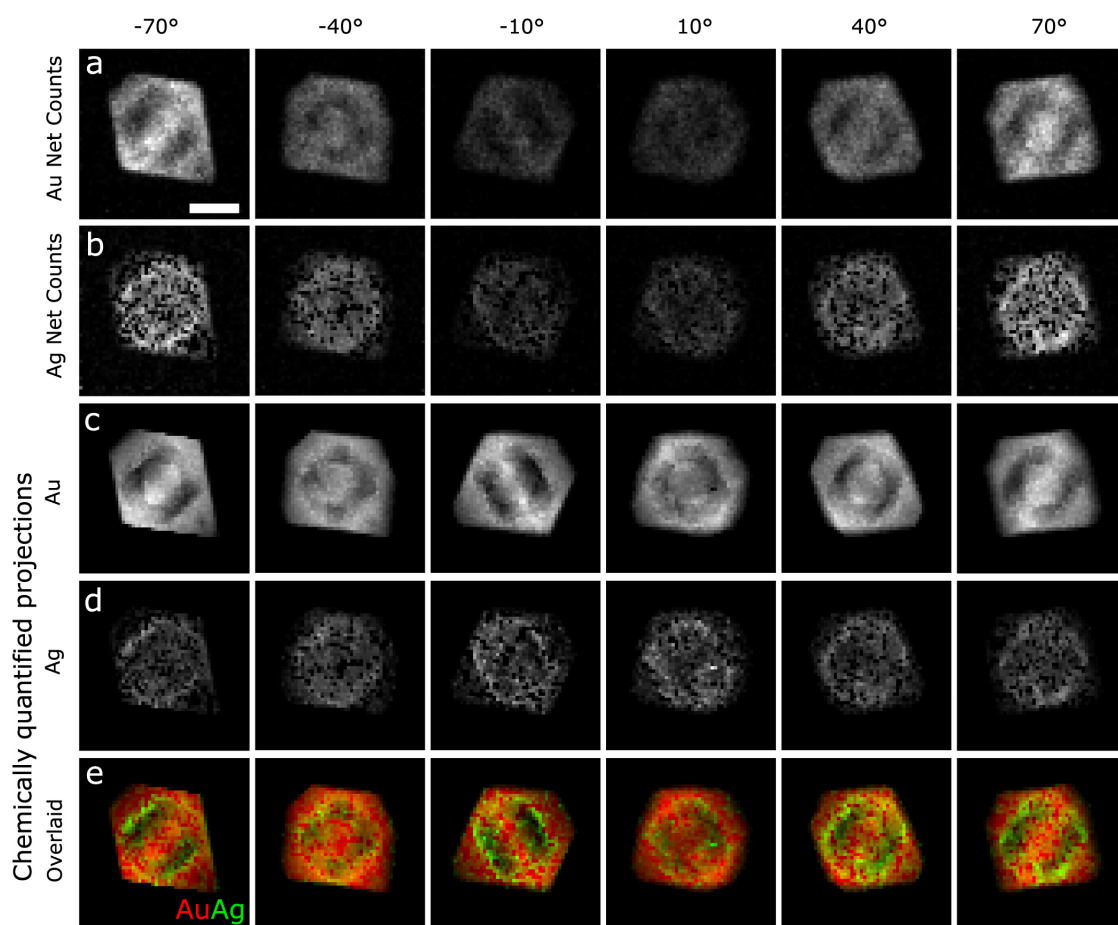


Figure 8.6: (a,b) Au and Ag net counts maps. The decrease of signal in projections close to 0° is due to shadowing effects. (c,d) Au and Ag chemically quantified projections obtained with the method presented in this paper. The signal now scales linearly with thickness and concentration of the elements, satisfying the projection requirement. (e) Au and Ag chemically quantified projections overlaid with different colors. The scale bar in (a) (first tile of the row) is 30 nm. To enable a correct visualization of the images, the intensity range is normalized between the maximum and the minimum value of each row of images.

In Figure 8.7a,b, 3D visualizations of reconstructions showing the outer and inner structure/composition are presented. Slices through the 3D volume and line profiles are shown in Figure 8.7c,d and Figure 8.7e,f respectively. For an EDXS tomographic series, it can be expected that the projection data is heavily affected by noise. Therefore, also the final reconstruction suffers from a relatively low signal-to-noise ratio which hampers the interpretation of the results. Often filtering of the projections^[54, 128, 160] and/or of the final reconstruction is applied.^[133] Here, a three-dimensional gaussian filtering of the final reconstructions was

performed (Figure 8.7c). Our results reveal that pure Ag is no longer present and that the inner walls of the cavity consist of a Au/Ag alloy with a variable Ag concentration ranging from 20% to 50%.

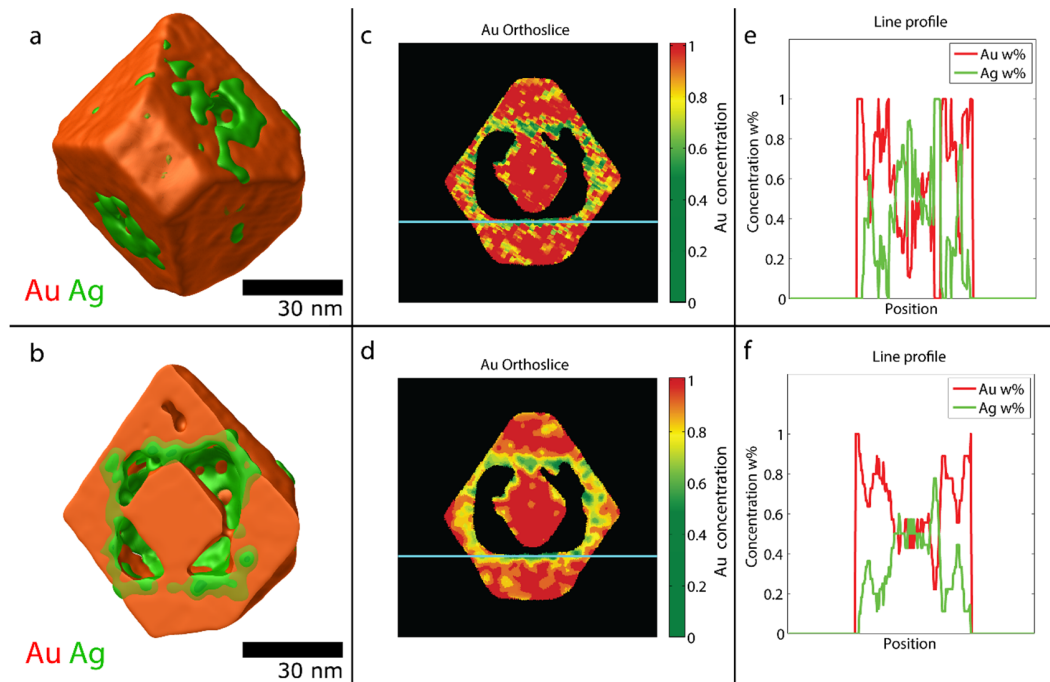


Figure 8.7: (a) Volume rendering of the Au (red) and Ag (green) quantified reconstructions obtained with the presented method. (b) Inner composition of the same reconstructions. (c) Slice through the Au reconstruction showing the concentration in every voxel, through a red-green color-map. (d) Same slice as (c) but after application of a Gaussian filter. In (c,d) pixel values not belonging to the particle are displayed in black. (e) Line profile, showing weight concentration values of the quantified reconstructions. The voxels along which the profile is extracted are indicated by the blue line in (c). (f) Line profile relative to (d). An interactive model and a movie of this reconstruction are available online in the tomography database (links in section 3.2.8).

Since Au and Ag have a large difference in the atomic number Z , it is rather straightforward in this case to qualitatively distinguish them in the 3D HAADF-STEM reconstruction. For comparison, Figure 8.8 therefore presents a slice through the chemically quantified reconstruction (Figure 8.8a) and the corresponding slice through the HAADF-STEM reconstruction (Figure 8.8b). It can be seen that an

excellent correspondence between both approaches is found. These results confirm the validity of our approach. Moreover, the technique that we propose here can also be applied for nanostructures in which elements with a small difference in Z are present, as in the case of the complex AuAgPt nanorattle shown in section 9.2.

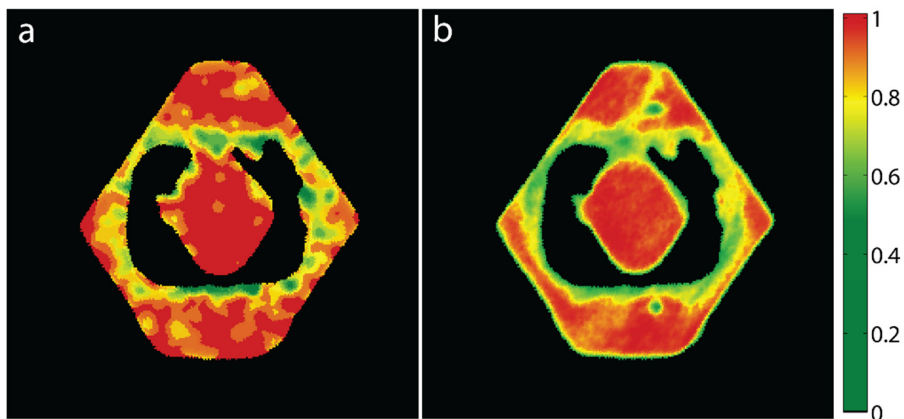


Figure 8.8: (a) EDXS 3D quantified reconstruction, after filtering with a 3D Gaussian filter to enable an easier interpretation, the color bar on the right reflects the concentration values of Au (b) Slice from the HAADF-STEM 3D reconstruction, arbitrarily scaled to match the values range of the EDXS reconstruction and enable the comparison of the elements distribution.

The Ag distribution, (green in Figure 8.8a, $\sim 50\%$ w% Ag), accurately matches the distribution of lighter values in the HAADF-STEM reconstruction slice, given by a lower Z -contrast in that area (in this case the values are scaled to arbitrary units), therefore confirming the presence of silver and quantifying its content.

It is worth stressing, that although HAADF-STEM provides qualitative information on the presence of Ag through Z -contrast, it is not possible to tell whether that Ag is pure or alloyed with Au based on the contrast. The ability to obtain such information is a clear demonstration of the power of the method presented, which allows to understand how the elements are actually distributed inside the structure. Further information on the growth mechanism of these Au/Ag nanorattles is presented in the next chapter, where we will discuss a series of materials science cases in which the technique has been applied to enable a quantitative chemical 3D characterization.

8.5 Error estimation

Unfortunately, classical error determination for the quantification in 3D is far from straightforward. It is not possible to propagate errors classically in 3D, as it is done for the 2D quantifications, since the

reconstruction is obtained from applying a complex iterative mathematical algorithm. This is a well-known problem in the field. Therefore, we here start from forward projecting the quantified reconstructions, to simulate an equivalent of the experimentally acquired 2D EDXS maps. By comparing these simulated maps, obtained from the reconstructions, with the experimental maps, we can measure what is the average error per pixel. This number tells us how accurate the reconstructions are, compared to the original data.

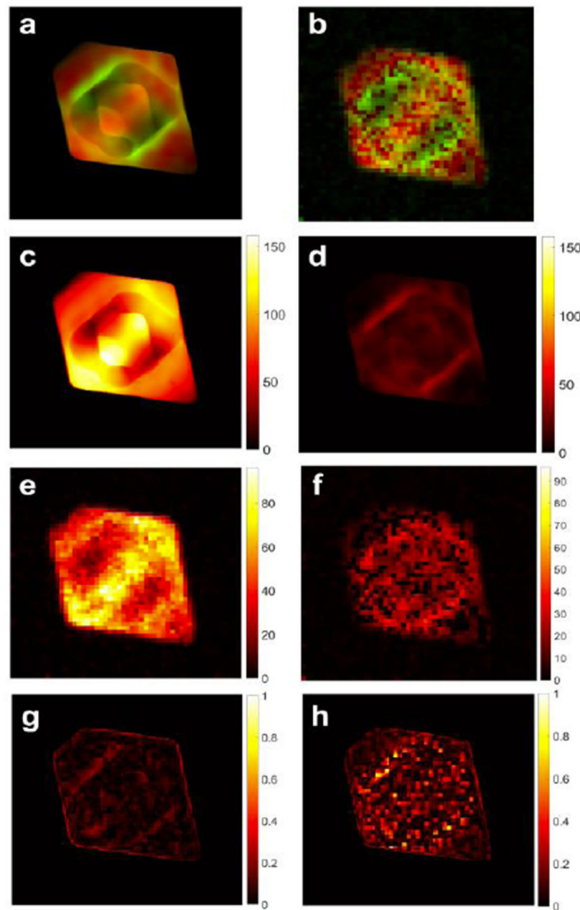


Figure 8.9: (a) Forward projections of the Au (red) and Ag (green) reconstructions, for particle of Figure 8.3 along the direction -70° . (b) 2D EDXS net counts maps for Au (red) and Ag (green) for the same particle in the same direction. (c,d) Au and Ag forward projections in a *temperature* color map, normalized on the total content of Au and Ag, respectively. (e,f) Au and Ag 2D EDXS maps in a *temperature* color map, normalized on the total content of Au and Ag, respectively. (g,h) Relative error maps obtained by calculating the root of the squared difference between figures (c,d) and (e,f), and dividing them (pixel-wise) by the forward projections.

From Figure 8.9g,h, it is possible to observe an example of error maps obtained by comparing the simulated forward projections of the reconstructions, and the experimental data. In order to be able to compare the

two, the maps are scaled on the total content of Au and Ag on every tilt angle, because otherwise shadowing effects on the original 2D EDXS maps would make the comparison meaningless. As it can be seen, the main errors for Au, occurs on pixels describing particles interfaces, where the low spatial resolution of EDXS is expected to introduce the bigger uncertainty on the transition from one element to the other, or from the particle to vacuum. For Ag on the other hand we can see that, the lower signal, due to the lower content of Ag for this particle, cause more noise and therefore a higher and random presence of errors (Figure 8.9h).

The standard deviation of the values in the error map is calculated, giving an estimation of the spreading of the values around this average. Here, the average pixel error is 6.1% for Au, with a standard deviation of 4.9%, meaning that the majority of the errors oscillates approximately between 0 and 11%. For Ag on the other hand, we have an average pixel error of 10.4%, with a standard deviation of 10.3%, meaning that the majority of the errors oscillates approximately between 0 and 21%. This higher uncertainty is associated with the higher noise of the Ag signal.

9 Quantitative 3D EDXS Tomography, Materials Science Studies

In this chapter the technique developed and presented in chapter 8 will be applied to a range of materials in order to characterize the composition of complex nanostructures. The information obtained is essential in understanding the structure and elemental distribution, allowing insights on the synthesis mechanisms beyond their formation.

9.1 Au@Ag nanorattles obtained by galvanic replacement

This section is based on the work published in the journal article of ref. ^[166]: “Galvanic replacement coupled to seeded growth as a route for shape-controlled synthesis of plasmonic nanorattles”, L. Polavarapu, D. Zanaga, T. Altantzis, S. Rodal-Cedeira, I. Pastoriza-Santos, J. Pérez-Juste, S. Bals, L. M. Liz-Marzán, *Journal of the American Chemical Society* 2016, 138, 11453.

In collaboration with the Bionanoplasmonics Laboratory from CIC biomaGUNE and the Departamento de Química Física from the Universidade de Vigo, in San Sebastian and Vigo respectively, we studied the formation mechanisms of nanorattles obtained via galvanic replacement.^[166] As already explained in the previous chapter, this type of reaction leads to complex hollow structures with intermixing of different chemical elements. The interesting aspect of this process is the possibility of tuning optical and catalytic properties by controlling the pores size and chemical composition.^[55, 160, 162, 163, 169-172] Nanorattles of Au@Ag show improved properties over their bulk counterparts, as plasmonic activity for surface enhanced Raman scattering (SERS), refractive index sensitivity and catalytic activity.^[173, 174]

In a previous study by our group,^[55] it was demonstrated an unconventional transformation of Ag nanocubes in Au@Ag hollow nanocages with complex metal distribution, when the reaction was carried out in a chlorinated organic solvent. In this case, a different final product is obtained when the galvanic reaction is performed with H₂AuCl₄ in the presence of a mild reducing agent.

9.1.1 HAADF-STEM and 2D EDXS analysis

To understand the mechanism behind the final products formation and the influence of H₂AuCl₄, different reactions are conducted starting from the same initial nanostructure, a gold rod encased in a rectangular silver cuboid. The starting structure is obtained by using single crystalline Au rods as seeds for epitaxial

growth of Ag. The synthesis of these structures was carried out by our collaborators and more details are available in ref.^[166].

Figure 9.1 shows TEM overview images of the synthesized products. The Au@Ag cuboids (Figure 9.1a) are then reacted, in a typical galvanic replacement setup, with HAuCl₄ in the presence of ascorbic acid. Different reactions are conducted with increasing concentrations (0.05, 0.1, 1, 4, 7 ml) of 0.5 mM HAuCl₄ aqueous solution added to a mixture of 5 mL of Au@Ag core-shell nanorods and 0.2 ml of 0.1 M ascorbic acids. In the first reaction, after initiation of the galvanic reaction with a small amount of HAuCl₄ (0.05 ml, 0.5 mM), the surface of the particles appears irregular due to the initial oxidation of Ag atoms (Figure 9.1b and Figure 9.2a). Upon further addition of HAuCl₄ (0.1 ml), we can observe a Au layer deposited on the outer Ag surface, with voids forming inside or around the structure (Figure 9.1c, Figure 9.2b), as expected in galvanic replacement. When more HAuCl₄ is added (1, 4, 7 ml for particles shown in Figure 9.1d,e,f and Figure 9.2c,d,e respectively), further deposition of Au on the external nanoparticle surface is clearly shown by the EDXS maps, resulting in what appears to be hollow octahedrons containing the initial gold rods. This is an example of unconventional morphological changes, however, it is not possible to understand the morphological or chemical architectures of the intermediate and final nanocrystals merely through 2D TEM/EDXS characterization as it does not provide sufficient information for these complex cases.

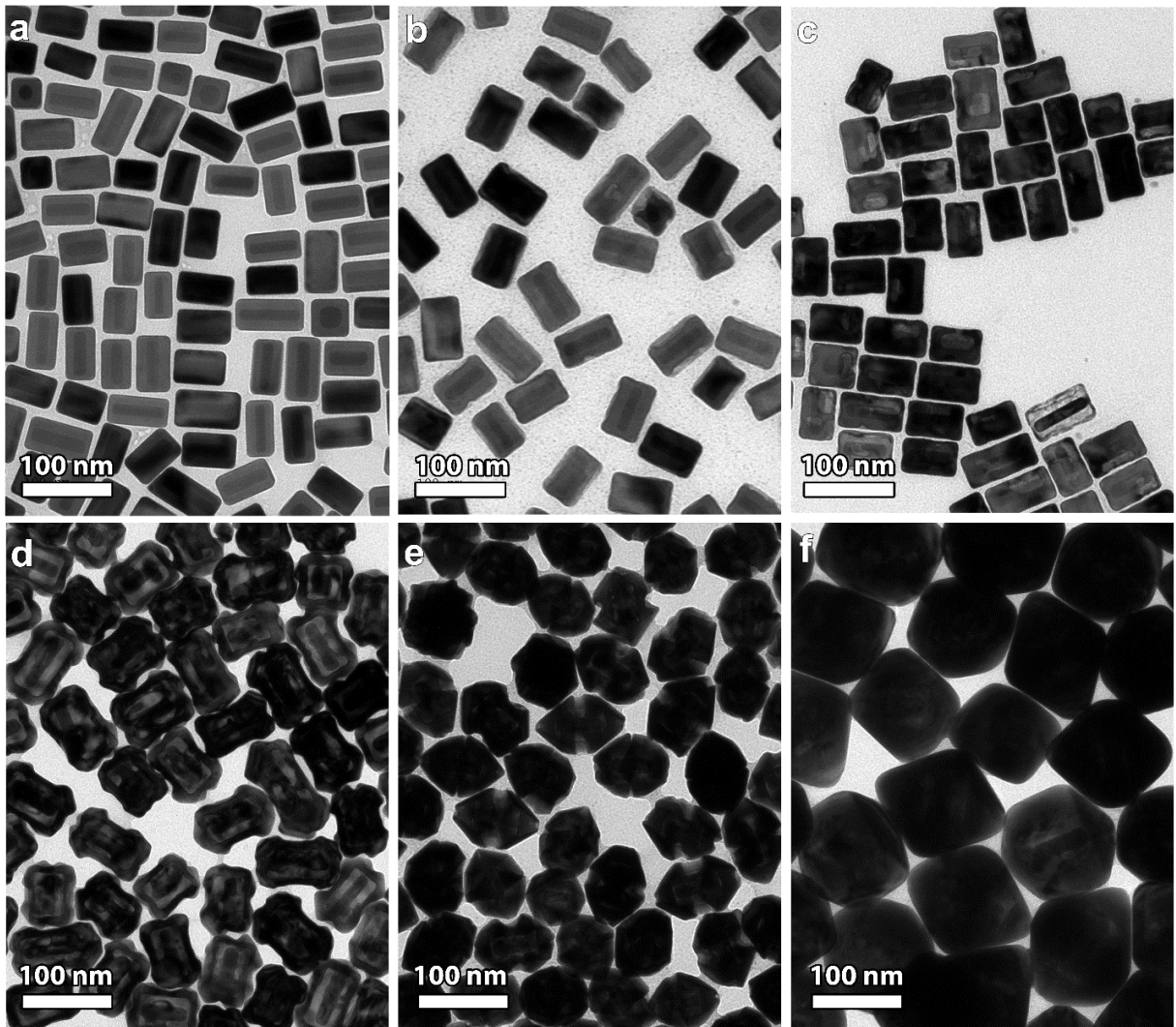


Figure 9.1: TEM overview images of Au@Ag core-shell nanorod structures before (a) and after (b-f) galvanic replacement with increasing amounts of 0.5 mM HAuCl₄.

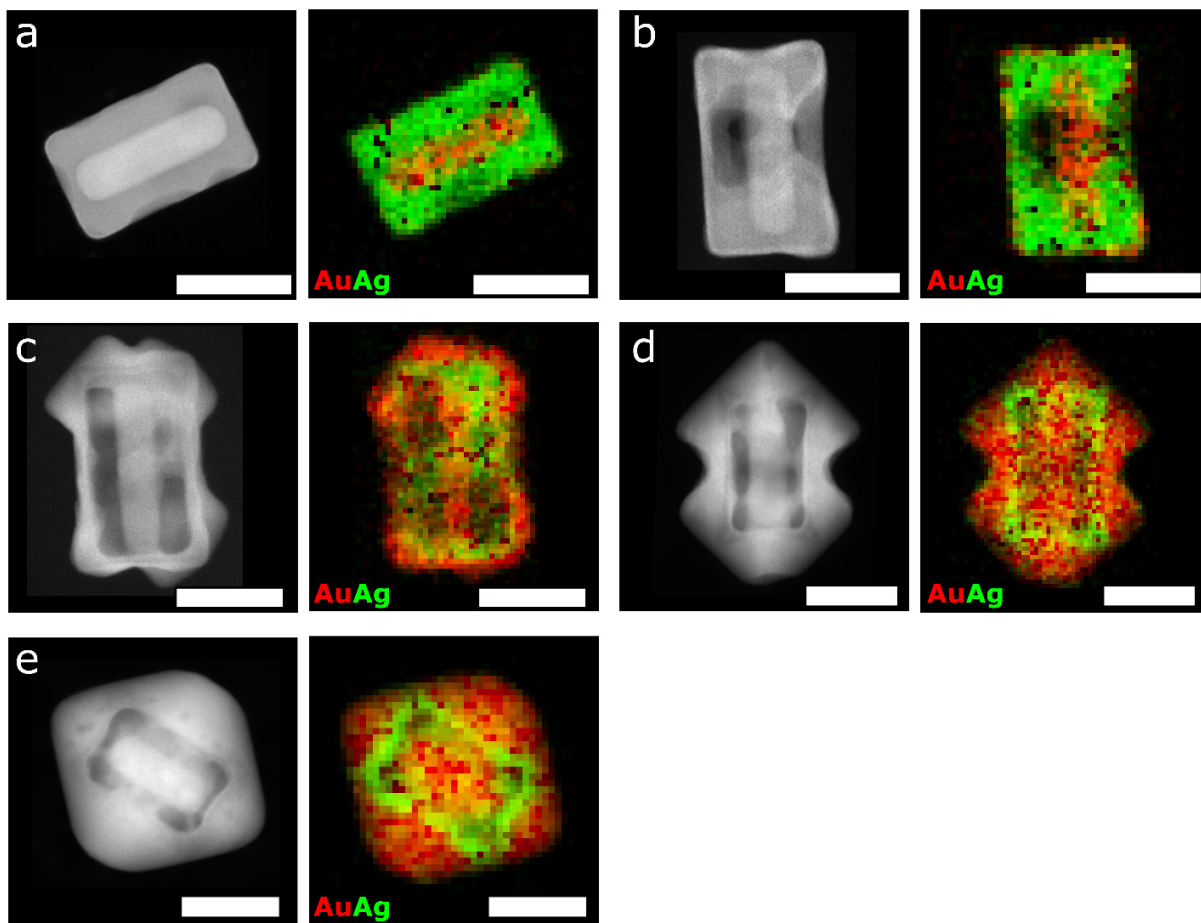


Figure 9.2: Higher magnification HAADF-STEM and EDXS maps of the nanorattles obtained by galvanic replacement with increasing amounts of 0.5 mM HAuCl₄. (a-e) correspond to Figure 9.1b-f. Scale bars are 40 nm.

9.1.2 3D quantitative EDXS tomography analysis

Unambiguous determination of the mechanism behind these nanoscale transformations can be achieved by carrying out electron tomography combined with EDXS in 3D. Tilt series of HAADF-STEM images and EDXS maps (Figure 9.2) were acquired and combined in a synergistic manner according to the approach described in the previous chapter. For each sample, TEM grids were prepared by drop casting a drop of sample solution on carbon coated copper grids. The observations were performed using an aberration-corrected cubed FEI-Titan 60-300 electron microscope operated at 200 kV. The HAADF-STEM tomography series were acquired over a tilt range from -72° to $+72^\circ$ and an increment of 3° using a Fischione model 2020 single tilt holder. The alignment of the series was performed using cross-correlation^[67] routines implemented in Matlab. The SIRT algorithm,^[35] as implemented in the ASTRA

toolbox,^[38, 40] was used to obtain the HAADF-STEM reconstructions. EDXS maps were acquired using the same instrument, equipped with a ChemiSTEM system.^[61] The elemental maps were acquired manually every 10 degrees, using a tilt range from -70° to $+70^\circ$ and a current of approximately 250 pA. For every map, 3 minutes of acquisition were used. Data was processed in Matlab, a two windows method^[17] was used to subtract the background radiation and obtain the net counts. Quantification was then performed using the ζ -factor method,^[136] with experimentally determined ζ -factors, according to the procedure defined in section 7.4.^[128] The ζ -factors values for the L lines of Au and Ag, at 200 kV, were respectively, $\zeta_{\text{Au}} = 1177 \pm 93 \text{ kg/m}^2$ and $\zeta_{\text{Ag}} = 492 \pm 46 \text{ kg/m}^2$.

The results of the analysis are summarized in Figure 9.3. The 3D reconstruction images in Figure 9.3 (i, ii, iii, iv, v) correspond to the 2D images of Figure 9.2 (a,b,c,d,e respectively). From the 3D reconstructions it appears that, in the first reactions (Figure 9.3a,b-i) the Ag shell is eroded due to the start of the galvanic replacement reaction, with formation of grooves on the Ag surface and deposition of small amounts of Au on the edges and corners of the rectangular cuboid. The higher density of Au on the corners as compared to the edges provides experimental evidence for higher reactivity of sharper sites, which agrees with previous reports on the difference in reactivity of truncated and sharp Ag nanocrystals reported by Lu et al.^[175] and the seed-mediated palladium deposition on edges of Au nanocrystals reported by DeSantis et al.^[176].

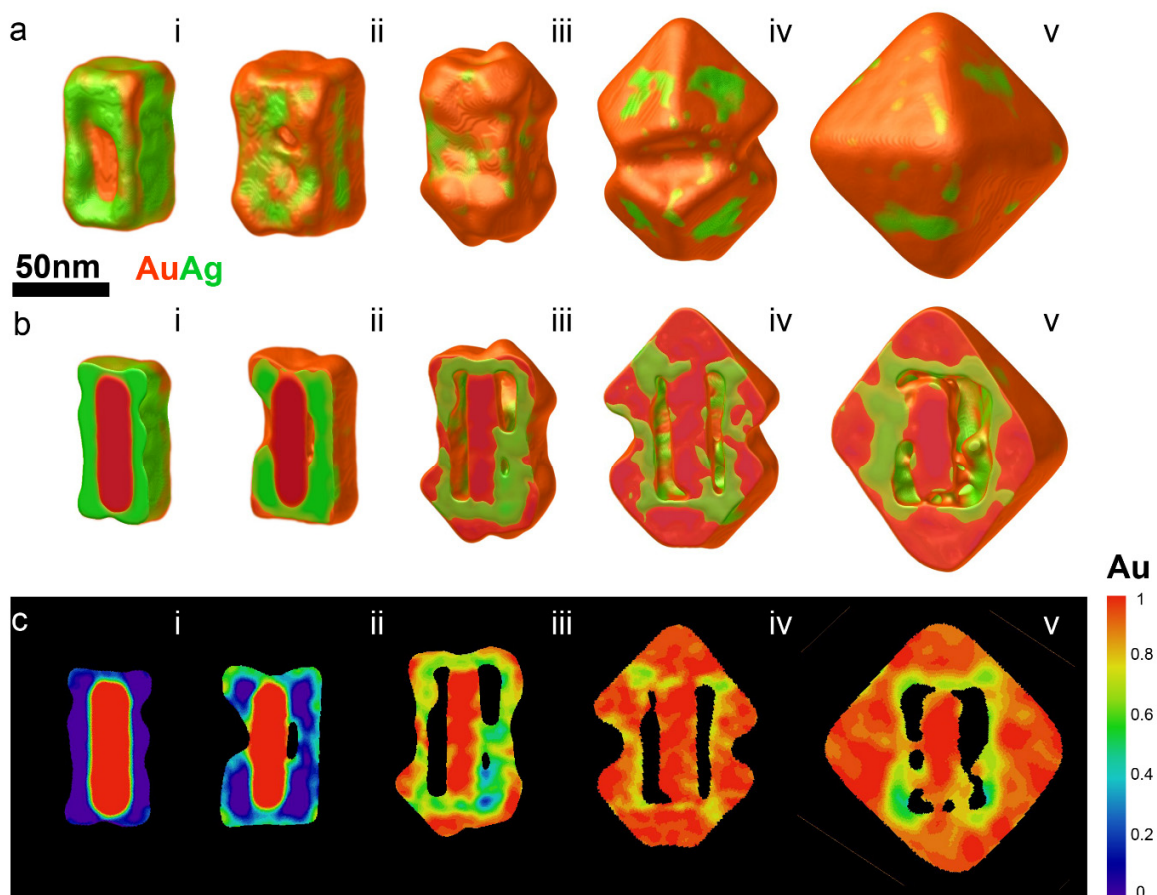


Figure 9.3: Quantitative EDXS tomography imaging. Transformation of Au@Ag nanorods into octahedral nanorattles with addition of increasing amounts of HAuCl_4 in consecutive reactions (stages i-v). (a) 3D reconstructions showing Au (red) and Ag (green) at each transformation. (b) Inner view of the 3D reconstructions. (c) EDXS 3D quantified reconstruction slices, where the color scale on the right reflects the percentage of Au. An interactive model and movies of these reconstruction are available online in the tomography database (links in section 3.2.8).

As the reaction proceeds (0.1 ml of HAuCl_4) (Figure 9.3a,b-ii), a thin layer of Au is deposited on the surface of the cuboid with holes on the facets. These results provide the experimental evidence for the reactivity of corners > edges > facets of a cuboid. Even though it is extremely difficult to identify the deposition of a thin Au shell either on edges or on facets based on 2D EDXS mapping alone, 3D EDXS tomography enabled an accurate visualization of the chemical architecture of the particles. Tomography data shows the formation of holes on the surface, through which the oxidized Ag^+ ions leach out, in a similar fashion to what already observed for other galvanic replacement reactions studies.^[55] With increasing the amount of HAuCl_4 , the hollow area extends with formation of an Au/Ag shell surrounded by a solid layer of Au, where

[1 1 1] facets start to grow (Figure 9.3a,b-iii). High-resolution STEM images further confirm the epitaxial relation between Au and Ag at the corners (Figure 9.4a,b).

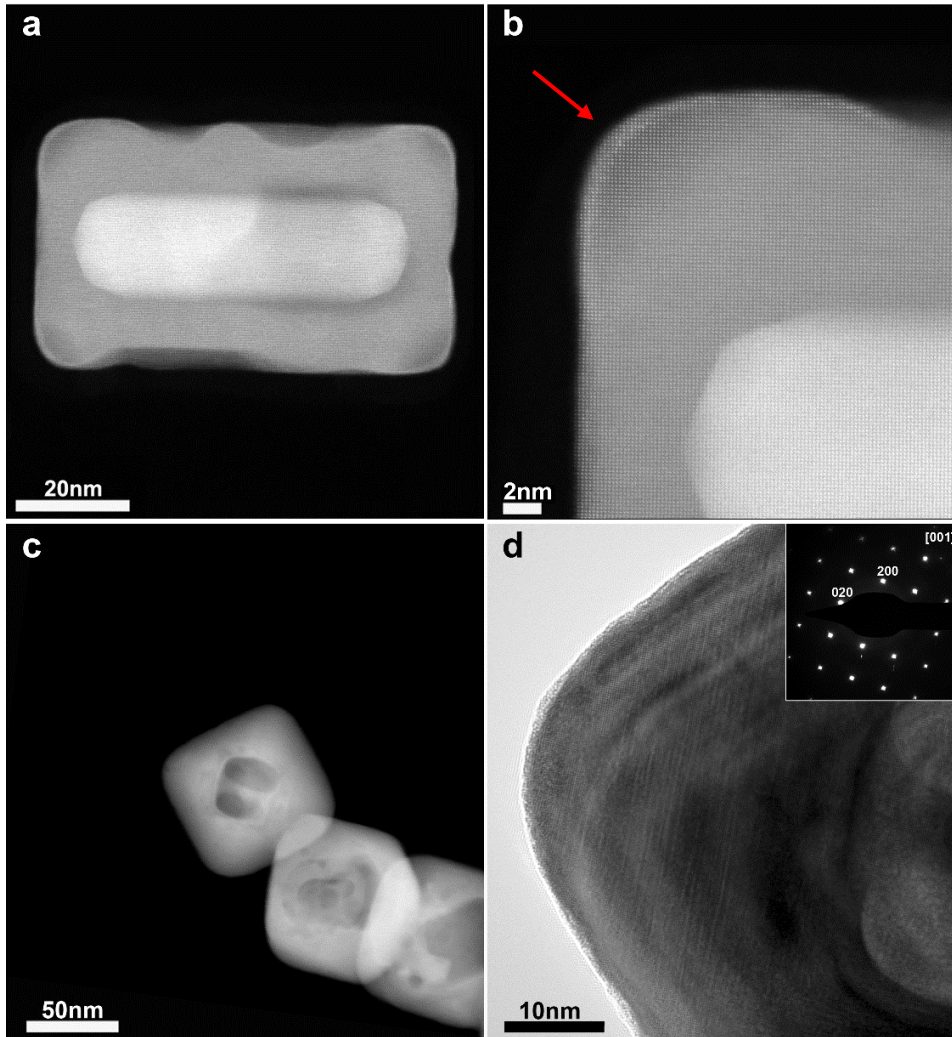


Figure 9.4: (a,b) High resolution STEM images of the particles at the initial stages of the galvanic replacement reaction. High density of Au deposition on particle corners (indicated by red arrow) is seen, which is a direct experimental evidence for higher reactivity of corners. (c) STEM image of an octahedral nanorattles in the last stage. (d) High resolution TEM image and respective selected area electron diffraction (SAED) pattern of final octahedral nanorattles, showing that the crystallinity is preserved throughout the reaction.

The growth of [1 1 1] facets leads to the formation of octahedral nanorattles, encasing an Au rod and showing a complex chemical distribution. High resolution TEM image (Figure 9.4d) and diffraction pattern (Figure 9.4d-inset) of the octahedra shows that these nanorattles retain a monocrystalline structure, and further confirm the orientation of facets. The total elements concentrations are also shown in Table 9.1, as expected, we see a decrease of Ag and an increase of Au concentrations with increasing addition of H₂AuCl₄.

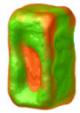
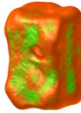
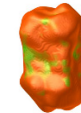
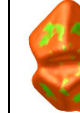

Particle					
Stage	i	ii	iii	iv	v
Au w%	33	44.8	78.2	90.8	88.3
Ag w%	67	55.2	21.8	9.2	11.2
Error ±	2.7	3	2.8	1	1.2

Table 9.1: Total Au and Ag concentrations for the nanorattles of Figure 9.3i-v.

At stage iii, as the galvanic replacement reaction proceeds, we observe the formation of a hollow Au/Ag alloy shell, with a composition of approximately 60:40 (Figure 9.3c-iii). Further addition of H₂AuCl₄ decreases the overall silver content as a consequence of Au overgrowth, but interestingly, EDXS tomography reveals that the inner Au/Ag alloy shell formed in stage iii retains the 60:40 Au/Ag composition (Figure 9.3c-v) and serves as a basis for the overgrowth of pure Au. Transmetalation of Au/Ag alloy nanocages generally leads to fragmentation,^[175] however, in the present system, seeded growth takes place on the outer Au/Ag shell, which is likely related to H₂AuCl₄ reduction by ascorbic acid, in a manner similar to the widely used seeded growth of Au nanoparticles.^[177, 178] Thus, 3D EDXS tomography unambiguously revealed the chemical architecture of the resulting nanorattles. This unusual transformation of the morphology and chemical architecture can also be observed when starting with nanoparticles with different morphology, such as Au@Ag core-shell nanocrystals (Au nanooctahedra@Ag nanocubes, an example of this initial structure is shown in Figure 7.5 and Figure 7.6, while the final product after the galvanic reaction is shown in Figure 8.7), indicating the versatility of this approach. In a conventional nanoscale galvanic replacement reaction on Au@Ag core-shell nanocrystals, we would expect to obtain cubic nanorattles.^[55] In this case, however, we find again that the resulting structures display an octahedral shape (Figure 8.7).

EDXS tomography analysis revealed that the final product is analogous in its complex chemical structure to the samples obtained when starting from Au@Ag nanorods, with the only difference being the octahedral cores in the center. This also includes the composition of the Au/Ag alloy inner shell (60:40; see Figure 8.7).

9.1.3 Galvanic replacement reaction mechanism in the presence of ascorbic acid.

The observations obtained through quantitative 3D EDXS tomography allows to generalize our conclusions regarding the effect of ascorbic acid on the galvanic replacement reaction on Ag@Au core-shell nanoparticles. Two important effects arise from the presence of ascorbic acid, which should be considered: i) the reduction of Au^{3+} into Au^+ by ascorbic acid significantly decreases the rate of galvanic replacement because only one Ag atom is involved, rather than three (in the absence of ascorbic acid),^[179, 180] which allows better control over the reaction progress; and ii) the mild reducing nature of ascorbic acid can also lead to the catalytic reduction of Au^+ into Au^0 on the metal nanoparticles surface (seeded growth).^[181] The quantitative EDXS tomography study suggests that galvanic replacement on Ag shells dominates during the early stages, whereas Au overgrowth on the outer Au/Ag shell hinders transmetalation on the alloy, in the presence of ascorbic acid.^[182, 183] We hypothesize that the reduction of Au^{3+} to Au^+ by ascorbic acid plays an essential role by changing the kinetics and stoichiometry of the galvanic replacement reaction. This may also influence the different chemical architecture of the resulting octahedral nanorattles, which is radically different to what has been previously reported for galvanic replacement in Ag nanocrystals, both at room temperature and at 100 °C.^[55, 170, 175]

In summary, quantitative EDXS tomography enabled the understanding of an unconventional morphological transformation of Au@Ag core-shell nanoparticles (either nanorods or nanocrystals) into octahedral nanorattles via galvanic replacement reaction coupled with co-reduction by ascorbic acid. The analysis revealed that galvanic replacement dominates in the case of a pure Ag shell, while seeded growth suppresses transmetalation of Au/Ag (~60:40) shell at later stages, eventually leading to an octahedral morphology with complex elemental distribution. This suggests that the shape of the hollow nanoparticles can be controlled beyond their template morphology in the presence of reducing agents, thus enabling additional tunability of their optical properties.

9.2 Quantitative EDXS tomography of a AuAgPt nanorattle

In the previous paragraph we demonstrated how the technique introduced in chapter 8 can be applied to resolve the complex structure of Au@Ag nanorattles, enabling an understanding of the formation

mechanism. In chapter 8 we were able to validate the approach by comparing a slice from the EDXS and HAADF-STEM reconstructions, thanks to the different contrast generated in HAADF-STEM by the different Z-number of Au and Ag. Here we will characterize a structure, similar to those presented in the previous paragraph, but this time obtained through a galvanic replacement reaction with Pt instead of Au. The final product is therefore expected to contain Au⁷⁹, Ag⁴⁷ and Pt⁷⁸. The similar Z-number for Pt and Au, hampers any qualitative evaluation of chemical distribution by means of HAADF-STEM tomography, making EDXS quantitative tomography the only technique able to yield nanoscale chemical information for these kind of structures. Figure 9.5 shows HAADF-STEM projections of the AuAgPt particle from different angles, along with the respective EDXS net counts maps. From the analysis of Figure 9.5d it appears that a layer of Pt is covers the outer surface of the particle.

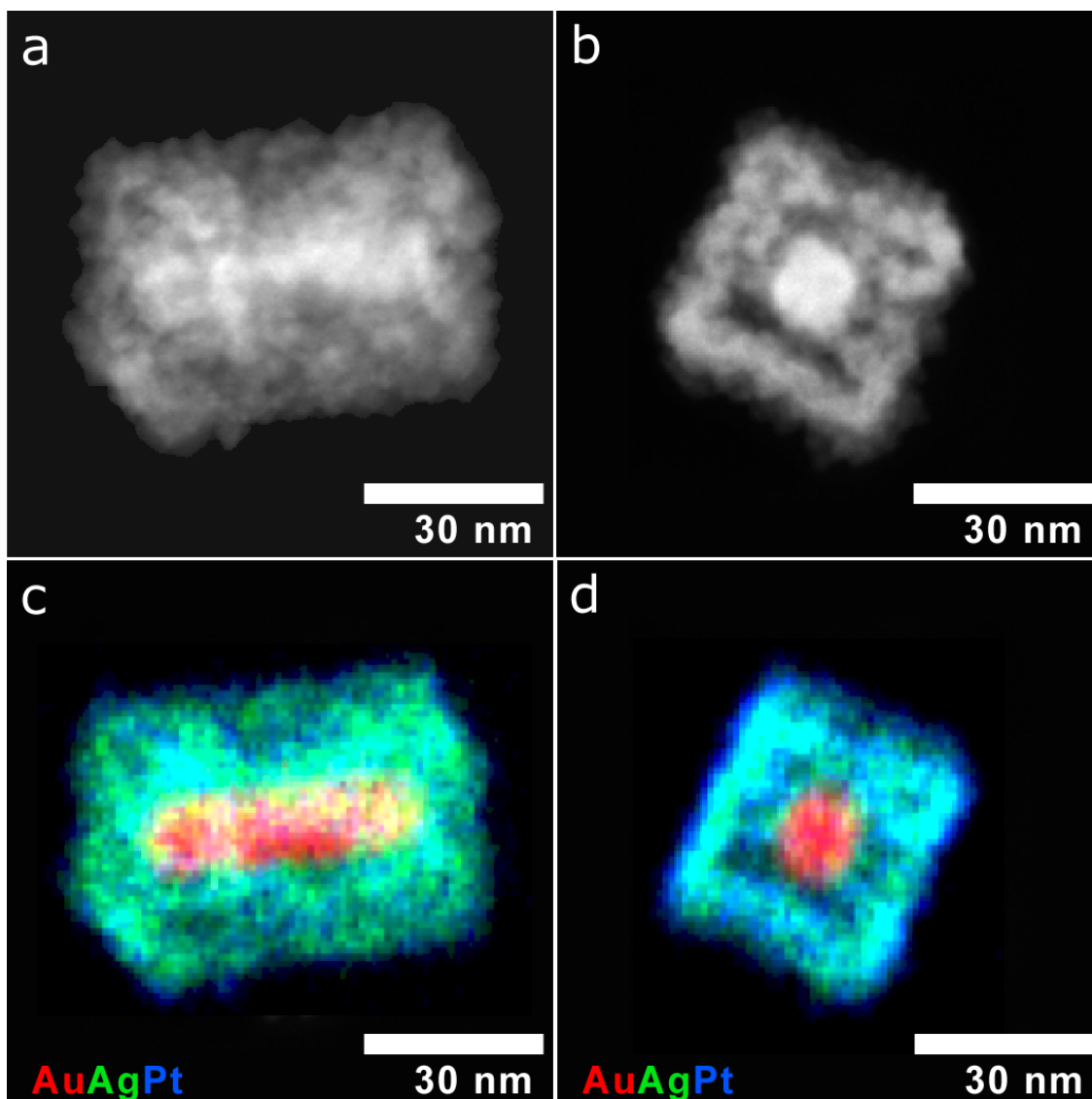


Figure 9.5: (a,b) HAADF-STEM projections of the structure from two different angles, top (b) and side (a) view. c,d) EDXS net counts maps along the same directions.

The TEM grid was prepared by drop casting a drop of sample solution on carbon coated copper grids. The observations (HAADF-STEM) were performed using an FEI Osiris operated at 120 kV. The HAADF-STEM tomography series was acquired over a tilt range from -65° to $+72^\circ$ and an increment of 3° using a Fischione model 2020 single tilt holder. The alignment of the series was performed using cross-correlation^[67] routines implemented in Matlab. The SIRT algorithm,^[35] as implemented in the ASTRA toolbox,^[38, 40] was used to obtain the HAADF-STEM reconstructions. EDXS maps were acquired using the same instrument, equipped with a ChemiSTEM system.^[61] The elemental maps were acquired manually every 10 degrees, using a tilt range from -70° to $+70^\circ$ and a current of approximately 150 pA. For every

map, 9 minutes of acquisition were used. Data was processed in Matlab, a two windows method^[17] was used to subtract the background radiation and obtain the net counts. Quantification was then performed using the ζ -factor method,^[136] with experimentally determined ζ -factors, according to the procedure defined in section 7.4.^[128] The SIRT reconstruction (Figure 9.6a,b,c), has been segmented, forward projected and combined with the quantified EDXS maps to obtain a quantitative EDXS 3D reconstruction (Figure 9.6d,e,f).

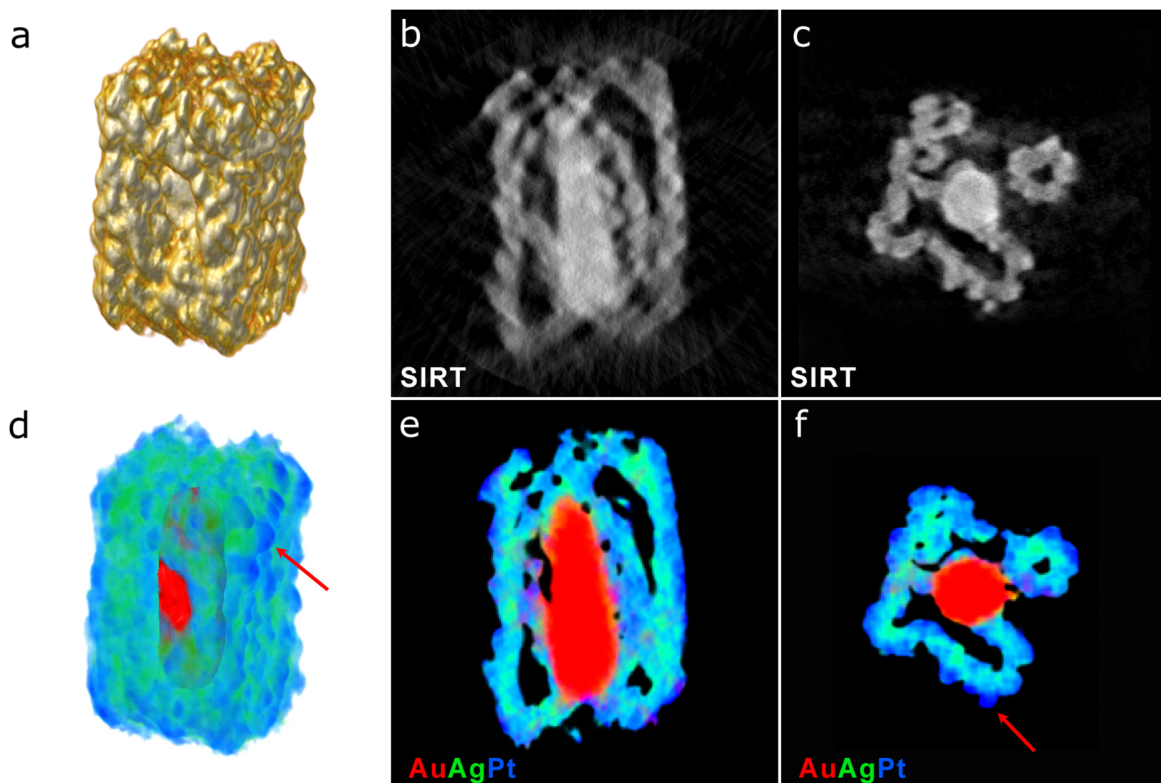


Figure 9.6: (a) HAAD-STEM tomography reconstruction (SIRT) rendering. (b,c) slices from the SIRT reconstruction. (d) Quantitative EDXS reconstruction rendering. (e,f) slices from the EDXS reconstruction. The arrows in (d,f) indicates different pure Pt protrusions on the surface, which in 2D projections (Figure 9.5d) convey the illusion of a pure Pt shell.

From the SIRT slices (Figure 9.6b,c) we can observe a small contrast difference between the central rod and the cage, but almost no contrast inside the cage walls. This lack of contrast can be explained through the interpretation of the EDXS reconstruction slices. In Figure 9.6e,f we see that the structure is not covered by an homogeneous Pt layer, as it could seem from the 2D EDXS maps only (Figure 9.5d), but instead pure Pt protrusions (examples highlighted by the red arrows in Figure 9.6d and Figure 9.6f), are over-grown on

the cage walls, which show an approximately average concentration of 50% Ag and 50% Pt. These concentrations and the inhomogeneous distribution of elements, explains the lack of contrast in the HAADF-STEM slices (Figure 9.6b,c). This example illustrates the importance of 3D EDXS against mere 2D EDXS analysis, which can often lead to wrong interpretation of projected data.

9.3 Quantitative determination of the residual silver in nanoporous gold catalyst

This section is based on the work published in the journal article of ref. ^[184]: “Quantitative determination of residual silver distribution in nanoporous gold and its influence on structure and catalytic performance”, C. Mahr, P. Kundu, A. Lackmann, D. Zanaga, K. Thiel, M. Schowalter, M. Schwan, S. Bals, A. Wittstock, A. Rosenauer, *Journal of Catalysis* 2017, 352, 52.

In collaboration with the Institute of Solid State Physics, the MAPEX Center for Materials and Processes and the Institute of Applied and Physical Chemistry from the University of Bremen, we studied the chemical distribution of Ag and Au in a nanoporous gold catalyst.^[184] Nanoporous gold (npAu) has attracted increasing interest over the last years because of its high catalytic activity.^[185-191] Furthermore, gold as a catalyst is particularly interesting because of its non-toxicity, chemical stability and its ability to promote chemical reactions at low temperatures.^[190] Nanoporous gold is usually obtained from a master alloy through a corrosion (free or electrochemical) in acid, during which the less noble metal (e.g. silver) is dissolved leaving behind a foam like structure, built up of ligaments and pores with high specific surface area (around 10 m²/g). This type of morphology is advantageous for a catalyst since it is penetrable by gases and liquids.^[192, 193] As a result of the synthesis process, small fractions of less than 1 at.% residual silver always remain in the npAu. It has been shown that the presence of silver in gold catalysts has a strong influence in the catalytic activity of Au,^[188, 190] therefore an accurate determination of the content and distribution of Ag is important to understand the origin of the advantages or drawbacks to the catalytic activity, caused by Ag. In literature, there are only limited information and speculations about the distribution of Ag in npAu,^[194] therefore we proceeded to characterize different npAu catalysts by means of quantitative EDXS tomography in order to obtain such information, and study the catalytic behavior of npAu with different concentration of Ag in the oxidation of CO with O₂.

In the study,^[184] it was observed that the catalytic oxidation of CO to CO₂, is enhanced by the presence of Ag, as also reported in ref.^[191]. The activity of a catalyst containing more than 10 at.% of Ag increases more than 100% relative to a catalyst with around 1 at.%. It is thought that the increased amount of Ag atoms on the surface, promotes bonding and activation of O₂, which can react with CO adsorbed on either Au or Ag

sites.^[195, 196] Further considerations of these hypothesis is subject to the possibility of performing a detailed morphological and elemental characterization of the material at the nanoscale, which was enabled by the techniques presented in the previous chapter. More details on the catalytic study can be found in the published work,^[184] here we will focus on the characterization of the material, showing how quantitative 3D EDXS tomography gives access to information otherwise not accessible, opening new possibilities for the understanding of these phenomena.

9.3.1 2D STEM and EDXS analysis

In order to investigate these nanoporous bulk samples, a thin, electron transparent lamella was prepared using a focused ion beam (FIB) lift-out technique.^[197] We proceeded to a first characterization by means of HAADF-STEM and EDXS in order to obtain an overview of the distribution and concentrations of elements. Three samples were analyzed, the starting master alloy (Figure 9.7e-f), and two npAu catalysts obtained from it, with different degrees of corrosion.

Two-dimensional elemental distribution mapping and tomography experiments have been performed using a FEI Osiris equipped with a ChemiSTEM system, operated at an acceleration voltage of 200 kV. For the STEM tomography measurements a tilt series from -78° to $+78^\circ$ with steps of 2° and a frame time of 10 s has been acquired. For the EDXS tomography, steps of 10° , a frame time of 400 s and a screen current of approximately 200 pA have been used. Measurements have been carried out using a 2050 Fischione tomography holder. HAADF-STEM and EDXS maps of the three samples are shown in Figure 9.7. Total concentrations for Au and Ag were calculated from the EDXS maps, extracting the net counts and using the ζ -factors given in section 8.4. The measured Ag concentrations for the samples are 71 ± 3 at.% for the master alloy and 8 ± 1 at.% and 11 ± 1 at.% for samples in Figure 9.7a,b and Figure 9.7c,d respectively.

From the 2D EDXS maps, it appears that clusters of segregated silver form in the porous structure as an effect of the dealloying. This is confirmed by the observation of a homogeneous elemental distribution in the master alloy, excluding that the formation of clusters occurs due to sample preparation or handling. This is a first important observation regarding the distribution of Ag in the material, the segregation of Ag during the synthesis. Unfortunately, 2D EDXS mapping does not allow further understanding of the possible surface distribution, e.g. whether the Ag clusters are situated inside the material or on the surface, or if the clusters are just patches of residual Ag or they actually formed due to Ag segregation.

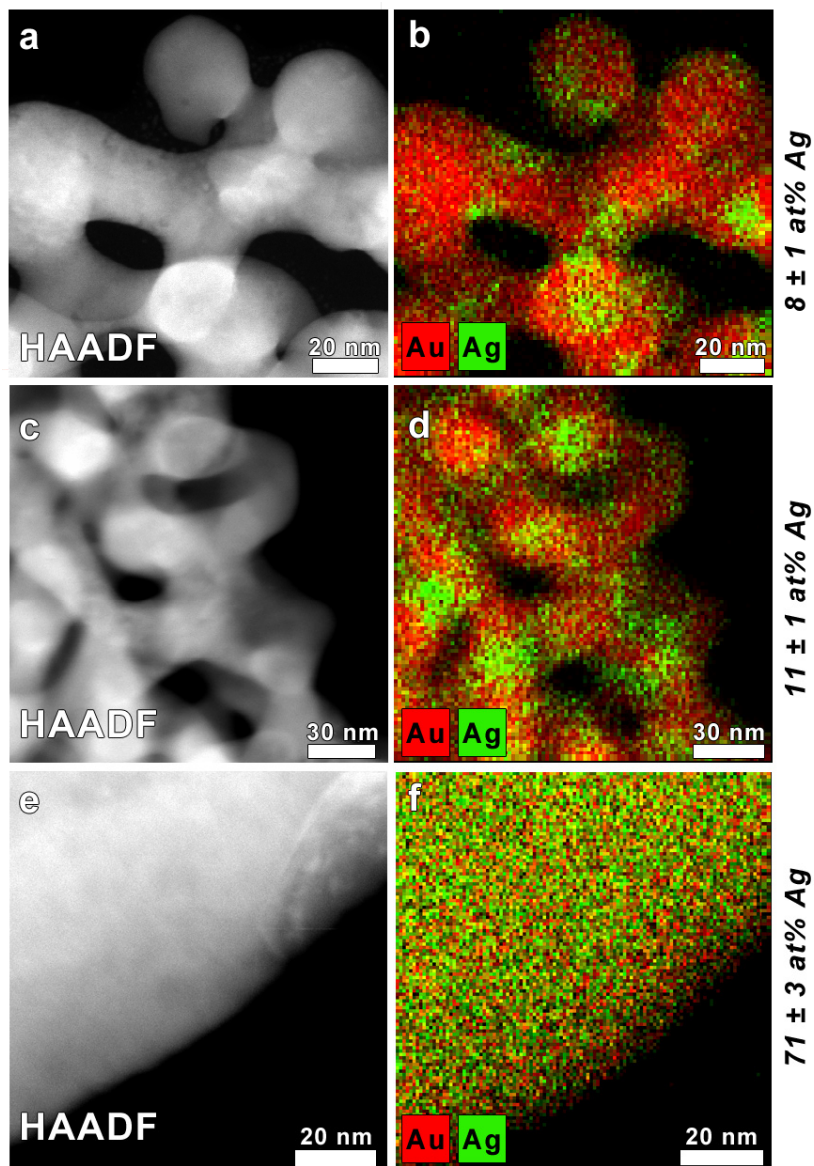


Figure 9.7: (a,c,e) HAADF-STEM images and (b,d,f) elemental distribution of gold (red signal) and silver (green signal) for three samples with different residual Ag concentrations. For the nanoporous samples Ag cluster formation is clearly visible in (b) and (d). These clusters cannot be seen in the parent alloy (f), indicating that clusters form during dealloying.

9.3.2 3D quantitative EDXS tomography.

In order to determine whether the Ag patches can be found on the surface or just inside the material, as we would expect in the case of residual Ag not involved in the corrosion reaction, we performed a quantitative EDXS tomography study on the same samples. Two needles shaped pillars were cut in the FIB, from the

bulk samples in order to perform the tomography study. Figure 9.8 shows renderings (Figure 9.8a,b,d,e) and quantified slices (Figure 9.8c,f) of the tomographic reconstructions of the samples. Figure 9.8a,b,c, and Figure 9.8d,e,f show results from the samples with average concentration 8 at.% and 11 at.% respectively.

From the reconstructions we can observe that the Ag clusters are located both inside the material and on the surface of the structure. This excludes that the Ag patches are only a residual unreacted of the master alloy, because buried inside the material. Further confirmation that the clusters are formed as an effect of the dealloying process is given by observing that the concentration of Ag in the clusters can even exceeds the starting concentration of the master alloy in certain points (see blue patches in Figure 9.8c) reaching concentrations between 80-90 at.%.

Summarizing, three main conclusions can be obtained from our characterization, first, the residual Ag in the nanoporous Au catalyst is mainly found in patches and clusters, second, these clusters can be found inside the ligaments as well as on the surface, and finally, the formation of these clusters is an effect of the dealloying process.

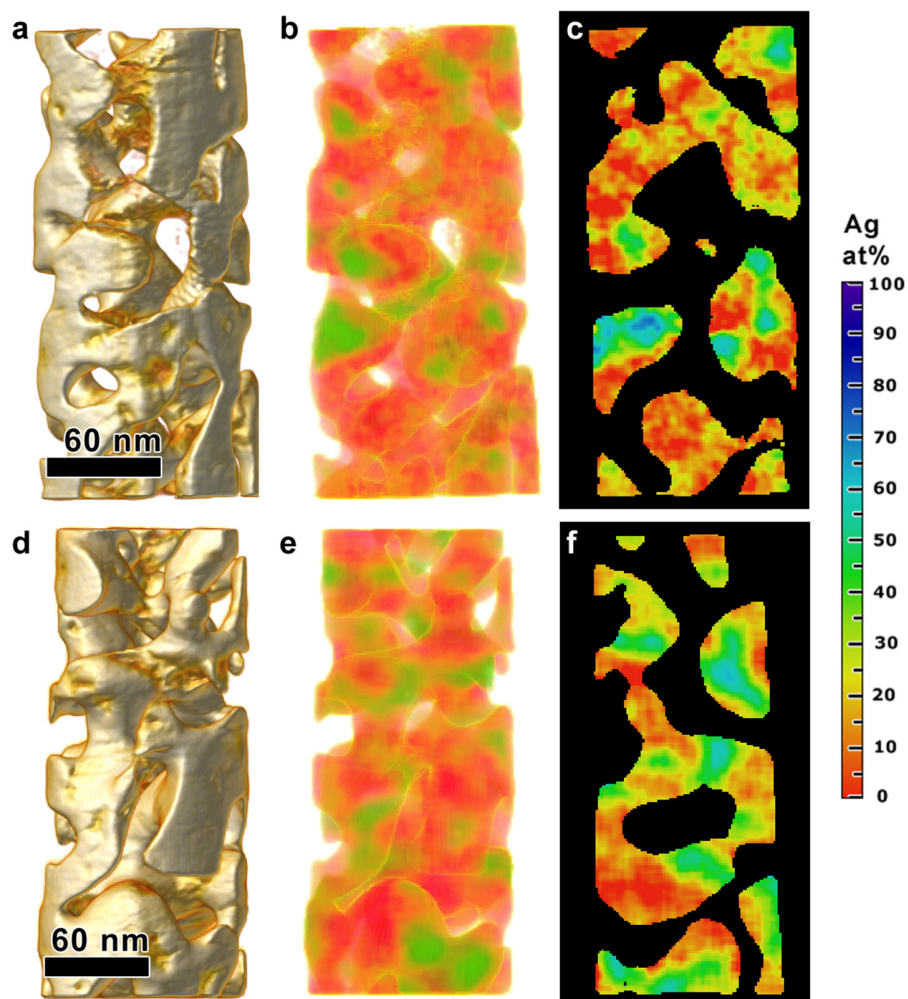


Figure 9.8: Tomographic reconstruction of the elemental distribution in nanoporous gold. (a, d) reconstructions of the sample from HAADF-STEM signal, (b, e) quantified elemental reconstructions, (c, f) single slices of the reconstructed quantified elemental distributions. (a, b, c) average Ag concentration of about 8 at.%, (d, e, f) average Ag concentration of about 11 at.%. Sample with lower local average Ag concentration shows higher Ag concentration in the Ag rich patches than samples with higher local average Ag concentration. The region between patches shows higher Ag concentrations for the sample with higher average Ag concentration. Silver enriched regions are distributed irregularly, both on the surface and inside the ligaments.

10 Conclusions and Outlook on Part III

10.1 Conclusions

In this third part it has been shown how the recent introduction of multiple detector systems such as the Super-X increased significantly the possibility of chemical characterization in the TEM. Detailed compositional characterization of small nanostructure became feasible thanks to the enhanced efficiency. Furthermore, the four symmetrical detectors opened the way to the combination of EDXS and tomography.^[52, 53] The increased collection efficiency further allowed quantitative EDXS characterizations to be performed, highlighting the lack of modern quantification techniques.

The adoption of the ζ -factor method^[136] and its extension to nanoparticles standards^[128] was therefore an important step towards quantitative studies in 3D. However, technical limitations such as detectors shadowing^[153, 161] hampered a proper combination of EDXS and tomography, limiting the characterization to qualitative studies.^[53-55, 132, 160] Although different methods were proposed to solve the shadowing issue,^[159-161] they all presented limiting drawbacks. Here, it was shown how the synergistic combination of quantitative 2D EDXS analysis and STEM tomography overcomes the shadowing problems, yielding a quantitative EDXS reconstruction. This is achieved by quantifying 2D EDXS data and then including prior knowledge about the thickness of the sample (obtained through a STEM tomography reconstruction).^[154] Furthermore, a series of materials science cases was presented in the previous chapter to demonstrate the advantages of the technique in characterizing morphology and composition of different systems.

The methods developed and presented in these chapters offer the unprecedented possibility of obtaining accurate 3D quantitative EDXS characterization of nanomaterials. This allows the determination of the concentrations of elements in every point of the investigated sample. Before its development this information was not accessible, and only qualitative information about the 3D compositions was obtained. Being able to determine the accurate 3D composition, opens the way to studies on the mechanisms behind the formation and synthesis of these nanostructures, and/or on the relationship between structure and properties, enabling further progress in the development of nanotechnologies based on hetero-nanomaterials.

10.2 Outlook

Future developments in the field of EDXS tomography will require advancements of both the instrument capabilities, both in terms of collection efficiency and software management of the acquisition. For

example, an increased efficiency and a better stability of the stage or/and an improved routine for the sample drift correction during the acquisition of an EDXS map, could open the way to atomic resolution mapping of nanostructures, and consequently to atomic resolution EDXS tomography. Besides the technological advancements, also improved reconstruction techniques, based on the combination of different signals that can be acquired simultaneously will help in expanding the capabilities of TEM in the chemical characterization of nanomaterials. It was recently proposed a design that enables the simultaneous acquisition of EDXS and EELS signal,^[198] and on the reconstruction algorithm side, a new approach based on the combination of EDXS and HAADF-STEM was also proposed.^[199] Sample stability is a main limiting obstacle to the chemical characterization, therefore exploiting all the possible information that can be acquired with one illumination will certainly enable an improvement in the reconstruction quality.

In chapter 7, it was also demonstrated how EDXS can be used for certain samples, to measure the volume of a nanoparticle or the thickness of thin-films. This information could serve as prior knowledge for advanced algorithms for electron tomography, and shows that more things can still be done with this powerful technique. New algorithms dedicated to EDXS or a combination of signals might be developed in the near future using new trending techniques based on artificial intelligence^[200] or compressed sensing. These techniques are already used in different fields, especially when dealing with limited data, which is one of the main issues affecting EDXS projections, given their low signal-to-noise ratio. The rate of evolution of these technologies is so high that we believe major improvements will come in the near future, granting better reconstructions at a parity of data quality.

10.3 Detailed list of contributions on part III

Sections 7.1-7.5

Ideation and implementation of the method presented, which enables the measurement of ζ -factors from pure element nanoparticles. Acquisition of all the data presented in the chapter, except for the EDXS map of Figure 7.7.

Section 7.6

Volume determination routines were implemented by J. Sanctorum, under my supervision.

Sections 7.6-7.7

All the work presented in these sections was performed by myself.

Sections 8.1-8.5

Ideation and implementation of the technique presented. Application of the method to experimental data acquired together with T. Altantzis.

Sections 9.1-9.3

Application of the technique presented in chapter 8 to several materials science cases to compute the quantified 3D elemental distributions. Experimental data acquired together with T. Altantzis (section 9.1), by myself (section 9.2) and together with P. Kundu (section 9.3).

11 Appendix A – Bond Order Parameters

Local bond order parameters analysis is a technique often used to determine crystal structures in the field of molecular simulations. The derivation based on spherical harmonics was first proposed by Steinhardt et al.^[113] in 1983. The method is used to reduce the complex vector representation of the bonds connecting a particle to its nearest neighbors, to a set of scalar parameters which are unique to a given configuration. The set of local bond order parameters form a fingerprint of the type of packing and since they are invariant relatively to rotations of the reference system, they allow the determination of grains with different orientation but showing the same kind of crystal structure.

A bond is defined as a vector \vec{r} connecting a pair of neighbouring atoms and its bond order parameters are calculated (Steinhardt et al.^[113] and Wang et al.^[114]) in the following manner:

$$Q_{lm}(\vec{r}) \stackrel{\text{def}}{=} Y_{lm}(\theta(\vec{r}), \varphi(\vec{r})) \quad (11.1)$$

where $\theta(\mathbf{r})$ and $\varphi(\mathbf{r})$ are the polar and azimuth angles of the bond \vec{r} relatively to a given system of reference, and $Y_{lm}(\theta(\mathbf{r}), \varphi(\mathbf{r}))$ the spherical harmonics. Averaged bond order parameters on all bonds for a given particle are then obtained:

$$\bar{Q}_{lm}(\vec{r}) \stackrel{\text{def}}{=} \frac{1}{N_b} \sum_{\text{bonds}} Q_{lm}(\vec{r}) \quad (11.2)$$

where N_b is the number of bonds. The first non-zero averages are obtained for $l = 4$ and $l = 6$, and to make the parameters rotationally invariant, only the following second order invariants combinations are considered:

$$Q_l \stackrel{\text{def}}{=} \sqrt{\frac{4\pi}{2l+1} \sum_{m=-l}^l |\bar{Q}_{lm}|^2} \quad (11.3)$$

together with the third-order invariants:

$$W_l \stackrel{\text{def}}{=} \sum_{\substack{m_1, m_2, m_3 \\ m_1 + m_2 + m_3 = 0}} \begin{pmatrix} l & l & l \\ m_1 & m_2 & m_3 \end{pmatrix} \bar{Q}_{lm_1} \bar{Q}_{lm_2} \bar{Q}_{lm_3} \quad (11.4)$$

where $\begin{pmatrix} l & l & l \\ m_1 & m_2 & m_3 \end{pmatrix}$ are the Wigner 3j symbols.^[201] Steinhardt et al.^[113] found that “ Q_l and W_l are the key to a kind of cluster ‘shape spectroscopy’ in liquids and glasses”, and that the normalized values:

$$\hat{W}_l \stackrel{\text{def}}{=} W_l / \left(\sum_m |\bar{Q}_{lm}|^2 \right)^{3/2} \quad (11.5)$$

are a sensitive measure of the orientational symmetries shown by systems of particles.

Usually the four bond order parameters Q_4 , Q_6 , \hat{W}_4 , \hat{W}_6 are sufficient to identify the crystal structure of a given point and its neighborhood. In Table 11.1 the values of these parameters are given as an example, for common crystal structures.

Geometry	Q_4	Q_6	\hat{W}_4	\hat{W}_6
fcc	0.19094	0.57452	-0.159317	-0.013161
hcp	0.09722	0.48476	0.134097	-0.012442
bcc	0.08202	0.50083	0.15932	0.01316
sc	0.76376	0.35355	0.15932	0.01316
liquid	0	0	0	0

Table 11.1: Literature values of the bond order parameters for common types packings.^[114]

12 References

- [1] S. Kinoshita, S. Yoshioka, "*Structural colors in nature: the role of regularity and irregularity in the structure*", ChemPhysChem **2005**, 6, 1442.
- [2] H. J. Ensikat, P. Ditsche-Kuru, C. Neinhuis, W. Barthlott, "*Superhydrophobicity in perfection: the outstanding properties of the lotus leaf*", Beilstein journal of nanotechnology **2011**, 2, 152.
- [3] J. W. Galusha, L. R. Richey, J. S. Gardner, J. N. Cha, M. H. Bartl, "*Discovery of a diamond-based photonic crystal structure in beetle scales*", Physical Review E **2008**, 77, 050904.
- [4] S. Kinoshita, S. Yoshioka, K. Kawagoe, "*Mechanisms of structural colour in the Morpho butterfly: cooperation of regularity and irregularity in an iridescent scale*", Proceedings of the Royal Society of London B: Biological Sciences **2002**, 269, 1417.
- [5] J. D. Joannopoulos, S. G. Johnson, J. N. Winn, R. D. Meade, *Photonic crystals: molding the flow of light*, Princeton university press, **2011**.
- [6] A. R. Parker, H. E. Townley, "*Biomimetics of photonic nanostructures*", Nature nanotechnology **2007**, 2, 347.
- [7] R. A. Potyrailo, R. K. Bonam, J. G. Hartley, T. A. Starkey, P. Vukusic, M. Vasudev, T. Bunning, R. R. Naik, Z. Tang, M. A. Palacios, "*Towards outperforming conventional sensor arrays with fabricated individual photonic vapour sensors inspired by Morpho butterflies*", Nature communications **2015**, 6.
- [8] P. Colomban, "The use of metal nanoparticles to produce yellow, red and iridescent colour, from bronze age to present times in lustre pottery and glass: solid state chemistry, spectroscopy and nanostructure", presented at *Journal of Nano Research*, **2009**.
- [9] I. Freestone, N. Meeks, M. Sax, C. Higgitt, "*The Lycurgus cup—a roman nanotechnology*", Gold bulletin **2007**, 40, 270.
- [10] M. Reibold, P. Paufler, A. Levin, W. Kochmann, N. Pätzke, D. Meyer, "*Materials: Carbon nanotubes in an ancient Damascus sabre*", Nature **2006**, 444, 286.
- [11] L. De Broglie, "*La nouvelle dynamique des quanta*", Electrons et photons. Rapports et discussions du cinquième Conseil de physique tenu à Bruxelles du 24 au 29 octobre 1927 sous les auspices de l'Institut international de physique Solvay **1928**, 105.
- [12] M. Knoll, E. Ruska, "*Das elektronenmikroskop*", Zeitschrift für Physik **1932**, 78, 318.

- [13] M. Von Ardenne, "*Das elektronen-rastermikroskop*", Zeitschrift für Physik A Hadrons and Nuclei **1938**, 109, 553.
- [14] A. V. Crewe, J. Wall, J. Langmore, "*Visibility of single atoms*", Science **1970**, 168, 1338.
- [15] M. Treacy, A. Howie, S. Pennycook, "Z-contrast of supported catalyst particles on the STEM. Electron Microscopy and Analysis 1979", presented at *Inst. of Phys. Conf. Ser.*, **1980**.
- [16] M. Isaacson, D. Johnson, "*The microanalysis of light elements using transmitted energy loss electrons*", Ultramicroscopy **1975**, 1, 33.
- [17] D. B. Williams, C. B. Carter, *The transmission electron microscope*, Springer, **1996**.
- [18] J. Goldstein, J. Costley, G. Lorimer, S. Reed, "*Quantitative X-ray analysis in the electron microscope*", Scanning Electron Microscopy **1977**, 1, 315.
- [19] R. Fitzgerald, K. Keil, K. F. Heinrich, "*Solid-state energy-dispersion spectrometer for electron-microprobe X-ray analysis*", Science **1968**, 159, 528.
- [20] J. Radon, "*On determination of functions by their integral values along certain multiplicities*", Ber. der Sachische Akademie der Wissenschaften Leipzig, (Germany) **1917**, 69, 262.
- [21] A. M. Cormack, "*Representation of a function by its line integrals, with some radiological applications*", Journal of applied physics **1963**, 34, 2722.
- [22] D. De Rosier, A. Klug, "*Reconstruction of three dimensional structures from electron micrographs*", Nature **1968**, 217, 130.
- [23] W. Hoppe, R. Langer, G. Knesch, C. Poppe, "*Protein-kristallstrukturanalyse mit elektronenstrahlen*", Naturwissenschaften **1968**, 55, 333.
- [24] R. G. Hart, "*Electron microscopy of unstained biological material: the polytropic montage*", Science **1968**, 159, 1464.
- [25] A. J. Koster, R. Grimm, D. Typke, R. Hegerl, A. Stoschek, J. Walz, W. Baumeister, "*Perspectives of molecular and cellular electron tomography*", Journal of structural biology **1997**, 120, 276.
- [26] P. A. Midgley, R. E. Dunin-Borkowski, "*Electron tomography and holography in materials science*", Nature materials **2009**, 8, 271.
- [27] J. Frank, *Electron tomography: methods for three-dimensional visualization of structures in the cell*, Springer Science & Business Media, **2008**.
- [28] A. Koster, U. Ziese, A. Verkleij, A. Janssen, K. De Jong, "*Three-dimensional transmission electron microscopy: a novel imaging and characterization technique with nanometer scale resolution for materials science*", The Journal of Physical Chemistry B **2000**, 104, 9368.

- [29] P. Midgley, M. Weyland, "*3D electron microscopy in the physical sciences: the development of Z-contrast and EFTEM tomography*", *Ultramicroscopy* **2003**, 96, 413.
- [30] R. N. Bracewell, "*Strip integration in radio astronomy*", *Australian Journal of Physics* **1956**, 9, 198.
- [31] P. Smith, T. Peters, R. Bates, "*Image reconstruction from finite numbers of projections*", *Journal of Physics A: Mathematical, Nuclear and General* **1973**, 6, 361.
- [32] Y. Yang, C. Chen, M. Scott, C. Ophus, R. Xu, A. Pryor, L. Wu, F. Sun, W. Theis, J. Zhou, "*Deciphering chemical order/disorder and material properties at the single-atom level*", *Nature* **2017**, 542, 75.
- [33] G. T. Herman, *Fundamentals of computerized tomography: image reconstruction from projections*, Springer Science & Business Media, **2009**.
- [34] B. Vainshtein, "*Finding structure of objects from projections*", *SOVIET PHYSICS CRYSTALLOGRAPHY, USSR* **1971**, 15, 781.
- [35] P. Gilbert, "*Iterative methods for the three-dimensional reconstruction of an object from projections*", *Journal of theoretical biology* **1972**, 36, 105.
- [36] H. Heidari, W. Van den Broek, S. Bals, "*A practical method to determine the effective resolution in incoherent experimental electron tomography*", *Ultramicroscopy* **2011**, 111, 330.
- [37] R. Gordon, R. Bender, G. T. Herman, "*Algebraic reconstruction techniques (ART) for three-dimensional electron microscopy and X-ray photography*", *Journal of theoretical Biology* **1970**, 29, 471.
- [38] W. van Aarle, W. J. Palenstijn, J. De Beenhouwer, T. Altantzis, S. Bals, K. J. Batenburg, J. Sijbers, "*The ASTRA Toolbox: A platform for advanced algorithm development in electron tomography*", *Ultramicroscopy* **2015**, 157, 35.
- [39] J. Gregor, T. Benson, "*Computational analysis and improvement of SIRT*", *IEEE Transactions on Medical Imaging* **2008**, 27, 918.
- [40] W. J. Palenstijn, K. J. Batenburg, J. Sijbers, "The ASTRA tomography toolbox", presented at *13th International Conference on Computational and Mathematical Methods in Science and Engineering. CMMSE*, **2013**.
- [41] F. Bleichrodt, T. Van Leeuwen, W. J. Palenstijn, W. Van Aarle, J. Sijbers, K. J. Batenburg, "*Easy implementation of advanced tomography algorithms using the ASTRA toolbox with Spot operators*", *Numerical Algorithms* **2015**.
- [42] T. van Leeuwen, F. Bleichrodt, W. Palenstijn, K. Batenburg, J. Sijbers, "A flexible Matlab/GPU toolbox for tomographic reconstruction based on the ASTRA and SPOT toolboxes", presented at *DGCI 2014: the 18th international conference on Discrete Geometry for Computer Imagery.*, Siena, **2014**.

- [43] W. J. Palenstijn, J. Bédorf, K. J. Batenburg, M. King, S. Glick, K. Mueller, "A distributed SIRT implementation for the ASTRA toolbox", presented at *Proc. Fully Three-Dimensional Image Reconstruct. Radiol. Nucl. Med.*, **2015**.
- [44] K. J. Batenburg, S. Bals, J. Sijbers, C. Kübel, P. Midgley, J. Hernandez, U. Kaiser, E. Encina, E. Coronado, G. Van Tendeloo, "3D imaging of nanomaterials by discrete tomography", *Ultramicroscopy* **2009**, 109, 730.
- [45] K. J. Batenburg, J. Sijbers, "DART: a practical reconstruction algorithm for discrete tomography", *Image Processing, IEEE Transactions on* **2011**, 20, 2542.
- [46] D. L. Donoho, "Compressed sensing", *IEEE Transactions on information theory* **2006**, 52, 1289.
- [47] L. I. Rudin, S. Osher, E. Fatemi, "Nonlinear total variation based noise removal algorithms", *Physica D: Nonlinear Phenomena* **1992**, 60, 259.
- [48] B. Goris, W. Van den Broek, K. J. Batenburg, H. H. Mezerji, S. Bals, "Electron tomography based on a total variation minimization reconstruction technique", *Ultramicroscopy* **2012**, 113, 120.
- [49] B. Goris, T. Roelandts, K. Batenburg, H. H. Mezerji, S. Bals, "Advanced reconstruction algorithms for electron tomography: from comparison to combination", *Ultramicroscopy* **2013**, 127, 40.
- [50] D. Zanaga, F. Bleichrodt, T. Altantzis, N. Winckelmans, W. J. Palenstijn, J. Sijbers, B. de Nijs, M. A. van Huis, A. Sánchez-Iglesias, L. M. Liz-Marzán, A. van Blaaderen, J. K. Batenburg, S. Bals, G. Van Tendeloo, "Quantitative 3D analysis of huge nanoparticle assemblies", *Nanoscale* **2016**, 8, 292.
- [51] P. W. Hawkes, in *Electron tomography*, Springer, **2007**, 83.
- [52] G. Möbus, R. C. Doole, B. J. Inkson, "Spectroscopic electron tomography", *Ultramicroscopy* **2003**, 96, 433.
- [53] A. Genç, H. Cheng, J. Winterstein, L. Pullan, B. Freitag, "3D chemical mapping using tomography with an enhanced XEDS system", *Microscopy and Analysis* **2012**, 116, 23.
- [54] A. Genc, L. Kovarik, M. Gu, H. Cheng, P. Plachinda, L. Pullan, B. Freitag, C. Wang, "XEDS STEM tomography for 3D chemical characterization of nanoscale particles", *Ultramicroscopy* **2013**, 131, 24.
- [55] B. Goris, L. Polavarapu, S. Bals, G. Van Tendeloo, L. M. Liz-Marzán, "Monitoring Galvanic Replacement Through Three-Dimensional Morphological and Chemical Mapping", *Nano Lett.* **2014**, 14, 3220.
- [56] K. Jarausch, P. Thomas, D. N. Leonard, R. Twesten, C. R. Booth, "Four-dimensional STEM-EELS: Enabling nano-scale chemical tomography", *Ultramicroscopy* **2009**, 109, 326.

- [57] G. Möbus, B. Inkson, "*Three-dimensional reconstruction of buried nanoparticles by element-sensitive tomography based on inelastically scattered electrons*", Applied Physics Letters **2001**, 79, 1369.
- [58] L. Yedra, A. Eljarrat, R. Arenal, E. Pellicer, M. Cabo, A. López-Ortega, M. Estrader, J. Sort, M. D. Baró, S. Estradé, "*EEL spectroscopic tomography: Towards a new dimension in nanomaterials analysis*", Ultramicroscopy **2012**, 122, 12.
- [59] M. H. Gass, K. K. Koziol, A. H. Windle, P. A. Midgley, "*Four-dimensional spectral tomography of carbonaceous nanocomposites*", Nano Letters **2006**, 6, 376.
- [60] O. Nicoletti, F. de La Peña, R. K. Leary, D. J. Holland, C. Ducati, P. A. Midgley, "*Three-dimensional imaging of localized surface plasmon resonances of metal nanoparticles*", Nature **2013**, 502, 80.
- [61] P. Schlossmacher, D. Klenov, B. Freitag, H. Von Harrach, "*Enhanced detection sensitivity with a new windowless XEDS system for AEM based on silicon drift detector technology*", Microscopy today **2010**, 18, 14.
- [62] S. Kawai, I. Onishi, T. Ishikawa, K. Yagi, T. Iwama, K. Miyatake, Y. Iwasawa, M. Matsushita, T. Kaneyama, Y. Kondo, "*A Double Silicon Drift Type Detector System for EDS with Ultrahigh Efficiency and Throughput for TEM*", Microscopy and Microanalysis **2014**, 20, 1150.
- [63] P. Schlossmacher, D. O. Klenov, B. Freitag, S. von Harrach, A. Steinbach, "*Nanoscale chemical compositional analysis with an innovative S/TEM-EDX system*", Microscopy and analysis **2010**, S5.
- [64] E. Fitchard, J. Aldridge, P. Reckwerdt, T. Mackie, "*Registration of synthetic tomographic projection data sets using cross-correlation*", Physics in medicine and biology **1998**, 43, 1645.
- [65] L. Houben, M. B. Sadan, "*Refinement procedure for the image alignment in high-resolution electron tomography*", Ultramicroscopy **2011**, 111, 1512.
- [66] B. Goris, J. De Beenhouwer, A. De Backer, D. Zanaga, J. K. Batenburg, A. Sánchez-Iglesias, L. M. Liz-Marzan, S. Van Aert, S. Bals, J. Sijbers, "*Measuring lattice strain in three dimensions through electron microscopy*", Nano letters **2015**, 15, 6996.
- [67] M. Guizar-Sicairos, S. T. Thurman, J. R. Fienup, "*Efficient subpixel image registration algorithms*", Optics letters **2008**, 33, 156.
- [68] A. Cheng, R. Henderson, D. Mastronarde, S. J. Ludtke, R. H. Schoenmakers, J. Short, R. Marabini, S. Dallakyan, D. Agard, M. Winn, "*MRC2014: Extensions to the MRC format header for electron cryo-microscopy and tomography*", Journal of structural biology **2015**, 192, 146.

- [69] W. Van den Broek, A. Rosenauer, B. Goris, G. Martinez, S. Bals, S. Van Aert, D. Van Dyck, "Correction of non-linear thickness effects in HAADF STEM electron tomography", *Ultramicroscopy* **2012**, 116, 8.
- [70] T. Altantzis, B. Goris, A. Sánchez-Iglesias, M. Grzelczak, L. M. Liz-Marzán, S. Bals, "Quantitative Structure Determination of Large Three-Dimensional Nanoparticle Assemblies", *Particle & Particle Systems Characterization* **2013**, 30, 84.
- [71] P. Ercius, M. Weyland, D. A. Muller, L. M. Gignac, "Three-dimensional imaging of nanovoids in copper interconnects using incoherent bright field tomography", *Applied physics letters* **2006**, 88, 243116.
- [72] J. R. Kremer, D. N. Mastrorade, J. R. McIntosh, "Computer visualization of three-dimensional image data using IMOD", *Journal of structural biology* **1996**, 116, 71.
- [73] C. Messaoudil, T. Boudier, C. O. Sorzano, S. Marco, "TomoJ: tomography software for three-dimensional reconstruction in transmission electron microscopy", *BMC bioinformatics* **2007**, 8, 288.
- [74] G. M. Whitesides, B. Grzybowski, "Self-assembly at all scales", *Science* **2002**, 295, 2418.
- [75] B. A. Grzybowski, C. E. Wilmer, J. Kim, K. P. Browne, K. J. Bishop, "Self-assembly: from crystals to cells", *Soft Matter* **2009**, 5, 1110.
- [76] D. Philp, J. F. Stoddart, "Self-assembly in natural and unnatural systems", *Angewandte Chemie International Edition* **1996**, 35, 1154.
- [77] C. Wagner, N. Harned, "EUV lithography: Lithography gets extreme", *Nature Photonics* **2010**, 4, 24.
- [78] D. G. Grier, "A revolution in optical manipulation", *Nature* **2003**, 424, 810.
- [79] A. Van Blaaderen, R. Ruel, P. Wiltzius, "Template-directed colloidal crystallization", *Nature* **1997**, 385, 321.
- [80] Y. A. Vlasov, B. Xiang-Zheng, J. C. Sturm, D. J. Norris, "On-chip natural assembly of silicon photonic bandgap crystals", *Nature* **2001**, 414, 289.
- [81] C. B. Murray, C. Kagan, M. Bawendi, "Synthesis and characterization of monodisperse nanocrystals and close-packed nanocrystal assemblies", *Annual Review of Materials Science* **2000**, 30, 545.
- [82] M. D. Porter, T. B. Bright, D. L. Allara, C. E. Chidsey, "Spontaneously organized molecular assemblies. 4. Structural characterization of n-alkyl thiol monolayers on gold by optical ellipsometry, infrared spectroscopy, and electrochemistry", *Journal of the American Chemical Society* **1987**, 109, 3559.
- [83] S. A. Claridge, A. Castleman Jr, S. N. Khanna, C. B. Murray, A. Sen, P. S. Weiss, "Cluster-assembled materials", *ACS Nano* **2009**, 3, 244.

- [84] N. A. Kotov, P. S. Weiss, "*Self-Assembly of Nanoparticles: A Snapshot*", ACS Nano **2014**, 8, 3101.
- [85] D. Vanmaekelbergh, L. K. Van Vugt, H. E. Bakker, F. T. Rabouw, B. de Nijs, R. J. van Dijk-Moes, M. A. van Huis, P. Baesjou, A. van Blaaderen, "*Shape-Dependent Multi-Exciton Emission and Whispering Gallery Modes in Supraparticles of CdSe/Multi-Shell Quantum Dots*", ACS Nano **2015**.
- [86] Y. Gao, Z. Tang, "*Design and application of inorganic nanoparticle superstructures: current status and future challenges*", Small **2011**, 7, 2133.
- [87] Y. Xia, Z. Tang, "*Monodisperse inorganic supraparticles: formation mechanism, properties and applications*", Chemical Communications **2012**, 48, 6320.
- [88] M. Grzelczak, J. Vermant, E. M. Furst, L. M. Liz-Marzán, "*Directed self-assembly of nanoparticles*", ACS Nano **2010**, 4, 3591.
- [89] C. Hamon, S. M. Novikov, L. Scarabelli, D. M. Solís, T. Altantzis, S. Bals, J. M. Taboada, F. Obelleiro, L. M. Liz-Marzán, "*Collective plasmonic properties in few-layer gold nanorod supercrystals*", ACS photonics **2015**, 2, 1482.
- [90] S. Guo, S. Dong, "*Metal nanomaterial-based self-assembly: development, electrochemical sensing and SERS applications*", Journal of Materials Chemistry **2011**, 21, 16704.
- [91] K. Kim, D. Shin, K. L. Kim, K. S. Shin, "*Electromagnetic field enhancement in the gap between two Au nanoparticles: the size of hot site probed by surface-enhanced Raman scattering*", Physical Chemistry Chemical Physics **2010**, 12, 3747.
- [92] L. Xu, H. Kuang, L. Wang, C. Xu, "*Gold nanorod ensembles as artificial molecules for applications in sensors*", Journal of Materials Chemistry **2011**, 21, 16759.
- [93] Y. Xu, S. Hou, Y. Liu, Y. Zhang, H. Wang, B. Zhang, "*Facile one-step room-temperature synthesis of Pt₃Ni nanoparticle networks with improved electrocatalytic properties*", Chemical Communications **2012**, 48, 2665.
- [94] S. Guo, S. Sun, "*FePt nanoparticles assembled on graphene as enhanced catalyst for oxygen reduction reaction*", Journal of the American Chemical Society **2012**, 134, 2492.
- [95] R. J. Tseng, C. Tsai, L. Ma, J. Ouyang, C. S. Ozkan, Y. Yang, "*Digital memory device based on tobacco mosaic virus conjugated with nanoparticles*", Nature nanotechnology **2006**, 1, 72.
- [96] H. Friedrich, C. J. Gommers, K. Overgaag, J. D. Meeldijk, W. H. Evers, B. d. Nijs, M. P. Boneschanscher, P. E. de Jongh, A. J. Verkleij, K. P. de Jong, A. van Blaaderen, D. Vanmaekelbergh, "*Quantitative structural analysis of binary nanocrystal superlattices by electron tomography*", Nano letters **2009**, 9, 2719.

- [97] I. Florea, A. Demortiere, C. Petit, H. Bulou, C. Hirlimann, O. Ersen, "3D quantitative analysis of platinum nanocrystal superlattices by electron tomography", *ACS Nano* **2012**, 6, 2574.
- [98] J. E. Galván-Moya, T. Altantzis, K. Nelissen, F. M. Peeters, M. Grzelczak, L. M. Liz-Marzán, S. Bals, G. Van Tendeloo, "Self-Organization of Highly Symmetric Nanoassemblies: A Matter of Competition", *ACS Nano* **2014**, 8, 3869.
- [99] W. H. Evers, H. Friedrich, L. Filion, M. Dijkstra, D. Vanmaekelbergh, "Observation of a ternary nanocrystal superlattice and its structural characterization by electron tomography", *Angewandte Chemie International Edition* **2009**, 48, 9655.
- [100] B. de Nijs, S. Dussi, F. Smalenburg, J. D. Meeldijk, D. J. Groenendijk, L. Filion, A. Imhof, A. van Blaaderen, M. Dijkstra, "Entropy-driven formation of large icosahedral colloidal clusters by spherical confinement", *Nature materials* **2015**, 14, 56.
- [101] N. Horst, A. Travasset, "Prediction of binary nanoparticle superlattices from soft potentials", *The Journal of chemical physics* **2016**, 144, 014502.
- [102] A. Sánchez-Iglesias, M. Grzelczak, T. Altantzis, B. Goris, J. Perez-Juste, S. Bals, G. Van Tendeloo, S. H. Donaldson Jr, B. F. Chmelka, J. N. Israelachvili, "Hydrophobic interactions modulate self-assembly of nanoparticles", *ACS Nano* **2012**, 6, 11059.
- [103] I. Loris, G. Nolet, I. Daubechies, F. Dahlen, "Tomographic inversion using ℓ_1 -norm regularization of wavelet coefficients", *Geophysical Journal International* **2007**, 170, 359.
- [104] R. Leary, Z. Saghi, P. A. Midgley, D. J. Holland, "Compressed sensing electron tomography", *Ultramicroscopy* **2013**, 131, 70.
- [105] Z. Saghi, D. J. Holland, R. Leary, A. Falqui, G. Bertoni, A. J. Sederman, L. F. Gladden, P. A. Midgley, "Three-dimensional morphology of iron oxide nanoparticles with reactive concave surfaces. A compressed sensing-electron tomography (CS-ET) approach", *Nano letters* **2011**, 11, 4666.
- [106] E. Van Den Berg, M. P. Friedlander, "Probing the Pareto frontier for basis pursuit solutions", *SIAM Journal on Scientific Computing* **2008**, 31, 890.
- [107] W. J. Palenstijn, K. J. Batenburg, J. Sijbers, "Performance improvements for iterative electron tomography reconstruction using graphics processing units (GPUs)", *Journal of structural biology* **2011**, 176, 250.
- [108] E. van den Berg, M. Friedlander, **2009**, <http://www.cs.ubc.ca/labs/scl/spot>, accessed: June, 2015.
- [109] M. I. Bodnarchuk, M. V. Kovalenko, H. Groiss, R. Resel, M. Reissner, G. Hesser, R. T. Lechner, W. Steiner, F. Schäffler, W. Heiss, "Exchange-Coupled Bimagnetic

Wüstite/Metal Ferrite Core/Shell Nanocrystals: Size, Shape, and Compositional Control", *Small* **2009**, 5, 2247.

[110] F. Bai, D. Wang, Z. Huo, W. Chen, L. Liu, X. Liang, C. Chen, X. Wang, Q. Peng, Y. Li, "A Versatile Bottom-up Assembly Approach to Colloidal Spheres from Nanocrystals", *Angewandte Chemie International Edition* **2007**, 46, 6650.

[111] M. V. Kovalenko, M. I. Bodnarchuk, R. T. Lechner, G. Hesser, F. Schäffler, W. Heiss, "Fatty acid salts as stabilizers in size-and shape-controlled nanocrystal synthesis: the case of inverse spinel iron oxide", *Journal of the American Chemical Society* **2007**, 129, 6352.

[112] T. Mason, J. Bibette, "Shear rupturing of droplets in complex fluids", *Langmuir* **1997**, 13, 4600.

[113] P. J. Steinhardt, D. R. Nelson, M. Ronchetti, "Bond-orientational order in liquids and glasses", *Physical Review B* **1983**, 28, 784.

[114] Y. Wang, S. Teitel, C. Dellago, "Melting of icosahedral gold nanoclusters from molecular dynamics simulations", *The Journal of chemical physics* **2005**, 122, 214722.

[115] D. Arthur, S. Vassilvitskii, "k-means++: The advantages of careful seeding", *Proceedings of the eighteenth annual ACM-SIAM symposium on Discrete algorithms* **2007**, 1027.

[116] A. L. Mackay, "A Dense Non-Crystallographic Packing of Equal Spheres", *Acta Crystallographica* **1962**, 15, 916.

[117] J. H. Conway, N. J. A. Sloane, E. Bannai, J. Leech, S. Norton, A. Odlyzko, R. Parker, L. Queen, B. Venkov, *Sphere packings, lattices and groups*, Vol. 3, Springer-Verlag New York, **1993**.

[118] D. R. Nelson, B. I. Halperin, "Pentagonal and icosahedral order in rapidly cooled metals", *Science* **1985**, 229, 233.

[119] Z. Yang, T. Altantzis, D. Zanaga, S. Bals, G. Van Tendeloo, M.-P. Pileni, "Supracrystalline colloidal eggs: epitaxial growth and freestanding three-dimensional supracrystals in nanoscaled colloidosomes", *J. Am. Chem. Soc* **2016**, 138, 3493.

[120] E. V. Shevchenko, D. V. Talapin, N. A. Kotov, S. O'Brien, C. B. Murray, "Structural diversity in binary nanoparticle superlattices", *Nature* **2006**, 439, 55.

[121] T. Paik, B. T. Diroll, C. R. Kagan, C. B. Murray, "Binary and ternary superlattices self-assembled from colloidal nanodisks and nanorods", *J. Am. Chem. Soc* **2015**, 137, 6662.

- [122] W. Pearson, "Laves structures, $MgCu_2$, $MgZn_2$, $MgNi_2$ ", Acta Crystallographica Section B: Structural Crystallography and Crystal Chemistry **1968**, 24, 7.
- [123] W. B. Pearson, *The crystal chemistry and physics of metals and alloys*, Wiley-Interscience, **1972**.
- [124] H. R. Vutukuri, F. Smallenburg, S. Badaire, A. Imhof, M. Dijkstra, A. Van Blaaderen, "An experimental and simulation study on the self-assembly of colloidal cubes in external electric fields", Soft Matter **2014**, 10, 9110.
- [125] Z. Nie, D. Fava, E. Kumacheva, S. Zou, G. C. Walker, M. Rubinstein, "Self-assembly of metal-polymer analogues of amphiphilic triblock copolymers", Nature materials **2007**, 6, 609.
- [126] M. Grzelczak, A. Sánchez-Iglesias, H. H. Mezerji, S. Bals, J. Pérez-Juste, L. M. Liz-Marzán, "Steric hindrance induces crosslike self-assembly of gold nanodumbbells", Nano letters **2012**, 12, 4380.
- [127] M. Grzelczak, A. Sánchez-Iglesias, L. M. Liz-Marzán, "A general approach toward polymer-coated plasmonic nanostructures", CrystEngComm **2014**, 16, 9425.
- [128] D. Zanaga, T. Altantzis, J. Sanctorem, B. Freitag, S. Bals, "An alternative approach for ζ -factor measurement using pure element nanoparticles", Ultramicroscopy **2016**, 164, 11.
- [129] D. Wang, Y. Li, "Bimetallic nanocrystals: liquid-phase synthesis and catalytic applications", Advanced Materials **2011**, 23, 1044.
- [130] G. Van Tendeloo, S. Bals, S. Van Aert, J. Verbeeck, D. Van Dyck, "Advanced electron microscopy for advanced materials", Advanced Materials **2012**, 24, 5655.
- [131] B. Goris, L. Polavarapu, S. Bals, G. Van Tendeloo, L. M. Liz-Marzán, "Monitoring galvanic replacement through three-dimensional morphological and chemical mapping", Nano letters **2014**, 14, 3220.
- [132] T. J. Slater, A. Macedo, S. L. Schroeder, M. G. Burke, P. O'Brien, P. H. Camargo, S. J. Haigh, "Correlating catalytic activity of Ag–Au nanoparticles with 3D compositional variations", Nano letters **2014**, 14, 1921.
- [133] P. Burdet, Z. Saghi, A. N. Filippin, A. Borrás, P. A. Midgley, "A novel 3D absorption correction method for quantitative EDX-STEM tomography", Ultramicroscopy **2015**.
- [134] G. Cliff, G. Lorimer, "The quantitative analysis of thin specimens", Journal of Microscopy **1975**, 103, 203.
- [135] Z. Horita, T. Sano, M. Nemoto, "A new form of the extrapolation method for absorption correction in quantitative X-ray microanalysis with the analytical electron microscope", Ultramicroscopy **1991**, 35, 27.

- [136] M. Watanabe, D. Williams, "*The quantitative analysis of thin specimens: a review of progress from the Cliff-Lorimer to the new ζ -factor methods*", *Journal of microscopy* **2006**, 221, 89.
- [137] D. Newbury, D. Williams, J. Goldstein, C. Fiori, "*Observation on the calculation of k AB factors for analytical electron microscopy*", *Analytical Electron Microscopy* **1984**, 2, 276.
- [138] T. Malis, S. Cheng, R. Egerton, "*EELS log-ratio technique for specimen-thickness measurement in the TEM*", *Journal of electron microscopy technique* **1988**, 8, 193.
- [139] G. Kothleitner, W. Grogger, M. Dienstleder, F. Hofer, "*Linking TEM Analytical Spectroscopies for an Assumptionless Compositional Analysis*", *Microscopy and Microanalysis* **2014**, 20, 678.
- [140] G. Van Tendeloo, D. Van Dyck, S. J. Pennycook, *Handbook of Nanoscopy*, John Wiley & Sons, **2012**.
- [141] H. Heidari, W. Van den Broek, S. Bals, "*Quantitative electron tomography: The effect of the three-dimensional point spread function*", *Ultramicroscopy* **2013**, 135, 1.
- [142] B. L. Henke, E. M. Gullikson, J. C. Davis, "*X-ray interactions: photoabsorption, scattering, transmission, and reflection at $E= 50\text{-}30,000$ eV, $Z= 1\text{-}92$* ", *Atomic data and nuclear data tables* **1993**, 54, 181.
- [143] L. Lyons, *A practical guide to data analysis for physical science students*, Cambridge University Press, **1991**.
- [144] J. R. Taylor, "*An Introduction To Error Analysis: The Study Of Uncertainties In Physical Measurements Author: John R. Taylor, Publisher*", **1996**.
- [145] W. J. Thompson, "*Poisson distributions*", *Computing in Science & Engineering* **2001**, 3, 78.
- [146] M. Galassi, J. Davies, J. Theiler, B. Gough, G. Jungman, P. Alken, M. Booth, F. Rossi, "*GNU Scientific Library Reference Manual-(v1. 12)*", *Network Theory Ltd* **2009**, 83.
- [147] E. Kreyszig, *Advanced engineering mathematics*, John Wiley & Sons, **1988**.
- [148] S. Bals, B. Goris, L. M. Liz-Marzán, G. Van Tendeloo, "*Three-Dimensional Characterization of Noble-Metal Nanoparticles and their Assemblies by Electron Tomography*", *Angewandte Chemie International Edition* **2014**, 53, 10600.
- [149] S. Mourdikoudis, M. Chirea, D. Zanaga, T. Altantzis, M. Mitrakas, S. Bals, L. M. Liz-Marzán, J. Pérez-Juste, I. Pastoriza-Santos, "*Governing the morphology of Pt–Au heteronanocrystals with improved electrocatalytic performance*", *Nanoscale* **2015**, 7, 8739.

- [150] S. Zhou, K. McIlwrath, G. Jackson, B. Eichhorn, "Enhanced CO tolerance for hydrogen activation in Au-Pt dendritic heteroaggregate nanostructures", *Journal of the American Chemical Society* **2006**, 128, 1780.
- [151] J. Zeng, J. Yang, J. Y. Lee, W. Zhou, "Preparation of carbon-supported core-shell Au-Pt nanoparticles for methanol oxidation reaction: the promotional effect of the Au core", *The Journal of Physical Chemistry B* **2006**, 110, 24606.
- [152] J. Sachtler, G. Somorjai, "Influence of ensemble size on CO chemisorption and catalytic n-hexane conversion by Au-Pt (111) bimetallic single-crystal surfaces", *Journal of Catalysis* **1983**, 81, 77.
- [153] J. Kraxner, M. Schäfer, O. Röschel, G. Kothleitner, G. Haberfehlner, M. Paller, W. Grogger, "Quantitative EDXS: Influence of geometry on a four detector system", *Ultramicroscopy* **2017**, 172, 30.
- [154] D. Zanaga, T. Altantzis, L. Polavarapu, L. M. Liz-Marzán, B. Freitag, S. Bals, "A New Method for Quantitative XEDS Tomography of Complex Heteronanostructures", *Particle & Particle Systems Characterization* **2016**, 33, 396.
- [155] I. Arslan, T. Yates, N. Browning, P. Midgley, "Embedded nanostructures revealed in three dimensions", *Science* **2005**, 309, 2195.
- [156] S. Pennycook, "Z-contrast STEM for materials science", *Ultramicroscopy* **1989**, 30, 58.
- [157] L. M. Liz-Marzán, "Tailoring surface plasmons through the morphology and assembly of metal nanoparticles", *Langmuir* **2006**, 22, 32.
- [158] N. Liakakos, C. Gatel, T. Blon, T. Altantzis, S. Lentijo-Mozo, C. c. Garcia-Marcelot, L.-M. Lacroix, M. Respaud, S. Bals, G. Van Tendeloo, "Co-Fe Nanodumbbells: Synthesis, Structure, and Magnetic Properties", *Nano letters* **2014**, 14, 2747.
- [159] B. Goris, B. Freitag, D. Zanaga, E. Bladt, T. Altantzis, J. Ringnalda, S. Bals, "Towards Quantitative EDX Results in 3 Dimensions", *Microscopy and Microanalysis* **2014**, 20, 766.
- [160] T. J. Slater, A. Janssen, P. H. Camargo, M. G. Burke, N. J. Zaluzec, S. J. Haigh, "STEM-EDX Tomography of Bimetallic Nanoparticles: A Methodological Investigation", *Ultramicroscopy* **2015**.
- [161] T. Slater, P. Camargo, M. Burke, N. Zaluzec, S. Haigh, "Understanding the limitations of the Super-X energy dispersive x-ray spectrometer as a function of specimen tilt angle for tomographic data acquisition in the S/TEM", presented at *Journal of Physics: Conference Series*, **2014**.

- [162] M. H. Oh, T. Yu, S.-H. Yu, B. Lim, K.-T. Ko, M.-G. Willinger, D.-H. Seo, B. H. Kim, M. G. Cho, J.-H. Park, "*Galvanic replacement reactions in metal oxide nanocrystals*", *Science* **2013**, 340, 964.
- [163] J. Chen, B. Wiley, J. McLellan, Y. Xiong, Z.-Y. Li, Y. Xia, "*Optical properties of Pd-Ag and Pt-Ag nanoboxes synthesized via galvanic replacement reactions*", *Nano letters* **2005**, 5, 2058.
- [164] Y. Sun, Y. Xia, "*Alloying and dealloying processes involved in the preparation of metal nanoshells through a galvanic replacement reaction*", *Nano Letters* **2003**, 3, 1569.
- [165] L. Polavarapu, L. M. Liz-Marzán, "*Growth and galvanic replacement of silver nanocubes in organic media*", *Nanoscale* **2013**, 5, 4355.
- [166] L. Polavarapu, D. Zanaga, T. Altantzis, S. Rodal-Cedeira, I. Pastoriza-Santos, J. Pérez-Juste, S. Bals, L. M. Liz-Marzán, "*Galvanic replacement coupled to seeded growth as a route for shape-controlled synthesis of plasmonic nanorattles*", *Journal of the American Chemical Society* **2016**, 138, 11453.
- [167] A. Chambolle, T. Pock, "*A first-order primal-dual algorithm for convex problems with applications to imaging*", *Journal of Mathematical Imaging and Vision* **2011**, 40, 120.
- [168] E. Y. Sidky, J. H. Jørgensen, X. Pan, "*Convex optimization problem prototyping for image reconstruction in computed tomography with the Chambolle–Pock algorithm*", *Physics in medicine and biology* **2012**, 57, 3065.
- [169] S. E. Skrabalak, J. Chen, Y. Sun, X. Lu, L. Au, C. M. Copley, Y. Xia, "*Gold nanocages: synthesis, properties, and applications*", *Accounts of chemical research* **2008**, 41, 1587.
- [170] E. Gonzalez, J. Arbiol, V. F. Puntes, "*Carving at the Nanoscale: Sequential Galvanic Exchange and Kirkendall Growth at Room Temperature*", *Science* **2011**, 334, 1377.
- [171] A. R. Tao, S. Habas, P. D. Yang, "*Shape control of colloidal metal nanocrystals*", *Small* **2008**, 4, 310.
- [172] X. Hong, D. S. Wang, S. F. Cai, H. P. Rong, Y. D. Li, "*Single-Crystalline Octahedral Au-Ag Nanoframes*", *J. Am. Chem. Soc.* **2012**, 134, 18165.
- [173] K.-K. Liu, S. Tadepalli, L. Tian, S. Singamaneni, "*Size-Dependent Surface Enhanced Raman Scattering Activity of Plasmonic Nanorattles*", *Chem. Mater.* **2015**, 27, 5261.
- [174] Y. Khalavka, J. Becker, C. Sönnichsen, "*Synthesis of Rod-Shaped Gold Nanorattles with Improved Plasmon Sensitivity and Catalytic Activity*", *J. Am. Chem. Soc.* **2009**, 131, 1871.

- [175] X. M. Lu, H. Y. Tuan, J. Y. Chen, Z. Y. Li, B. A. Korgel, Y. N. Xia, "*Mechanistic studies on the galvanic replacement reaction between multiply twinned particles of Ag and HAuCl₄ in an organic medium*", *J. Am. Chem. Soc.* **2007**, 129, 1733.
- [176] C. J. DeSantis, A. C. Sue, M. M. Bower, S. E. Skrabalak, "*Seed-Mediated Co-reduction: A Versatile Route to Architecturally Controlled Bimetallic Nanostructures*", *ACS Nano* **2012**, 6, 2617.
- [177] R. G. Weiner, M. R. Kunz, S. E. Skrabalak, "*Seeding a New Kind of Garden: Synthesis of Architecturally Defined Multimetallic Nanostructures by Seed-Mediated Co-Reduction*", *Acc. Chem. Res.* **2015**, 48, 2688.
- [178] Y.-C. Tsao, S. Rej, C.-Y. Chiu, M. H. Huang, "*Aqueous Phase Synthesis of Au–Ag Core–Shell Nanocrystals with Tunable Shapes and Their Optical and Catalytic Properties*", *J. Am. Chem. Soc.* **2014**, 136, 396.
- [179] L. Au, Y. Chen, F. Zhou, P. H. C. Camargo, B. Lim, Z.-Y. Li, D. S. Ginger, Y. Xia, "*Synthesis and optical properties of cubic gold nanoframes*", *Nano Research* **2008**, 1, 441.
- [180] L. Au, X. Lu, Y. Xia, "*A Comparative Study of Galvanic Replacement Reactions Involving Ag Nanocubes and AuCl₂– or AuCl₄–*", *Adv. Mater.* **2008**, 20, 2517.
- [181] R. G. Weiner, S. E. Skrabalak, "*Seed-Mediated Co-reduction as a Route To Shape-Controlled Trimetallic Nanocrystals*", *Chem. Mater.* **2016**, 28, 4139.
- [182] Y. Yang, J. Liu, Z.-W. Fu, D. Qin, "*Galvanic Replacement-Free Deposition of Au on Ag for Core–Shell Nanocubes with Enhanced Chemical Stability and SERS Activity*", *J. Am. Chem. Soc.* **2014**, 136, 8153.
- [183] J. Zhang, S. A. Winget, Y. Wu, D. Su, X. Sun, Z.-X. Xie, D. Qin, "*Ag@Au Concave Cuboctahedra: A Unique Probe for Monitoring Au-Catalyzed Reduction and Oxidation Reactions by Surface-Enhanced Raman Spectroscopy*", *ACS Nano* **2016**, 10, 2607.
- [184] C. Mahr, P. Kundu, A. Lackmann, D. Zanaga, K. Thiel, M. Schowalter, M. Schwan, S. Bals, A. Wittstock, A. Rosenauer, "*Quantitative determination of residual silver distribution in nanoporous gold and its influence on structure and catalytic performance*", *Journal of Catalysis* **2017**, 352, 52.
- [185] V. Zielasek, B. Jürgens, C. Schulz, J. Biener, M. M. Biener, A. V. Hamza, M. Bäumer, "*Gold catalysts: nanoporous gold foams*", *Angewandte Chemie International Edition* **2006**, 45, 8241.
- [186] J. Zhang, P. Liu, H. Ma, Y. Ding, "*Nanostructured porous gold for methanol electro-oxidation*", *The Journal of Physical Chemistry C* **2007**, 111, 10382.
- [187] C. Xu, J. Su, X. Xu, P. Liu, H. Zhao, F. Tian, Y. Ding, "*Low temperature CO oxidation over unsupported nanoporous gold*", *Journal of the American Chemical Society* **2007**, 129, 42.

- [188] H. Yin, C. Zhou, C. Xu, P. Liu, X. Xu, Y. Ding, "Aerobic oxidation of D-glucose on support-free nanoporous gold", *The Journal of Physical Chemistry C* **2008**, 112, 9673.
- [189] Y. Ding, M. Chen, "Nanoporous metals for catalytic and optical applications", *MRS bulletin* **2009**, 34, 569.
- [190] A. Wittstock, V. Zielasek, J. Biener, C. Friend, M. Bäumer, "Nanoporous gold catalysts for selective gas-phase oxidative coupling of methanol at low temperature", *Science* **2010**, 327, 319.
- [191] A. Wittstock, J. Biener, M. Bäumer, "Nanoporous gold: a new material for catalytic and sensor applications", *Physical Chemistry Chemical Physics* **2010**, 12, 12919.
- [192] H. Pickering, P. Swann, "Electron metallography of chemical attack upon some alloys susceptible to stress corrosion cracking", *Corrosion* **1963**, 19, 373t.
- [193] A. Forty, "Corrosion micromorphology of noble metal alloys and depletion gilding", *Nature* **1979**, 282, 597.
- [194] T. Krekeler, A. V. Straßer, M. Graf, K. Wang, C. Hartig, M. Ritter, J. Weissmüller, "Silver-rich clusters in nanoporous gold", *Materials Research Letters* **2017**, 1.
- [195] L. V. Moskaleva, S. Röhe, A. Wittstock, V. Zielasek, T. Klüner, K. M. Neyman, M. Bäumer, "Silver residues as a possible key to a remarkable oxidative catalytic activity of nanoporous gold", *Physical Chemistry Chemical Physics* **2011**, 13, 4529.
- [196] L. V. Moskaleva, V. Zielasek, T. Klüner, K. M. Neyman, M. Bäumer, "CO oxidation by co-adsorbed atomic O on the Au (321) surface with Ag impurities: A mechanistic study from first-principles calculations", *Chemical Physics Letters* **2012**, 525, 87.
- [197] L. A. Giannuzzi, F. A. Stevie, "A review of focused ion beam milling techniques for TEM specimen preparation", *Micron* **1999**, 30, 197.
- [198] G. Haberfehlner, A. Orthacker, M. Albu, J. Li, G. Kothleitner, "Nanoscale voxel spectroscopy by simultaneous EELS and EDS tomography", *Nanoscale* **2014**, 6, 14563.
- [199] Z. Zhong, B. Goris, R. Schoenmakers, S. Bals, K. J. Batenburg, "3D structure and chemical composition reconstructed simultaneously from HAADF-STEM images and EDS-STEM maps", presented at *European Microscopy Congress 2016: Proceedings*.
- [200] E. Bladt, D. M. Pelt, S. Bals, K. J. Batenburg, "Electron tomography based on highly limited data using a neural network reconstruction technique", *Ultramicroscopy* **2015**, 158, 81.
- [201] L. D. Landau, E. M. Lifshitz, "Quantum mechanics: non-relativistic theory", **1958**.

List of scientific contributions

Journal articles

1. *Governing the morphology of Pt–Au heteronanocrystals with improved electrocatalytic performance.*

Mourdikoudis, S.; Chirea, M.; Zanaga, D.; Altantzis, T.; Mitrakas, M.; Bals, S.; Marzán, L.M.; Pérez-Juste, J.; Pastoriza-Santos, I.
Nanoscale 7.19 (2015): 8739-8747.

Contribution: TEM and electron tomography acquisition, reconstruction and analysis of the characterized nanoparticles.

2. *Measuring lattice strain in three dimensions through electron microscopy.*

Goris, B.; de Beenhouwer, J.; de Backer, A.; Zanaga, D.; Batenburg, K.J.; Sánchez-Iglesias, A.; Liz-Marzán, L.M.; Van Aert, S.; Bals, S.; Sijbers, J.; Van Tendeloo, G.
Nano letters 15.10 (2015): 6996-7001.

Contribution: Alignment and processing of the electron tomography data, structural analysis of the reconstructed lattice.

3. *An alternative approach for ζ -factor measurement using pure element nanoparticles*

Zanaga, D.; Altantzis, T.; Sanctorum, J.; Freitag, B.; Bals, S.
Ultramicroscopy 164 (2016): 11-16.

Contribution: Methodology development and electron tomography/EDXS data acquisition.

4. *Quantitative 3D analysis of huge nanoparticle assemblies*

Zanaga, D.; Bleichrodt, F.; Altantzis, T.; Winckelmans, N.; Palenstijn, W.J.; Sijbers, J.; de Nijs, B.; van Huis, M.A.; Sanchez-Iglesias, A.; Liz-Marzán, L.M.; van Blaaderen, A.; Joost Batenburg, K.; Bals, S.; Van Tendeloo, G.
Nanoscale 8.1 (2016): 292-299.

Contribution: Technique development for 3D nanoparticle assemblies, electron tomography data acquisition, tilt series processing, SSR reconstructions computation and structural analysis.

5. *Supracrystalline Colloidal Eggs: Epitaxial Growth and Freestanding Three-Dimensional Supracrystals in Nanoscaled Colloidosomes*

Yang, Z.; Altantzis, T.; Zanaga, D.; Bals, S.; Van Tendeloo, G.; Pileni, M.-P.
Journal of the American Chemical Society 138.10 (2016): 3493-3500.

Contribution: Tilt series processing, SSR reconstruction computation and structural analysis.

6. *A New Method for Quantitative XEDS Tomography of Complex Heteronanostructures*

Zanaga, D.; Altantzis, T.; Polavarapu, L.; Liz-Marzán, L.M.; Freitag, B.; Bals, S.
Particle & Particle Systems Characterization 33 (2016): 396–403

Contribution: Technique development, electron tomography and EDXS data acquisition, processing, reconstructions computation, analysis and interpretation.

7. *Galvanic Replacement Coupled to Seeded Growth as a Route for Shape-Controlled Synthesis of Plasmonic Nanorattles*

Polavarapu, L.; Zanaga, D.; Altantzis, T.; Rodal-Cedeira, S.; Pastoriza-Santos, I.; Pérez-Juste, J.; Bals, S.; Liz-Marzán, L.M.

Journal of the American Chemical Society 138.36 (2016): 11453-11456.

Contribution: Electron tomography and EDXS data acquisition, processing, reconstructions computation, analysis and interpretation.

8. *Quantitative determination of residual silver distribution in nanoporous gold and its influence on structure and catalytic performance.*

Mahr C.; Kundu P.; Lackmann A.; Zanaga D.; Thiel K.; Schowalter M.; Schwan M.; Bals S.; Wittstock A.; Rosenauer, A.

Journal of Catalysis, (2017) 352, 52-58.

Contribution: Electron tomography and EDXS data acquisition, processing, reconstructions computation, analysis and interpretation.

9. *Composite Supraparticles with Tunable Light Emission*

Montanarella, F.; Altantzis, T.; Zanaga, D.; Rabouw, F. T.; Bals, S.; Baesjou, P.; Vanmaekelbergh, D; van Blaaderen, A.

ACS Nano, (2017), 11 (9), 9136–9142

Contribution: Tilt series processing and reconstruction, structural analysis and interpretation.

10. *Designing Diameter-modulated Heterostructure Nanowires of PbTe/Te by Controlled Dewetting*

Kumar, A.; Kundu, S.; Kundu, P.; Zanaga, D.; Bals, S.; Ravishankar, N.

Submitted

Contribution: Electron tomography/EDXS tilt series processing, reconstruction and analysis.

11. *Advanced electron tomography of nanoparticle assemblies*

Altantzis, T.; Zanaga, D.; Bals, S.

EPL (Europhysics Letters), (2017), 119.3: 38001.

Contribution: writing of portions of the article.

12. *Real space analysis of binary supraparticles with Laves phase*

Wang, D.; Wu, Y.; Zanaga, D.; van der Wee, E. B.; Altantzis T.; Dasgupta, T., Dijkstra, M.; Bals, S.; Murray, C. B.; van Blaaderen, A.

In preparation.

Contribution: Tilt series acquisition, processing, SSR reconstruction computation and structural analysis.

Oral and Poster presentations

A new method for quantitative XEDS tomography of complex hetero-nanostructures

Zanaga, D.; Altantzis, T.; Polavarapu, L.; Liz-Marzán, L.M.; Freitag, B.; Bals, S.

Oral presentation at EMC 2016, held in Lyon (France) from the 28th of August to the 2nd of September 2016

Quantitative 3D analysis of huge nanoparticles assemblies

Zanaga, D.; Bleichrodt, F.; Altantzis, T.; Winckelmans, N.; Palenstijn, W.J.; Sijbers, J.; de Nijs, B.; van Huis, M.A.; Sanchez-Iglesias, A.; Liz-Marzan, L.M.; van Blaaderen, A.; Joost Batenburg, K.; Bals, S.; Van Tendeloo, G.

Poster presentation at EMC 2016, held in Lyon (France) from the 28th of August to the 2nd of September 2016

Quantitative 3D analysis of huge nanoparticles assemblies

Zanaga, D.; Bleichrodt, F.; Altantzis, T.; Winckelmans, N.; Palenstijn, W.J.; Sijbers, J.; de Nijs, B.; van Huis, M.A.; Sanchez-Iglesias, A.; Liz-Marzan, L.M.; van Blaaderen, A.; Joost Batenburg, K.; Bals, S.; Van Tendeloo, G.

Oral presentation at the Chemical Research in Flanders - CRF symposium, held in Blakenberge (Belgium), October 24-26, 2016

Acknowledgements

I would like to thank my supervisor Prof. Dr. Bals for giving me the opportunity of working in such a successful team of talented researchers, providing guidance and managing the exciting research project of which I was part. I would also like to thank all the professors working at EMAT and the members of my PhD committee, who helped, through their comments, suggestions and questions, to shape this thesis to its final form.

My gratitude goes to all the colleagues and collaborators that participated to the projects presented in this thesis; many thanks to Dr. Thomas Altantzis and Dr. Hamed Heidari Mezerji for the teachings, discussions, assistance and help, and to Prof. Luis M. Liz-Marzán and Prof. Alfons van Blaaderen for providing the wonderful samples investigated.

I would also like to thank Lydia Cassiers and Hilde Evans for their administrative assistance, Liesbet Laurens and Dr. Andrea La Porta for her help with the design of the cover for the book, Dr. Eva Bladt for the translations, Dr. Tine Derez and Stijn Van den Broeck for the sample preparations and Niek Lousberg and Dr. Armand Béch  for the technical support at the microscopes.

Many thanks also go to all my colleagues at EMAT and especially to the friends I met here and with whom I shared happy moments and countless amazing Belgian beers: Thomas, Martin, Antonis, Andrea and Marnik.

Finally, I would like to thank my family, my parents Paola and Corrado and my brother Francesco, for always supporting me and believing in me, and my lifelong friends Giorgio, Diego, Umberto and Enrico for the fun, holidays and (remote) company. Special thanks go to my beloved girlfriend, Alessandra, for the sacrifices she had to make to follow me in this adventure, for trusting and supporting me in every moment and for always being by my side.